

## Emergent nonlinear dynamics in photonic lattices

Présentée le 19 janvier 2024

Faculté des sciences et techniques de l'ingénieur  
Laboratoire de photonique et mesures quantiques (STI/SB)  
Programme doctoral en physique

pour l'obtention du grade de Docteur ès Sciences

par

**Aleksandr TUSNIN**

Acceptée sur proposition du jury

Prof. F. Carbone, président du jury  
Prof. T. Kippenberg, directeur de thèse  
Prof. S. Turitsyn, rapporteur  
Dr F. Leo, rapporteur  
Prof. O. Martin, rapporteur



To my mother Inna and my grandparents Nina and Grigory, who gave me everything they  
could and even more...





# Acknowledgements

First, I would like to express my sincere gratitude to my scientific advisor, Prof. Tobias J. Kippenberg, who gave me the opportunity to explore uncharted territories. His support allowed me to approach and overcome challenging problems, fostering an environment where my curiosity and creativity flourished.

I extend my deepest gratitude to my good friend and colleague, Alexey Tikan, for his invaluable support throughout the entire journey of this thesis. Alexey played a pivotal role in ensuring a smooth start to the thesis, and his continued assistance in generating new ideas during countless discussions significantly enriched the research process. Beyond his intellectual contributions, Alexey's unwavering emotional support proved to be crucial for the success of my Ph.D. I am sincerely thankful for everything, and I extend my best wishes to him for continued success in his future endeavors.

I am equally indebted to Antonella Ragnelli, Kathleen Vionnet, and Marta Divall. Antonella who played pivotal roles in shaping my experience as a Ph.D. student. Antonella, your unwavering support over the course of these four and a half years has been invaluable. Whether it was navigating grant proposals, compiling reports, or managing the chronos, your dedication and assistance were instrumental. Kathleen, your support in both administrative matters and personal aspects has greatly eased the challenges of academic life, allowing me to focus more on the scientific pursuit. Marta, your steadfast commitment to the seamless operation of the lab has not gone unnoticed. Your efforts have undoubtedly streamlined the achievement of experiment-related goals within the scope of my thesis. I extend my heartfelt thanks to each of you for your indispensable contributions to my Ph.D. journey.

I extend my sincere thanks to Johann Riemensberger, whose expertise proved invaluable during our SciMe sessions, paper discussions, and in the BM lab whenever support was needed. Johann, your guidance has been crucial, and I am grateful for your willingness to share your knowledge.

I express my appreciation to Yang Liu for the collaborative moments we shared, particularly in our work on mode-locked lasers. Working with you was a pleasure, and I always valued your support, especially during the most challenging moments.

A special thanks goes to Nils Engelsen for his consistent efforts in organizing the renowned beer parties. These events, with their diverse selection of beers, provided not only enjoyable moments but also served as one of the best team-building activities outside the lab. Nils, I

## Acknowledgements

---

truly appreciate your contributions to the team's camaraderie.

I would like to express my heartfelt gratitude to all members of LPQM for their warm welcome when I first joined the lab and for their unwavering support throughout these years. The camaraderie and collaboration within the group have been instrumental in making my Ph.D. journey a fulfilling and enriching experience. Special thanks go to Arslan Raja for his endless positivity and engaging conversations, and to Anat Siddharth for his consistently positive energy and readiness to assist others in various lab activities. I also express my appreciation to Nikolay Kuznetsov for his dedicated work in the lab and his assistance in the BM lab, and to Alisa Davydova for the thoughtful questions and enjoyable discussions we've had. Additionally, I would like to acknowledge Andrey Gelash for our insightful discussions about science and his positive energy, despite joining the team only a few months before my defense.

I extend a special and heartfelt thanks to Mikhail Churaev, a close friend from the very first day in the lab. Misha played a major role in helping me integrate quickly and has been a constant source of support throughout these years. Our conversations, ranging from work-related matters to discussions about skis, music, history, and various other topics, have made this Ph.D. journey more than just a job. Misha, thanks to you, this Ph.D. experience has been enriched in ways that extend beyond the academic realm.

I am incredibly thankful to Anton Lukashchuk, who not only became a close friend during this Ph.D. journey but also played a crucial role in enhancing my understanding of many optics concepts. Anton, I am also grateful to you for always being extremely active and producing many fun ideas no matter where, be it EPFL, group dinner, ski resort, or just during the parties! Your vibrant contributions have added a unique and enjoyable dimension to my Ph.D. experience, and I am sincerely grateful for your friendship and intellectual camaraderie.

I thank Grigorii Likhachev for his diverse life stories, each serving as a valuable lesson. Grisha's openness to share his experiences, coupled with his willingness to assist in the lab, is truly appreciated. His contributions have not only enriched my understanding but have also created a welcoming and supportive environment that I am grateful for.

I thank Dmitrii Pidgayko for the shared moments and his unwavering dedication to executing job tasks with precision. Dima, our connection since our studies at NSU has been enduring, but I want to specifically acknowledge and appreciate the two years we spent working together at EPFL. Your commitment and collaboration have significantly enriched my professional experience, and I am grateful for the friendship we shared during this time.

I extend my sincere thanks to Andrea Triscari. Andrea, your open-mindedness and thorough approach to any subject have been truly appreciated. I'm grateful for the collaborative experience, and I'm pleased to have shared some knowledge with you. Our collaboration was enjoyable, and I'm thankful for the moments of fun we had together. Moreover, thank you for introducing me to some Italian and making the learning experience enjoyable.

I express my gratitude to Miles Anderson for his invaluable assistance in helping me integrate right from the beginning, as well as his willingness to share his knowledge about experiments

and simulations. Miles, it has always been a pleasure to engage in discussions with you on any matter, and I genuinely appreciate your passion for physics. I am fortunate to have worked closely with you throughout these years.

I extend a special thanks to Andrey Voloshin. Andrey, I truly appreciate the moments we shared; they have consistently been filled with joy and fun. Additionally, I am grateful for your valuable advice, which has proven to be immensely helpful to me.

I thank Vladimir Shadymov for his constant support and friendship. Vovan, you are a big man with a big heart. I genuinely appreciate the moments we spent together; they were truly enjoyable and filled with fun.

I extend my heartfelt gratitude to Danila Puzyrev for the meaningful time we spent together in Bath. Danila, despite not knowing each other before my visit to your lab, the two months we spent together allowed us to quickly become good friends, and this connection holds great importance to me. Your teachings have been invaluable for this thesis, and our shared experiences during our time in the UK added a delightful dimension to our collaboration.

I extend my heartfelt thanks to the entire *Bande de ski* – Anton, Misha, Dima, and Grisha—for the countless memorable times we spent flexing and skiing together. Grisha, a special thank you for driving to various resorts and discovering new locations. I'll forever remember the adventure of searching for your lost phone in the powder. I didn't realize before how truly fun it is, and I appreciate your guidance in discovering this enjoyable skill. Anton, your attempts to teach me corks, backflips, and the art of taming dogs and wild cats on a snowboard were not only entertaining but also appreciated. It was a joy to witness your perseverance at M and L kickers, leading to eventual success! I hope the leg you broke while casually riding off-piste won't pose any issues in the future. Misha, thank you for sharing the snowboarding experience with me, adding your distinctive style to it. Additionally, your designed jerseys not only added flair but also enhanced the style of our riding. I am truly grateful for the friendship and fun we shared on the slopes.

I extend my heartfelt thanks to all members of the *Diable Rabattable* band — Andrey Chernev, Asya Dolgikh, Serhii Shyshkanov, Gabrielle Gambardella, Anastasia Komarova, and Misha. You all constitute an integral part of my life, and it is through music that we became friends. I am grateful for the years we spent together, sharing everything and finding unity in the magic of music. Thank you for your unwavering enthusiasm and for coming together to create this band.

I am incredibly thankful to all my friends around the world who have supported me throughout the years. A special appreciation goes to Kirill Nesterov, Kirill Shuklin, Dinar Musin, and Anton Drobinin – my dear friends from Perm – who consistently cheered me up and were always ready to help my family in Perm when I couldn't be there myself. Equally, I extend my thanks to the friends within our university community *BHYK*, particularly to Ivan Popkov, Sergei Tumanov, Egor Sedov, Roman Tostoguzov, Anatolii Lebedev, and Dmitrii Rabusov. It brings me great joy that, even after so many years, we still share many things in common, and our friendship continues to strengthen.

## Acknowledgements

---

I would like to express my sincere gratitude to Prof. David Abramovich Shapiro, my former supervisor at NSU. David Abramovich, thanks to your guidance, I learned how to approach the most challenging problems and find solutions to them. The knowledge and experience you generously shared played a pivotal role in shaping me into a physicist with a strong background in various scientific areas. Furthermore, I deeply appreciate your support during my studies in France, which was instrumental in my development as a scientist. It is with immense gratitude that I acknowledge your significant contribution to my journey, ultimately leading to the successful completion of my Ph.D. at EPFL.

Je tiens à remercier Claude et Bernard Grangier pour les deux premières années où ils m'ont accueilli à Lausanne. J'ai énormément apprécié les moments partagés avec vous. Au cours de ces années, vous m'avez montré la véritable gentillesse humaine par votre exemple à travers vos nombreuses activités bénévoles. Grâce à vous, j'ai appris beaucoup de choses. C'est un grand plaisir d'avoir partagé ces années avec vous et un grand honneur d'être votre ami.

Finally, I want to express my immense gratitude to my family – my mother Inna Tusnina, grandmother Nina Rakintseva, and my wife Anna Matveeva together with our cat Persik. Anya, you have been my unwavering support throughout these years, and everything I have achieved would have been impossible without you. You are the light of my life, always by my side, even during the darkest times. I am grateful to share the joy of life with you and our adorable, silly cat Persik. Мама и бабушка, я безмерно благодарен вам за вашу поддержку во всех моих начинаниях и тем более в моем стремлении к образованию и исследованиям. Именно благодаря вам и вашей самоотверженности, я смог влиться в Новосибирске, Париже и Лозанне, и теперь результаты этой диссертации во многом обязаны именно вам. Спасибо вам больше за всё что вы мне дали!

*Lausanne, December 18, 2023*

A. T.

# Abstract

Since the discovery of dissipative Kerr solitons in optical microresonators, significant progress has been made in the understanding of the underlying physical principles from the fundamental side and generation of broadband coherent optical Kerr frequency combs from the applied side. Rich nonlinear dynamics of the discovered coherent dissipative structures have been explored and widely applied from distance measurements and telecommunication to neuromorphic optical computing. However, these studies were mostly limited to the single-resonator case, in which the nonlinear dynamics is essentially one-dimensional. On the other hand, increasing the number of particles (i.e., resonators) and creating new dimensions in photonic devices are expected to provide a plethora of novel dynamical effects with a fundamental and technological potential, which however remains an uncharted territory, with the large capacity for both theoretical and experimental explorations.

With this thesis, we explore this direction by investigating the nonlinear dynamics in various lattices of nonlinear optical microresonators, extending the conventional single-resonator paradigm. We consider two types of photonic lattices: synthetic and spatial. Providing the analytical, numerical, and experimental studies, we investigate emerging four-wave mixing processes, chaotic states, and formation of coherent structures. In the synthetic frequency dimension framework, we consider electro-optically and dispersion modulated resonators, demonstrating the formation of novel nonlinear states as well and related new four-wave mixing pathways that result in the spectral broadening of frequency combs. In the case of coupled resonators, we investigate parametric processes, existence and stability of coherent structures and demonstrate potential applications for optical parametric oscillators and microwave signal generation. We also develop a general theory of nonlinear dynamics and Kerr frequency comb formation in lattices of resonators, demonstrating the multidimensional nature of the nonlinear processes in such systems. We investigate in detail the two-dimensional spatio-temporal dynamics in chains of equally coupled resonators. Finally, we describe an open-source software – PyCOrE, developed during the course of this thesis, which allows simulation of nonlinear dynamics in the systems under consideration.

**Keywords:** dissipative Kerr solitons, nonlinear photonics, nonlinear dynamics, spatio-temporal locking, optical parametric oscillators, modulation instability.



# Résumé

Depuis la découverte de solitons dissipatifs de Kerr dans les microrésonateurs optiques, des progrès significatifs ont été réalisés dans la compréhension des principes physiques sous-jacents du côté fondamental et la génération de peignes de fréquence de Kerr optiques cohérents à large bande du côté appliqué. La dynamique non linéaire riche des structures dissipatives cohérentes découvertes a été explorée et largement appliquée des mesures de distance et de télécommunication au calcul optique neuromorphique. Cependant, ces études ont été principalement limitées au cas de résonateur unique, dans lequel la dynamique non linéaire est essentiellement unidimensionnelle. D'autre part, l'augmentation du nombre de particules (c'est-à-dire des résonateurs) et la création de nouvelles dimensions dans les dispositifs photoniques devraient fournir une pléthore d'effets dynamiques nouveaux avec un potentiel fondamental et technologique, qui reste cependant un territoire inexploré, avec la grande capacité pour les explorations théoriques et expérimentales.

Avec cette thèse, nous explorons cette direction en étudiant la dynamique non linéaire dans divers réseaux de microrésonateurs optiques non linéaires, en étendant le paradigme conventionnel à résonateur unique. Nous considérons deux types de réseaux photoniques : synthétique et spatial. En fournissant les études analytiques, numériques et expérimentales, nous étudions les processus de mélange à quatre ondes émergents, les états chaotiques et la formation de structures cohérentes. Dans le cadre de la dimension de fréquence synthétique, nous considérons les résonateurs modulés électro-optiquement et de dispersion, démontrant la formation de nouveaux états non linéaires ainsi que de nouvelles voies de mélange à quatre ondes connexes qui entraînent l'élargissement spectral des peignes de fréquence. Dans le cas des résonateurs couplés, nous étudions les processus paramétriques, l'existence et la stabilité de structures cohérentes et démontrons des applications potentielles pour les oscillateurs paramétriques optiques et la génération de signaux micro-ondes. Nous développons également une théorie générale de la dynamique non linéaire et de la formation de peignes de fréquence de Kerr dans les réseaux de résonateurs, démontrant la nature multidimensionnelle des processus non linéaires dans de tels systèmes. Nous étudions en détail la dynamique spatio-temporelle bidimensionnelle dans les chaînes de résonateurs également couplés. Enfin, nous décrivons un logiciel open-source – PyCORE, développé au cours de cette thèse, qui permet la simulation de dynamiques non linéaires dans les systèmes considérés.

**Mots-clés :** solitons dissipatifs de Kerr, photonique non linéaire, dynamique non linéaire, verrouillage spatio-temporel, oscillateurs paramétriques optiques, instabilité modulationnelle.





# Publication List

## Main publications

- **A. Tusnin**, A. Tikan, and T. J. Kippenberg, “Nonlinear states and dynamics in a synthetic frequency dimension,” *Physical Review A* **102**, (2020)
- **A. Tusnin**, A. Tikan, K. Komagata, and T. J. Kippenberg, “Nonlinear dynamics and Kerr frequency comb formation in lattices of coupled microresonators,” *Communications Physics* **6**, (2023)
- **A. Tusnin**, A. Tikan, and T. J. Kippenberg, “Dissipative Kerr solitons at the edge state of the Su-Schrieffer-Heeger model”, *Journal of Physics: Conference Series*, Volume 2015, 012159 (2021)
- A. Tikan, **A. Tusnin**, J. Riemensberger, M. Churaev, X. Ji, K. Komagata, R. N. Wang, J. Liu, and T. J. Kippenberg, “Protected generation of dissipative Kerr solitons in supermodes of coupled optical microresonators”, *Science Advances* **8**, (2022)
- D. Pidgayko, **A. Tusnin**, J. Riemensberger, A. Stroganov, A. Tikan, and T. J. Kippenberg, “Voltage-tunable optical parametric oscillator with an alternating dispersion dimer integrated on a chip,” *Optica* **10**, (2023)
- A. Triscari, **A. Tusnin**, A. Tikan, and T. J. Kippenberg, “Quiet point engineering for low-noise microwave generation with soliton microcombs,” *Communications Physics* **6**, (2023)
- K. Komagata, **A. Tusnin**, J. Riemensberger, M. Churaev, H. Guo, A. Tikan, and T. J. Kippenberg, “Dissipative Kerr solitons in a photonic dimer on both sides of exceptional point,” *Communications Physics* **4**, (2021)
- M.H. Anderson, A. Tikan, **A. Tusnin**, J. Riemensberger, A. Davydova, R. N. Wang, and T. J. Kippenberg, “Dissipative solitons and switching waves in dispersion-modulated Kerr cavities,” *Physical Review X* **13** (2023)

## Publication List

---

### Additional contributions

- A. Lukashchuk, J. Riemensberger, **A. Tusnin**, J. Liu, and T. J. Kippenberg, “Chaotic micro-comb based parallel ranging,” *Nature Photonics* (2023)
- Y. Yang, J. W. Henke, A.S. Raja, F.J. Kappert, G. Huang, G. Arend, Z. Qiu, A. Feist, R. N. Wang, **A. Tusnin**, A. Tikan, C. Ropers, and T. J. Kippenberg, “Free-electron interaction with nonlinear optical states in microresonators,” *arXiv:2307.12142* (2023) (accepted to publication in *Science*)

# Contents

<b>Acknowledgements</b>	<b>i</b>
<b>Abstract (English/Français)</b>	<b>v</b>
<b>Publication List</b>	<b>ix</b>
<b>Introduction</b>	<b>1</b>
<b>I Synthetic Dimensions</b>	<b>13</b>
<b>1 Synthetic frequency dimension in electro-optic modulated cavities</b>	<b>15</b>
1.1 Introduction . . . . .	15
1.2 Theory . . . . .	16
1.3 Numerical simulations . . . . .	20
1.3.1 Dynamics of dissipative solitons and platicons . . . . .	20
1.3.2 Confined MI region . . . . .	22
1.3.3 Band Soliton . . . . .	24
1.3.4 Chimera-like states . . . . .	27
1.4 Conclusion . . . . .	28
<b>2 Synthetic frequency dimension in a dispersion-modulated resonator</b>	<b>31</b>
2.1 Introduction . . . . .	31
2.2 Two-dimensional photon transfer . . . . .	32
2.3 Modulation instability . . . . .	34
2.3.1 Faraday instability . . . . .	35
2.4 Dissipative Kerr Solitons And Switching Waves . . . . .	38
2.4.1 Dissipative Kerr solitons . . . . .	38
2.4.2 Switching Waves . . . . .	38
2.5 Conclusion . . . . .	40
<b>II Lattices Of Resonators</b>	<b>41</b>
<b>3 Optical Parametric Oscillations in a Photonic Dimer</b>	<b>43</b>
3.1 Introduction . . . . .	43

## Contents

---

3.2	Description of the parametric gain . . . . .	44
3.3	Experimental Demonstration . . . . .	46
3.4	Pump suppression . . . . .	49
3.5	Conclusion . . . . .	50
<b>4</b>	<b>Quiet points in a coupled resonator system</b>	<b>51</b>
4.1	Introduction . . . . .	51
4.2	QP with a single-mode displacement . . . . .	52
4.3	Two-mode displacement for QP engineering . . . . .	55
4.4	Dynamical simulation of the phase noise transfer . . . . .	57
4.5	Conclusion . . . . .	58
<b>5</b>	<b>Dissipative Kerr solitons in dimers</b>	<b>61</b>
5.1	Introduction . . . . .	61
5.1.1	Exceptional point as a demarcation of the critical coupling conditions . . . . .	61
5.1.2	Critical coupling conditions . . . . .	63
5.1.3	Eigenvalues and exceptional points . . . . .	64
5.2	Critically coupled resonators: split resonance . . . . .	65
5.2.1	Four-wave mixing pathways between supermodes . . . . .	65
5.2.2	Nonlinear dynamics and soliton generation in split resonance regime . . . . .	67
5.2.3	Experimental and numerical evidences of the deterministic single soliton generation . . . . .	72
5.3	Critically coupled resonators: split dissipation . . . . .	74
5.3.1	Phase diagram: inter-resonator coupling vs pump power . . . . .	74
5.3.2	Deterministic soliton crystal and efficient comb generation . . . . .	76
5.3.3	Bright-dark solitons coexistence and their interaction with periodic coherent structures . . . . .	77
5.4	Conclusion . . . . .	79
<b>6</b>	<b>Avoided mode-crossings and dissipative solitons in coupled resonators</b>	<b>81</b>
6.1	Introduction . . . . .	81
6.1.1	Photonic dimer . . . . .	82
6.1.2	Photonic trimer and plaquette . . . . .	83
6.1.3	Model of mode crossing suppression . . . . .	84
6.2	Protection of topological states in the Su–Schrieffer–Heeger model . . . . .	87
6.3	Conclusion . . . . .	88
<b>7</b>	<b>Nonlinear dynamics in lattices of coupled resonators</b>	<b>91</b>
7.1	Introduction . . . . .	91
7.2	General theory . . . . .	92
7.3	Chain of equally coupled resonators . . . . .	94
7.3.1	Spatial eigenstates and pump projection on the chain . . . . .	94
7.3.2	Modulation instability gain lobes. . . . .	95

7.3.3	Wave collapse . . . . .	97
7.3.4	Coherent dissipative structures . . . . .	98
7.4	Su-Schrieffer-Heeger model . . . . .	101
7.5	Conclusion . . . . .	105
<b>8</b>	<b>Conclusion and Outlook</b>	<b>107</b>
<b>A</b>	<b>Appendix to chapter 3</b>	<b>111</b>
A.1	Pump suppression . . . . .	111
A.2	Resonators design . . . . .	112
A.3	Experimental setup and uncoupled dispersion . . . . .	113
A.4	Detuning calibration . . . . .	113
<b>B</b>	<b>Appendix to chapter 4 — Quiet points in a coupled resonator system</b>	<b>117</b>
B.1	Newton-Raphson method . . . . .	117
B.2	Dynamical simulation of the noise transduction. . . . .	119
<b>C</b>	<b>Appendix to chapter 5 — Dissipative kerr solitons in dimers</b>	<b>123</b>
C.1	Projection into supermodes . . . . .	123
C.1.1	Single longitudinal mode closed system . . . . .	123
C.1.2	Derivation with complex inter-resonator detuning . . . . .	124
<b>D</b>	<b>Appendix to chapter 6 — Avoided mode-crossings and dissipative solitons in coupled resonators</b>	<b>127</b>
D.1	Numerical simulations of soliton generation in a degenerate photonic plaquette	127
D.2	Additional experimental data . . . . .	128
D.3	Mode interactions in two evanescently coupled resonators . . . . .	130
D.4	Matrix model . . . . .	133
D.5	FDTD simulations of the coupling section . . . . .	134
<b>E</b>	<b>Appendix: numerical simulations with PyCOrE</b>	<b>137</b>
E.1	Functionality and utilities . . . . .	137
E.2	Installation . . . . .	138
E.3	Solver architecture . . . . .	139
E.3.1	Code structure . . . . .	140
E.4	Examples . . . . .	151
E.4.1	Single LLE soft excitaton . . . . .	151
E.4.2	Hard seeding of solitons . . . . .	153
E.4.3	Nonlinear dispersion relation . . . . .	155
E.4.4	Two coupled resonators . . . . .	161
	<b>Bibliography</b>	<b>182</b>
	<b>Curriculum Vitae</b>	<b>183</b>



# Introduction

Nonlinear phenomena have been extensively studied in various physical systems over the past decades [1]. Unlike linear systems, where the principle of superposition holds true (the combination of two solutions of the governing equation results in another valid solution), nonlinear systems described by nonlinear partial differential equations (PDEs) lack this property. Interactions between different solutions (e.g., waves) can result in complex and unexpected dynamics [2].

One of the manifests of nonlinear phenomena is chaos – a particular state of a system characterized by extremely sensitive dependence on initial conditions. One of such chaotic systems is the Lorenz model for cellular convection [3]. Another phenomenon characterized by irregular behavior is turbulence, which is commonly observed in fluid and air flows, magnetohydrodynamics, and other fields [4]. Despite its extreme complexity, turbulence plays a crucial role in various systems, enabling the effective distribution of energy across turbulent cascades [5]. However, nonlinear interactions also result in self-organization effects when ordered structures emerge from an initially disordered system state [2]. Such pattern formation plays an important role in understanding complex systems and has been observed in many models, including the Brusselator system [6], Gross-Pitaevsky equation [7] for Bose-Einstein condensate, and the Lugiato-Lefever equation (LLE) [8, 9, 10]. Another important aspect in such systems is the existence of localized and self-sustaining wave-like solutions called solitons [11, 12, 13, 14]. Their existence relies on the delicate balance between dispersion (diffraction) that tends to broaden the pulse and nonlinearity, responsible for the focusing. Although this thesis primarily focuses on the study of nonlinear interactions arising from four-wave mixing (FWM) processes in optical microresonators [15], a branch of nonlinear optics, it also delves into various phenomena that manifest across different areas of physics. These effects encompass many nonlinear phenomena discussed earlier, such as Turing pattern formation [16], dynamics of dissipative solitons (DKS) [15], wave collapses [17], and more. We investigate these phenomena using the LLE as a basis, modifying it according to the specific characteristics of the studied systems. Our research covers synthetic dimensions and lattices of coupled microresonators, where we connect our observations with existing models and explore potential applications in the field of optical frequency combs.

### Solitons

Solitons, as localized pulses, can arise in both conservative and open systems and play a crucial role in understanding the nonlinear dynamics of a given model. Their investigation is often sufficient to fully describe field dynamics in many conservative models, which can be generalized further to open systems with gain and loss.

Since soliton initial discovery by Scott Russell in 1834 [18], soliton theory has undergone several significant developments. The first model inspired by Russell's findings was the description of waves on shallow water surfaces through the Korteweg–de Vries (KDV) equation. The "solitary-wave pulses" were initially discovered through numerical simulations by N. J. Zabusky and M. D. Kruskal [19], leading to the development of the inverse scattering transform (IST) [20]—a foundational concept in soliton theory for many conservative nonlinear equations [21].

The general idea behind this method lies in the transformation of the original nonlinear problem (e.g., initial value problem for the KDV equation) into a linear scattering problem, which is less challenging to understand due to existing methods for linear equations. As a result, the temporal evolution of the nonlinear field is mapped onto the dynamics of the scattering data. In this approach, a significant challenge lies in identifying the suitable linear equation. Later, Zakharov and Shabat extended the method, introducing a systematic approach to discovering these equations [22], which led to the demonstration of integrability of many other nonlinear PDE [23, 24], including the Nonlinear Schrödinger equation (NLSE) [22].

In nonlinear optics, the NLSE plays a crucial role as it serves as a fundamental model for many optical effects, including self-phase modulation (SPM), self-focusing or defocusing, solitons, and more, all of which are caused by optical Kerr nonlinearity [25]. The NLSE describes light propagation in various optical platforms, including bulk nonlinear media [26, 27] and optical fibers [28, 29], for which the equation for the optical field envelope  $E$  can be written as

$$\frac{\partial E}{\partial z} = -i \frac{\beta_2}{2} \frac{\partial^2 E}{\partial \tau^2} + i\gamma |E|^2 E, \quad (1)$$

where  $z$  is longitudinal coordinate along the fiber (waveguide),  $\tau$  is the time window for the pulse,  $\beta_2$  is the group velocity dispersion, and  $\gamma = \omega_0 n_2 / c A_{\text{eff}}$ , where  $\omega_0$  is the carrier frequency,  $n_2$  is the nonlinear refractive index,  $c$  is the speed of light,  $A_{\text{eff}}$  is the effective mode area. Fused silica fibers, known for their extremely low propagation losses, have not only revolutionized the field of optical communications [30] but have also provided an excellent platform for testing the NLSE. Extensive experimental studies on temporal solitons, breathers, integrable turbulence, rogue waves, and more [29, 31, 32, 33, 34, 35] have successfully demonstrated a high degree of agreement with the theoretical predictions, significantly advancing our understanding of nonlinear physics.



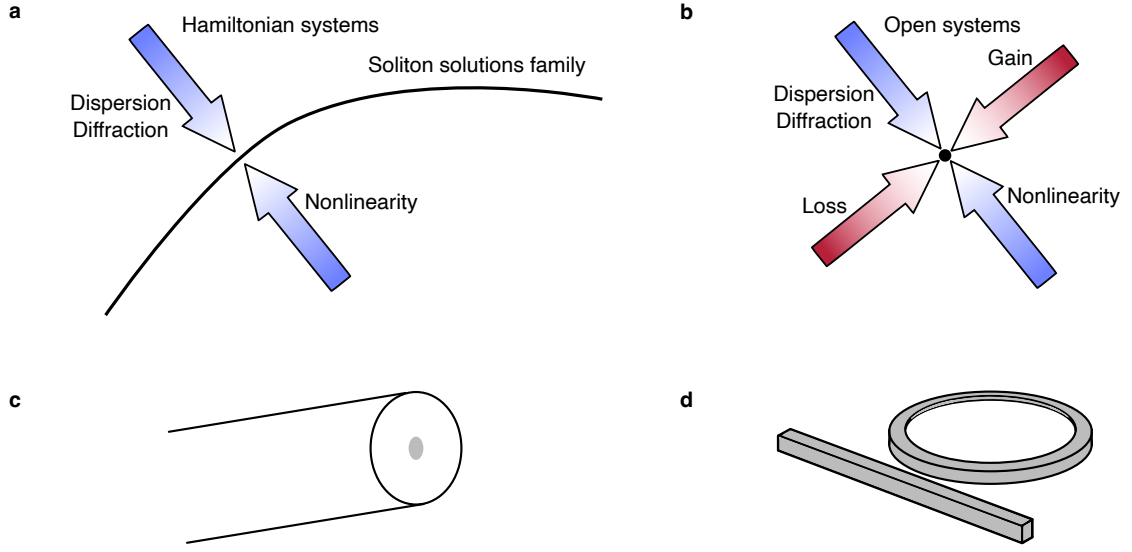


Figure 1: **Schematics of soliton balance in different systems.** a) Hamiltonian and b) open systems with gain and loss. c) Schematics of an optical fiber in panel (c) and of a microresonator in panel (d). The figure design is inspired by Ref. [36]

## Dissipative Solitons

Integrable models, such as KDV or NLSE, have a distinct property due to their conservative nature: the soliton solutions, existing due to the balance between dispersion and nonlinearity, usually form a family of solutions, e.g., NLSE solitons with the same amplitude can also have different velocities [22]. Schematically, this concept can be represented as in Fig. 1a. On the other hand, open systems require an additional balance between gain and loss to maintain localized solutions [37, 36]. As a result, such *dissipative* solitons are characterized as dynamical attractors and can possess non-trivial energy flows within themselves to maintain the loss-gain balance (see Fig. 1b). Consequently, interactions between such solitons can result in the annihilation or the formation of soliton molecules [38], in contrast to their conservative counterparts that do not interact during the collision and acquire only an additional phase shift [39, 40]. This striking difference can be observed in two seemingly close systems: an optical fiber, schematically presented in Fig. 1c, and an optical microresonator, shown in Fig. 1d.

However, conservative models can be connected to the dissipative using standard approaches, such as modulation instability analysis, or they can be treated in the perturbative way, where the terms responsible for the gain and loss are considered as corrections to the unperturbed Hamiltonian. The approaches such as the method of moments [41], Lagrangian method [42], and IST-based perturbation theory [43, 44], help to reduce system's complexity and understand soliton interactions.

### Dissipative Kerr Solitons

In context of this thesis, an integrable basis model is the NLSE presented in Eq. (1). However, here we work with resonant systems, i.e., the optical waveguide is closed in a loop, forming a resonator, with an output coupler at  $z = L$ , which introduces losses in the system and allows for synchronous pumping. To include this element into the model, one can impose the boundary conditions at  $z = L$

$$E^{n+1}(\tau, z = 0) = \sqrt{\Theta} E_{\text{in}} + \sqrt{1 - \Theta} e^{i\phi_0} E^n(\tau, z = L), \quad (2)$$

connecting the optical field at  $n$  and  $n + 1$  roundtrips,  $\Theta$  is the coupling coefficient of the coupler,  $E_{\text{in}}$  is the input field that compensates the energy losses from the cavity,  $\phi_0$  is the phase acquired by the pulse during its propagation in the cavity. This condition, together with Eq. (1), corresponds to the approach known as Ikeda map, which is often used to describe resonant systems [45, 46, 47]. However, to facilitate the analytical treatment, this equation can be reduced to the mean-field model known as the LLE

$$\frac{\partial A}{\partial \tau} = i \frac{D_2}{2} \frac{\partial^2 A}{\partial \varphi^2} + i g_0 |A|^2 A - \left( \frac{\kappa_0 + \kappa_{\text{ex}}}{2} + i \delta \omega_0 \right) A + \sqrt{\kappa_{\text{ex}}} S_{\text{in}} \quad (3)$$

that describes temporal evolution of optical field envelope in a microresonator (see Fig. 1d). First two terms constitute the NLSE, while the last two terms represent the loss and the external forcing. The optical field envelope  $A$  is normalized such as  $\int |A|^2 d\varphi / 2\pi$  represents the number of photons circulating in the cavity.  $D_1 = (\omega_1 - \omega_0) / 2 = 2\pi / \beta_1 L_R$  is the mode spacing in the vicinity of the pump mode  $\omega_0$ .  $L_R$  is the cavity length,  $\beta_1 = n_g / c$  is the group velocity defined via the group index  $n_g$  and speed of light  $c$ ,  $\varphi$  is the azimuth coordinate inside the resonator,  $g_0$  is the single photon Kerr frequency shift,  $\kappa_0$  is the loss rate of the resonator arising due to the internal and scattering losses,  $\kappa_{\text{ex}}$  is the coupling rate to the bus waveguide,  $\delta \omega_0$  is the pump-cavity detuning,  $S_{\text{in}} = \sqrt{P / \hbar \omega}$  is the pump term, and  $D_2$  is the group velocity dispersion (GVD) defined through the integrated dispersion  $D_{\text{int}}(\mu) = \omega_\mu - \mu D_1 = \beta_2 D_1^2 / \beta_1$ , where  $\omega_\mu$  is the frequency of the  $\mu$ -th optical resonance. In general, the GVD depends on the mode profile since its value is defined by the material and geometric dispersion. Positive (negative)  $D_2 > (<) 0$  corresponds to the anomalous (normal) GVD. For example, the fundamental mode TE 00 in Fig. 2a is mainly localized in the waveguide, which has a different refractive index compared to its surroundings. On the other hand, the higher order mode TE 10 shown in Fig. 2b has a larger effective area and "feels" the surrounding material more, resulting in a different effective refractive index due to the geometric dispersion. Due to this effect, the actual position of the resonators modes are not equally spaced, as shown in Fig. 2c, and the integrated dispersion  $D_{\text{int}}(\mu)$ , presented in Fig. 2d, is introduced as a deviation measure of the actual resonance position from the equidistant grid. The dispersion profile can be engineered via changing the cavity geometry, resulting in the generation of different optical pulses.

During the last decades, the LLE was extensively studied in context of passive optical systems under external forcing for both, spatial and temporal self-organization effects [10, 48, 49, 50,

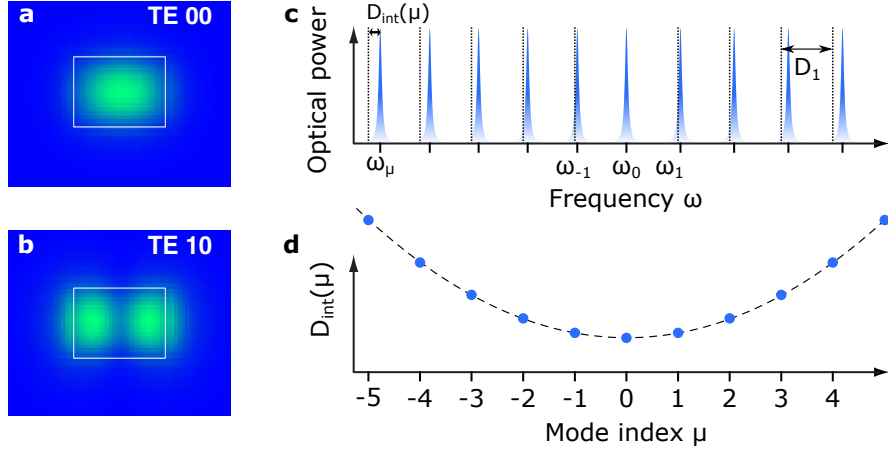


Figure 2: **Dispersion of optical modes.** Spatial mode profiles in an optical waveguide for the fundamental TE 00 mode in panel a) and the higher-order mode TE 10 in panel b). c) Schematics of the cavity resonances of a given mode family. d) Corresponding integrated dispersion profile  $D_{\text{int}}(\mu)$ .

51]. It can also be written in the dimensionless units as

$$\frac{\partial \Psi}{\partial t} = i d_2 \frac{\partial^2 \Psi}{\partial \varphi^2} + i |\Psi|^2 \Psi - (1 + i \zeta_0) \Psi + f, \quad (4)$$

where  $t = \tau \kappa / 2$ ,  $\zeta_0 = 2\delta\omega_0/\kappa$  with  $\kappa = \kappa_0 + \kappa_{\text{ex}}$ ,  $d_2 = D_2/\kappa$ ,  $\Psi = \sqrt{2g_0/\kappa} A$ ,  $f = \sqrt{8\kappa_0 g_0/\kappa^3} S_{\text{in}}$ . This model, which depends only on two parameters  $\zeta_0$  and  $f$ , captures with a very high accuracy in the limit of high cavity finesse<sup>1</sup>  $\mathcal{F} \gg 1$ . Interestingly, the rich dynamics and the whole the variety of states inherent to the LLE can be tracked only through two parameters  $\zeta_0$  and  $f^2$  and can be mapped on the stability chart that demonstrates existence regions of Turing rolls, chaotic states, breathers, and DKS, shown in Fig. 3a. Instead, for low finesse cavities or in the high power regime ( $f^2 \gg 1$ ), the Ikeda map scheme presented in Eq. (1,2) should be used to describe the cavity dynamics [52]. However, the mean-field form helps to employ different methods that we present below to analyze the dynamics.

### Bistability

Bistability is ubiquitous in nonlinear systems, and the LLE is no exception. To analyze it, one simply needs to neglect the dispersion term in Eq. (4) and derive the governing equation for  $I = |\Psi|^2$ , considering only stationary solutions. The resulting equation

$$I(1 + (I - \zeta_0)^2) - f^2 = 0 \quad (5)$$

<sup>1</sup> $\mathcal{F} = \tau_{\text{ph}}/T_R = 2\pi \cdot \text{FSR}/\kappa \gg 1$ , where  $\tau_{\text{ph}}$  is the photon lifetime inside the microresonator,  $\kappa = 1/\tau_{\text{ph}}$ ,  $T_R$  is the roundtrip time and the free spectral range (FSR) defined as  $\text{FSR} = 2\pi/T_R$ . Finesse defines the number of roundtrips one photon makes before decaying.

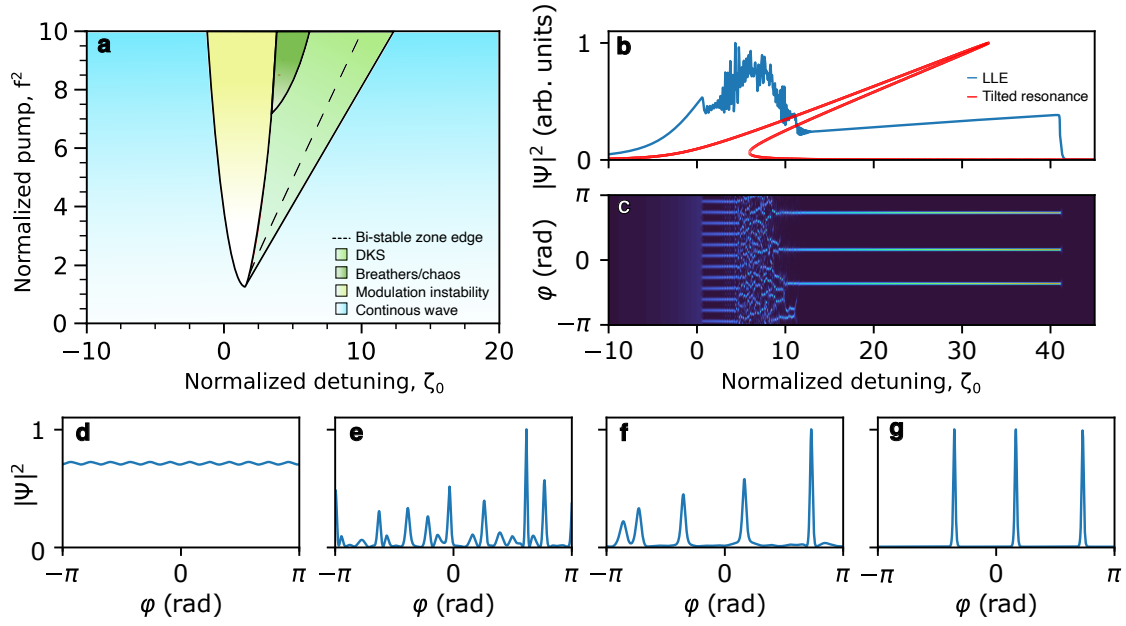


Figure 3: **Dissipative Kerr solitons (DKS).** a) Numerically reconstructed stability chart of the LLE. b) The cavity response as a function of detuning ( $\zeta_0$ ) at pump power  $f^2 = 33$ . Blue line corresponds to the simulations of the Lugiato-Lefever equation (LLE) (4), red line shows the stationary solutions of the dispersionless LLE, demonstrating the bistable region. c) Spatial-temporal dynamics of  $|\Psi|^2$  corresponding to panel (b). (d-g) Snapshots of different LLE solutions: Turing rolls (d), chaotic MI state (e), breathers (f), and DKS (g).

is cubic in  $I$ ; hence, it has three solutions. Under low pump power conditions ( $f^2 \ll 1$ ), there is always one real and a couple of complex conjugate roots. However, for  $f^2 > 8\sqrt{3}/9$ , a region with three possible real solutions appears (see red line in Fig. 3b) [53]. The upper and lower branches are the stable solutions, while the middle one is unstable, resulting in the name *bistable region*. Interestingly, this region almost covers the soliton existence range shown in the stability chart in Fig. 3a (the edge of the bistable zone depicted as the dashed line). The exact soliton existence range can be obtained via the Lagrangian perturbative approach, which can be found in Ref. [48, 54] and in chapter 1.

Once the dispersion is taken into account, the resonance response shows additional features (blue line in Fig. 3b). Before the bistable zone, the curve does not follow a smooth profile anymore and shows a breaking point, followed by incoherent dynamics and oscillating and constant behavior afterwards. Resolving the field along the azimuth coordinate  $\varphi$  as shown in Fig. 3c, one can observe formation of pulses that we describe below.

### Turing Rolls

First, in the vicinity of  $\zeta_0 \approx 1$ , the continuous wave (CW) field breaks into several pulses known as Turing rolls (or cnoidal waves) [16]. The main mechanism responsible for this behavior is modulation instability (MI), which plays a major role in many Kerr nonlinear cavities with anomalous dispersion ( $d_2 > 0$ ). Due to the four-wave mixing processes, photons from the pump mode are converted into a couple of sidebands, forming a modulated field profile shown in Fig. 3d. The modulation depth and period depend on the pump power, detuning, dispersion value, and losses [55]. Increasing the pump power and detuning, these structures can experience different instabilities [16, 51], but they can also emerge as a periodic train of pulses, connecting them closely to single DKS and soliton crystals [56, 50].

Moreover, in most experiments involving frequency comb generation with microresonators, in order to access the soliton state, the cavity is first excited in the Turing rolls regime. The optical spectra of Turing rolls can be as large as DKS and achieve high conversion efficiency [57]. Due to these properties, these dissipative structures can be used as chip-scale optical hyperparametric oscillators (OPOs) [58, 59].

### Chaotic States and Breathers

Since the LLE is an open system, stable structures exist only within a specific region of parameter space as dynamical attractors [38]. Outside of these regions, the generated structures can experience different instabilities, such as Hopf or saddle-node bifurcations [60, 61, 62, 51]. The resulting field dynamics can be completely incoherent, as shown in Fig. 3c in the region  $\zeta_0 \in (5, 7)$  and in Fig. 3e, manifesting collisions between different pulses, or breathing, leading to periodic oscillations of the generated structures (e.g., soliton breathers in Fig. 3f). In the highly nonlinear regime, field dynamics becomes turbulent with positive Lyapunov expo-

## Introduction

---

nents and can induce the appearance of rogue waves in such resonators [9, 63]. Despite its unpredictable dynamics, chaotic states are found to be useful for soliton switching [64] and in chaotic lidar [65].

## Localized Structures

Tuning the laser frequency further beyond the chaotic states region results in the extraction of several pulses that, if they are well separated, do not interact anymore and can coexist together (see Fig. 3b,c,g). The exact form of these solutions is not known to date, however it can be approximated using the Lagrangian perturbative approach [48, 54] as

$$\Psi = \Psi_{CW} + \sqrt{2\zeta_0} \operatorname{sech} \left( \sqrt{\frac{\zeta_0}{d_2}} \varphi \right) e^{i\phi_S}, \quad (6)$$

where  $\operatorname{sech}$  is the hyperbolic secant,  $\phi_S = \arccos \frac{\sqrt{8\zeta_0}}{f\pi}$  is the DKS phase, and  $\Psi_{CW} = \sqrt{I}$  is the lower branch of the CW solution of Eq. (5). The exponential in the latter yields the soliton existence range as

$$\zeta_{\max} = \frac{\pi^2 f^2}{8}. \quad (7)$$

The Lagrangian approach proposes to treat the LLE as a perturbed NLSE, resulting in a soliton solution close to the fundamental soliton in NLSE. However, the main difference here is that the soliton exists on a CW background and propagates without any changes; this situation in NLSE corresponds to the Kuznetsov-Ma breather – a soliton solution experiencing periodic dynamics in time [11, 66, 67]. This difference is also encompassed by the non-preserved IST spectrum introduced in Refs. [68, 69, 70], which shows that discrete eigenvalues identifying the solitonic content indeed correspond to the Kuznetsov-Ma breather.

In the normal dispersion regime, the nonlinear dynamics of such cavities drastically differ due to the different dynamics of MI. While in the anomalous dispersion case, the regime of positive parametric gain can be readily achieved [53], for pure normal dispersion, the MI gain lobes appear only in a narrow region of parameters and are very challenging to observe [71]. As a result, chaotic dynamics similar to Fig. 3c,e do not occur, and soft excitation (via external laser tuning through the MI region) of coherent structures remains challenging. However, normal-dispersion cavities support dark solitons [53] (also known as platicons [72] due to their flat top profile) that also exist in the cavity bistable region. Their existence is ensured due to the coexistence of two CW solutions: lower and upper branch roots of Eq. (5) interconnected via the so-called switching waves [73]. In practice, platicons are usually generated in a system with mode-crossings that change the phase-matching condition and facilitate the comb generation [74, 75]. It is also important to note that DKS and platicons are related to each other, as shown in Ref. [76]. In this paper, the authors investigated the dynamics of so-called zero-dispersion solitons, where 3rd order dispersion dominates over the group velocity dispersion, and demonstrated that these solutions form a family of structures

that include DKS in the pure anomalous and platicons in the pure normal dispersion regimes.

Concluding, microresonator frequency combs and DKS in particular have attracted significant attention after their first discovery in 2014 [77] due to the possibility of generation coherent and broadband microresonator frequency combs [15]. These properties resulted in novel applications from distance measurements and telecommunication to neuromorphic optical computing [78, 79, 80, 81, 82, 83].

## Photonic lattices

With this thesis, we aim to extend the conventional single-resonator systems in two ways that result in the photonic lattices: via creating synthetic dimensions [84] or a photonic crystal of coupled microresonators [85]. Increasing the number of particles and creating new dimensions in photonic devices are expected to provide a plethora of novel dynamical effects with a fundamental and technological potential, which exploration both theoretically and experimentally remains uncharted territory.

## Synthetic Dimensions

The idea of unification of physical theories by using higher dimensional models beyond the usual space-time paradigm has arisen in the early years of development of quantum mechanics [86] and became an important precursor for modern unification theories [87]. However, investigation of effects presented in higher dimensions faces apparent challenges related to the number of dimensions provided by conventional physical systems. Boada and co-authors [84] have proposed to address these challenges by extending the well-established quantum simulator platform based on cold atoms with an additional *synthetic dimension*. The essence of the proposed idea was to encode an additional dimension into another degree of freedom (atomic spin state in this case) in the way that effective Hamiltonian is analogous to a higher-dimensional one.

Since then, the concept of synthetic dimensions has been extended and used in various branches of physics [88]. It acquired special significance in photonics, where it provides platform for exploring otherwise hardly accessible physical phenomena [89] and employment of synthetic dimensions allows for the dimensional extension employing only internal degrees of freedom of a system. This approach has been successfully applied to simulating particle random walk [90], effects of Bloch oscillations [91], unidirectional invisibility and unconventional reflection in parity-time symmetric systems [92], Anderson localization [93, 94], etc. Recently, synthetic dimensions have been used in the studies of topological photonics [95, 96, 97]. Observation of a large variety of topological effects employing the synthetic frequency dimension has been proposed theoretically [98, 99, 100] or realized experimentally [101, 102, 103, 104, 105]. Synthetic dimensions in photonics can be realized using different physical mechanisms [106]. For example, coupled oscillating waveguides [101], pair of coupled unequal loops [107] and

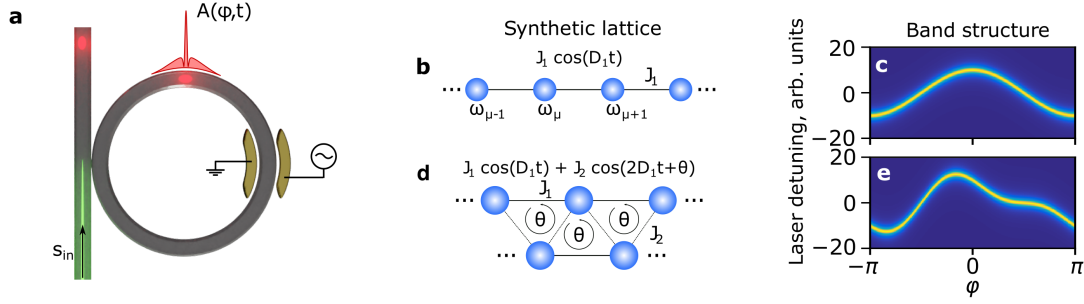


**Figure 4: Synthetic frequency dimensions.** a) Schematics of a ring resonator with an electro-optical modulator. b) One-dimensional synthetic crystal created under single tone modulation. c) Corresponding cosine band structure represented as resolved cavity response as a function of laser detuning and azimuth coordinate  $\phi$ . d) Two-dimensional synthetic crystal created under two-tone modulation. e) Corresponding band structure.

phase modulation inside a ring cavity [108] allows for encoding a synthetic dimension into spatial discrete models, arrival time of pulses, and resonator modes, respectively. We will refer to the latter case as *synthetic frequency dimensions*. It can be created by inserting an electro-optical (EO) modulator into the ring resonator circumference [108, 109, 110]. Modulating intracavity field at a frequency equal to an integer number of free spectral ranges (FSRs) (Fig. 4a), one can establish an effective photon flux between different optical modes supported by the resonator. In the case of the nearest-neighbor coupling (single FSR modulation) this system becomes similar to one-dimensional chain of identical atoms (see Fig. 4b). However, in contrast to solid state physics, the modulated cavity modes play the role of a direct space, whereas time acts as a reciprocal one. Hence, exciting a cavity with an external laser which operates at a frequency  $\omega_p$  close to the resonant  $\omega_0$  and measuring the intracavity field response as a function of detuning  $\omega_0 - \omega_p$ , one can readily obtain a cosine-like band structure of the chain [99] (see Fig. 4c). Furthermore, applying dual-tone modulation creates an effective two-dimensional frequency crystal (Fig. 4d) with controllable coupling strength (applied voltage) and phase flux (relative modulation phase) as introduced in the pioneering work by Dutt et al. [99]. Due to non-zero phase flux, the corresponding band structure has non-reciprocal profile (Fig. 4e). Introducing an additional amplitude modulator opens new possibilities in realization of non-Hermitian Hamiltonians with nontrivial controllable topological band winding that can be controlled [111].

## Resonator lattices

Arrays of optical waveguides and integrated on-chip microresonators that successfully emulate different many-body Hamiltonians have opened new avenues for light control [112, 113, 114, 115, 116, 117]. In the context of nonlinear photonics, such lattices attract significant interest due to the rich physics that remains to be explored, considering the wide range of dispersion modifications and nonlinear interactions [118].



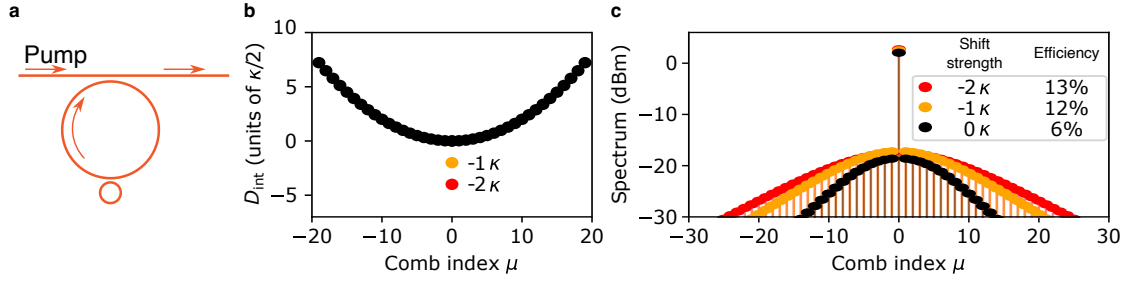


Figure 5: **Coupled resonator structure for efficient microcomb generation.** a) Schematics of two coupled resonators with different free spectral ranges. b) Integrated dispersion profile with the tunable pump mode. c) Output soliton spectra for different mode displacements.

Recent advances in ultra-low loss nonlinear integrated platforms, particularly silicon nitride [119, 120], have dramatically reduced the threshold for optical parametric oscillations. As a result, dissipative coherent structures have been successfully generated in two coupled resonators [121, 122, 123, 124, 125]. The spatial overlap of optical modes in both cavities induces interaction between them, resulting in the frequency splitting. For example, Helgason and co-authors proposed considering a system of two microresonators with different FSRs, as depicted in Fig. 5a [124]. If the radius ratio of the rings is chosen correctly, the smooth dispersion profile  $D_{\text{int}}$  acquires an additional mode crossing whose position and strength can be controlled (see Fig. 5b). Therefore, pumping the system at the mode crossing with a correctly adjusted mode shift results in the reproducible generation of DKS with high conversion efficiency, allowing for the production of microcombs with high conversion efficiency (see Fig. 5c). In the case of two coupled resonators with identical FSRs (Fig. 6a), each optical mode begins to interact, resulting in the splitting of every optical mode in the integrated dispersion profile, as shown in Fig. 6b. In such a system, Tikan and co-authors demonstrated the generation of DKS (see Fig. 6c) and a variety of emergent nonlinear dynamics [122], such as soliton hopping and recurrent dispersive waves.

As shown above, even the simplest case of two coupled resonators demonstrates rich and unexpected dynamics. Therefore, 1D and 2D lattices become even more attractive for investigation of nonlinear processes and frequency comb generation. The history of 1D chains of resonators began in 1999 with a theoretical paper on coupled resonator optical waveguides (CROWs) by Yariv and co-authors [126]. In their paper, the authors developed the first idea of a photonic band structure in such a system and discussed the corresponding group velocity, which can be close to 0, opening an opportunity to create a slow light waveguide. Later, CROWs were demonstrated experimentally and used as optical filters, delay lines, and for optical parametric oscillators [85].

Adding more resonators and engineering the coupling between them creates an opportunity to study effects of topological physics. For example, in topologically non-trivial lattices, light can propagate through the whole system (i.e., excite the bulk modes), but also be localized at the edges, exciting the edge states that are immune against various perturbations [95]. In

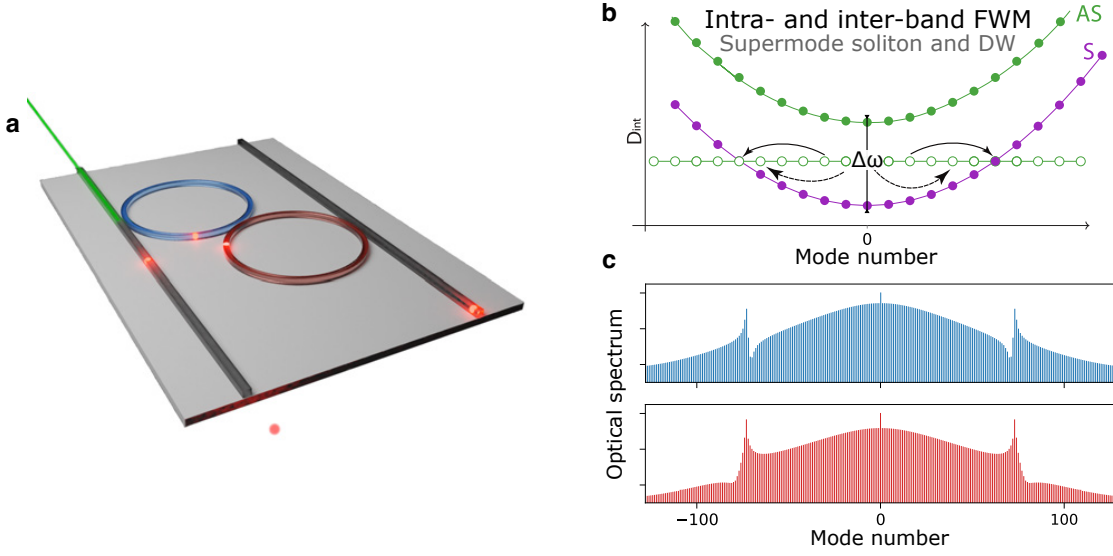


Figure 6: **Dissipative Kerr solitons in a photonic dimer** a) Schematics of two coupled microresonators. b) Four-wave mixing pathways between the hybridized supermodes. c) Simulated optical spectra in bus and drop waveguides (colors are preserved).

2018, two papers on the theory of topological insulator lasers based on the Haldane model and their experimental demonstration were published [113, 114]. In these works, the authors demonstrated the superior laser efficiency of the edge states with respect to trivial ones, in addition to the natural protection of the edge modes due to the topology against disorder. Kerr comb dynamics in large lattices were largely unexplored due to computational and fabrication challenges until the recent work by Mittal and co-authors [127]. In their work, the authors considered the Haldane model with Kerr nonlinear resonators and demonstrated numerically the formation of traveling edge state dissipative Kerr solitons. So far, this remains the sole study addressing multimode optical ring cavities with Kerr nonlinearity, and there is still a considerable gap in comprehending nonlinear interactions.

In this thesis, we aim to explore nonlinear dynamics, including four-wave mixing and the formation of coherent dissipative structures, in different optical lattices, formed in synthetic and real dimensions; thus, bridging the fields of Kerr frequency combs and collective dynamics in arrays of microresonators. The first two chapters are devoted to the investigation of synthetic frequency dimensions created by electro-optic phase modulation and periodic modulation of dispersion of a single cavity. The second part, from chapters 3 to 7, covers lattices of coupled resonators from the dimer configuration to the Su-Schrieffer-Heeger model.

# **Synthetic Dimensions** **Part I**



# 1 Synthetic frequency dimension in electro-optic modulated cavities

This chapter reports on the investigation of nonlinear dynamics in a synthetic frequency crystal created by an electro-optical modulator in a ring cavity. The results are partially adapted from A. Tusnin *et al.*, “Nonlinear states and dynamics in a synthetic frequency dimension,” *Physical Review A* **102**, 023518 (2020).

## 1.1 Introduction

Recently, synthetic dimensions in photonics attracted significant interest for investigation complex Hamiltonians and band structures. However, the role of nonlinearity in such systems dimension is hardly explored. This is of particular importance for simulating locally interacting Hamiltonians [128, 129, 130] in complex many-body systems which are actively investigated in the context of photonic quantum simulators development [88]. Yuan and co-authors have proposed a scheme that employs Kerr nonlinearity to achieve the local interaction between the simulated particles [129]. They have simulated a synthetic state governing by an effective Bose-Hubbard Hamiltonian and successfully explored the photon blockade effect. Even though this approach requires fulfillment of very restrictive conditions (such as zero dispersion and conserved total number of photons, which restrains this study to low-power regime), it is nonetheless very powerful since experimental platforms for realizing synthetic frequency dimensions often include materials with nonzero  $\chi^{(3)}$  optical susceptibility.

The present chapter investigates the nonlinear dynamics in a dispersive cavity with  $\chi^{(2)}$  and  $\chi^{(3)}$  optical susceptibilities where voltage-induced phase modulation creates a synthetic frequency dimension. Starting from the coupled-mode formalism, we derive mean-field Gross-Pitaevskii equation with a cosine potential which describes nonlinear dynamics of resonantly modulated intracavity field in microresonators and fiber loop cavities [131]. We found that the modulation leads to predictable dissipative Kerr solitons (DKSs) [77, 15] emergence and possibility of generation soliton crystals on-demand [56, 132, 50]. We found that the modulation instability (MI) becomes bounded by the curved bi-stability region. Surprisingly, with increasing of the coupling rate, new stable coherent structures emerge in the MI region, which we call *Band*

*Soliton.* These states appear to be dispersionless which makes them of particular interest in the context of synthetic frequency dimensions. Introducing a second tone to the intracavity phase modulation, we effectively create a nontrivial geometry which enables a nonreciprocal photon transfer [99]. This leads to the coexistence of stable coherent and chaotic regions which we interpret as chimera-like states [133]. Our results highlight the rich Physics that can be accessed in synthetic dimensions with cubic nonlinearity.

### 1.2 Theory

We consider an optical ring coupled to a bus waveguide with external coupling rate  $\kappa_{\text{ex}}$  (Fig. 1.1(a)). The cavity excited by a monochromatic laser with photon flux  $s_{\text{in}} = \sqrt{P/\hbar\omega_p}$  ( $P$  is the input power) and frequency  $\omega_p$ , which is close to resonance frequency  $\omega_0$ . We suppose the modes being not equally spaced due to the dispersion, so the mode frequency ( $\omega_\mu$ ) depends on the mode number ( $\mu$ ) as  $\omega_\mu = \omega_0 + D_1\mu + \mu^2 D_2/2$ , where  $D_1/2\pi$  equals to FSR, and  $D_2$  characterizes the group velocity dispersion (GVD) (Fig. 1.1(f)). A synthetic frequency dimension is created by an EO modulator at one part of the ring with modulation frequency  $\Omega = sD_1$  with  $s \in \mathbb{N}$  [106]. If modulator consists of  $\chi^{(2)}$  active material, then it changes locally refractive index  $n(\phi, t)$  and provides with linear coupling between different modes, which can be described by the equations of motion for the amplitudes  $a_\mu$  as (see Supplementary Note 1 in Ref. [99]),

$$\frac{\partial a_\nu(t)}{\partial t} = -i\omega_\nu a_\nu(t) + i \sum_\mu J_{\mu-\nu}(t) a_\mu(t). \quad (1.1)$$

Let us suppose that the coupling coefficient does not depend on  $\mu$  and depends harmonically on time as  $J_{\mu-\nu} = J_s \cos(\Omega t + \theta)$ , where  $\Omega$  is the modulation frequency and  $\theta$  is the modulation phase. Under the transformation into rotating frame ( $a_\nu = b_\nu e^{-i\omega_\nu t}$ ), the equation reads

$$\dot{b}_\nu e^{-i\omega_\nu t} = \frac{i}{2} \sum_\mu J_s b_\mu e^{-i\omega_\mu t} (e^{i\Omega t + i\theta} + e^{-i\Omega t - i\theta}) \quad (1.2)$$

( $\dot{b}_\mu$  indicates time derivative). Supposing that we pump the resonator near to frequency  $\omega_0$  such that

$$\omega_\mu = \omega_0 + \mu D_1 + D_2 \frac{\mu^2}{2}, \quad (1.3)$$

and modulation frequency  $\Omega$  is chosen as  $\Omega = sD_1$ , where  $s$  is an integer, the RHS of Eq. (1.2) incorporates two exponentials

$$\omega_\mu + sD_1 - \omega_\nu = D_1(\mu + s - \nu) + \frac{D_2}{2}(\mu^2 - \nu^2), \quad (1.4)$$

$$\omega_\mu - sD_1 - \omega_\nu = D_1(\mu - s - \nu) + \frac{D_2}{2}(\mu^2 - \nu^2). \quad (1.5)$$

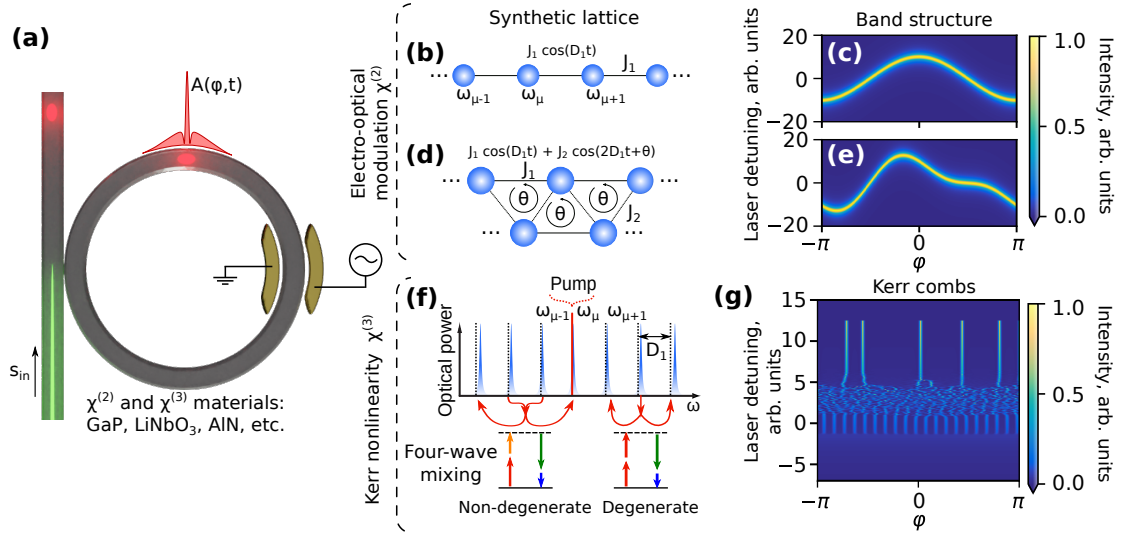


Figure 1.1: **Dynamically modulated optical cavity with  $\chi^{(2)}$  and  $\chi^{(3)}$  susceptibilities.** (a) Optical cavity with an integrated EO (electro-optical) modulator. The modulation frequency is integer number of FSRs (free spectral ranges):  $\Omega = sD_1$ , where  $s \in \mathbb{N}$ . Due to the modulation, modes with frequencies  $\omega_\mu$  and  $\omega_{\mu+s}$  become coupled with coupling strength  $J_s$  creating a synthetic lattice.  $A(\phi, t)$  represents slowly varying envelope of the interactivity field in the rotating frame  $\phi = \phi - D_1 t$ , where  $\phi$  is the polar angle. (b) Schematics of the lattice with the nearest neighbor coupling ( $s = 1$ ). (c) Corresponding cavity field response with  $J_1 = 10\kappa/2$ , which represents the band structure. (d,e) the same as (b,c) but in the case of dual-tone modulation with relative phase  $\theta = \pi/2$  and  $J_2 = 0.45J_1$ . (f) Displacement of the cavity resonance (in blue) from their exact equidistant positions (black dotted lines) due to the presence of dispersion. (g) Conventional nonlinear dynamics in a Kerr optical microresonator with anomalous group velocity dispersion.

## Chapter 1. Synthetic frequency dimension in electro-optic modulated cavities

---

Therefore, the resonant interaction appears between modes  $\mu = \nu \pm s$ , and the equation 1.2 simplifies to

$$\dot{b}_\nu = \frac{iJ_s}{2} (e^{i\theta} b_{\nu+s} e^{-i\frac{D_2 s}{2}(2\nu+s)t} + e^{-i\theta} b_{\nu-s} e^{i\frac{D_2 s}{2}(2\nu-s)t}). \quad (1.6)$$

Now we aim to find the corresponding equation of the cavity field. In optical cavity the field envelop may be presented as Fourier series

$$A(\phi, t) = \sum_{\mu} a_{\mu} e^{i\mu\phi} = \sum_{\mu} b_{\mu} e^{i(\mu\phi - \omega_{\mu} t)}. \quad (1.7)$$

Taking the time derivative, one obtains

$$\dot{A} = \sum_{\mu} (\dot{b}_{\mu} - i\omega_{\mu} b_{\mu}) e^{i(\mu\phi - \omega_{\mu} t)}. \quad (1.8)$$

Let us consider only the first term. Substituting Eq. (1.6) yields

$$\sum_{\mu} \dot{b}_{\mu} e^{i(\mu\phi - \omega_{\mu} t)} = i \sum_{\mu} e^{i(\mu\phi - \omega_{\mu} t)} J_s (a_{\mu-s} e^{i\frac{D_2 s}{2}(2\mu-s)t + i\theta} + a_{\mu+s} e^{-i\frac{D_2 s}{2}(2\mu+s)t - i\theta}). \quad (1.9)$$

One may readily rearrange the exponentials relations

$$\begin{aligned} \omega_{\mu-s} &= \omega_{\mu} - sD_1 + \frac{D_2}{2}(s^2 - 2\mu s) \\ \omega_{\mu+s} &= \omega_{\mu} + sD_1 + \frac{D_2}{2}(s^2 + 2\mu s), \end{aligned}$$

and the summation yields that modulation creates a potential for the electric field

$$J_s \cos(\phi s - sD_1 t + \theta). \quad (1.10)$$

Therefore, in the frame  $\varphi$  rotating with speed  $D_1$  such that  $\varphi = \phi - D_1 t$ , electric field obeys the following equation

$$\dot{A} = iJ_s \cos(s\varphi + \theta) A. \quad (1.11)$$

This result, combined with the Lugiato-Lefever formalism for Kerr combs in optical cavities [14], gives the equation the mean field equation for driven-dissipative nonlinear cavity with resonant modulation that can be presented as

$$\frac{\partial A}{\partial t} = -\left(\frac{\kappa}{2} + i\delta\omega\right)A + \frac{iD_2}{2} \frac{\partial^2 A}{\partial \varphi^2} + 2iJ_s \cos(s\varphi + \theta)A + ig_0|A|^2 A + \sqrt{\kappa_{\text{ex}}}s_{\text{in}}. \quad (1.12)$$

In the normalized units, the equation takes form

$$\frac{\partial \Psi}{\partial \tau} = -(1 + i\zeta_0)\Psi + id_2 \frac{\partial^2 \Psi}{\partial \varphi^2} + i|\Psi|^2 \Psi + iJ \cos(s\varphi + \theta)\Psi + f, \quad (1.13)$$



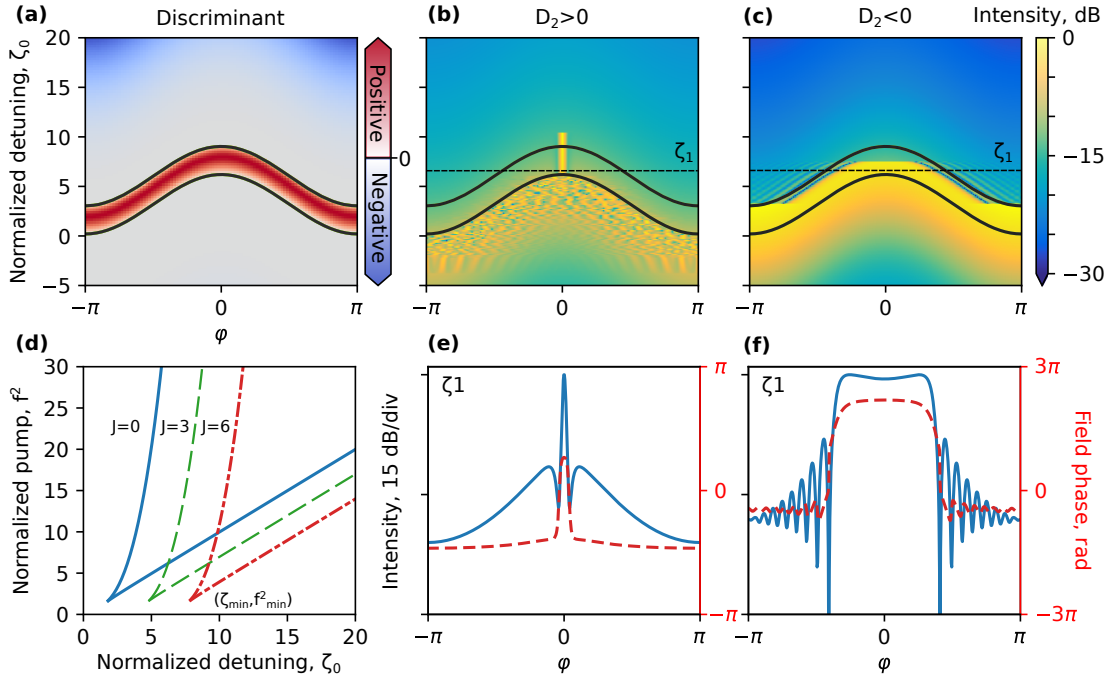


Figure 1.2: **Bi-stable branches and DKS (dissipative Kerr soliton)/platicon-existence range.** (a) Value of the discriminant  $\Delta$  (Eq. (1.15)) for coupling rate  $J = 3$  and pump  $f^2 = 6$  as a function of  $\zeta_0$  and  $\varphi$ ; (b) and (c) intracavity field in the case of anomalous and normal GVD (group velocity dispersion), respectively. Black solid lines represent value  $\Delta = 0$  and indicate the bi-stable zone. A novel dynamics is observed in chaotic regime: MI (modulation instability) does not penetrate the bi-stable region. Soliton existence range is almost covered by the bi-stable region at  $\varphi = 0$ . (d) Bi-stability range at  $\varphi = 0$  for coupling values  $J = 0$  (solid),  $J = 3$  (dashed), and  $J = 6$  (dot-dashed). With increase of coupling  $J$ , the bi-stable zone shifts into the effectively red detuned region ( $\zeta_0 > 0$ ) preserving its width. (e) Amplitude (solid blue) and phase (dashed red) profiles of DKS for detuning  $\zeta_1 = 6.3$  (dashed lines on (b,c)). (f) The same in the case of normal dispersion.

where normalized variables  $\tau = t/\tau_{\text{ph}}$ ,  $\tau_{\text{ph}} = 2/\kappa$  is photon lifetime,  $d_2 = D_2/\kappa$ ,  $\zeta_0 = 2\delta\omega/\kappa$ ,  $\delta\omega = \omega_0 - \omega_p$ ,  $J = 2J_s/\kappa$ ,  $f = \sqrt{8\kappa_{\text{ex}}g_0/\kappa^3}s_{\text{in}}$ ,  $\Psi = \sqrt{2g_0/\kappa}A$ ,  $\kappa = \kappa_{\text{ex}} + \kappa_0$ ,  $\kappa_0$  is intrinsic loss rate,  $g_0$  is single-photon Kerr frequency shift,  $A$  describes the optical field envelope and normalized such that  $\int_0^{2\pi} |A|^2 d\varphi/2\pi$  is the number of photons inside the cavity.

Let us begin with the analysis of stable solutions in the dispersionless limit ( $d_2 = 0$ ). Introducing  $I = |\Psi|^2$ , one can readily derive the cubic equation

$$\left(1 + (I + J \cos(s\varphi) - \zeta_0)^2\right)I = f^2. \quad (1.14)$$

The roots of this equation can be analyzed through its discriminant  $\Delta$ . Since the cubic equation (1.14) is written for real value  $|\Psi|^2$ , the solution has to be real as well. However, it is well known that a cubic equation always possesses three roots, and they are characterized through

its discriminant  $\Delta$ . In our case, the discriminant has the following form

$$\begin{aligned} \Delta = & -27f^4 - 4(1 + \zeta_0^2)^2 + 4f^2\zeta_0(9 + \zeta_0^2) + 4J\cos(s\varphi) \times \\ & \times \left[ -3f^2(3 + \zeta_0^2) + 4\zeta_0(1 + \zeta_0^2) - J\cos(s\varphi) \times \right. \\ & \left. \times \left( 2 - 3f^2\zeta_0 + 6\zeta_0^2 + J\cos(s\varphi)(f^2 - 4\zeta_0^2 + J\cos(s\varphi)) \right) \right]. \end{aligned} \quad (1.15)$$

Solving the equation  $\Delta = 0$ , we find values  $f^2$  and  $\zeta_0$  which determine the bi-stable zone. Depending on the sign of  $\Delta$ , there are three scenarios for solutions of Eq. (1.14): if  $\Delta < 0$  there is one real root and two complex conjugated roots, if  $\Delta = 0$  roots are real and at least two of them are equal, if  $\Delta > 0$  roots are real distinct numbers. Thus, negative (positive) discriminant corresponds to mono-stable (bi-stable) solutions, and in order to determine the bi-stability zone one needs to find  $f^2$  and  $\zeta_0$  such that the discriminant equals to zero. Since Eq. (1.14) explicitly depends on  $\varphi$ , the discriminant becomes  $\varphi$  dependent, therefore *different spatial parts* of the cavity are found at *different parts of the stability diagram at the same value of laser detuning* (see Fig. 1.2(a)). The threshold value  $f^2$  which corresponds to the triple real root of Eq. (1.14) can be obtained analytically, and it equals to  $f_{min}^2 = 8\sqrt{3}/9$ , which coincides with the critical value for the resonance tilt for LLE [53]. Remarkably, this result does not depend on  $\varphi$ , despite the  $\varphi$  dependence of Eq. (1.14).

### 1.3 Numerical simulations

#### 1.3.1 Dynamics of dissipative solitons and platicons

For further analysis we consider the case  $s = 1$ . In Fig. 1.2(a) we show the values of the discriminant  $\Delta$  as a function of  $\varphi$  and  $\zeta_0$  for pump rate  $f^2 = 6$  and coupling  $J = 3$ . As one can see, the presence of the potential leads to bending of the bi-stable zone in a way, that for a given detuning the system can be simultaneously on the mono-stable and bi-stable branches. With increasing of coupling strength  $J$ , the bistability zone bends further and goes deeper into the effectively red detuned region ( $\zeta_0 > 0$ ) (see Fig. 1.2(a)).

We continue the further analysis by performing numerical simulation of GPE (1.13), taking  $d_2 = \pm 0.01$  and scanning the cavity from blue- ( $\zeta_0 < 0$ ) to red-detuned side. We employ numerical integration utilizing the split-step Fourier method [29]. The positive (negative) value of  $d_2$  corresponds to anomalous (normal) dispersion regimes. We analyze these cases separately.

**Anomalous dispersion.** We observe that the presence of the potential in GPE (1.13) breaks the translational symmetry along  $\varphi$  coordinate and leads to confinement of the MI region [133]. We observe that chaotic patterns do not penetrate into bi-stable zone, and DKS appear at

the center of the cavity (Fig. 1.2(b)). The latter might be qualitatively understood through the analysis of the steady-state dispersionless linear solution, which can be considered as a background for the dissipative nonlinear structures in the cavity. The intracavity field can be expressed as

$$\Psi = \frac{f}{1 + i(\zeta_0 - J \cos(\varphi))}. \quad (1.16)$$

Depending on normalized detuning, the field intensity has one ( $\zeta_0 > J$ ,  $\varphi_0 = 0$ ) or two ( $\zeta_0 < J$ ,  $\varphi_{\pm} = \pm \arccos(\zeta_0/J)$ ) maxima. When the modulated background has only one peak, a single DKS can be formed on it. Numerical simulations show that the DKS appears on the peak of the modulated background in the bi-stable region (Fig. 1.2(b)) [134]. The width of this region as a function of  $f^2$  and  $J$  can be calculated analytically, and we present it in Fig. 1.2(d) for coupling rates  $J = 0, 3, 6$ . Surprisingly, this zone simply shifts into the effectively red-detuned region linearly with  $J$ , and the critical detuning for  $f_{\min}^2$  is

$$\zeta_{\min} = \sqrt{3} + J. \quad (1.17)$$

In order to calculate the soliton existence range, we employ the Lagrangian perturbative approach [48, 54]. First of all, we introduce the change of variable  $\Theta = 1/\sqrt{2d_2}\varphi$  to the equation (1.13). Thus, the equation for the Lagrangian density can be written as follows:

$$\begin{aligned} \mathcal{L} = & \frac{i}{2} \left( \Psi^* \frac{\partial \Psi}{\partial \tau} - \Psi \frac{\partial \Psi^*}{\partial \tau} \right) - \frac{1}{2} \left| \frac{\partial \Psi}{\partial \Theta} \right|^2 + \\ & + \frac{1}{2} |\Psi|^4 + (J \cos(\alpha \Theta) - \zeta_0) |\Psi|^2, \end{aligned} \quad (1.18)$$

where  $\alpha = 2d_2$ . The dissipative function is introduced in the form:

$$\mathcal{R} = -i\Psi + if. \quad (1.19)$$

The Lagrangian  $L = \int \mathcal{L} d\Theta$  obeys:

$$\frac{\partial L}{\partial q_i} - \frac{d}{d\tau} \frac{\partial L}{\partial \dot{q}_i} = \int \left( \mathcal{R} \frac{\partial \Psi^*}{\partial q_i} + \mathcal{R}^* \frac{\partial \Psi}{\partial q_i} \right) d\Theta. \quad (1.20)$$

Using the ansatz of a stationary soliton  $\Psi = B \text{sech}(B\Theta) e^{i\phi_S}$ , we integrate it over  $\Theta$  on the interval  $(-\infty, +\infty)$  (under the assumption  $D_2/\kappa \ll 1$ ). As a result, the Lagrangian takes form

$$L = -2B \frac{\partial \phi_S}{\partial \tau} + \frac{1}{3} B^3 - 2B \phi_S + \frac{J\alpha\pi}{\sinh(\frac{\alpha\pi}{2B})}. \quad (1.21)$$

The right hand side of Eq. (1.20) is not affected by the presence of the potential and coincides

## Chapter 1. Synthetic frequency dimension in electro-optic modulated cavities

---

with Refs. [48, 54]. Considering  $q_1 = B$  and  $q_2 = \phi_S$  in Eq. (1.20), we get

$$\frac{dB}{d\tau} = -2B + \pi f \cos \phi_S, \quad (1.22)$$

$$\frac{d\phi_S}{d\tau} = \frac{1}{2}B^2 - \zeta_0 + J\delta^2 \frac{\cosh \delta}{\sinh \delta} \frac{1}{\sinh \delta}, \quad (1.23)$$

where we define  $\delta = \alpha\pi/2B$ . Considering  $\alpha \ll 1$  and using Taylor expansion we obtain the stable solution

$$B^2 = 2(\zeta_0 - J), \quad (1.24)$$

$$\cos \phi_S = \frac{2B}{\pi f}. \quad (1.25)$$

From the latter we obtain the analytical expression of the maximum detuning for stable soliton in the presence of nearest-neighbor coupling

$$\zeta_{\max} = \pi^2 f^2 / 8 + J. \quad (1.26)$$

This result generalizes the known expression for the soliton existence range to single-tone EO modulated cavity. Similarly to bi-stable zone, the maximum detuning  $\zeta_{\max}$  simply shifts by  $J$ .

Increasing the modulation frequency (i.e. increasing of  $s$  in Eq. (1.13)) leads to period multiplication of the modulated background and allows for creating soliton crystals [56, 50] with  $s$  equally spaced DKS. Alternatively, applying several modulation signals and having control of the modulation phase, one can control positions and the number of DKS in the cavity, which enables controlled soliton tweezing [134], and as shown later, leads to a new dynamics.

**Normal dispersion.** In the context of the conventional LLE with normal GVD ( $d_2 < 0$ ), the dark solitons (also called platons) are hard to excite by simple laser tuning (soft excitation) for relatively small detunings and pump rates [53]. In order to create them, one needs to use additional methods, such as pumped modulation [72], or pumping in the avoided mode crossings [74, 135]. In this context, EO modulation provides with an effective flux of photons from the pumped resonance to sidebands, making platons accessible without additional perturbations. In Fig. 1.2(c) one can see platicon generation in the resonantly modulated cavity. In contrast to the DKS, the platons appear only when one part of the cavity passes the whole bi-stable region; however, Fig. 1.2(d) can still indicate approximate platicon existence range.

### 1.3.2 Confined MI region

Let us restrict our consideration for the case of anomalous GVD ( $d_2 > 0$ ). In the conventional LLE formalism, in order to generate DKS via the soft excitation, one needs to scan

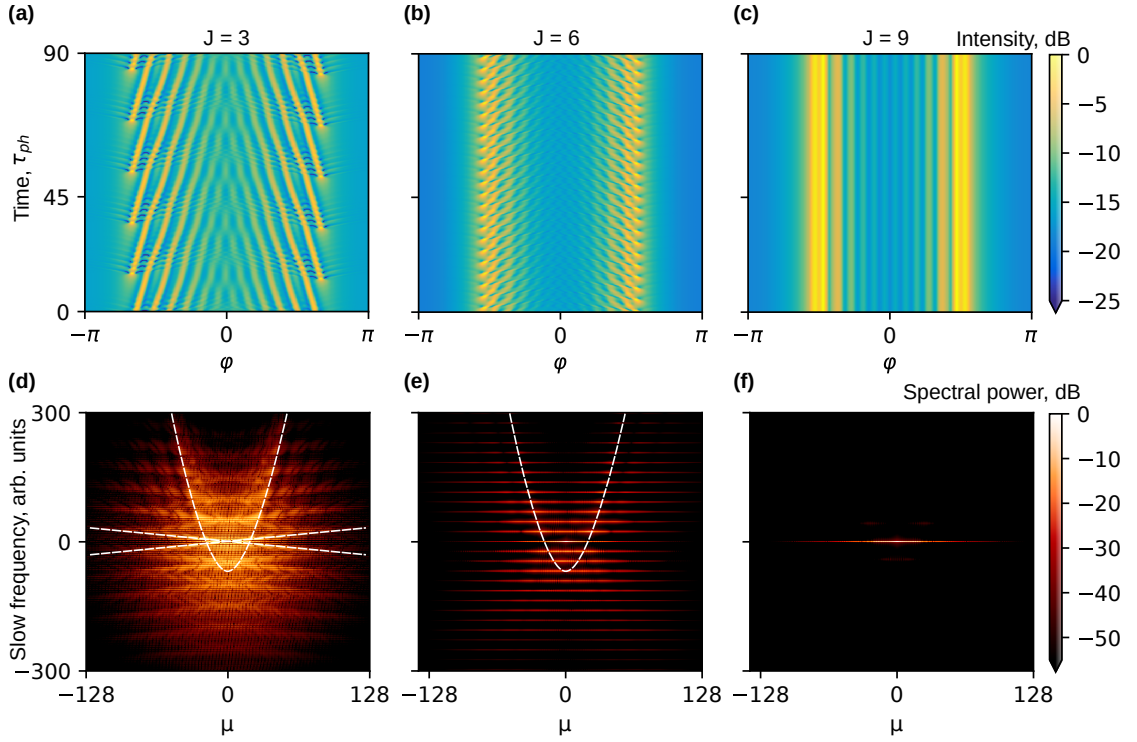


Figure 1.3: **Dynamics of the confined MI (modulation instability) region in the presence of potential.** (a-c) Spatio-temporal diagrams of the intracavity field for  $f^2 = 6$ ,  $\zeta_0 = 1.28$ . Coupling  $J = 3$  corresponds to (a),  $J = 6$  (b), and  $J = 9$  (c). (d-f) Corresponding NDR (nonlinear dispersion relation) which represents effective nonlinear dispersion relation of the system. One can notice how the dispersion relation transforms with increase of  $J$ . For  $J = 3$  the system consists of constantly appearing and colliding dispersionless structures (lines with opposite slopes in (d)) which radiate dispersive waves (parabola in (d)), for  $J = 6$  (b,e) the field oscillates as a whole and forms a ladder in the NDR profile, which indicates periodic breathing in time. Further increase of  $J$  (c,f) transforms the field into dispersionless stable dissipative structure.

the resonance through the MI region. In this region, coherent structures randomly appear and collide with each other, and may give birth to rogue waves [136]. However, due to the modulated background, the nonlinear structures appear and interact at different parts of the resonator differently (Fig. 1.3(a-f)). In order to investigate the role of coupling  $J$ , we explore spatio-temporal diagrams at a fixed pump rate, detuning and coupling rate and its nonlinear dispersion relation (NDR). First of all, we chose simulation parameters as in Fig. 1.2(b), but with fixed detuning  $\zeta_0 = 1.3$ . On the spatio-temporal diagram Fig. 1.3(a) one can see how nonlinear structures periodically arise and oscillate in the vicinity of background maxima  $\varphi_{\pm}$ , propagate towards the maximum of the background phase at  $\varphi \approx 0$  (red dashed line in Fig. 1.4(b)) and annihilate. There are several distinct structures on the corresponding NDR (Fig. 1.3(d)): the periodic lines along the slow frequency axis with opposite slopes correspond to the colliding structures which locally have conventional DKS (dissipative Kerr soliton) profile; the parabola corresponds to dispersive waves which are emitted by the breathing DKS on the background. With increasing of the detuning these structures come closer, get smaller group velocity, and interact more chaotically while the field in the vicinity  $\varphi = \pm\pi$  rests unperturbed. Thus, we observe that for relatively small coupling rates the potential leads to confinement of the MI (modulation instability) state.

However, with increasing coupling strength ( $J = 6, 9$ ), we observe how this constantly interacting solitons are transformed into a new stable dispersionless structure (Fig. 1.3(b,c,e,f)). For coupling rate  $J = 6$ , we observe that the field starts to periodically oscillate in time. The corresponding NDR consists of a ladder of lines, which signifies the appearance of a new dispersionless breathing structure. Further increasing of the coupling ( $J = 9$ ) stabilizes this structure, it becomes coherent and *dispersionless*. In the following sections we further explore this novel state.

### 1.3.3 Band Soliton

With increase of coupling strength  $J$ , we observe that the *MI region is getting stabilized at a certain detuning range, and new stable (i.e. coherent) nonlinear structures emerge*. In a linear dispersionless case with the nearest-neighbor coupling ( $s = 1$ ), the intracavity field response for different detunings represents a band structure of a one-dimensional synthetic crystal. However, the presence of FWM introduces global nonlinear coupling between the modes, which efficiency is given by the chromatic dispersion. The latter signifies that the eigenfunction basis (see Ref. [99]) is modified, and the intracavity field response can no longer be considered as a band structure.

The Fig. 1.4(a) demonstrates this difference: the deterministic dispersionless response (see upper right inset) transforms into a complex structure, which contains localized chaotic and stable states. However, the notion of band structure remains important even in the nonlinear regime [137, 138]. We observe that there is a threshold value of  $J$  for a given pump rate  $f$  when the novel coherent structures appear. Comparing nonlinear response (Fig. 1.4(a)) with

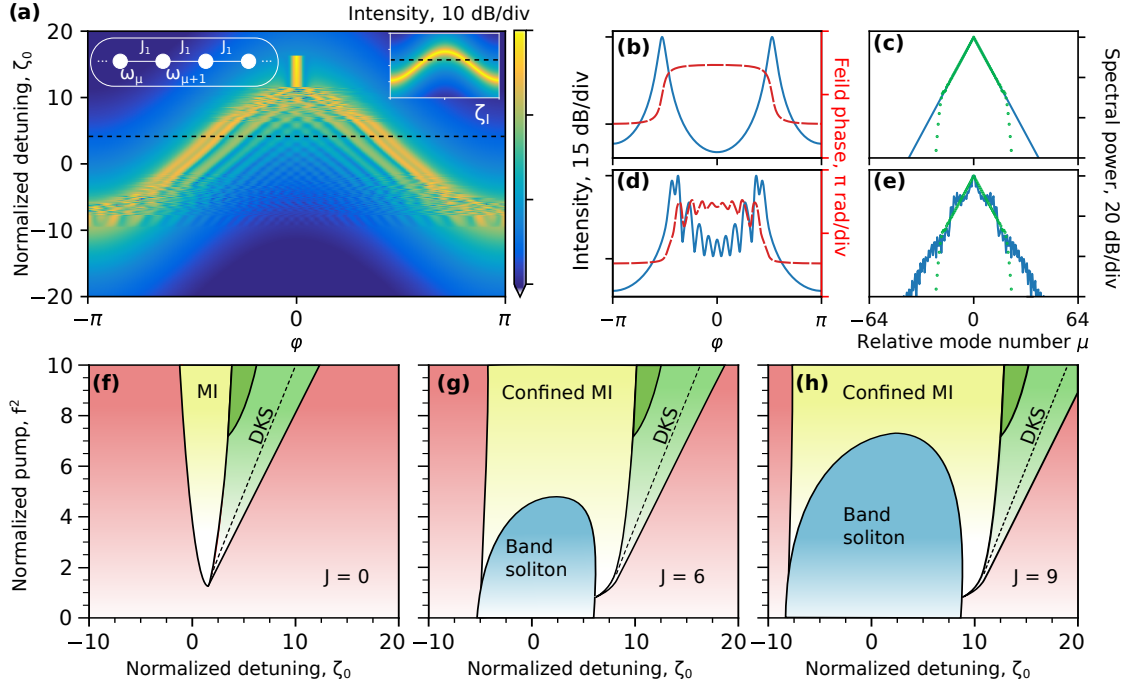


Figure 1.4: **New nonlinear states termed Band Solitons for single-tone modulation.** (a) Intracavity field for potential  $J \cos \varphi$ , coupling strength  $J = 9$ , and pump rate  $f^2 = 6$ . Band solitons emerge in the detuning range  $\zeta_0 \in [-3.5, 7]$ . Insets show the linear dispersionless case: schematics of the lattice for coupling  $J \cos \varphi$  in linear case without dispersion (upper left) and corresponding cavity response (upper right). Horizontal line corresponds to detuning  $\zeta_1 = 4$ , for which we examine field and spectrum profiles (b-e). (b) Linear field intensity (solid blue line) and phase (dashed red line). (c) Linear field spectrum without dispersion (solid blue line) and with dispersion  $d_2 = 0.01$  (dotted green line). (d) Nonlinear field intensity (solid blue line) and phase (dashed red line). (e) Nonlinear field spectrum (solid blue line) and corresponding linear spectrum with dispersion (dotted green line). (f-h) Phase diagrams for coupling strengths  $J = 0$ ,  $J = 6$  and  $J = 9$ . The red zone corresponds to continuous wave; the yellow zone indicates the confined MI (modulation instability) state; the green zone corresponds to the soliton existence range, which is predicted analytically. The dashed line indicates the end of the bi-stable region. The dark green region depicts DKS breathers. The blue zone indicates existence range of *band solitons*, a new type of dissipative coherent structure that appears in a conventional ( $J = 0$ ) chaotic MI region.

dispersionless linear one (inset in the Fig. 1.4(a)), we notice that these structures emerge in the center of the band structure, thus we call them *band solitons*. In analogy to solid state physics, we can introduce the notion of synthetic Bloch waves (BW) [99], existing in the frequency space. Their group velocity reaches its maximum in the part of the band structure with the highest slope steepness. The latter signifies that the stable nonlinear states appear due to the interplay between FWM and linear BW. When the coupling strength is smaller than the threshold value, linear waves do not have sufficient velocity to redistribute perturbations induced by FWM. This regime corresponds to the confined MI. However, when the coupling strength exceeds the threshold value, the group velocity of the BW in the center of the band increases as well, and the BW can propagate faster along the frequency space and redistribute perturbations induced by FWM, leading to locking between the modes and the emergence of new coherent states. This reasoning can also be applied to the explanation of the conventional DKS states existence. As we have shown in previous sections, DKS appears exactly at the top of the band structure, where the group velocity of the BW equals to zero; hence the photon flux from the pump is provided only due to FWM, and the synthetic BWs do not affect this process. Due to this fact, this soliton corresponds to conventional soliton in optical  $\chi^{(3)}$  microcavities.

Now we investigate the field's amplitude, phase and spectrum at  $\zeta_1 = 4$  (Fig. 1.4(d,e)). In the linear dispersionless case, the solution can be found analytically (Eq. (1.16)), and the field incorporates two maxima (Fig. 1.4(b)). Corresponding spectral profile (Fig. 1.4(c), solid blue line) decays exponentially with mode number  $\mu$ , showing that the coupling rests the same for all the modes. Dispersion shifts the modes, decreasing coupling efficiency for higher-order modes and leading to truncation of the spectrum and emergence of a conventional EO comb (green dots on the Fig. 1.4(c,e)) [139]. However, FWM shifts the resonances, enhancing coupling between the modes by restoring translational symmetry in the frequency space (see Fig. 1.4(e), solid blue line). The spectrum of this new state incorporates a flat part near the pump (at  $-10$  dB level) and decays slower than the EO comb, which signifies the restored coupling between the modes beyond the cut-off [139, 140, 141].

In order to investigate stability of these states, we scan the cavity for different pump rates and coupling strengths. In Fig. 1.4(g,h) we present the phase diagram for single-tone modulation with coupling strengths  $J = 6$  and  $J = 9$  respectively and compare it with the conventional LLE model (Fig. 1.4(f)). The presence of the potential significantly changes the system dynamics, especially the MI region has new features. Band solitons emerge in a region around  $\zeta_0 = 0$ . With increasing  $J$ , their existence range increases along both axes. One can notice that this existence range is asymmetric, while in the linear case the band structure is symmetric (Fig. 1.4(a) upper right inset). However, FWM induces self-phase modulation, leading to the frequency shift towards the effectively red-detuned zone, and the whole band obtains an offset from  $\zeta_0 = 0$ . The band solitons transform to conventional EO combs at the low pump rates when FWM process becomes negligible. With increase of the pump rate, the band solitons start to breath, become unstable and transform to confined MI. Since the transition from the breathing state to the chaotic one is smooth, we joined these regions and labeled them as *confined MI* in Fig. 1.4(g,h) (note, we do not indicate here a narrow region of stable MI, which always manifest



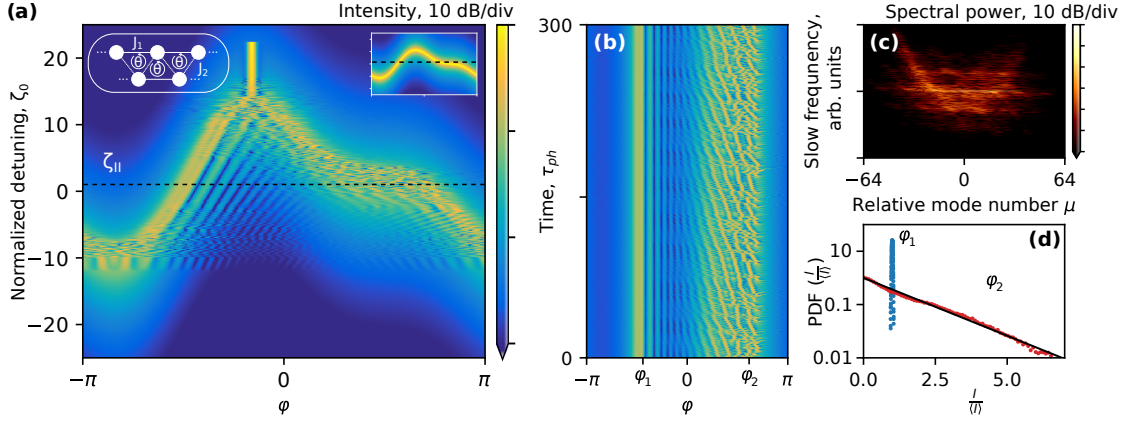


Figure 1.5: **Appearance of chimera-like states in the case of dual-tone modulation.** (a) Intracavity field for potential  $J(\cos \varphi + 0.45 \cos(2\varphi + \theta))$ , coupling strength  $J = 9$  with relative phase  $\theta = \pi/2$  and  $f^2 = 9$ . Insets: corresponding schematics of lattice (upper left) in linear case without dispersion and the cavity response (upper right). Horizontal line corresponds to detuning  $\zeta_{II} = 1.9$ , for which we examine spatio-temporal diagram (b), NDR (nonlinear dispersion relation) (c). (d) Single point PDF (probability density function) of the normalized intensity for two intracavity coordinates  $\varphi_1 = -1.4$  (blue) and  $\varphi_2 = 1.8$  (red). Black solid line corresponds to exponential PDF  $\exp -\frac{I}{\langle I \rangle}$ .

itself at negative values of detuning). This region appears to be wider than MI region in the conventional LLE model (Fig. 1.4(f)).

### 1.3.4 Chimera-like states

Using two modulation frequencies and controlling the relative phase between them, one introduces a two-dimensional synthetic lattice [99] in the frequency space (Fig. 1.5(a) upper left inset). The phase flux between the nodes can be controlled in this arrangement by the relative modulation phase. In particular, one can obtain asymmetric band structure introducing nonreciprocal frequency conversion (Fig. 1.5(a) upper right inset) [99]. We investigate nonlinear dynamics for a dual-tone modulation corresponding to the effective potential  $J(\cos \varphi + 0.45 \cos(2\varphi + \theta))$  with coupling  $J = 9$  and the relative phase  $\theta = \pi/2$ . Nonreciprocal photon flow introduces a significant asymmetry in the corresponding spectral profile (Fig. 1.5(c)) [142]. However, in contrast to the single tone modulation, it is possible to find a region where one side of the band structure is almost flat while another one has a maximum of its slope ( $\zeta_0 \approx 2$  in Fig. 1.5(a)). Therefore, for certain coupling rates fully chaotic dynamics manifests itself in a part of the cavity where the synthetic band structure slope (and hence the photon flow due to the linear BWs) is small, while another side can support a novel coherent band soliton existence. A similar intriguing feature was recently observed in systems with local coupling [56, 133]. Following these works, we refer to the observed phenomenon as *chimera-like state*.

In order to investigate the chimera-like state, we extract the complex field envelope at the detuning value  $\zeta_{II} = 1.9$  (black dashed line in Fig. 1.5(a)) and numerically propagate fixing all the parameters. The dynamics of the field modulus is shown in Fig. 1.5(b). Nonreciprocal photon transfer breaks the underlying symmetry of the system which also follows from the NDR (see Fig. 1.5(c)). Computing the single point probability density function (PDF) of the intensity variation  $I/\langle I \rangle$  ( $\langle I \rangle$  is averaged intensity in time) in coherent ( $\varphi_1 = -1.4$ ) and incoherent ( $\varphi_2 = 1.8$ ) regions using  $3 \times 10^5$  samples, we show that the PDF at  $\varphi_2$  approaches the exponential (i.e. Gaussian distribution for the real part of the field) which can be considered as a signature of a fully developed MI stage [136] (also [143, 144]), while at  $\varphi_1$  it is close to the delta-like distribution. Such states have no counterparts in DKS-based on  $\chi^{(3)}$  and single-tone driving.

### 1.4 Conclusion

In summary, we proposed a theoretical model which describes nonlinear dynamics of a modulated optical cavity with  $\chi^{(2)}$  and  $\chi^{(3)}$  optical susceptibilities and second order GVD. We have shown that in the linear dispersionless limit the model describes the physics of a ring with a synthetic frequency dimension. Considering the dynamics of the full model, we found that despite the presence of GVD which breaks the translational symmetry there are coherent dispersionless structures for which the coupling remains resonant. There are two types of structures we have observed. First is found in the region of zero group velocity of the synthetic Bloch waves. They correspond to conventional DKS solutions of LLE but living on a modulated background. Applying different modulation signals, one can directly control the background modulation, hence control number and positions of DKS, making soliton crystals and soliton tweezing readily accessible. The second type of the structures is found at the maximum of the synthetic Bloch waves group velocity. Coherence of these novel structures, that we called Band Solitons, relies on the efficient photon transfer due to the linear mode coupling and Kerr nonlinearity which compensates the effect of dispersion. Therefore, such structures can be considered as *nonlinear states in the synthetic frequency dimension*. We generalized this result by including far neighbor coupling (double-tone modulation) into the model. We found that due to the nonreciprocal photon transfer the symmetry of the system is broken which leads to the coexistence of stable coherent structures and chaos. We interpret these as the appearance of chimera-like states in the system.

We would like to emphasize that the proposed model can be used for further investigation of the synthetic frequency dimension as well as for simulations of EO combs in  $\chi^{(2)}$  resonators. It can be readily generalized for an arbitrary dispersion profile, which can incorporate either higher order dispersion  $D_3$ ,  $D_4$ , or avoided mode crossings. Also, the potential of this model in the investigation of nonlinear effects in the synthetic frequency dimension in resonator lattices is of high interest. For example, by simulating a set of coupled GPE, one may explore the nonlinear dynamics of topological states, that can be created by changing the relative modulation phase of each ring.

As a physical platform for the model one can consider a high-Q optical microcavity with  $\chi^{(2)}$  and  $\chi^{(3)}$  optical susceptibilities. With recent success in fabrication process, it has become possible to create optical cavities based on lithium niobate [145, 139] or aluminum nitride [146], as well as gallium phosphide [147] photonic platforms. These materials are of particular interest because they possess both quadratic and cubic susceptibilities, and it has been successfully used for generation of Kerr-based [145, 148], EO-combs [139], and Pockels soliton [146].

In addition to the integrated platforms, our model was experimentally verified in a fiber loop cavity with an EO modulator in Ref. [149]. Through their research, the authors successfully experimentally demonstrated the emergence of the confined modulation instability region that we observed in Fig. 1.3b together with the generation of dissipative Kerr soliton in the stop-band of the synthetic band structure. Moreover, the authors investigated Bloch oscillations in the soliton regime by intentionally detuning the EOM frequency from the cavity's free spectral range.



## 2 Synthetic frequency dimension in a dispersion-modulated resonator

This chapter reports on the investigation of optical frequency combs and two-dimensional four-wave mixing processes in dispersion-modulated cavities. The results are partially adapted from M. Anderson *et al*, "Dissipative solitons and switching waves in dispersion-modulated Kerr cavities," *Physical Review X* **13**, 011040 (2023).

### 2.1 Introduction

To achieve sufficiently low propagation losses, high-Q microresonators usually require wide waveguides that possess not only the fundamental mode, but also a set of high-order optical modes. Their excitation often obstructs the formation of coherent structures; therefore, to avoid their influence on the comb generation, one can introduce a so-called mode filtering section [150]. This section is a narrow single-mode segment of the resonator which acts as a loss channel for higher-order modes (schematically shown in Fig. 2.1a). However, with the narrowing waveguide's width, the fundamental mode experiences a change in the refractive index, resulting in the modification of the integrated dispersion profile, creating a dispersion-modulated cavity. Remarkably, such modulated systems have been studied (predominantly in fiber resonators) in the context of the competition between the Faraday instability and conventional modulation instability [151, 152, 153]. It has also been shown that the periodic modulation leads to resonant dispersive wave emission [154].

In this chapter, we propose to treat the parametric processes in dispersion-modulated cavities in a two-dimensional setting from the synthetic frequency dimension perspective. In contrast to the previous chapter, there is no need in additional elements (e.g., electro-optical modulator), and the additional dimension is created via changing one of the parameters of the cavity – waveguide width. This periodic modulation induces Floquet dynamics inside the cavity and results in the creation of an additional synthetic frequency dimension, which is reciprocal to the temporal axis of the resonator dynamics. We demonstrate, that the integrated

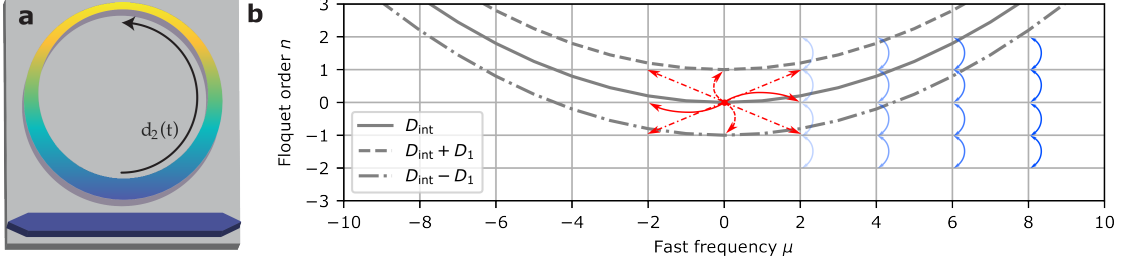


Figure 2.1: **Dispersion-modulated microresonator.** (a) Schematics of the microresonator with varying width of the waveguide. (b) Integrated dispersion profile and schematics of photon interactions in case of sinusoidal dispersion modulation. Grey solid line – initial dispersion of the resonator; grey dashed (dot-dashed) line corresponds to the dispersion of  $+(-)1$  Floquet order separated by  $D_1$ ; red lines represent the two-dimensional XPM four-wave mixing processes (solid lines – interband XPM for  $n = 0$ , dashed lines – interband XPM for  $\mu = 0$ , dot-dashed lines – 2D XPM); blue lines – linear coupling between the nearest Floquet orders that increases quadratically with comb index  $\mu$ .

dispersion is translated along the Floquet axis with a constant period equal to one free spectral range (FSR) and four-wave mixing processes occur between these bands in an effective two-dimensional frequency lattice (see Fig. 2.1b). We analyze these processes and investigate stability of continuous wave (CW) solution in the normal and anomalous regimes, describing the modulation and Faraday instabilities.

## 2.2 Two-dimensional photon transfer

While propagating along the ring circumference, the optical mode experiences variations in refractive index, resulting in periodic changes in group velocity dispersion. To capture the non-linear behavior of the cavity, we employ an extended version of the Lugiato-Lefever equation (LLE). This particular form of the LLE incorporates a dispersion term that varies periodically in time [155] with a period  $T_r$  equal to the resonator round-trip time. In the dimensionless units, the equation can be expressed as:

$$\frac{\partial \Psi}{\partial t} = -(1 + i\zeta_0)\Psi + i[d_2^{(0)} + d_2(t)]\frac{\partial^2 \Psi}{\partial \varphi^2} + i|\Psi|^2\Psi + f(\varphi). \quad (2.1)$$

Here,  $\Psi(\varphi, t)$  represents the slowly-varying envelope of the optical field within the microresonator. The function  $f(\varphi)$  describes the driving force that can be CW or pulsed. The variable  $\varphi$  corresponds to the azimuthal coordinate inside the cavity, observed from the frame moving with the velocity  $d_1 = 2D_1/\kappa$ , where  $D_1 = 2\pi/T_r$  denotes the distance between consecutive resonator modes and  $1/T_r$  is the free spectral range (FSR). The normalized laser detuning takes form  $\zeta_0 = 2\delta\omega_0/\kappa$ , while  $\kappa = \kappa_0 + \kappa_{\text{ex}}$  represents the total linewidth of the resonator, incorporating the internal linewidth  $\kappa_0$  and the coupling to the bus waveguide  $\kappa_{\text{ex}}$ . The dispersion coefficients  $d_2^{(0)}$  and  $d_2(t)$  are associated with the dispersion effect, where  $d_2^{(0)}$  as the averaged resonator dispersion and  $d_2(t)$  is the periodic modulation with period  $T = T_r\kappa/2 = \pi\kappa/D_1$ .

The time variable  $t$  is normalized by the photon lifetime, such that  $d_2^{(0)} = D_2^{(0)}/\kappa$  and  $t = t'\kappa/2$ , with  $t'$  representing real laboratory time. First, we suppose the driving function  $f(\varphi, t)$  has a period  $T$ . To find solutions for the field  $\Psi$  with the symmetry  $\Psi(t + T) = \Psi(t)$ , we can utilize the Fourier transform

$$d_2(t) = \sum_n \tilde{d}_2^{(n)} e^{-i d_1 n t}, \quad (2.2)$$

$$\Psi(\varphi, t) = \sum_{n\mu} \tilde{\psi}_{n\mu} e^{i\mu\varphi - i d_1 n t}. \quad (2.3)$$

Consequently, we derive an effective two-dimensional equation that governs the Floquet dynamics (note that for simplicity, we assume  $f$  to be constant, although the equation can be readily generalized):

$$\begin{aligned} \frac{\partial \tilde{\psi}_{n\mu}}{\partial t} = & -(1 + i[\zeta_0 - n d_1] + i d_2^{(0)} \mu^2) \tilde{\psi}_{n\mu} - \\ & - i \sum_m \tilde{d}_2^{(n-m)} \mu^2 \tilde{\psi}_{m\mu} + i \sum_{\substack{n_1, n_2, n_3 \\ \mu_1, \mu_2, \mu_3}} \tilde{\psi}_{n_1 \mu_1} \tilde{\psi}_{n_2 \mu_2} \tilde{\psi}_{n_3 \mu_3}^* \delta_{\text{FWM}} + \delta_{n,0} f. \end{aligned} \quad (2.4)$$

In this context, the conservation law  $\delta_{\text{FWM}} = \delta(\mu_1 + \mu_2 - \mu_3 - \mu) \delta(n_1 + n_2 - n_3 - n)$  governs the 2D Four-Wave Mixing (FWM) processes in the fast ( $\mu$ ) - slow ( $n$ ) frequency space as schematically shown as red lines in Fig. 2.1b. Therefore, we can infer that the periodically varying dispersion, which introduces a time-dependent dispersion term in the LLE, induces coupling between distinct Floquet orders ( $n$ ) of the intracavity field. Effectively, it leads to a breathing with a multiple of FSR frequency. The coupling strength between the Floquet bands scales *quadratically* with the comb index  $\mu$ , resulting in the increased coupling rate for higher mode numbers  $|\mu|$  (see blue lines in Fig. 2.1b). As a result, periodic modulation of the dispersion results in an effective dimensionality extension of the model: in addition to the fast frequency ( $\mu$ ), the slow frequency with the grid defined by the Floquet orders ( $n$ ) acts as an additional orthogonal dimension. Due to the nonlinear (FWM) and linear coupling between the Floquet bands, the photons can occupy different sites on the two-dimensional  $\mu - n$  plane.

It is important to note the absence of dispersion along the  $n$  direction (i.e., the modes are evenly spaced with a frequency spacing  $D_1$ ). This fact gives us hope for dissipative Kerr solitons (DKS) and switching waves (SW) to be stable against transverse perturbations that are inherent to the 2D NLSE [156, 157]. Even though, such statement for our systems requires a rigorous proof, we still observe generation of stable SW and DKS as shown in details in Ref. [158].

In the actual devices, the resonator's mode-stripping section is not just a simple sine function, and the Fourier decomposition of the dispersion in Eq. (2.2) has many harmonics. In this case, each Fourier amplitude  $\tilde{d}_2^{(n)}$  corresponds to the coupling strength between Floquet orders separated by  $n \times \text{FSR}$ . However, for simplicity we consider the case of harmonic modulation (presented in Fig. 2.1b), i.e.,  $\tilde{d}_2^{(1)} = \tilde{d}_2^{(-1)} = \Delta/2$  and we neglect the higher-order terms by assuming  $\tilde{d}_2^{(n)} \ll \tilde{d}_2^{(1)}$ .

### 2.3 Modulation instability

While the governing equation in the form of Eq. (2.4) helps to qualitatively understand the properties of the system, we return to the original version of LLE (2.1) to quantitatively analyze the modulation instability gain lobes on the  $n - \mu$  plane. In the limit of harmonic modulation, we are able to develop an analytical derivation and analyze the linear stability of the CW background field. We assume the optical field  $\psi(t) = \psi_0(\varphi, t) + \xi(\varphi, t)$ , where  $\psi_0(\varphi, t)$  is a solution of Eq. (2.1) with an unmodulated dispersion term and the small perturbation  $\xi(\varphi, t) \ll \psi_0(\varphi, t)$  obeys the linearized equation

$$\frac{\partial \xi}{\partial t} = -(1 + i\zeta_0)\xi + i\left(d_2^{(0)} + \Delta \frac{e^{id_1 t} + e^{-id_1 t}}{2}\right) \frac{\partial^2}{\partial \varphi^2} \xi + i(2|\psi_0|^2 \xi + \psi_0^2 \xi^*) + \Delta \frac{\partial^2 \psi_0}{\partial \varphi^2} \cos d_1 t. \quad (2.5)$$

Furthermore, we use  $\xi = A(t) \exp i\mu\varphi + B^*(t) \exp -i\mu\varphi$  as an ansatz to derive the coupled mode equations for the modes  $A$  and  $B$

$$\begin{cases} \frac{\partial A}{\partial t} = -(1 + i\zeta_0)A - i\left(d_2^{(0)} + \Delta \frac{e^{id_1 t} + e^{-id_1 t}}{2}\right) \mu^2 A + i(2|\psi_0|^2 A + \psi_0^2 B) + \Delta \frac{\partial^2 \psi_0}{\partial \varphi^2} \cos d_1 t, \\ \frac{\partial B}{\partial t} = -(1 - i\zeta_0)B + i\left(d_2^{(0)} + \Delta \frac{e^{id_1 t} + e^{-id_1 t}}{2}\right) \mu^2 B - i(2|\psi_0|^2 B + \psi_0^2 A) + \Delta \frac{\partial^2 \psi_0}{\partial \varphi^2} \cos d_1 t. \end{cases} \quad (2.6)$$

Our next step to capture the 2D FWM processes consists in the assumption  $A = \alpha_0 + \alpha_+ \exp id_1 t + \alpha_- \exp -id_1 t$ ,  $B = \beta_0 + \beta_+ \exp id_1 t + \beta_- \exp -id_1 t$ , where the amplitudes obey

$$\frac{d}{dt} \mathbb{Y} = \mathbb{M} \mathbb{Y}, \quad (2.7)$$

where  $\mathbb{Y} = [\alpha_0, \alpha_+, \alpha_-, \beta_0, \beta_+, \beta_-]^T$  and the matrix

$$\mathbb{M} = \begin{pmatrix} m_{00} & -i\mu^2 \Delta/2 & -i\mu^2 \Delta/2 & i\psi_0^2 & 0 & 0 & 0 \\ -i\mu^2 \Delta/2 & m_{11} & 0 & 0 & i\psi_0^2 & 0 & 0 \\ -i\mu^2 \Delta/2 & 0 & m_{22} & 0 & 0 & i\psi_0^2 & 0 \\ -i\psi_0^{*2} & 0 & 0 & m_{00}^* & i\mu^2 \Delta/2 & i\mu^2 \Delta/2 & 0 \\ 0 & -i\psi_0^{*2} & 0 & i\mu^2 \Delta/2 & m_{11}^* & 0 & 0 \\ 0 & 0 & -i\psi_0^{*2} & i\mu^2 \Delta/2 & 0 & m_{22}^* & 0 \end{pmatrix}, \quad (2.8)$$

where  $m_{00} = -(1 + i\zeta_0) - i\mu^2 d_2^{(0)} + 2i|\psi_0|^2$ ,  $y_{11} = m_{00} - id_1$ , and  $m_{22} = m_{00} + id_1$ . The eigenvalues  $\lambda_j$  of this matrix help to analyze modulationally unstable solution: the real part  $\text{Re}\lambda_j$  represents the gain rate, and the imaginary part  $\text{Im}\lambda_j$  reveals the phase-matching condition for such solutions to be unstable. We analyze the eigenvalues  $\lambda_j$  numerically as shown in Fig. 2.2 for the cases of dominating anomalous (panel a) and normal (panel b) dispersion. In both cases,  $\text{Im}\lambda_j$  reflect the appearance of the dispersion parabolas in the Floquet bands with  $\pm 1D_1$  offsets and their complex-conjugated counterparts due to the nonlinear term. However, the parametric gain lobes drastically differ for these two dispersion regimes. In the case of anomalous dispersion (Fig. 2.2a), there are three regions with positive gain. First region, with the largest value  $\text{Re}(\lambda_j)$  appears due to the crossings of the dispersion parabola and its



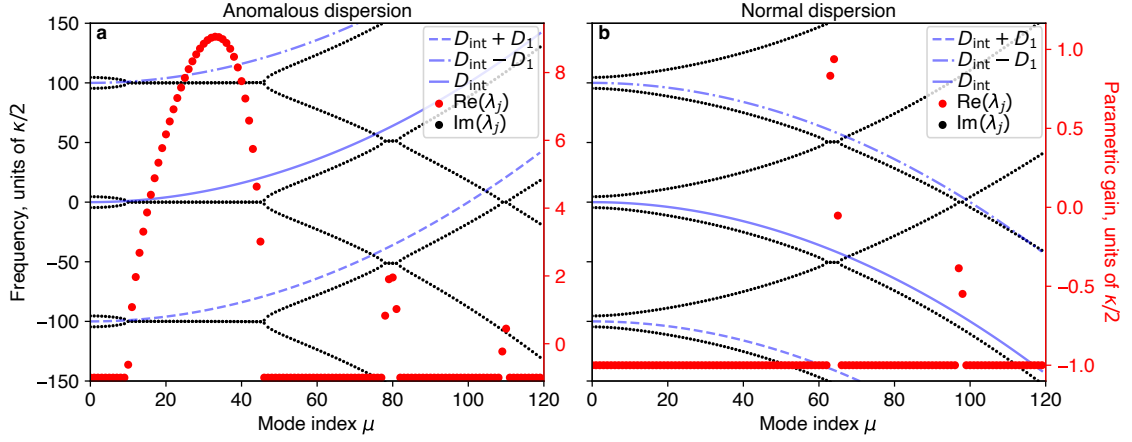


Figure 2.2: **Eigenvalues of the matrix (2.8).** (a) Anomalous dispersion, (b) normal dispersion. Red (black) dots represent the parametric gain (frequency) of the modes  $\alpha_0, \alpha_+, \alpha_-, \beta_0, \beta_+, \beta_-$ . Blue solid lines show the integrated dispersion profile  $d_2^{(0)}\mu^2$ ; dotted and dash-dotted lines correspond to the integrated dispersion in for  $\pm 1$  Floquet orders. Numerical values of the parameters:  $d_1 = 100$ ,  $d_{2,\text{anom}}^{(0)} = 0.005 = -d_{2,\text{norm}}^{(0)}$ ,  $\Delta = 0.5d_{2,\text{norm}}^{(0)}$ ,  $f^2 = 20$ ,  $\zeta_0 = 9.08$ .

conjugated counterpart from the same Floquet band. Effectively, this modulation instability corresponds to the classical Turing instability with breathing frequency of one FSR. In other words, this process is very similar to the XPM process in a single microresonator. In contrast, the second region of the unstable modes appears due to the crossing between the parabolas from 0th order Floquet order with the parabolas from  $\pm 1$ st bands. Since the frequencies of the unstable solutions are separated by  $d_1/2$  from the pump mode ( $\mu = 0$ ), the temporal dynamics of the pump mode with these sidebands would have period  $2T_r$ , i.e., the field would go back to its initial state every second roundtrip, experiencing period-doubling dynamics. This effect is attributed to the Faraday instability (FI) and we further investigate it in detail. The crossings of the parabolas from 1st and  $-1$ st bands gives rise to the third gain lobe, which has no off-set from the pump mode. In the normal dispersion regime, there is no Turing instability and only second and third regions are present, however the third region of the gain lobes does not have positive values for the chosen parameters of pump  $f$  and detuning  $\zeta_0$ .

### 2.3.1 Faraday instability

In this section, we focus on the Faraday instability. To simplify the analytical treatment, we reduce the dimensionality of the matrix (2.8), neglecting the solutions that are in-phase with the pump mode, and consider only the oscillating modes, i.e., we assume  $A = \alpha_+ \exp id_1/2t + \alpha_- \exp -id_1/2t$ ,  $B = \beta_+ \exp id_1 t/2 + \beta_- \exp -id_1 t/2$ . Effectively, we restrict ourselves to the

## Chapter 2. Synthetic frequency dimension in a dispersion-modulated resonator

period-doubling solutions. The resulting matrix takes form

$$\mathbb{M} = \begin{pmatrix} m_{00} & -i\mu^2\Delta/2 & i\psi_0^2 & 0 \\ -i\mu^2\Delta/2 & m_{11} & 0 & i\psi_0^2 \\ -i\psi_0^{*2} & 0 & m_{00}^* & i\mu^2\Delta/2 \\ 0 & -i\psi_0^{*2} & i\mu^2\Delta/2 & m_{11}^* \end{pmatrix}, \quad (2.9)$$

where  $m_{00} = -(1 + i\zeta_0) - id_1/2 - i\mu^2 d_2^{(0)} + 2i|\psi_0|^2$  and  $m_{11} = y_{00} + id_1$ . This matrix has degenerate eigenvalues that read

$$\lambda_{1,2} = -1 + \frac{i}{2} \left( \Delta^2 \mu^4 + d_1^2 + 4 \left( d_2^{(0)} \mu^2 + \zeta_0 \right)^2 + 12|\psi_0|^4 - 16|\psi_0|^2 \left( d_2^{(0)} \mu^2 + \zeta_0 \right) - \right. \\ \left. - 4 \sqrt{|\psi_0|^4 (4\Delta^2 \mu^4 + 3d_1^2) + (\Delta^2 \mu^4 + d_1^2) \left( d_2^{(0)} \mu^2 + \zeta_0 \right) \left( d_2^{(0)} \mu^2 + \zeta_0 - 4|\psi_0|^2 \right)} \right)^{1/2} \quad (2.10)$$

$$\lambda_{3,4} = \lambda_1^*. \quad (2.11)$$

To find which comb indexes start to experience positive parametric gain, we need to look for the roots of the expression under the square root in Eq. (2.10), i.e., we need to solve an equation  $\text{Im}(\lambda_1) = 0$ . The resulting expression is quite cumbersome and difficult to analyze. However, we can write an approximate expression for the mode indexes  $\mu \gg 1$  separated far away from the pump mode, neglecting terms  $\psi_0$  and  $\zeta_0$  that are linked via the Eq. 2.1. The resulting expression reads

$$\mu \approx \pm \sqrt{\frac{d_1}{2\sqrt{(d_2^{(0)})^2 - (\Delta/2)^2}}} \approx \pm \sqrt{\frac{D_1}{D_2^{(0)}}}. \quad (2.12)$$

This expression can be obtained from simpler considerations: one just needs to find an intersection between the unperturbed dispersion profile with a conjugated parabola from the 1st Floquet band, i.e., solve an equation  $d_2^{(0)} \mu^2 = -d_2^{(0)} \mu^2 + d_1$ . However, analyzing the eigenvalues we quantitatively prove that these sidebands are the result of phase matching between the original 0th order parabola and the conjugated 1st order parabola. Additionally, we can observe that sidebands appear further away from the pump with increasing modulation depth  $\Delta/d_2^{(0)}$ .

Next, we numerically investigate FI efficiency as a function of  $\Delta/d_2^{(0)}$ . We fix the pump power to  $f^2 = 15$  and compute the maximal value of the parametric gain as a function of pump detuning  $\zeta_0$  for different modulation depths:  $\Delta/d_2^{(0)} = 0.1, 0.3, 0.5, 0.7$  as depicted in Fig. 2.3. For the chosen pump power, the CW solution  $\psi_0$  follows the famous tilted resonance curve with bi-stable behavior. In the bi-stable regime we choose the stable solution with highest amplitude; therefore, one can observe the edge of the bi-stable region - a diagonal line in Fig. 2.3. The instability tongues that form above this line appear due to the higher amplitude of the value  $\psi_0$  and can have positive values of the parametric gain, while the region below this line is computed always for the small values of  $\psi_0$  that are already out of the resonance. In

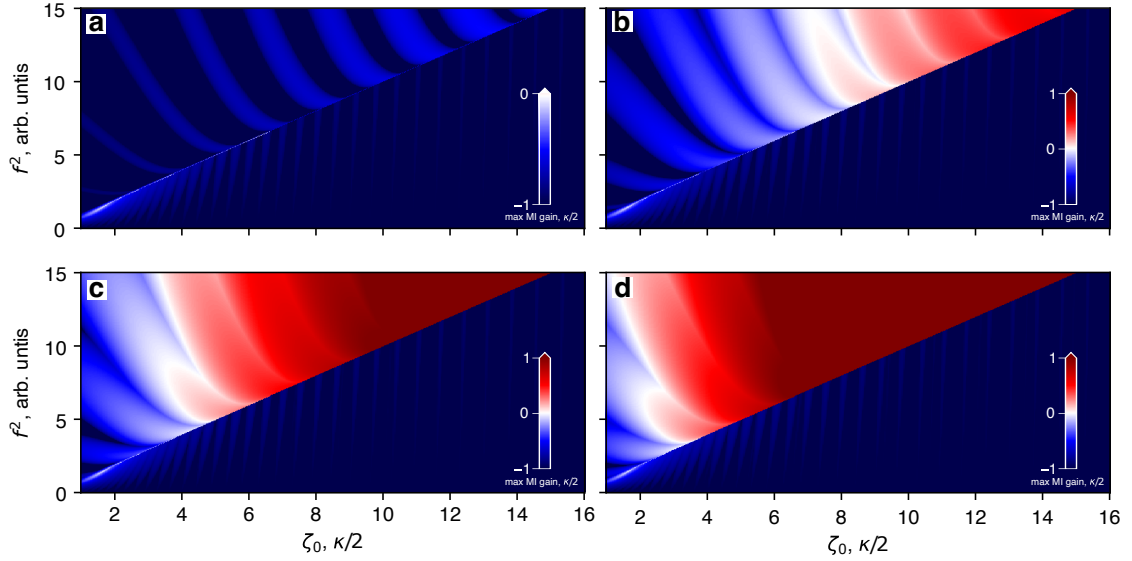


Figure 2.3: **Maximum Faraday instability gain as a function of pump power and detuning for different modulation depths.** (a)  $\Delta/d_2^{(0)} = 0.1$ , (b)  $\Delta/d_2^{(0)} = 0.3$ , (c)  $\Delta/d_2^{(0)} = 0.5$ , (d)  $\Delta/d_2^{(0)} = 0.7$ . The colormaps are centered at  $\max(\text{Re}(\lambda_j)) = 0$  to visually distinguish the borders of the unstable regions. Simulation parameters are the same as in Fig. 2.2, but pump power is  $f^2 = 15$ .

the following, we focus only on the upper part of these plots. For a shallow modulation depth ( $\Delta/d_2^{(0)} = 0.1$ , Fig. 2.3a), there are nine instability tongues, but their values are still negative. However, with increasing value of  $\Delta/d_2^{(0)}$ , the instability tongues become wider with higher value of the parametric gain and start to merge for higher detuning and pump power (see Fig. 2.3(b-d)). Thus, period-doubling can be observed with moderate pump power for higher modulation depth values.

To verify our analytical findings, we make a numerical experiment by solving Eq. 2.1 using the split-step Fourier method. The results, presented in Fig. 2.4, show the dynamics of the cavity with normal dispersion  $d_2^{(0)} = 0.0027$  and modulation depth  $\Delta/d_2^{(0)} = 0.5$ . Indeed, we observe a period-doubling dynamics (Fig. 2.4a,b), while optical spectrum in Fig. 2.4c reveals the actual position of the primary sidebands which is close to the approximate position  $\mu = 98$  obtained via Eq. (2.12). Reconstructing the NDR (Fig. 2.4d), we obtain direct access to the field in the Fourier basis (Eq. (2.2,2.3)). We observe the main dispersion parabola and its conjugated counter-part with the FI sidebands separated by  $d_1/2$  from the pump mode. Additionally, we also observe a pair of sidebands from the third MI region that we discussed in section 2.3 and showed in Fig. 2.2b that are in-phase with the pump line.

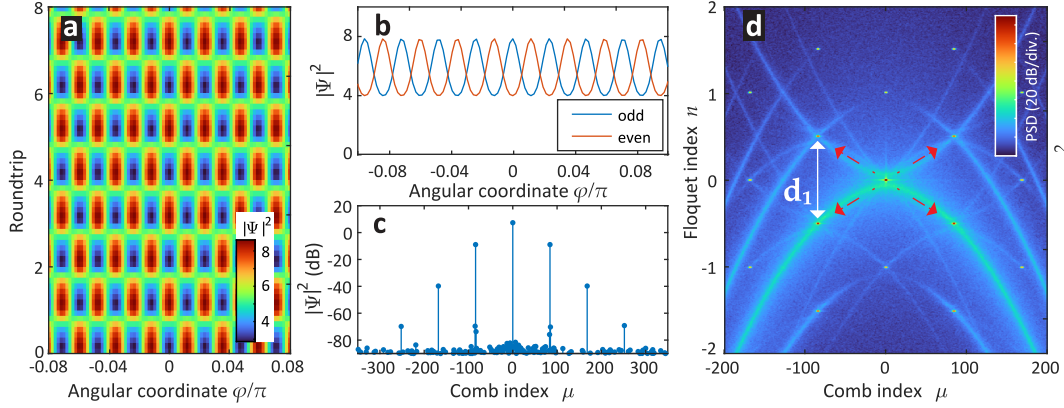


Figure 2.4: **Faraday instability numerical simulation.** (a) Resolved dynamics of the intracavity field as a function of roundtrip number. (b) Comparison of the field profiles at  $t = t_0$  (blue line) and  $t = t_0 + T_r$  (red line). (c) Snapshot of the corresponding optical spectrum. (d) Reconstructed nonlinear dispersion relation of the dynamics. Simulation parameters:  $f^2 = 10$ ,  $\zeta_0 = 5$ ,  $\Delta = 0.5d_2^{(0)}$ ,  $d_2^{(0)} = 0.0027$ ,  $d_1/2\pi = 8$ .

## 2.4 Dissipative Kerr Solitons And Switching Waves

To further investigate the role of the dispersion-induced Faraday instabilities on the dissipative structures in a microresonator, we provide numerical simulations of LLE 2.1 in the normal and anomalous dispersion regime (see Fig. 2.5). In the former, we generate DKS with CW pump, while for the latter we generate SW in the pulse-pumped regime to facilitate the excitation of the state.

### 2.4.1 Dissipative Kerr solitons

The simulated DKS is presented in Fig 2.5(a-e), for the conventional and modulated cavities. The generated soliton exists on a modulated background shown in Fig. 2.5(a,c) that corresponds to the higher-order dispersive waves (Fig. 2.5b) in the spectral domain. These dispersive waves originate from the instability appearing due to the phase-matching between 1st and  $-1$ st Floquet bands (see gain lobes with the smallest parametric gain in Fig. 2.2a). Even though, the parametric gain value of this instability is the smallest for the analysis of CW solution and Turing instability dominates, it plays an important role for solitons that are prone to Turing instability. The resulted dispersive waves are phase-matched to the main soliton spectrum and can be also attributed to Kelly sidebands that are observed in systems with periodic amplification and soliton fiber lasers [159, 160, 161].

### 2.4.2 Switching Waves

The SW simulation is presented in Fig. 2.5(f-g). In contrast to the unmodulated cavity, the generated pulse experiences period doubled dynamics with its profile changing every second

## 2.4 Dissipative Kerr Solitons And Switching Waves

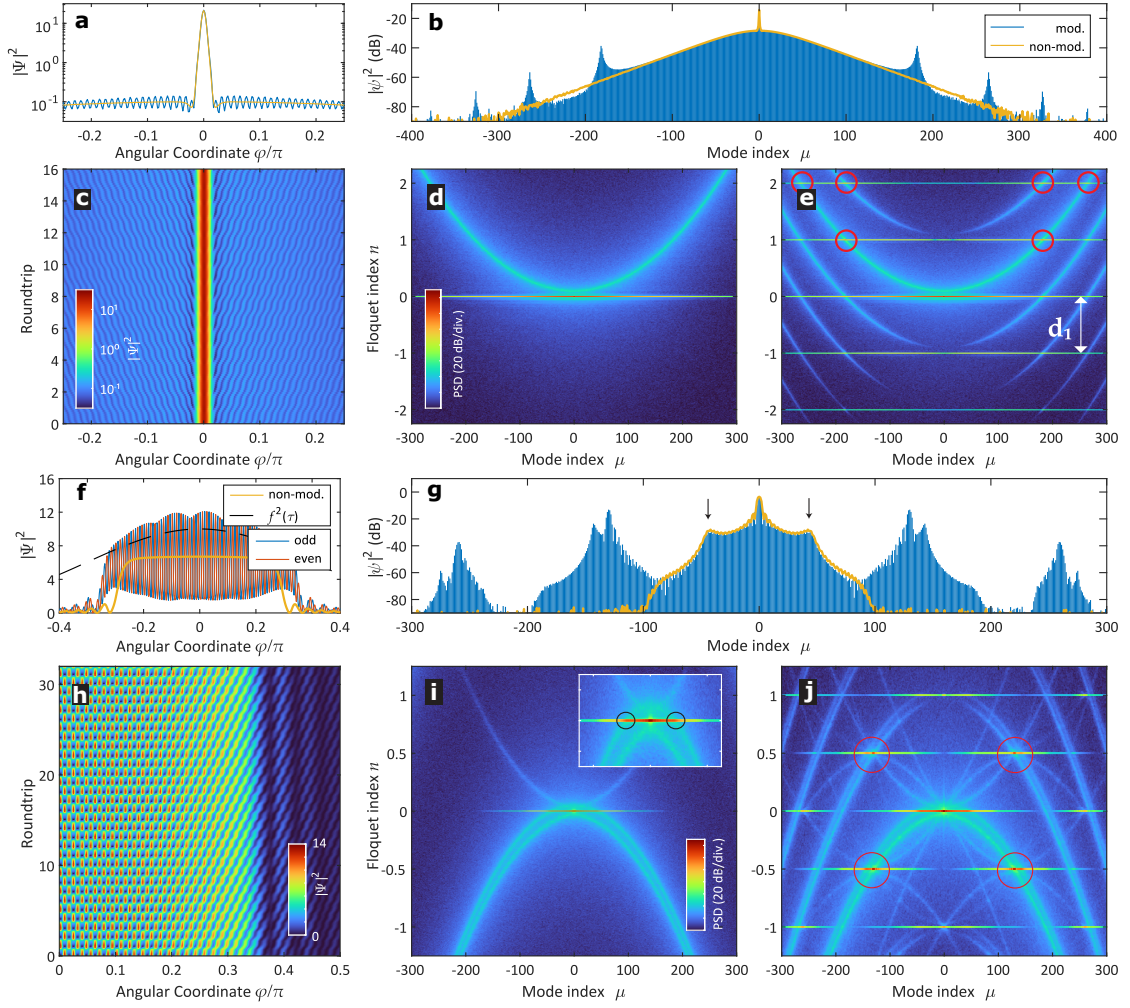


**Figure 2.5: Dissipative Kerr solitons (DKS) and switching waves (SW).** (a) DKS field snapshot with (blue) and without (yellow) modulation. (b) Corresponding fast frequency power spectrum. (c) Spatiotemporal diagram of the modulated DKS propagating in time. (d,e) DKS nonlinear dispersion relations with (d) and without (e) modulation. Red circles show higher-order dispersion waves from the third MI region. (f) SW snapshot with (blue) and without (yellow) modulation under pulse-driven conditions. (g) Corresponding power spectrum. (h) Spatiotemporal diagram of an SW in the modulated cavity. (i,j) SW nonlinear dispersion relations with (d) and without (e) modulation. Red circles show the FI-originated sidebands. Simulation parameters:  $f^2 = 10$ ,  $\Delta = 0.7d_2^{(0)}$ ,  $d_1/2\pi = 16$ ,  $d_2^{(0)} = 0.0027$ , detuning  $\zeta_0 = 10$  for the DKS and  $\zeta_0 = 6$  for the SW case.

roundtrip as shown in Fig. 2.5f,h. Analyzing the SW spectrum and NDR in Fig. 2.5g,j we observe that the Faraday instability is responsible for the spectral extension of the switching waves, resulting in the generation of powerful satellite combs. There is a reciprocal locking in repetition rate between these satellite combs and the core switching wave structure, similar to the primary sidebands analyzed in section 2.3.1. Additionally, due to the high photon occupancy in these sidebands, nonlinear modulation creates additional phase-matching conditions between the dispersion curves from different Floquet bands as shown in Fig. 2.3.1j, also resulting in the generation of the higher-order dispersion waves locked to the pump mode, similar to the Kelly sidebands in the DKS regime.

## 2.5 Conclusion

In summary, we studied theoretically four-wave mixing in a cavity with a mode-filtering section that periodically modulated its integrated dispersion. Using the comb index  $\mu$  and spectral harmonics of temporal oscillations of the optical field, we present a method of analyzing this system in two dimensions. Using the comb index  $\mu$  and spectral harmonics of temporal oscillations of the optical field, we present a method of analyzing this system in two dimensions. In other words, periodic modulation of the dispersion creates a synthetic slow frequency dimension, which reflects temporal oscillations of the optical field. Providing modulation instability analysis in the anomalous and normal dispersion regimes, we demonstrate new four-wave mixing pathways arising due to the created Floquet bands. With a focus on the normal dispersion regime, we investigate Faraday instability in detail that results in period-doubling of the optical field dynamics. Providing numerical simulations, we show how the discovered instabilities result in the generation of higher-order dispersive waves and Faraday-instability induced sidebands in the DKS or SW regimes. The discovered four-wave mixing pathways pave the way towards efficient spectral extension of the optical frequency combs in low free-spectral range optical microresonators ( $\sim 10$  GHz), as demonstrated experimentally in M. Anderson et al., “Dissipative Solitons and Switching Waves in Dispersion-Modulated Kerr Cavities”, *Physical Review X*, **13**, (2023).

Regarding practical significance, in scenarios where achieving highly uniform dispersion in a specific waveguide platform proves challenging, the proposed approach with the consecutive four-wave mixing dynamics can yield valuable outcomes. The deliberate dispersion modulation naturally induces the creation of numerous higher-order dispersive waves. These waves effectively broaden the spectrum of a soliton microcomb far beyond the point where the main part of the comb merges with optical noise. Employing this deliberate strategy has the potential to further expand an already wide-ranging soliton microcomb to the extent where it could span an octave and be self-referenced using the  $f$ - $2f$  technique, as demonstrated in previous research (Spencer et al., 2018) [81].

# **Lattices Of Resonators Part II**





## 3 Optical Parametric Oscillations in a Photonic Dimer

This chapter reports on the study of optical parametric oscillators in a photonic dimer with alternating dispersion. These results are partially adapted from D. Pidgaiko *et al.*, “Voltage-tunable optical parametric oscillator with an alternating dispersion dimer integrated on a chip,” *Optica* **10**, (2023).

### 3.1 Introduction

In the first part of this thesis, we reported on nonlinear dynamics in synthetic photonic lattices. In second part, we investigate four-wave mixing (FWM) processes in arrays of optical resonators. Specifically, in this chapter, we study the generation of primary sidebands in a system of two coupled high-Q microresonators with opposite signs of group velocity dispersion (GVD) (see Fig. 3.1a). We show that the FWM arising in this system enables us to achieve a broadband voltage-tunable optical parametric oscillator (OPO).

Modern integrated photonics demonstrates remarkable growth and is quickly approaching the ultimate lab-on-chip level of performance [162, 163]. Among other integrated components, OPOs have garnered significant attention within the scientific community. After the first demonstration of an ultralow-threshold OPO in a high-Q toroid cavity [164], there has been ongoing effort to improve key parameters such as output power, conversion efficiency, and wavelength tunability [58, 59, 165, 166, 57, 167]. These compact and versatile devices hold immense potential for a wide range of applications [168], including optical communications [169] and photon pair generation [170]. The integration of OPOs on a chip offers several advantages, including enhanced stability, reduced footprint, and compatibility with existing semiconductor manufacturing processes [125]. These factors make chip-integrated OPOs highly attractive for practical applications where space constraints and cost-effectiveness are crucial considerations. One of the key properties of integrated OPOs is the tunability of signal and idler wavelengths [171, 172, 173]. However, an outstanding challenge remains: the

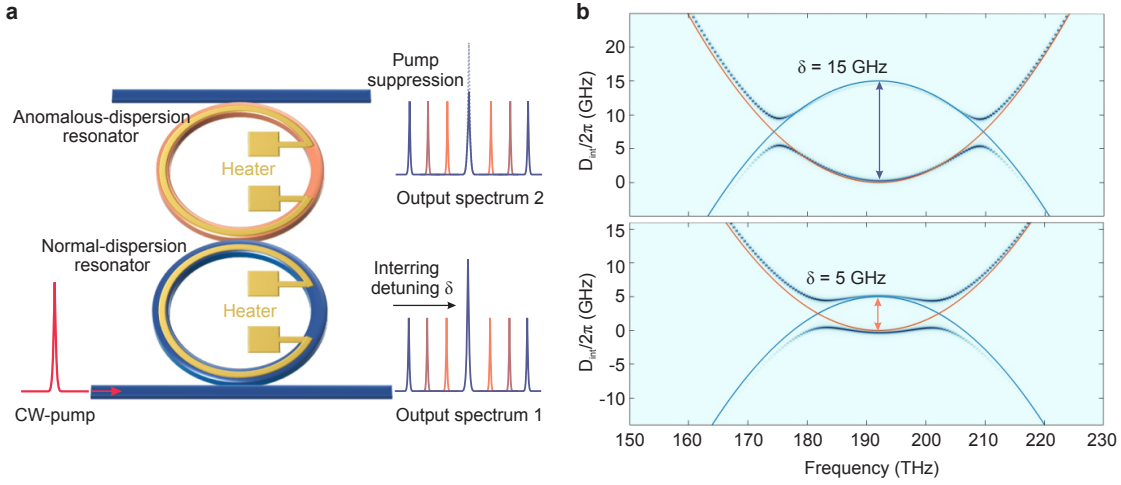


Figure 3.1: **Parametric gain in the alternating-dispersion dimer.** (a) Schematics of two coupled resonators with opposite group velocity dispersions. The external laser excites the system through the normal dispersion resonator. The output signal is measured from both add and drop ports. The signal collected from the drop port demonstrates the pump filtering effect. (b) Integrated dispersion hybridization for different interring detunings (voltages applied to the heater)..

realization of wavelength tunability without relying on a broadly tunable (often exceeding units of THz) and expensive external pump laser.

Here, we propose an OPO based on a hybrid-dispersion photonic dimer, which refers to a system comprising two coupled optical microring resonators with opposite signs of GVD, as qualitatively depicted in Fig. 3.1b. We investigate the theoretical formation of primary sidebands and validate these findings through experimental confirmation using high-Q  $\text{Si}_3\text{N}_4$  microresonators. The process of optical coupling results in the hybridization of the initial dispersion profiles of the two rings. The hybridization of these dispersion profiles is controlled using integrated heaters, which in turn govern the positioning of the interacting optical modes. By applying voltage to an integrated heater device, we can dynamically adjust the curvature of the dispersion profile. This adjustment leads to a modification of the spectral position of the parametric gain maxima and, consequently, the frequencies of the signal and idler. Our approach facilitates a tunable OPO with a nearly fixed pump laser operating wavelength, with the signal/idler to pump tuning range exceeding previous schemes by a factor of 50 [172, 173]. This result overcomes the limitations of prior techniques.

## 3.2 Description of the parametric gain

We start with theoretical discription of the primary sidebands generation in a photonic dimer. The coupled Lugiato-Lefever equation that govern the dynamics in such system can be written

in the following way:

$$\frac{dA}{dt} = -(\kappa_A/2 + i(\delta\omega + \delta_A))A + i\frac{D_2^A}{2}\frac{\partial^2}{\partial\varphi^2}A + iJB + ig_0^A|A|^2A + \sqrt{\kappa_{\text{ex}}^A S_{\text{in}}^A}, \quad (3.1)$$

$$\frac{dB}{dt} = -(\kappa_B/2 + i(\delta\omega + \delta_B))B + i\frac{D_2^B}{2}\frac{\partial^2}{\partial\varphi^2}B + iJA + ig_0^B|B|^2B + \sqrt{\kappa_{\text{ex}}^B S_{\text{in}}^B}, \quad (3.2)$$

where  $A$  ( $B$ ) describes the optical field envelope in the resonator with anomalous (normal) dispersion;  $\kappa_{A(B)} = \kappa_0 + \kappa_{\text{ex}}^{A(B)}$  is the total linewidth composed of the internal linewidth  $\kappa_0$  and the coupling to the bus waveguide;  $\delta\omega$  is the laser-cavity detuning,  $\delta_{A(B)}$  is the frequency detuning of resonator anomalous (normal) dispersion resonators;  $S_{\text{in}}^{A(B)} = \sqrt{P_{\text{in}}^{A(B)}/\hbar\omega}$  is the pump term with  $P_{\text{in}}^{A(B)}$  as an input power;  $D_2^{A(B)}$  is the group-velocity dispersion;  $J$  is the coupling strength between two resonators;  $g_0^{A(B)}$  is the single-photon Kerr frequency shift.

To analyze the modulation instability (MI) gain lobes, we use the following Ansatz

$$A = A_0 + a_\mu(t)e^{i\mu\varphi} + a_{-\mu}^*(t)e^{-i\mu\varphi}, \quad (3.3)$$

$$B = B_0 + b_\mu(t)e^{i\mu\varphi} + b_{-\mu}^*(t)e^{-i\mu\varphi}, \quad (3.4)$$

where the CW solution  $A_0$  are  $B_0$  supposed to be constant in time and obey the equation

$$0 = -(\kappa_A/2 + i(\delta\omega + \delta_A))A_0 + iJB_0 + ig_0^A|A_0|^2A_0 + \sqrt{\kappa_{\text{ex}}^A S_{\text{in}}^A} \quad (3.5)$$

$$0 = -(\kappa_B/2 + i(\delta\omega + \delta_B))B_0 + iJA_0 + ig_0^B|B_0|^2B_0 + \sqrt{\kappa_{\text{ex}}^B S_{\text{in}}^B}. \quad (3.6)$$

The amplitudes  $a_\mu$  and  $b_\mu$  are assumed to be small enough so their dynamics in time can be linearized in the vicinity of the stable solutions  $A_0$  and  $B_0$ . The resulting linearized system of equations takes form

$$\dot{a}_\mu = -(\kappa_A/2 + i(\delta\omega + \delta_A))a_\mu - i\frac{D_2^A}{2}\mu^2 a_\mu + iJb_\mu + ig_0^A(2|A_0|^2 a_\mu + A_0^{2*} a_{-\mu}^*) \quad (3.7)$$

$$\dot{a}_{-\mu}^* = -(\kappa_A/2 - i(\delta\omega + \delta_A))a_{-\mu}^* + i\frac{D_2^A}{2}\mu^2 a_{-\mu}^* - iJb_{-\mu}^* - ig_0^A(2|A_0|^2 a_{-\mu}^* + A_0^2 a_\mu) \quad (3.8)$$

$$\dot{b}_\mu = -(\kappa_B/2 + i(\delta\omega + \delta_B))b_\mu - i\frac{D_2^B}{2}\mu^2 b_\mu + iJa_\mu + ig_0^B(2|B_0|^2 b_\mu + B_0^{2*} b_{-\mu}^*) \quad (3.9)$$

$$\dot{b}_{-\mu}^* = -(\kappa_B/2 - i(\delta\omega + \delta_B))b_{-\mu}^* + i\frac{D_2^B}{2}\mu^2 b_{-\mu}^* - iJa_{-\mu}^* - ig_0^B(2|B_0|^2 b_{-\mu}^* + B_0^2 b_\mu). \quad (3.10)$$

This system of equations can be rewritten in matrix form for the unknown vector  $X$  in the form

$$\dot{X} = \mathbb{M}X, \text{ where } X = (a_\mu, a_{-\mu}^*, b_\mu, b_{-\mu}^*)^T. \quad (3.11)$$

The parametric gain rate for the OPO sidebands can be then inferred from the analysis of the eigenvalues  $\lambda_j$  ( $j=1,2,3,4$ ) of the matrix  $M$ . To compute this matrix, we solve numerically equations (3.5,3.6) imitating experimental tuning of the pump laser from the blue to red-

detuned zones of the resonances.

In Fig. 3.2 we present the computed MI gain lobes and the structure of the eigenvalues  $\lambda_j$ . To compute it, we used  $\kappa_0/2\pi = 60$  MHz,  $D_2^A/2\pi = 12.6$  MHz,  $D_2^B/2\pi = -1.1$  MHz,  $\kappa_{\text{ex}}^A = \kappa_0$ ,  $\kappa_{\text{ex}}^B = 2\kappa_0$ ,  $P_{\text{in}}^{A(B)} = 0.3$  W. In Fig. 3.2(a-d) we consider the excitation of the anomalous dispersion resonator. We observe, that for the constant resonator detuning  $\delta_B$  ( $\delta_A = 0$ ), the MI gain lobes correspond to the conventional single-resonator case (see Fig. 3.2b). As shown in Fig. 3.2c, the gain lobes almost do not change their position as they are dominated by the conventional Turing instability in the anomalous dispersion (see Fig. 3.2d). However, when we pump the normal dispersion ring (see Fig. 3.2(e-f)) and tune  $\delta_A$  ( $\delta_B = 0$ ), we observe the desired effect. Since we pump the region with normal dispersion, Turing instability does not manifest, and the sidebands experience positive parametric gain due to the new phase-matching conditions. For the fixed pump detuning, the gain lobes change their position as shown in Fig. 3.2g. The eigenvalues in Fig. 3.2h show, that the new phase matching condition occurs due to the crossing of the anomalous and normal dispersion parabolas. Thus, one can estimate the position of the modes with positive parametric gain via simple formula

$$\mu = \pm \sqrt{\frac{2\delta_A}{D_2^A - D_2^B}}. \quad (3.12)$$

The latter estimation works in the limit  $\delta_A \gg J$ . To achieve bigger tunability, one needs to reduce the group velocity dispersion of both resonators.

A calculated hybridized dispersion profile at different detunings is shown in Fig. 3.1b. Here one can see that the optical modes of the resonators are split the most in the vicinity of the initial integrated dispersion crossings. Qualitatively, it results in the additional phase-matching condition for the four-wave mixing processes that we aimed to exploit for the OPO generation.

### 3.3 Experimental Demonstration

We demonstrate the voltage-tunable OPO using a  $\text{Si}_3\text{N}_4$  dimer with a free spectral range (FSR) of 458 GHz and GVDs  $D_2^A/2\pi = 12.6$  MHz and  $D_2^B/2\pi = -1.2$  MHz for anomalous and normal resonators (for the resonator design procedure, refer to appendix A.2).

First, we perform numerical signal/idler generation experiments using simulations of two coupled LLEs. Building upon the outcomes of the preceding section, we keep the normal dispersion resonator pumped at a fixed pump detuning and power while varying the detuning of the anomalous resonator (i.e.,  $\delta_A$ , setting  $\delta_B = 0$ ; in the following, we denote  $\delta_A$  as  $\delta$ ). The generated signal and idler spectral positions, as depicted in Fig. 3.3a, closely match the results shown in Fig. 3.2g. This agreement underscores the ability to achieve OPO signal tunability of 20 THz while maintaining a fixed pump laser frequency.

The experimental measurements are conducted on dimers fabricated by Ligentech SA (as

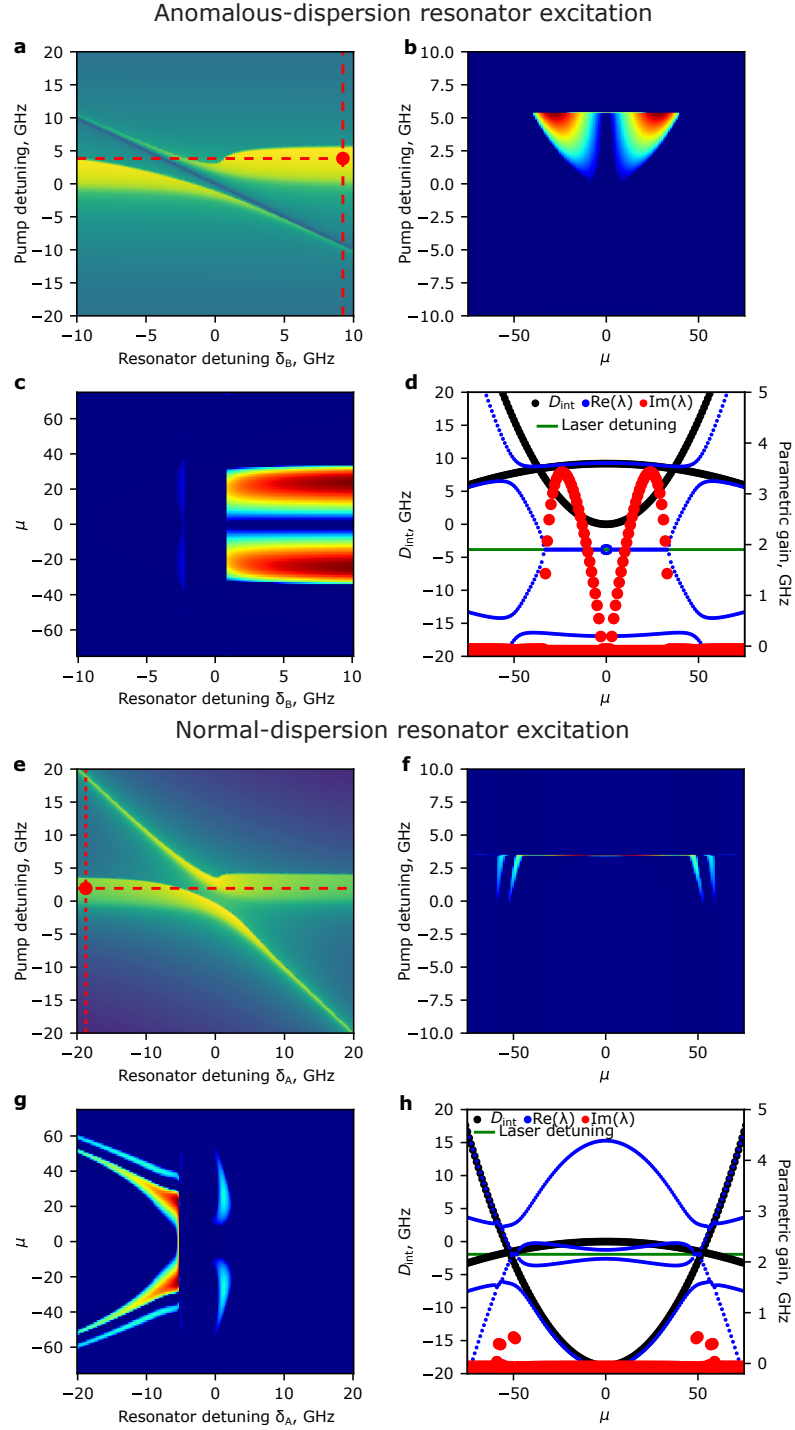
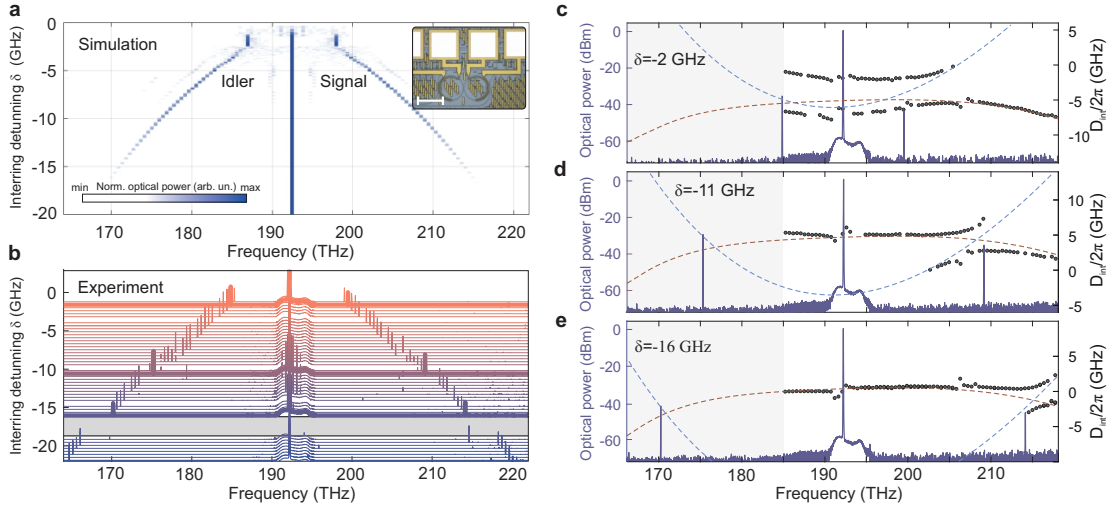


Figure 3.2: **Modulation instability (MI) gain lobes.** a) Field response in one of the resonators for different pump and resonator detunings  $\delta$ . b) MI gain lobes as a function of pump detuning along vertical dashed line in a). c) MI gain lobes along the horizontal dashed line in a). d) Integrated dispersion and eigenvalues  $\lambda_j$  structure for the point in panel a). (e-f) The same, but for the excitation of the normal dispersion resonator.



**Figure 3.3: Voltage-controlled OPO.** (a and b) LLE-based numerical and experimental OPO tuning by thermal tuning of the normal-dispersion resonator. Inset in (a) is a photo of the experimental dimer. Thick lines in (b) are optical spectra with interring detunings  $\delta$  equal to -16 GHz, -11 GHz and -2 GHz, respectively. The gap corresponds to the region forbidden by mode crossings. (c-e) OPO spectra combined with integrated dispersion measurements for the same interring detuning.

shown in the inset of Fig. 3.3a). All the experimental data presented in Fig. 3.3b originate from a single experimental device (refer to the experimental setup in appendix A.3). The observed wide range of operating wavelengths and the precise control over the OPO's signal/idler position are evident. Notably, gaps in Fig. 3.3(b) correspond to parameter ranges where sidebands are generated in parasitic mode crossings or parametric oscillations are not detected.

In contrast to numerical simulations, realizing the tunable OPO experimentally necessitated adjusting the pump frequency due to the initially designed relative inter-ring detunings of the resonators. To achieve signal and idler tuning, we heated the normal dispersion resonator and adjusted the pump frequency to stay in resonance. This pump frequency adjustment occurs within a 20 GHz bandwidth, yielding an approximate 20 THz OPO signal/idler tuning range. Thus, the laser tunability requirements are orders of magnitude lower than those demanded by previous schemes. It's worth noting that piezoelectric actuators can further alleviate these requirements, offering the potential to significantly reduce the tuning range of the pump laser.

To establish a direct correlation between signal/idler frequency tuning and dispersion hybridization, we conducted dispersion characterization measurements for each interring detuning value illustrated in Fig. 3.3b. The outcomes for specific detunings are marked as dots in Fig. 3.3c-e and are overlaid with the corresponding optical spectra (depicted as thick lines in Fig. 3.3b). In order to emphasize the influence of hybridization on the dispersion profile, we incorporated the fitted dispersion for the uncoupled regime, as indicated by the dashed lines (for details on the fitting procedure, refer to appendix A.4). This approach enables a

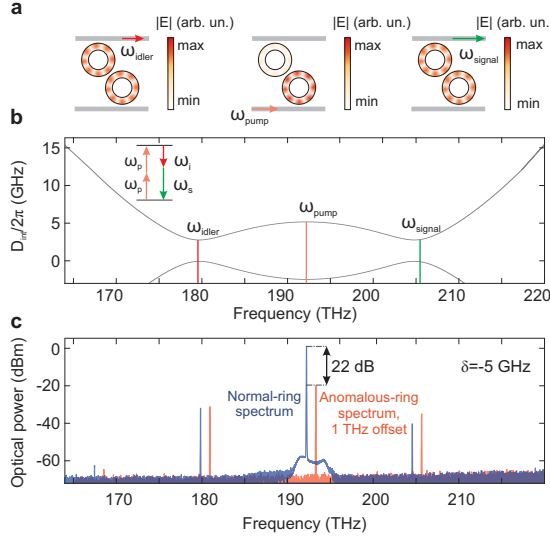


Figure 3.4: **OPO pump suppression in the drop-port output.** (a) Layout for pump suppression effect. At the pump frequency, the optical power is localized in the normal-dispersion ring. In the vicinity of the strongest mode interaction, power is distributed equally. (b) Schematic representation of hybridized dispersion with pump, signal, and idler frequencies separation. (c) The experimental optical spectrum for both rings at  $\delta = -5$  GHz. Blue and red colors indicate the add/drop port measurements of the optical spectrum, respectively.

clear observation: the signal/idler lines emerge in proximity to the region of stronger mode interaction and closely track it as we manipulate the inter-ring detuning.

### 3.4 Pump suppression

One of the key applications that can be influenced by the voltage-tunable OPO is quantum communication [170]. In this context, the presence of a strong pump often poses a challenge for sensitive quantum detectors. Our scheme, based on coupled resonators, offers the potential for efficient pump filtering. Two factors contribute to this process: pump mode hybridization and utilization of the drop port. Notably, mode hybridization modifies the dispersion curvature at distinct mode frequencies (refer to Fig. 3.4a in the vicinity of 192 THz). Importantly, the hybridized pump mode predominantly resides within the normal dispersion resonator. Conversely, near the crossing point of the original dispersion profiles—occurring at the point of strongest interaction (205 THz in Fig. 3.4a)—optical power leaks into the auxiliary resonator. This design enables the detection of signal/idler lines with suppressed pump on the second ring drop port. The dependence of pump suppression on interring detuning is calculated and presented in appendix A.1. However, it is noteworthy that in the fabricated device, the placement of the drop port led to a cross-talk effect at the output. As shown in Fig. 3.4b, this results in a consistent pump suppression of approximately 22 dB and a partial enhancement of the sideband power.

Finally, it should be noted that there are several potential improvements that could significantly enhance the system's performance. Firstly, the incorporation of integrated actuators would effectively eliminate thermal cross-talk between resonators and negate the need for pump laser tunability. Secondly, a more refined optimization of the dispersion profile could extend the operation bandwidth to encompass octave-spanning regimes, further enhancing pump suppression at the drop port. Thirdly, optimizing the bus-to-ring coupling would amplify the efficiency of the OPO. Given these potential enhancements, we firmly believe that our proof-of-concept device has the potential to evolve into a reliable tool for modern photonic applications.

### 3.5 Conclusion

In conclusion, the development of a broadband voltage-tunable OPO integrated on a chip represents a remarkable achievement in the field of integrated photonics. Our approach, based on two coupled resonators with opposing dispersion characteristics, offers extraordinary tunability while circumventing the necessity for a broadly tunable and costly laser source. This breakthrough paves the way for the realization of compact, cost-effective, and highly tunable OPOs, capable of seamless integration into diverse photonic systems. This has the potential to revolutionize the realms of optical communications, sensing, and quantum information processing. By harnessing this concept, we showcase the potential for a groundbreaking leap in voltage-tunable OPOs that can be seamlessly integrated on-chip. Moreover, achieving broadband voltage tunability without reliance on a broadly tunable laser marks a significant stride forward in the realm of integrated photonics. This advancement not only obviates the need for expensive external laser sources but also elevates the device's overall efficiency and performance.



## 4 Quiet points in a coupled resonator system

This chapter reports on the quiet point investigation in a coupled resonator system for low-noise microwave generation. These results are partially adapted from A. Triscari *et al.*, “Quiet point engineering for low-noise microwave generation with soliton microcombs,” *Communications Physics* **6**, (2023).

### 4.1 Introduction

In the previous section, we investigated modulation instability of CW solution in a photonic dimer and its application for OPO generation with optical microresonators. We demonstrated how mode interactions modify the dispersion profile and how this changes the stability of the plane wave solutions. In this section, we focus on the dynamics of a single DKS in a photonic dimer system with its applications to the low-noise microwave generation. We consider a system of two coupled resonators with different free spectral ranges (see Fig. 4.1a). The main resonator is used to generate the DKS, while the mode interaction with the auxiliary resonator results in a single-mode displacement on the integrated dispersion profile as schematically shown in Fig. 4.1b. Modification of the dispersion profile results in the generation of the dispersive wave that allow for compensation of the Raman shift.

To understand the transduction of phase noise to the soliton (i.e., DKS repetition rate  $\omega_{\text{rep}}$ ) we consider Raman scattering and the DW recoil as the main noise transfer mechanisms (cf. Fig. 4.1a), and aim to reduce the repetition rate susceptibility to the laser detuning fluctuations  $\delta\omega$ , i.e., minimize  $|\frac{\partial\omega_{\text{rep}}}{\partial\delta\omega}| \propto |\frac{\partial}{\partial\delta\omega}(\Omega_{\text{Raman}} + \Omega_{\text{DW}})|$  [174]. To introduce the presence of a DW, we consider a simplified model of AMX, characterized by a single mode displacement at position  $\bar{\mu}$  and strength  $\Delta_{\bar{\mu}}$ , in the integrated dispersion profile, as shown in Fig. 4.1b. The corresponding spectrum of the generated DKS has a typical  $\text{sech}^2$  shape with a frequency shift  $\Omega$  and dispersive wave at  $\bar{\mu}$  (Fig. 4.1c). To qualitatively explain the noise reduction mechanism, we start by separately analyzing the Raman and DW contributions to the DKS repetition rate

response. We consider the simplest case of sinusoidal frequency modulation of the pump detuning around a constant value  $\delta\omega$  as presented in Fig. 4.1d-i. In the presence of the Raman effect only, the DKS's group velocity is in-phase with the detuning change (c.f. Fig. 4.1d). In the nonlinear dispersion relation (NDR) representation [175], the DKS dynamics has a butterfly-shaped profile, revealing the transfer of the laser detuning modulation to the soliton group velocity  $v_g$  (i.e., the tilt of the soliton line in Fig. 4.1e) that directly reflects the repetition rate change [176]. Equally, the NDR representation clearly shows the comb-line dependent frequency noise multiplication mechanism induced by the repetition rate variation [177, 178] (i.e., phase noise multiplication). In the presence of an AMX, the laser detuning dependence of the DKS's group velocity can exhibit the opposite sign as shown in Fig. 4.1f. Represented in the NDR, the soliton forms a similar butterfly shape with enhanced photon occupancy at the displaced mode (Fig. 4.1g). These two effects, combined together, can then counteract due to the opposite dependence, resulting in the reduction of the detuning noise transfer (Fig. 4.1h,i). In the following, we identify a QP by reconstructing the group velocity manifold  $v_g$  as a function of  $\delta\omega$  and parameters of the AMX i.e., mode index  $\bar{\mu}$  and its displacement from the unperturbed dispersion profile  $\Delta_{\bar{\mu}}$ , further computing its extrema along the laser detuning direction. To compute the actual value  $v_g$ , we employ the Newton-Raphson method with group velocity as a variable parameter.

Since we focus on the dynamics of a single soliton in the main cavity, we model the system using a modified LLE with Raman term. In the normalized form, it reads

$$\frac{\partial\psi}{\partial t} = -(1 + i\zeta_0)\psi + \frac{i}{2}\partial_\theta^2\psi + i|\psi|^2\psi + f + v_g\partial_\theta\psi - i\Delta_{\bar{\mu}}\psi_{\bar{\mu}}e^{i\bar{m}\theta} - i\tau\psi\partial_\theta|\psi|^2. \quad (4.1)$$

Here the mode index becomes non-integer  $m = \mu\sqrt{2D_2/\kappa}$ , where  $\mu$  is an integer mode index,  $\kappa$  is the total loss rate, and  $D_2$  is the second-order integrated dispersion. The last three terms represent group velocity change  $v_g$ , modification of the  $D_{\text{int}}$  by the AMX at the mode  $\bar{\mu}$ , and the Raman scattering, respectively.

### 4.2 QP with a single-mode displacement

To investigate the DKS group velocity response to the detuning variations  $\zeta_0$ , we look for a single-soliton equilibrium solution  $\psi_{\text{DKS}}$  and its relative group velocity  $v_g$  for the parameter set  $(f, \zeta_0, \bar{\mu}, \Delta_{\bar{\mu}})$  using the Newton-Raphson approach for Eq. (4.1). To reduce the dimensionality of the parameter space, we fix the pump power  $f^2 = 6$ ,  $|\bar{\mu}| = 21$ , and sweep the detuning value within the soliton existence range (given by  $\pi^2 f^2/8$  [77] in the unperturbed case) and the  $\Delta_{\bar{\mu}}$  in the vicinity of the dispersive wave resonance. As a result, we obtain a soliton solution and the corresponding group velocity  $v_g$  for every point on the  $(\Delta_{\bar{\mu}}, \zeta_0)$ -subspace, both for blue- ( $\bar{\mu} < 0$ ) and red-side ( $\bar{\mu} > 0$ ) mode shifts (cf. Fig. 4.2). First, we focus on the blue-sided displacement (i.e.  $\bar{\mu} < 0$ ). The presence of the shifted mode results in the generation of the DW (see Fig. 4.2a), whose strength depends on the phase matching condition with the DKS. The acquired group velocity due to the recoil increases in the vicinity of the DW resonance

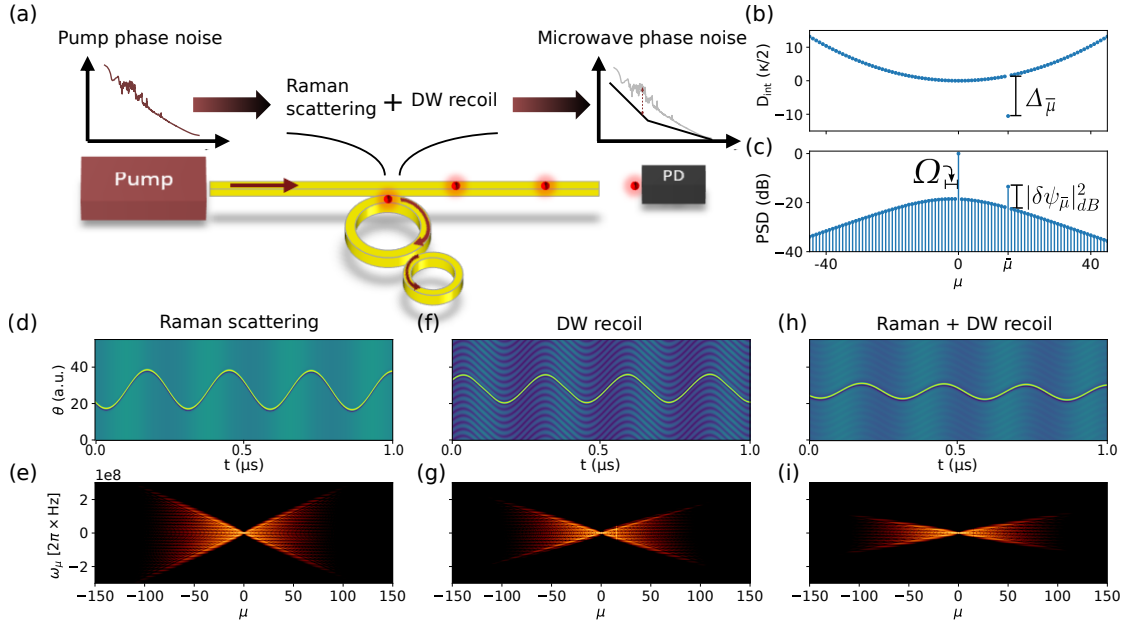


**Figure 4.1: The concept of the quiet point engineering using coupled resonators.** (a) Schematic of the phase-noise reduction in a microresonator. The auxiliary cavity is required to control the dispersive wave (DW) recoil in order to balance the effect of Raman scattering. (b) Example of the considered integrated dispersion profile with shifted resonance for a single spatial mode (i.e. localized AMX); the shifted mode number is  $\bar{\mu} = 15$  and the resonance is shifted from the perfect parabolic profile by  $\Delta_{\bar{\mu}} = -4$ . (c) Power spectral density of stable soliton solution both in the presence of Raman scattering and AMX for the integrated dispersion given in (b); the presence of Raman scattering and AMX results in a detuning dependent frequency shift  $\Omega$  of the soliton spectrum responsible for the noise transduction mechanism. The shift induced by AMX on the dispersion profile leads to a perturbation  $\delta\psi_{\bar{\mu}}$  of the occupancy of the displaced mode  $\bar{\mu}$  with respect to the perfect hyperbolic secant profile resulting in the generation of dispersive waves. (d-e) Real-space (d) and Fourier-space (e) soliton dynamics driven with a sinusoidal detuning ( $\zeta_0(t) = 4 + 0.4 \cos(\alpha t + \varphi)$ ,  $\alpha = 0.0033$ ,  $\varphi = -200$ ) in presence of Raman scattering only (left), AMX (center) and both (right) for the dispersion profile in (b).

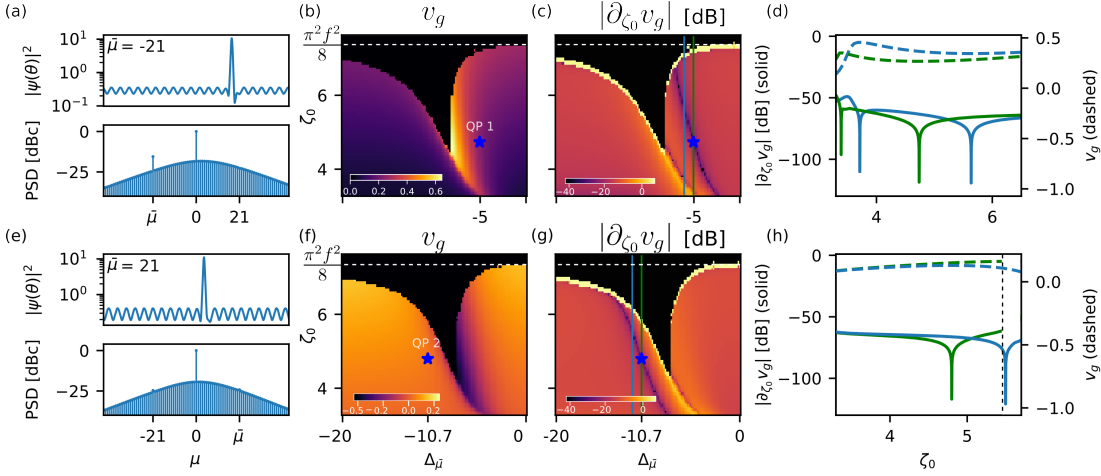


Figure 4.2: **Quiet point identification via group velocity detection and dynamics in the 2D space of detuning-mode crossing strength** (a-d) Simulation results obtained with the Newton-Raphson algorithm for  $(\Delta\bar{\mu}, \zeta_0; \bar{\mu} = -21, f^2 = 6, \tau = 5 \cdot 10^{-3})$ , i.e. in presence of Raman scattering and single mode resonance shift. a) Single soliton solution for  $(\Delta\bar{\mu} = -5, \zeta_0 = 4.73)$  (blue star). The single mode shift leads to a periodic modulation of the constant background with period  $\frac{2\pi}{|\bar{\mu}|}$ . (b) single soliton group velocity  $v_g$  in  $(\Delta\bar{\mu}, \zeta_0)$ -plane. The black area indicates the region of parameters where the method does not converge. The white dashed line highlights the existence range of the single DKS solution. The colormap shows how the soliton existence range is reduced in the presence of a higher value of the group velocity related to the increasing intensity of the DW that perturbs the DKS state. (c)  $10\log_{10}|\frac{\partial v_g}{\partial \zeta_0}|$  as a measure of the DKS repetition rate susceptibility to the variation of laser detuning. The smallest value of the susceptibility is obtained for a continuous line of operating point in the  $(\Delta\bar{\mu}, \zeta_0)$ -plane, here called the QP line (dark blue). (d) Comparison of the susceptibility (solid) and group velocity (dashed) profiles for two different sections of the QP line [green and light blue lines in subplot (c)]. (e-h) Similar results for opposite mode displacement, i.e.  $(\Delta\bar{\mu}, \zeta_0; \bar{\mu} = 21, f^2 = 6, \tau = 5 \cdot 10^{-3})$ .

as shown in Fig. 4.2b. After a given value of detuning, the DW destabilizes the DKS and the equilibrium state cannot be achieved anymore (the absence of the soliton solution is depicted in black in Fig. 4.2b).

Increasing the normalized mode shift strength  $\Delta_{\bar{\mu}}$ , we observe that the effect of the DW on the soliton is substantially reduced and the soliton existence range approaches the value estimated for the unperturbed LLE (see white dashed line in Fig. 4.2b). Next, we compute the group velocity directional derivative  $\partial_{\zeta_0} v_g$  shown in Fig. 4.2c. As a result, we observed a family of solutions with  $\partial_{\zeta_0} v_g = 0$  that correspond to the QPs. Crucially, due to the lack of control, prior experimental works have reported only a slice (vertical line cut) of the map for the fixed  $\Delta_{\bar{\mu}}$  as depicted in Fig. 4.2d. Dashed lines represent the interpolated group velocity as a function of detuning  $\zeta_0$  for two values  $\Delta_{\bar{\mu}} = -6.85, -5$  while the solid lines represent the response  $\partial_{\zeta_0} v_g$  on a logarithmic scale (directly reflecting the noise transduction). For both values  $\Delta_{\bar{\mu}}$  there are two points with zero derivative  $\partial_{\zeta_0} v_g$ . We followed the same procedure for the red-side mode displacement  $\bar{\mu} > 0$  (same side as for the Raman frequency shift) and observed similar behavior for the soliton states, group velocity, and its derivative (Fig. 4.2(e-h)). Qualitatively, the soliton profile and its existence range remain the same as in the previous case, but the QP line is shifted now towards the higher mode-displacement amplitudes where the soliton existence range is narrowed.

### 4.3 Two-mode displacement for QP engineering

Next, we investigate the region where the two QPs (for displaced modes on the blue and the red side of the pump) can co-exist and interact. First, as an example of the novel dynamics, we fix the displaced mode index  $\bar{\mu} = -21$  and the displacement strength  $\Delta_{\bar{\mu}} = -5.00$  scanning the displacement  $\Delta_{-\bar{\mu}}$ , of the mode  $\bar{\mu}' = -\bar{\mu}$  for different detunings  $\zeta_0$ . The Newton-Raphson results for the single soliton state are shown in Fig. 4.3(a-d). As in the case of a single-mode displacement, the DKS coexists with a single-period DW background (the periodicity is given by  $|\bar{\mu}|$ ). In this case, we discovered that the single soliton solution exists for  $\Delta_{-\bar{\mu}} < -7$ . For large negative displacements ( $\Delta_{-\bar{\mu}} \approx -20$ ),  $\bar{\mu}'$  is out of resonance and the QP detuning value corresponds to the one in Fig. 4.2c. Reducing the displacement  $|\Delta_{-\bar{\mu}}|$ , the soliton starts being resonant also to mode  $\bar{\mu}'$  resulting in an effective bending of the QP line, converging to the single mode one for red-shifted mode (Fig. 4.2.f). While in the case of a single-mode displacement, the QP line is always tilted (see Fig 4.2c,g) which narrows down the noise suppression region for a fixed value of  $\Delta_{\bar{\mu}}$ , displacing two modes, we are crucially able to *engineer a flat susceptibility* over a wide range of laser detunings  $\zeta_0$ . We refer to this state of the system as engineered QP (EQP). The flat susceptibility region is achieved at  $\Delta_{-\bar{\mu}} = -12.52$  (cf. Fig. 4.3c). In Fig. 4.3d, we compare  $v_g$  and its susceptibility  $\partial_{\zeta_0} v_g$  for the single mode displacement (green lines in Fig. 4.2d) with the case in Fig. 4.3c (gray lines). The latter clearly shows a flatter response profile that can be practically beneficial for accessing the QP regime. The effect of this is depicted in Fig. 4.3d, which shows an order of magnitude broadening of the QP detuning bandwidth. We repeat the same procedure, fixing the mode  $\bar{\mu} = 21$  with

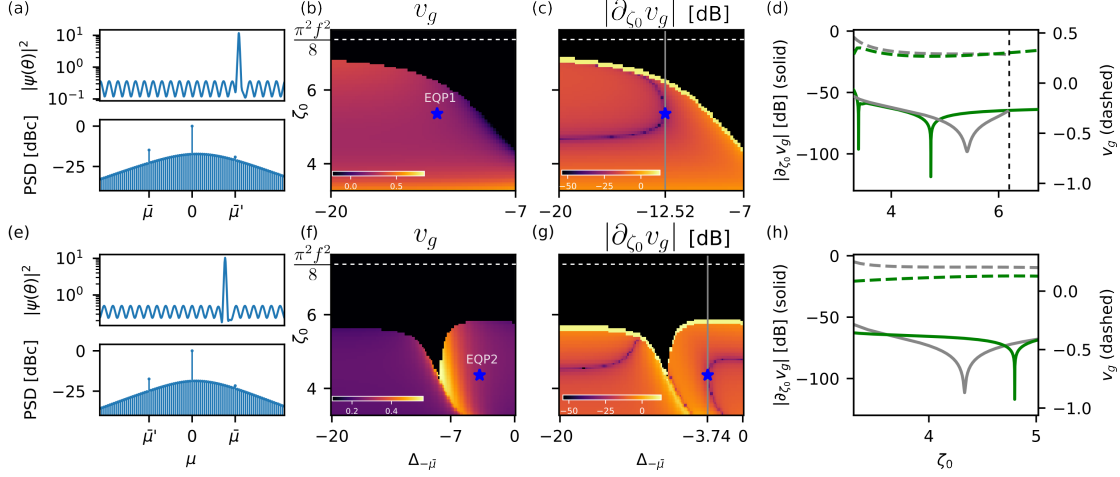


Figure 4.3: **Quiet point engineering** (a-d) Newton-Raphson simulations for a dispersion profile with two modes displaced:  $\bar{\mu}$  and  $\bar{\mu}' = -\bar{\mu}$ , i.e.  $(\Delta_{-\bar{\mu}}, \zeta_0; \bar{\mu} = -21, \Delta_{\bar{\mu}} = -5, f^2 = 6, \tau = 5 \cdot 10^{-3})$ . (a) Equilibrium DKS solution for the EQP, i.e.  $(\Delta_{-\bar{\mu}} = -12.52, \zeta_0 = 5.41)$  (blue star). (b) Value of the group velocity in the subspace of parameters  $(\Delta_{-\bar{\mu}}, \zeta_0; f^2, \tau, \Delta_{\bar{\mu}})$  and (c) its detuning directional derivative  $(10 \log_{10} |\frac{\partial v_g}{\partial \zeta_0}|)$ . (d) Comparison of detuning response between single mode displaced quiet point QP1 (green line, see Fig. 2.c) and engineered quiet point (EQP1) with second mode displaced (gray line in subplot c). (e-h) Similar plots for the case for  $\bar{\mu} = 21$ ,  $\Delta_{\bar{\mu}} = -10.7$ ,  $\bar{\mu}' = -21$ ,  $\Delta_{-\bar{\mu}} = -3.74$

$\Delta_{\bar{\mu}} = -10.7$  and shifting the mode  $\bar{\mu}' = -\bar{\mu}$  by  $\Delta_{-\bar{\mu}}$ . Simulation results in Fig. 4.3(e-h) show qualitatively similar behavior, with shorter DKS existence range (defined by the fixed mode  $\bar{\mu} = 21$ , see Fig. 4.2f). However, in this case, we find two QP families for a single DKS solution. The flattest response is achieved at  $\Delta_{-\bar{\mu}} = -3.74$  (see Fig. 4.3(g,h)). In this way, we observe that careful control over the two-mode displacement can extend the noise suppression region of the QP in the parameter space.

Using the Newton-Raphson method, we identified the quiet point regimes, however we omitted the question of stability of these solutions. To estimate it, we perform linear stability analysis: we numerically investigate the eigenvalues  $\lambda$  of the Jacobian operator associated with (4.1) for each particular soliton state found in the previous section. In particular, we focus on the eigenvalues with the biggest real part. In case of positive value, the corresponding eigenfuctions are responsible for the linear growth of any perturbation around the equilibrium. The real part of the latter ( $\max \text{Re}\{\lambda\}$ ) are plotted in Fig. 4.4.a-d. We observe that the soliton solutions are linearly stable almost everywhere in the considered subspace, and in particular at the QPs. Exceptions are for a narrow region in correspondence with the reduced existence range (reminding an instability tongue). In those regions there exist at least one eigenvalue with positive real part. From the actual structure of the spectrum of the Jacobian, computed for the quiet point states, (Fig. 4.4.e-h) we find that these instabilities are due to Hopf bifurcations, characterized by the vanishing real parts of a pair of the complex conjugated soft modes. In this region of parameter space, those will be responsible for the transition from stable solitons

#### 4.4 Dynamical simulation of the phase noise transfer

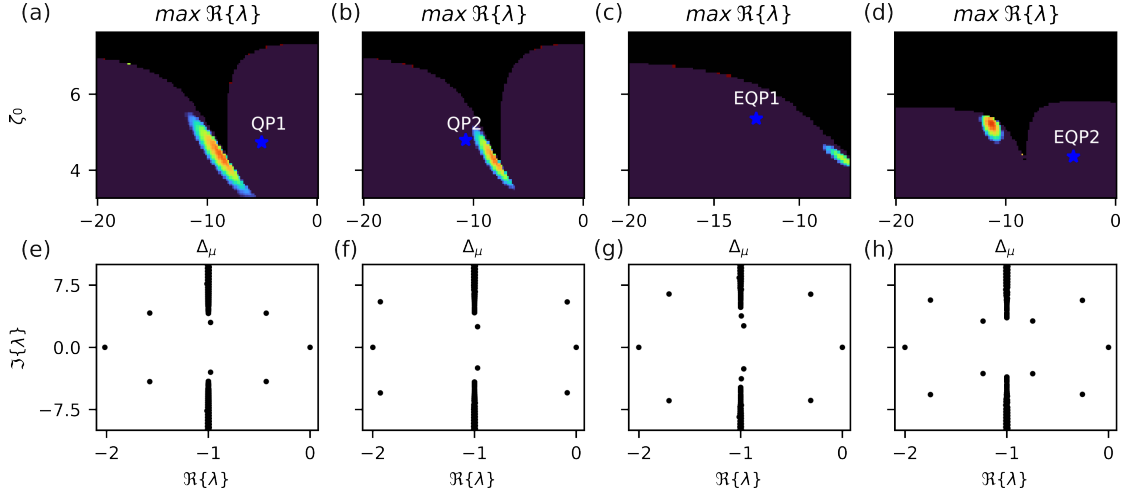
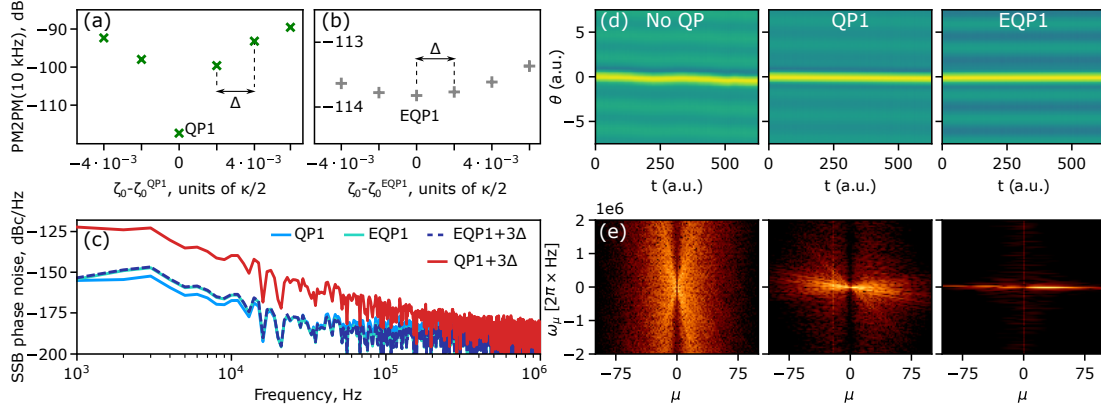


Figure 4.4: **Linear stability of the quiet points** (a-d) Value of the real part of the Jacobian eigenvalue ( $\lambda$ ) with highest real part, in the parameters subspaces considered in fig. 2.b,2.f,3.b,3.f respectively. The analysis shows there are regions within the DKS existence range in which the soliton solutions are linearly unstable (colored regions) but those do not include the analyzed QP that is consequently considered stable. (e-h) Detail on the spectrum of the Jacobian for the cases in (a-d). The spectrum shows that the instabilities arising in the colored regions are due to the Hopf bifurcation, considered the presence of pairs of conjugated soft modes approaching  $\text{Re}\{\lambda\} = 0$ .

to breathing states.

#### 4.4 Dynamical simulation of the phase noise transfer

To compare the phase noise performance of different operating points, the dynamical evolution has been simulated with the step-adaptative Dormand-Prince Runge-Kutta method of Order 8(5,3) [179]. We perform the direct dynamical simulations of the LLE adding a realistic noise to the detuning term measured experimentally from the Topical CTL 1550 laser having a standard deviation of 5 kHz. In this way, we simulate two DKS operating points: QP1 (see Fig. 4.2.b) and EQP1 (see Fig. 4.3b). The difference between the phase noise transfer performance at different operating points can be clearly seen in Fig. 4.5a,b. A series of numerical experiments confirm the conclusion obtained with the stationary solver analysis. Indeed, changing the central frequency of the pump by the value of  $10^{-3} \kappa$ , we clearly observe that the overall noise transduction from the pump to the soliton repetition rate (PM2PM at 10 kHz offset, where PM stands for phase noise) performance of EQP1 increases by 0.5 dB for  $3 \cdot 10^{-3} \kappa$ , while in the case of QP<sub>1</sub>, we observe  $> 28$  dB of the transduction enhancement. Corresponding single-sideband (SSB) phase noise performance is depicted in Fig. 4.5c. As one can see, the fluctuations of the central frequency of the pump laser do not visibly affect the performance of the system at EQP1.



**Figure 4.5: Dynamical simulations of the noise transfer for different operating points.** PM2PM coefficient (ratio between the microwave phase noise and the pump laser phase noise) at 10 kHz modulation frequency in the vicinity of QP1 (green crosses in panel a) and EQP1 (gray crosses in panel b). (c) SSB phase noise plot for exact laser detuning corresponding to QP1 and EQP1 as well as a deviation of  $3\Delta = 3 \cdot 10^{-3} \kappa$ . (d) Spatiotemporal diagram of the DKS evolution under the influence of amplified pump phase noise. (e) Nonlinear dispersion relation, for different operating points. The noise transduction to the soliton repetition rate is greatly reduced in the presence of two engineered mode-crossings.

Next, we verify that in the case of the noisy pump lasers (standard deviation of  $8\% \kappa/2$ ) EPQ leads to a significant noise reduction due to the larger noise suppression region. We employed the same phase noise data, scaling it to obtain the detuning fluctuation of the order of the width of the standard QP, i.e.  $8\% \kappa/2$ . In the parameter regime outside of the QP region the influence of the pump fluctuations on the DKS dynamics is visible directly from the spatiotemporal diagram (see Fig. 4.3d). To distinguish the performance of QP1 and EQP1, we can use the NDR to represent its effect (Fig. 4.3e). We observe a clear suppression of the noise multiplication in the case of EQP1. This confirms our predictions based on the group velocity variation obtained with the stationary solution solver.

## 4.5 Conclusion

In summary, we have demonstrated a method to increase the effectiveness of QPs, that are central to achieving low phase noise soliton microcombs for microwave generation. Our work shows that engineering QP introduced via two dedicated and controllable mode crossings enables one to create broader regions of enhanced noise suppression. Our work is directly implementable using current technology and provides a new approach to the enduring challenge of obtaining thermal noise-limited micro-wave generation from integrated soliton microcombs, which in contrast to crystalline resonators employ materials such as silicon nitride or silica, that do exhibit a Raman self-frequency shift.

These results were obtained via a semi-analytical approach, based on the Newton-Raphson



method, studied the phenomenology of QP in the presence of Raman scattering, dispersive waves, and detuning noise, within a simplified model of AMX. This allowed us to obtain several insights (i) QPs can be achieved by placing AMX on both blue- and red-detuned sides of the pump. This highlights the fact that not the absolute value of the frequency shift must be compensated, but its derivative over the laser detuning. (ii) Engineering the interaction of two QPs leads to further reduction of the noise transfer. (iii) The EQPs predicted in this work are linearly stable and characterized by more than 28 dB reduction of the PM2PM coefficient with respect to a generic QP described in the literature when a detuning deviation of the order of 0.03% of  $\kappa$  is introduced. We anticipate that the detuning-dependent variation of the repetition rate can be completely eliminated by further controlling the integrated dispersion profile for example by corrugating the microresonator circumference [180], which is however outside the scope of this work.



## 5 Dissipative Kerr solitons in dimers

This chapter reports on the investigation of dissipative Kerr solitons in a photonic dimer in two coupling regimes: split resonance and split dissipation. The results are partially adapted from K. Komagata *et al.*, “Dissipative Kerr solitons in a photonic dimer on both sides of exceptional point,” *Communications Physics* **4**, 159 (2021).

### 5.1 Introduction

In the previous section, we considered two coupled resonators as a platform to control group velocity of a conventional DKS via introducing coupling for a single optical mode. In the following sections we will focus on the lattices of identical resonators where each optical mode of one resonator is interacting with its neighbor’s counterpart.

In this chapter, we investigate a passive photonic dimer with a hidden  $\mathcal{PT}$ -symmetry (further referred to as  $\mathcal{PT}$ -symmetry for simplicity) in linear and nonlinear multimode regimes. In the linear regime, we analyze conditions for the critical coupling and demonstrate that the line of EPs is a demarcation of these conditions. The exceptional point line splits the parameter space into two parts which we refer to as split resonance ( $\mathcal{PT}$  symmetric) and split dissipation ( $\mathcal{PT}$ -symmetry broken). In the split resonance regime, we show new insights into the effects previously reported in [122], using the supermode basis representation. Further, we investigate the nonlinear dynamics in the split dissipation regime which includes single-resonator dissipative Kerr soliton (DKS), dark-bright DKSs pairs, and highly-efficient perfect soliton crystals. Finally, we demonstrate switching of the soliton-generating cavity caused by the nonlinear alteration of the  $\mathcal{PT}$  symmetry.

#### 5.1.1 Exceptional point as a demarcation of the critical coupling conditions

We consider the system of two identical multimode resonators [Fig. 5.1(a)] (i.e., identical intrinsic loss rate  $\kappa_0$ , mode spacing  $D_1$ , dispersion  $D_2$ , and single-photon Kerr frequency shift  $g_0$ ). A global offset between the resonant frequencies  $\omega_\mu$  of their respective modes  $\mu$

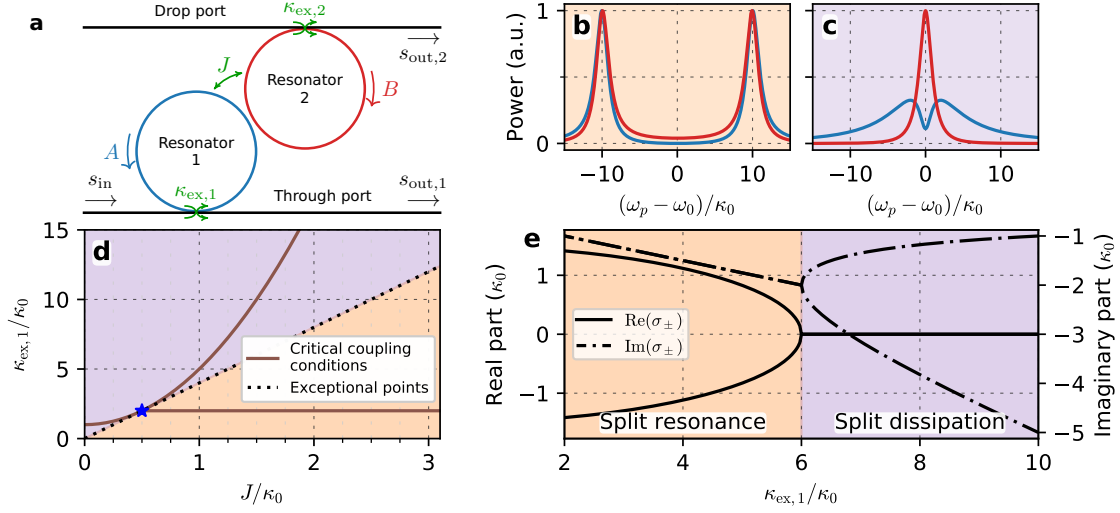


**Figure 5.1: Linear analysis of the photonic dimer.** (a) Schematic of the two resonators. (b,c) Field intensity in the resonator 1 (blue) and 2 (red) as a function of the laser detuning. (b) Shows a typical resonance splitting at critical coupling for  $J = 10\kappa_0$ , (c) the same for the split dissipation regime at critical coupling for  $J = 1.5\kappa_0$ . (d) Critical coupling coefficients as a function of  $J$  for  $\kappa_{ex,2} = 0$ , in the split dissipation (resonances) regime above (below) the exceptional point line (dotted). The two conditions branch off at the exceptional point of  $J = 1/2\kappa_0$ , highlighted by the star. (e) Real and imaginary parts of the eigenvalues as a function of  $\kappa_{ex,1}$  for  $J = 1.5\kappa_0$ .

is introduced with the inter-resonator detuning  $\delta$ . The two resonators are coupled to each other by the evanescent field with the rate  $J_{\mu}$ , which generally depends on the mode number. Each resonator is coupled to a waveguide (through and drop ports) with the rates  $\kappa_{ex,i}$ ,  $i = 1, 2$ . Resonator 1 is pumped by a continuous wave (CW) laser at frequency  $\omega_p$ . Nonlinear dynamics in such photonic dimer can be described by two coupled Lugiato-Lefever equations (LLEs), which in Fourier space is expressed as follows [181, 122]:

$$\begin{aligned} \frac{d}{dt} A_{\mu} &= -[\frac{1}{2}(\kappa_0 + \kappa_{ex,1}) + i(\omega_{\mu} + \frac{1}{2}\delta - \mu D_1 - \omega_p)] A_{\mu} + i g_0 \mathcal{F}[|A|^2]_{\mu} + i J_{\mu} B_{\mu} + \delta_{\mu,0} \sqrt{\kappa_{ex,1}} s_{in} \\ \frac{d}{dt} B_{\mu} &= -[\frac{1}{2}(\kappa_0 + \kappa_{ex,2}) + i(\omega_{\mu} - \frac{1}{2}\delta - \mu D_1 - \omega_p)] B_{\mu} + i g_0 \mathcal{F}[|B|^2]_{\mu} + i J_{\mu} A_{\mu}, \end{aligned} \quad (5.1)$$

where  $g_0 = \frac{\hbar \omega_0^2 c n_2}{n_0^2 V_{eff}}$  is the Kerr coefficient,  $c$  stands for the speed of light in vacuum,  $\hbar$  - the Planck constant,  $\omega_0$  - the frequency of the pumped mode,  $V_{eff}$  - the effective mode volume,  $n_0$  and  $n_2$  are linear and nonlinear refractive indexes, respectively,  $\delta_{\mu,0}$  is the Kronecker delta,  $s_{in} = \sqrt{\frac{P_{in}}{\hbar \omega_0}}$  - the input pump field amplitude,  $A_{\mu}$ ,  $B_{\mu}$  are the field amplitudes of the modes with index  $\mu$  in the first and second resonator, respectively. The variables  $A$ ,  $B$  are the slowly varying intra-resonator field envelopes, and  $\mathcal{F}[\dots]_{\mu}$  denotes the  $\mu^{\text{th}}$ -component of the discrete Fourier transform.

Modes of each resonator with identical angular momentum are linearly coupled with the inter-

resonator coupling rate  $J_\mu$ . In contrast, the Kerr nonlinearity couples all the modes within each resonator via four-wave mixing (FWM) processes. The interplay between the linear coupling in the spatial dimension and the nonlinear coupling in the frequency dimension is the source of the rich dynamics of the system.

In the present section, we restrict ourselves to a linear and single mode analysis by considering only the central mode  $\mu = 0$  with  $g_0 = 0$ . The critical coupling conditions are of particular interest for maximizing the pump transfer to the resonators and the eigenvalue analysis of the coupled mode matrix for finding the EP conditions, which separate two conceptually different dimer states.

### 5.1.2 Critical coupling conditions

Let us analyze the condition for critical coupling. In the linear single-mode representation, Eq. 5.1 is simplified as follows:

$$i \frac{d}{dt} \begin{pmatrix} A \\ B \end{pmatrix} = M \begin{pmatrix} A \\ B \end{pmatrix} + \sqrt{\kappa_{\text{ex},1}} \begin{pmatrix} s_{\text{in}} \\ 0 \end{pmatrix}, \quad M = \begin{pmatrix} \frac{1}{2}\delta - \frac{i}{4}\Delta\kappa_{\text{ex}} & -J \\ -J & -\frac{1}{2}\delta + \frac{i}{4}\Delta\kappa_{\text{ex}} \end{pmatrix} + (\omega_0 - \omega_p - \frac{i}{2}\kappa_{\text{ex}})I, \\ s_{\text{out},1} = s_{\text{in}} - \sqrt{\kappa_{\text{ex},1}}A, \quad s_{\text{out},2} = \sqrt{\kappa_{\text{ex},2}}B. \quad (5.2)$$

In Eq. 5.2, we defined the external coupling mismatch  $\Delta\kappa_{\text{ex}} = \kappa_{\text{ex},1} - \kappa_{\text{ex},2}$  and the average external coupling  $\kappa_{\text{ex}} = \frac{1}{2}(\kappa_{\text{ex},1} + \kappa_{\text{ex},2})$ . The identity matrix is denoted as  $I$ . Critical coupling is achieved when the transmission via the through port [Fig. 5.1(a)] vanishes, i.e.  $s_{\text{out},1} = 0$ . In the case of a single resonator, critical coupling is achieved when the external coupling rate matches the loss, i.e.  $\kappa_{\text{ex}} = \kappa_0$  [182, 183]. For two resonators, the conditions are easily found in case of  $\delta = 0$ . There are two possibilities

$$\kappa_{\text{ex},1}/\kappa_0 = \frac{4(J/\kappa_0)^2 + \kappa_{\text{ex},2}/\kappa_0 + 1}{\kappa_{\text{ex},2}/\kappa_0 + 1} \quad (5.3)$$

$$\kappa_{\text{ex},1}/\kappa_0 = 2 + \kappa_{\text{ex},2}/\kappa_0. \quad (5.4)$$

Eq. 5.3 is a natural generalization of the critical coupling conditions for a single resonator that can be achieved by setting  $J$  to zero. Eq. 5.4 satisfies the critical coupling condition at  $\omega_p = \omega_0 \pm \sqrt{4J^2 - (\kappa_0 + \kappa_{\text{ex},2})^2}$ . This condition requires strong coupling, i.e.  $J > \frac{1}{2}(\kappa_0 + \kappa_{\text{ex},2})$ . The critical coupling conditions are shown in Fig. 5.1(d) for  $\kappa_{\text{ex},2} = 0$ . Typical cavity field intensities for both cases are plotted in Fig. 5.1(b,c) as a function laser detuning.

The first critical coupling condition given by Eq. 5.3 has a quadratic dependence on the inter-resonator coupling rate [Fig. 5.1(d)]. It leads to a broad resonance with a dip in the first resonator (blue) and a narrow resonance in the second resonator (red) at the same resonance frequency [Fig. 5.1(c)]. The second critical coupling condition (Eq. 5.4) branches off the first one at  $J/\kappa_0 = 0.5$  and does not depend on the inter-resonator coupling rate. It features split resonances with identical linewidths [Fig. 5.1(b)].

Experimental implementation of the multimode photonic dimer demonstrated the presence of the non-vanishing inter-resonator detuning  $\delta$  caused by the fabrication imperfectness. Nonetheless, the possibility to control and manipulate  $\delta$ , and thereby establish control over the output solitonic spectrum, has been demonstrated and efficiently implemented by imprinting heaters directly on the photonic device [184, 122]. Critical coupling at non-vanishing  $\delta$  is possible as well. The inter-resonator detuning introduces asymmetry in the distribution of the supermodes (eigenvectors) in each resonator. Thus, the supermode confined in the first (second) resonator requires smaller (larger)  $\kappa_{\text{ex},1}$  to be critically coupled. It follows that in general when  $\delta \neq 0$  only one supermode can be critically coupled for a given value of  $\kappa_{\text{ex},1}$ .

The qualitative behavior of the photonic dimer can be anticipated by examining the eigenvalues of the system Eq. 5.2. Operating with a naturally Non-Hermitian system, we can exploit the concept of EP [185] to shed light on the nature of each critical coupling conditions

### 5.1.3 Eigenvalues and exceptional points

The eigenvalues of the matrix  $M$  defined in Eq. 5.2 in case of  $\delta = 0$ ,  $\kappa_{\text{ex},2} = 0$ , and  $\omega_0 = \omega_p$  are given by

$$\sigma_{\pm} = -i(\frac{1}{2}\kappa_0 + \frac{1}{4}\kappa_{\text{ex},1}) \pm \frac{1}{4}\sqrt{16J^2 - \kappa_{\text{ex},1}^2}, \quad (5.5)$$

where the real (imaginary) part corresponds to resonance frequency (loss rate). The eigenvalues are shown in Fig. 5.1(e) as a function of  $\kappa_{\text{ex},1}$  for an inter-resonator coupling  $J = 1.5\kappa_0$ . Two different regions of *split resonance* and *split dissipation* are identified and shaded in Fig. 5.1 with orange and purple, respectively. For  $\kappa_{\text{ex},1} < 6\kappa_0$ , the eigenvalues have degenerate imaginary part and split real parts, associated with the split resonances as depicted in Fig. 5.1(b). In contrast,  $\kappa_{\text{ex},1} > 6\kappa_0$  leads to degenerate real parts and split imaginary parts, i.e. to identical resonance frequencies but different loss rates, as can be seen in Fig. 5.1(c). The two regions correspond to the  $\mathcal{PT}$ -symmetric and  $\mathcal{PT}$ -symmetry broken states, respectively.

An EP is found between the two regions at  $\kappa_{\text{ex},1} = 6\kappa_0$ , where the system eigenvalues become degenerate and the two eigenvectors coalesce because of the vanishing square root in Eq. 5.5. *EPs lie along the line defined by  $\kappa_{\text{ex},1} = 4J$ , which separates the two critical coupling conditions in the  $(J, \kappa_{\text{ex},1})$  plane.* Remarkably, the two critical coupling conditions and the EP line fork at  $J = \frac{1}{2}\kappa_0$ ,  $\kappa_{\text{ex},1} = 2\kappa_0$ . This particular point is highlighted by the blue star in Fig. 5.1(d). It is the only EP that satisfies a critical coupling condition. This point also marks the entry into the strong coupling regime ( $J > \frac{1}{2}\kappa_0$ ). Above reasoning is valid when  $\kappa_{\text{ex},2} = 0$ . In the general case ( $\kappa_{\text{ex},2} \neq 0$ ) the line of EPs can cross the line corresponding to critical coupling conditions.

Concluding, there are two types of critical coupling conditions in the photonic dimer. These conditions are found on both sides of the EPs, such that critical coupling can be achieved in the  $\mathcal{PT}$ -symmetric as well as  $\mathcal{PT}$ -symmetry broken states. In the next sections, we examine the versatile nonlinear dynamics and dissipative Kerr soliton generation in these states.

## 5.2 Critically coupled resonators: split resonance

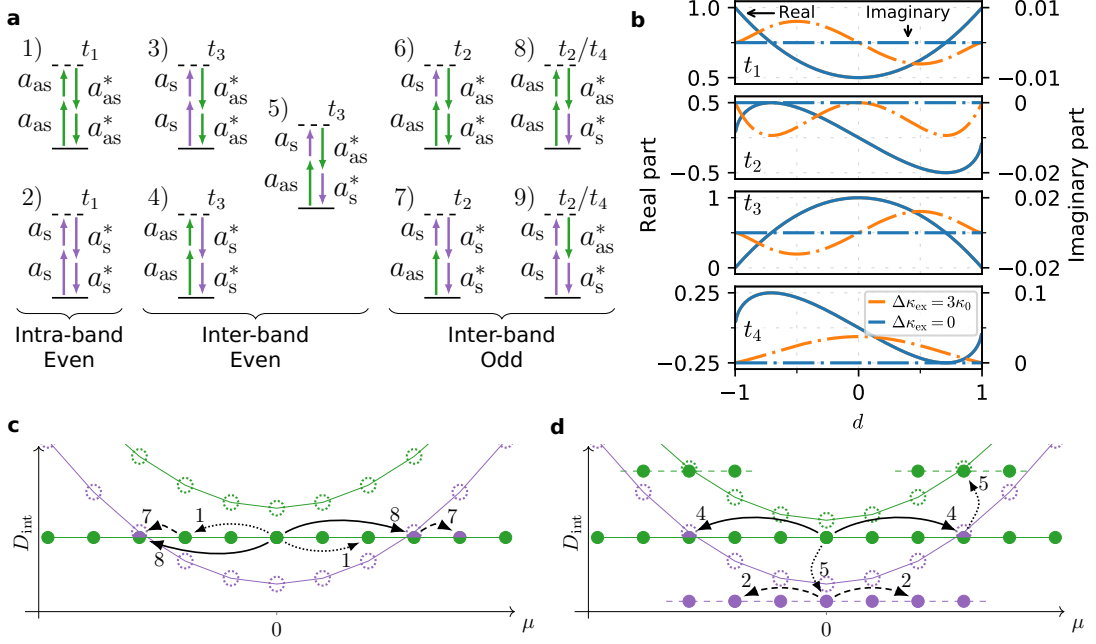


Figure 5.2: **FWM pathways between the dimer supermodes.** (a) Table of the 9 possible FWM pathways with corresponding coefficients  $t_i$ . (b) Real (solid) and imaginary (dashed) part of nonlinear coupling coefficients as a function of the normalized inter-resonator detuning  $d$  for 2 values of the external coupling mismatch  $\Delta\kappa_{ex}$  in the split resonance regime ( $J = 20\kappa_0$ ).  $\Delta\kappa_{ex}$  is the source of the imaginary component, which however is small compared to the real part, except for  $t_4$  around  $d = 0$ . (c,d) Schematic integrated dispersion profile with emphasized FWM pathways. The labeling indexes are specified in (a). Empty dashed circles denotes cold cavity mode, filled circle denotes Kerr comb mode, and color codes AS (green) or S (purple) mode family. (c) GS generated in the AS supermodes via conventional FWM (even intra-band processes) and the emergence of commensurate dispersive waves via odd inter-band processes. (d) Soliton in the AS supermodes and the generation of a soliton in the S supermodes caused by even processes.

## 5.2 Critically coupled resonators: split resonance

In the present section we discuss the case of the split resonance ( $\mathcal{PT}$ -symmetric). We revisit ideas presented earlier in [122] by looking at the nonlinear dynamics from the supermode perspective. We demonstrate a separability of the gear soliton (GS) dynamics from dispersive waves (DWs) living in the S supermodes. Finally, we show how this representation explains the origin of soliton hopping effect. An essential part of the investigation of the dynamics inherent to the photonic dimer and described by Eq. 5.1 relies on numerical simulations.

### 5.2.1 Four-wave mixing pathways between supermodes

The linear part of Eq. 5.1 can be diagonalized by a linear transformation on each pair of modes with index  $\mu$ . We define the complex inter-resonator detuning  $\delta_c = \delta - i\frac{1}{2}\Delta\kappa_{ex}$ . If the

## Chapter 5. Dissipative Kerr solitons in dimers

inter-resonator coupling is independent of the wavelength, the complex frequency splitting  $\Delta\omega_c = \sqrt{4J^2 + \delta_c^2}$ , and the (complex) normalized inter-resonator detuning

$$d_c \equiv \delta_c / \Delta\omega_c$$

are independent of the mode index. Therefore, the non-unitary transformation diagonalizing the linear part of Eq. 5.1 is given by  $A_{s,\mu} = \alpha A_\mu + \beta B_\mu$ ,  $A_{as,\mu} = \beta A_\mu - \alpha B_\mu$ , where

$$\alpha \equiv \frac{\sqrt{1-d_c}}{\sqrt{2}}, \quad \beta \equiv \frac{\sqrt{1+d_c}}{\sqrt{2}}. \quad (5.6)$$

Here S and AS stand for the symmetric (S) and antisymmetric (AS) mode, as they are completely symmetric (antisymmetric) at  $d_c = 0$  in the split resonance regime. Then, by defining the spatial envelope of the field in the S and AS modes  $A_s(\theta) = \sum_\mu A_{s,\mu} e^{i\mu\theta}$ ,  $A_{as}(\theta) = \sum_\mu A_{as,\mu} e^{i\mu\theta}$ , we can express Eq. 3.2 in the supermode basis (see an alternative Hamiltonian formulation in [122]):

$$\begin{aligned} \frac{d}{dt} A_{s,\mu} = & [-i(\omega_\mu - \mu D_1 - \omega_p - \frac{1}{2} \text{Re}(\Delta\omega_c)) \\ & - \frac{1}{2}(\kappa_0 + \kappa_{\text{ex}} + \text{Im}(\Delta\omega_c))] A_{s,\mu} \\ & + \delta_{\mu,0} \alpha \sqrt{\kappa_{\text{ex},1}} s_{\text{in}} + i g_0 \mathcal{F} [t_1 A_{s,\mu} |A_{s,\mu}|^2 \\ & + t_2 A_{as,\mu} |A_{s,\mu}|^2 + t_4 A_{s,\mu}^2 A_{as,\mu}^* + t_3 A_{s,\mu} |A_{s,\mu}|^2 \\ & + \frac{1}{2} t_3 A_{as,\mu}^2 A_{s,\mu}^* - \frac{1}{2} t_2 A_{as,\mu} |A_{as,\mu}|^2]_\mu \end{aligned} \quad (5.7a)$$

$$\begin{aligned} \frac{d}{dt} A_{as,\mu} = & [-i(\omega_\mu - \mu D_1 - \omega_p + \frac{1}{2} \text{Re}(\Delta\omega_c)) \\ & - \frac{1}{2}(\kappa_0 + \kappa_{\text{ex}} - \text{Im}(\Delta\omega_c))] A_{as,\mu} \\ & + \delta_{\mu,0} \beta \sqrt{\kappa_{\text{ex},1}} s_{\text{in}} + i g_0 \mathcal{F} [\frac{1}{2} t_2 A_{s,\mu} |A_{s,\mu}|^2 \\ & + t_3 A_{as,\mu} |A_{s,\mu}|^2 + \frac{1}{2} t_3 A_{s,\mu}^2 A_{as,\mu}^* - t_2 A_{s,\mu} |A_{as,\mu}|^2 \\ & - t_4 A_{as,\mu}^2 A_{s,\mu}^* + t_1 A_{as,\mu} |A_{as,\mu}|^2]_\mu. \end{aligned} \quad (5.7b)$$

As one can see, the linear anti-diagonal terms are eliminated in the supermode basis, while the nonlinear terms (diagonal in the resonator basis) induce nonlinear coupling between the supermodes. In particular, we identify FWM processes between the supermodes. The efficiencies of FWM pathways are associated with nonlinear coupling coefficients  $t_i$ ,  $i = 1, \dots, 4$ , defined in Eq. C.14 of Appendix C.1. For example, the term  $\frac{1}{2} t_3 A_{as,\mu}^2 A_{s,\mu}^*$  in Eq. 5.7a signifies the annihilation of two photons in  $A_{as,\mu}$  and the creation of two photons in  $A_{as,\mu}$ , and the rate of the process is proportional to  $g_0 t_3$ . The 9 different non-linear processes from Eq. 5.7 are depicted in Fig. 5.2(a), where they are arranged in categories corresponding to intra-band even processes, inter-band even processes and inter-band odd processes.

We refer to a nonlinear process as intra-band when two annihilated and two created photons are from the same supermode family, while inter-band processes imply nonlinear mixing



## 5.2 Critically coupled resonators: split resonance

of photons belonging to different supermodes, inspired by the concept of Bloch bands in condensed matter Physics. The number parity of the process (even or odd) refers to the number of photons from each supermode family that is involved. We note that processes (2,4,7,9) are the counterparts of processes (1,3,6,8) for permuted supermodes index. Schemes of possible FWM pathways between the supermodes (while a solitonic state is generated in the AS supermode family) are shown in Fig. 5.2(c,d) These processes are distinguished by the nature of FWM: Fig. 5.2(c) shows odd processes (except the conventional even process #1), while Fig. 5.2(d) shows even processes leading to soliton hopping (see Sec. 5.2.2).

While the index  $\mu$  has been omitted in Fig. 5.2(a) for readability, both the mode number and the energy have to be conserved in a FWM process. We employ the concept of integrated dispersion  $D_{\text{int}}(\mu) = \omega_\mu - (\omega_0 + D_1\mu)$  to depict the processes which satisfy the phase matching conditions.

The real and imaginary parts of the nonlinear coupling coefficients are shown in Fig. 5.2(b) as a function of the normalized inter-resonator detuning  $d = \delta / \sqrt{4J^2 + \delta^2}$  with solid and dashed dotted lines, respectively. The parameters are chosen in the split resonance regime with  $J = 20\kappa_0$ . Vanishing and non-vanishing  $\Delta\kappa_{\text{ex}}$  are considered, emphasizing that the imaginary parts of all the nonlinear coupling coefficients originate from the external coupling mismatch. The imaginary part, however, generally constitutes only a small fraction of the absolute value of the nonlinear coupling coefficients.

Coefficient  $t_1$  is responsible for the intra-band processes, that is, the usual FWM within the same mode family (S) or (AS). It has its lowest value equal to 0.5 at the maximum hybridization ( $d = 0$ ). In contrast, coefficient  $t_3$  is maximized at  $d = 0$  and causes inter-band and even processes. The coefficients  $t_2$  and  $t_4$  are responsible for inter-band and odd processes. Their real parts are odd with respect to  $d$ . Therefore, there are no odd FWM processes at  $d = 0$ , unless an external coupling mismatch is present. In this case, coefficient  $t_4$  has a non-vanishing absolute value.

### 5.2.2 Nonlinear dynamics and soliton generation in split resonance regime

The type of the critical coupling conditions corresponding to the split resonances allows for accessing dynamical states characterized by efficient generation of bright dissipative Kerr solitons in both cavities. Emergent dynamical effects described in [122] are found in this regime. In this section, we provide an additional (to the result already shown in [122]) and complementary description of these phenomena by representing the inter-resonator field in the hybridized supermodes basis.

#### Modulation Instability state

We restrict ourselves to the AS supermodes pumping scheme since we did not observe dynamics different from the single resonator case when exciting the S supermode family. Fig. 5.3(a,b)

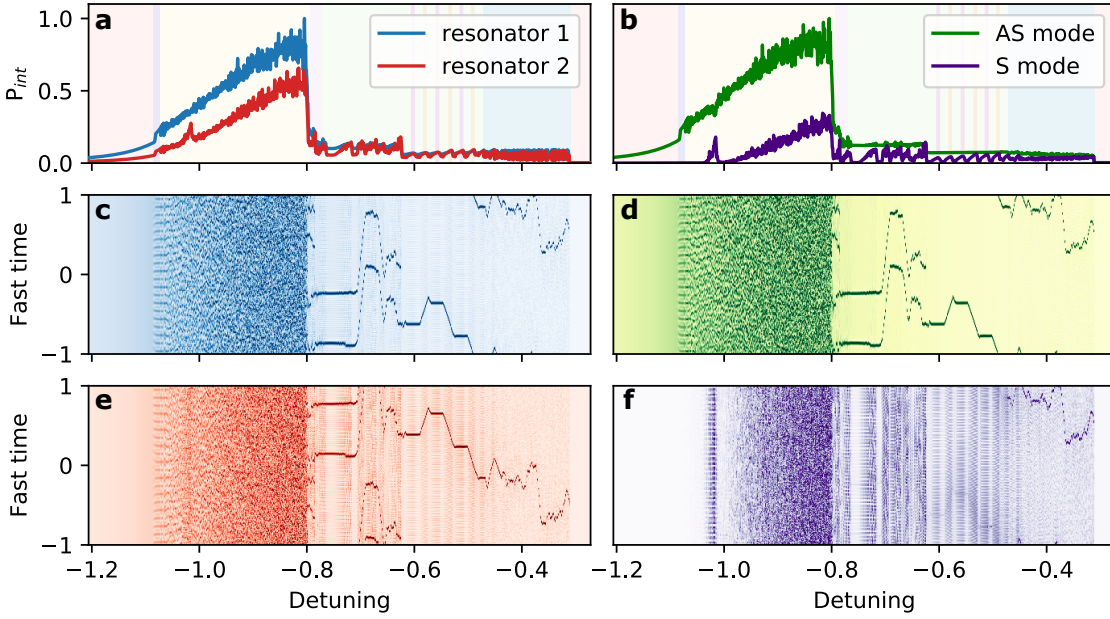


Figure 5.3: **Numerical simulations of the split resonance regime ( $\mathcal{PT}$ -symmetric case).** (a) Intracavity field power evolution in resonator basis. (b) Intracavity field power evolution in supermode basis. Spatiotemporal diagrams for the field evolution in first resonator (c), AS mode (d), second resonator (e), S mode (f). Parameters of numerical simulations are close to the exact critical coupling conditions:  $\kappa_0/2\pi = 50$  MHz,  $\kappa_{\text{ex},1}/2\pi = 100$  MHz,  $\kappa_{\text{ex},2}/2\pi = 20$  MHz,  $\delta/2\pi = 4$  GHz,  $J/2\pi = 4.5$  GHz, the pump power was fixed to 1.2 W.

show the intracavity power evolution as a function of laser detuning in the resonator and supermode basis, respectively. It is numerically generated by exciting the system in a soft manner, i.e. adiabatically changing the laser detuning  $\xi = \omega_0 - \omega_p$  from blue to red side of the AS hybridized resonance. Initial dynamics is found to be similar to the single resonator case. We observe the formation of primary combs in the AS supermode family followed by cnoidal waves (Turing rolls). The subsequent chaotic modulation instability stage [yellow area in Fig. 5.3(a,b)] already demonstrates a significant difference. Namely, the average intracavity power evolution in the second resonator, which is depicted by the red line, as a function of normalized detuning  $\xi/\Delta\omega$  exhibits a local maximum inside the modulation instability area which corresponds to the efficient photon transfer to the S supermodes [violet curve in Fig. 5.3(b)]. At these values of detuning ( $\xi/\Delta\omega \approx -1$ ), we observe an enhancement of spectral components distinct from the modulation instability gain region. The mode number of the components corresponds exactly to the distance from the pumped mode to the lower (S supermodes) parabola for a given value of the laser detuning, as described in [122]. This is a first signature of the interaction between the supermodes.

Fig. 5.3(c,d) provide the underlying evolution of intracavity power (spatiotemporal diagram) in the supermode basis. The modulation instability region in the conventional basis does not differ for the single-particle dynamics. However, the supermode basis reveals that the transfer of photons to the S supermode family occurs after a certain detuning threshold. As follows from the spatiotemporal diagram of the AS state, it occurs in the developed AS supermodes modulation instability stage, where collision and annihilation of unstable coherent structures lead to the enhancement of wings in the optical spectrum [136] and thereby populates the modes in vicinity of the symmetric resonances.

### Breathing state

As in conventional single resonator systems above a threshold pump power level, the modulation instability region is followed by the breathing solitons region [violet area in Fig. 5.3(a,b)]. Breathing originates from the Hopf bifurcation as demonstrated for the single resonator case [62]. It manifests itself as a periodic oscillation of localized coherent structures (similar to solitons on a finite background, such as Kuznetsov-Ma soliton [11, 67] — a solution of the nonlinear Schrödinger equation), which radiates DWs at every cycle of oscillation. Fig. 5.4(a) shows the intracavity power evolution. Breathers in the photonic dimer exist in both resonators and oscillate *in phase*. However, the intracavity trace is found to be randomly deviating from the average because of the photon transfer to the S supermodes and, therefore, the generation of additional DWs.

The periodic oscillation of a coherent structure in slow time results in the appearance of a ladder of equally-spaced lines on the nonlinear dispersion relation [186]. The presence of such ladder has been experimentally demonstrated (see [122] supplementary information) by reconstructing the comb spectrum with high resolution. Indeed, as follows from Fig. 5.4(c,e) the breathing frequency is given by the frequency offset between the lines. The same reasoning

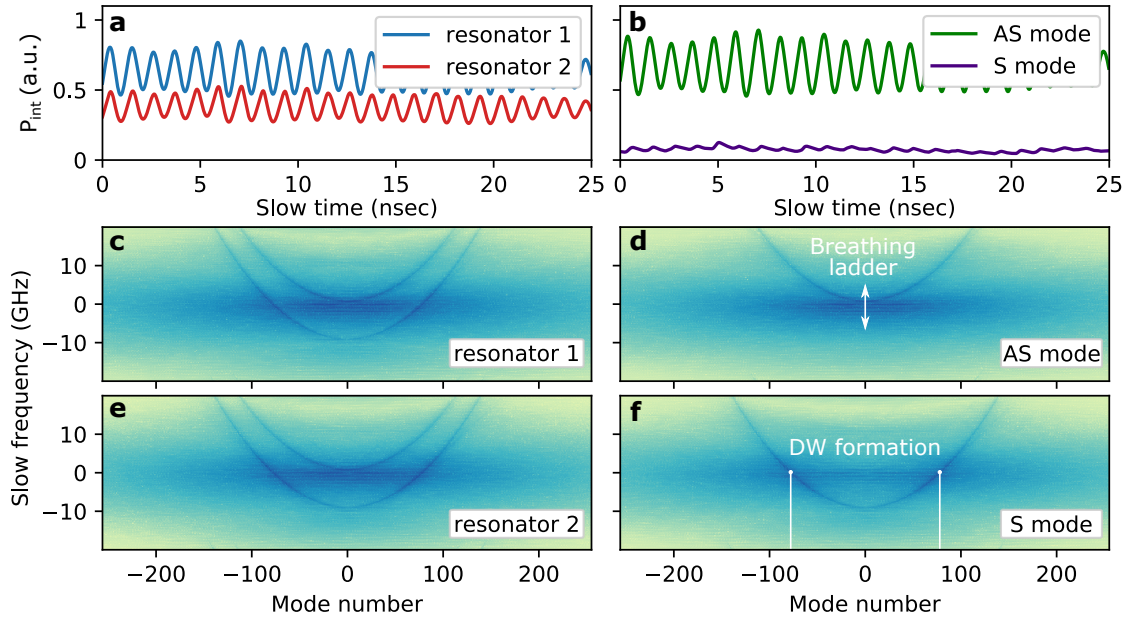


Figure 5.4: **Breathing state.** (a,b) Intracavity power evolution with a fixed pump laser detuning (a) in the first and second resonator (shown by blue and red lines) and (b) in the supermode basis (green and violet for AS and S mode families, respectively). (c-f) Nonlinear dispersion relations (c,e) for the first and second resonators (d,f) for AS and S supermode families.

can be applied to the single resonator breathing states. There, it has been demonstrated experimentally that the breathing frequency linearly depends on the pump laser detuning [187]. Therefore, we can make a conjecture that the breathing occurs due to the photon transfer between the Kerr-shifted dispersion parabola and the first solitonic line given by the laser detuning, while the breathing frequency is the corresponding gap. In the points where the ladder crosses the AS supermodes parabola enhancement of the comb power is observed. Therefore, optical spectrum of a breather contains a set of sidebands [187].

In the supermode basis [see Fig. 5.4(b)] it becomes evident that the breathing occurs mostly in AS supermode families. Therefore, the breathing dynamics in the AS mode family does not show significant difference from the conventional breathing found in the single resonator case as follows from the nonlinear dispersion relation [Fig. 5.4(d)], although it demonstrates significant differences in the resonator basis. Fig. 5.4(f) shows the nonlinear dispersion relation for the S supermode family. The origin of the DWs which perturb the breathing state can be seen as an enhancement of the certain supermodes in the S family ( $\mu \approx \pm 70$ ) in the places where the ladder from AS supermodes crosses the S parabola.

### Soliton hopping state

The soliton hopping state recently predicted in the photonic dimer [122] is characterized by a periodic energy exchange between the coupled resonators in the presence of temporally-

## 5.2 Critically coupled resonators: split resonance

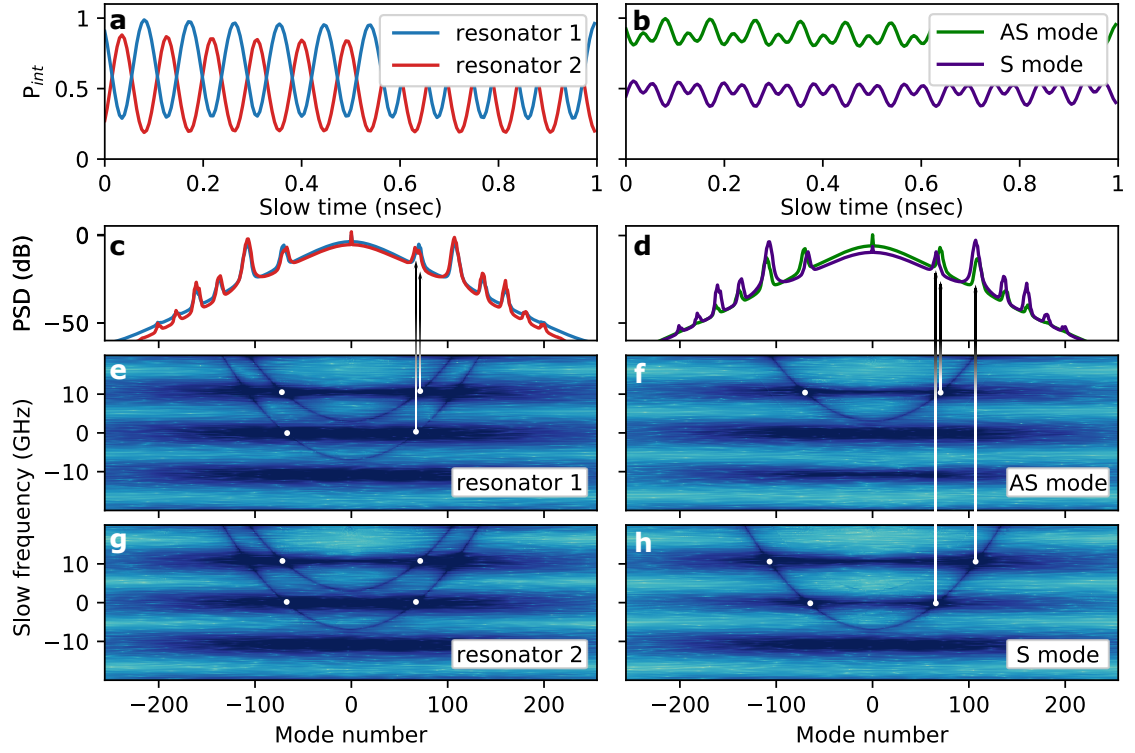


Figure 5.5: **Soliton hopping state.** (a,b) Intracavity field power evolution and power spectral density (PSD) at fixed laser detuning corresponding to the the soliton hopping regime, in supermode basis. (c,d) Nonlinear dispersion relation for AS and S supermode families, respectively. White dots show points on the nonlinear dispersion relation where the spectral components are enhanced. Arrows connect these points with the corresponding spectral components.

localized coherent structures. Inter-resonator oscillations have a frequency equal to the splitting between the supermode parabolas. The average power modulation is much stronger than in the breathing state, which leads to the enhanced sideband amplitudes in the optical spectrum [see Fig. 5.5(b)].

The spatiotemporal diagrams for the diagonalized system [see Fig. 5.3(c,d)] reveal a remarkable insight about the soliton hopping state. The soliton hopping range [blue area in Fig. 5.3(a,b)] coincides with the emergence of a localized coherent structure in the S supermodes family accompanied by a characteristic solitonic step in the average intracavity power evolution as follow from Fig. 5.3(b). This coherent structure is generated via the emerged FWM pathways depicted in Fig. 5.2(d). Soliton in AS supermode family acts in this case as a source of photons which triggers the parametric processes, thereby resonantly populating the S parabola in the vicinity of the 0<sup>th</sup> mode (i.e. with the offset  $-\Delta\omega$ ) via the process #5 (photons from AS and S supermodes annihilate creating photons from AS and S supermodes). Energy conservation is ensured by populating supermodes offset by approximately  $+\Delta\omega$ . Cascaded parametric process #2 (a pair of S supermode photons annihilates creating another pair of S supermode photons) populates the neighbouring S supermodes similarly to the CW-pumped single resonator. Therefore, we assume that the coherent structure generated in S supermodes is a GS (i.e. supermode dissipative Kerr soliton). Thus, the origin of the oscillatory behavior can be seen as a time periodic interference of coherent structures living in different supermodes.

Fig. 5.5(a) shows the dimer dynamics at fixed pump laser detuning, in the soliton hopping regime in AS and S supermodes representation. It can be obtained numerically by seeding the solitonic state in the AS supermode and further tune into the soliton hopping state. The average power exhibits small amplitude oscillations around a certain value. Periodic oscillations in slow time results in the series of sidebands (also similar to Kelly-sidebands widely present in the mode-locked lasers [159]) in the optical spectrum as has been shown in [122]. Corresponding nonlinear dispersion relation shows a ladder of lines similar to the breathing state discussed in above, but the spacing between them is equal to the splitting between the DWs parabolas. The origin of the double maxima spectral sidebands is well seen in the supermode basis [see Fig. 5.5(b)]. They appear due to the different Kerr nonlinearity-induced shift of supermodes in the presence of inter-resonator detuning. White dots indicate the point where the ladder crosses dispersive parabolas and the continuing arrows indicate the corresponding spectral components enhancement. Both nonlinear dispersion relations depicted in Fig. 5.5(d,c) contain a corresponding DW parabola and the hopping ladder. Since the ladder crosses parabolas at slightly different mode numbers, sidebands have two maxima.

### 5.2.3 Experimental and numerical evidences of the deterministic single soliton generation

Deterministic generation of a single soliton state in optical microresonators is essential for a turn-key dissipative Kerr soliton-based broadband frequency combs generation. Indeed,

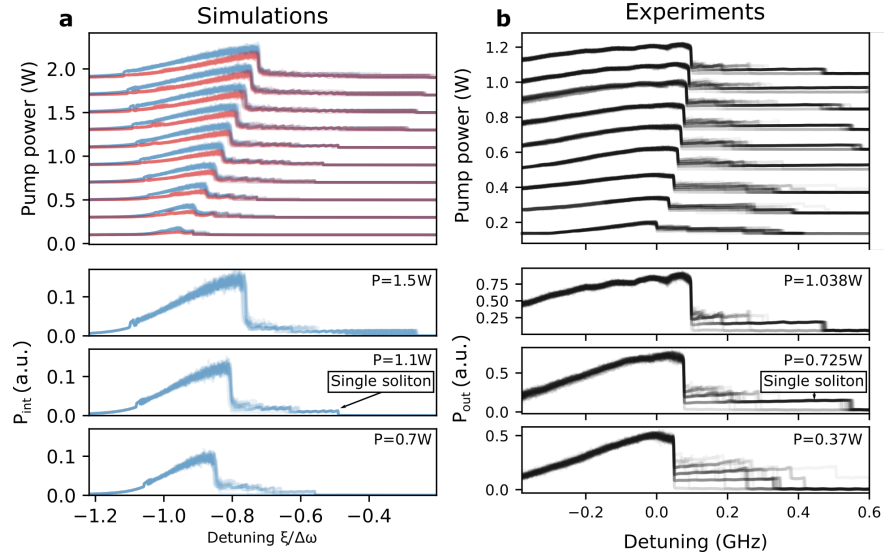


Figure 5.6: **Experimental and numerical evidences of single GS generation.** Numerical (a) and experimental (b) confirmations. (a, top) Simulation of average intracavity field evolution for different input powers as a function of pump laser detuning. For every value of the pump power there are 10 traces superimposed. (a, bottom) Examples at three different powers. Single GSs are depicted by arrow. (b) Experimental confirmation obtained by piezo-tuning of central frequency of a widely tunable external cavity diode laser over the AS resonance. For every value of the pump power there are 50 generated light traces superimposed.

passing the chaotic modulation instability stage, soliton arrangement inside the cavity can be arbitrary which leads to a non-homogeneous spectral profile due the interference of different solitonic components. One way to control and structure the soliton arrangement inside the cavity is to introduce a background modulation which leads to the generation of perfect soliton crystals [50]. However, the single soliton state is, nonetheless, difficult to achieve in this configuration.

Another way to naturally fall into the single soliton state has been described in [188]. It has been proposed to employ a strong avoided mode crossing with higher-order modes of the resonator, which leads to an extensive cavity Cerenkov radiation [189]. In this case, the soliton, being a line on the nonlinear dispersion relation [190], crosses the distorted cavity mode, which leads to effective photon transfer towards the higher-order modes [174]. In this way, every soliton acts as a "source" of DWs. Therefore, if the energy of the DWs is sufficient to perturb the solitonic states the number of solitons will decay towards unity, where the state will be stabilized.

Here, we present a deterministic version of this mechanism utilizing discovered properties of the photonic dimer [122]. Due to the more complex dispersion landscape, the single soliton generation process does not require any additional interaction with higher-order mode, even though it is shown to be enhanced for certain supermodes due to the underlying symmetry that we discuss in chapter 6 of this thesis. Indeed, the periodic intra-resonator

field enhancement due to the crossing of the S supermode parabola is found to be sufficient to trigger the process discussed in [188]. In order to verify this claim, we investigate both numerically and experimentally the GSs generation. Fig. 5.6 shows the qualitative comparison of numerical and experimental phase diagrams. As follows from the numerical simulations of coupled LLEs 5.1, single soliton generation occurs when passing a threshold power of 0.9 W. A similar result follows from the experimental investigations. Figure 5.6(b) shows 50 traces of the generated combs power at different values of the pump power as a function of the laser detuning from the position of AS resonance. The central frequency of a widely tunable external cavity diode laser has been controlled by the piezo-tuning technique.

### 5.3 Critically coupled resonators: split dissipation

Passing through an EP, which exhibits a singularity of nonlinear interactions efficiency, we enter the domain of split dissipation ( $\mathcal{PT}$ -symmetry broken phase), which exhibits drastically different dynamical features. We study soliton generation in this region and show that  $\mathcal{PT}$ -symmetry breaking leads to soliton generation in either cavities. The soliton localization can be switched by increasing the pump power and thereby flipping the broken  $\mathcal{PT}$ -symmetry. Four distinct dynamical states are identified, we observe among them on-demand perfect soliton crystals generation, which can be a promising alternative to the existing technology relying on the resonator's mode interaction [50].

#### 5.3.1 Phase diagram: inter-resonator coupling vs pump power

We numerically explore the phase diagram under the condition of critical coupling in the nondegenerate dissipation regime [see Fig. 5.7(a)]. In Fig. 5.7(a),  $\kappa_{\text{ex},1}$  is varied with  $J$  in the way that the critical coupling condition (Eq. 5.3) is satisfied across the phase diagram and the dimer is in a state of broken  $\mathcal{PT}$ -symmetry (split dissipation). An EP is found at  $J = 0.5\kappa_0$  [see Fig. 5.1(d)]. We selected 14 values of pump power distributed logarithmically from 0.01 W to 1.5 W and 13 values of inter-resonator detuning distributed linearly from  $0\kappa_0$  to  $2.4\kappa_0$ . For each set of parameters, we employ the conventional soliton generation scheme by scanning the resonance from blue to red-detuned side. The spatiotemporal and spectrum evolution diagrams in the resonator basis is used to identify the stable soliton state that is generated during the scan. Colors in Fig 5.7(a) correspond to different stationary states attainable in the split dissipation regime. Thus, for different points on the phase diagram, the value of detuning is not the same. If several stationary states are identified, we choose the first state in the soliton existence range. The phase diagram is averaged over 3 realizations and the pump laser frequency is swept at the speed  $\frac{1}{10}\kappa_0^2/2\pi$ , corresponding to a change of frequency  $\kappa_0$  every 10 photon lifetimes ( $2\pi/\kappa_0$ ).



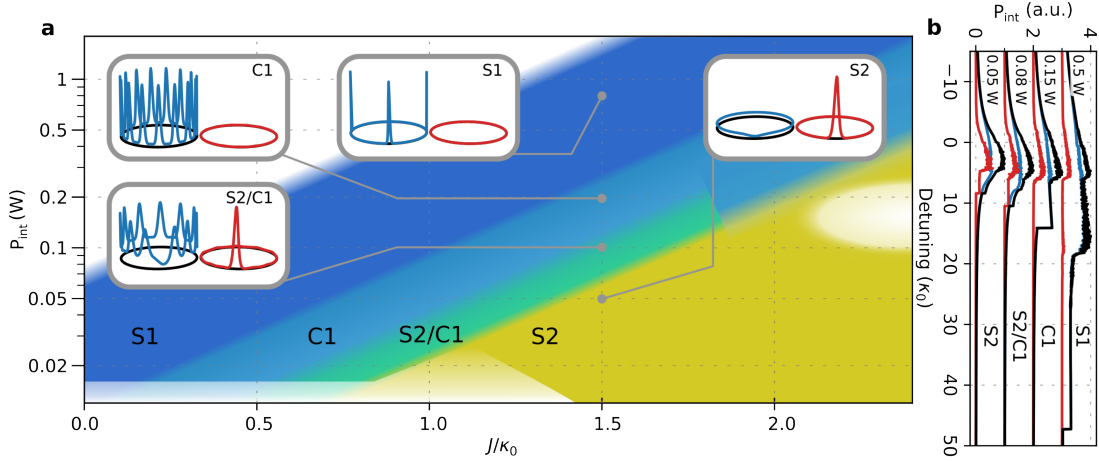


Figure 5.7: Phase diagram for critically coupled photonic dimer under the split dissipation ( $\mathcal{PT}$ -symmetry broken) condition. (a) Schematic phase diagram represented as a function of input power and  $J$ . Four states are identified: soliton in resonator 1 (S1, blue region), soliton crystal in resonator 1 (C1, cyan region), coexistence of soliton in resonator 2 and periodic coherent structure resonator 1 (S2/C1, green region), and soliton in resonator 2 (S2, yellow region). The insets show the intracavity field intensity in the resonators 1 (blue) and 2 (red), at the parameter indicated by the grey dot. White color refers to the absence of stable solitonic state. (b) Intracavity power traces at different input powers for  $J/2\pi = 70$  MHz. Parameters for the simulations are  $\kappa_0/2\pi = 50$  MHz,  $\kappa_{\text{ex},2} = 0$ ,  $\delta = 0$ ,  $D_1/2\pi = 180$  GHz,  $D_2/2\pi = 4$  MHz.

### Dynamical states in split dissipation regime

We differentiate four dynamical states in this regime: multi or single soliton in resonator 1 (S1, blue region), soliton crystal in resonator 1 (C1, cyan region), coexistence of periodic coherent structures in resonator 1 and soliton in resonator 2 (S2/C1, green region), and soliton in resonator 2 (S2, yellow region). The parameter regions enabling their generation are coloured on the phase diagram and their characteristic intracavity intensity profile are shown in the insets. White region refer to the absence of solitonic states.

At weak inter-resonator coupling ( $J < \frac{1}{2}\kappa_0$ ), the system qualitatively follows the single resonator dynamics and features the S1 state, where DKSs exist in resonator 1 while resonator 2 only features their low-power projection. Increasing the inter-resonator coupling, dynamical regions corresponding to states C1, S2/C1, and eventually S2 are accessed.

The states are almost exactly partitioned in the resonator basis. For example, state S1 is confined in resonator 1 although a negligible amount ( $\ll 1\%$ ) is found in resonator 2. That is, the field amplitude distribution between the resonators does not follow the supermode distribution which is given by linear analysis. We assume that the nonlinearity changes the field distribution of the supermode, making them localized in the resonators. These supermodes are referred to as high-loss (confined in resonator 1) and low-loss (confined in resonator 2).

### Parametric switching of the soliton-localisation

In the range of  $1.2\kappa_0 \lesssim J \lesssim 1.8\kappa_0$ , the four stable states can also be accessed by changing the pump power. Fig. 5.7(b) shows the intracavity power evolution as a function of the laser detuning for pump power levels corresponding to four dynamical states in this range of  $J$ . Therefore, gradually increasing the pump power, states S2, S2/C1, C1, and S1 can be sequentially accessed.

In this process, the soliton-localization switches from resonator 2 to resonator 1. Linear analysis predicts that the resonant soliton will be confined in the low-loss supermode while the red-detuned CW background will be in the high-loss supermode [see Fig. 5.1(c)] as is the case for state S2 [inset of Fig. 5.7(a)]. However, despite the field distribution predicted by the linear analysis, the presence of nonlinearity in the system introduces a mechanism allowing for the parametric switching between the cavities.

Indeed, at low pump power, only the low-loss supermode has a quality factor sufficient for the soliton generation, resulting in state S2. At higher pump powers, both supermodes can sustain a coherent structure, leading to the coexistence of soliton and periodic coherent structure that has been observed in a limited intermediate range of parameters. Above a threshold, solitons are not generated in resonator 2. Moreover, in the C1 and S1 state, the parametric gain is able to compensate the difference of losses between the supermodes, and invert the  $\mathcal{PT}$  symmetry: the parametric gain (via intra-band FWM) is larger in the supermode localized in resonator 1 than in the other supermode making the state of broken  $\mathcal{PT}$ -symmetry flipped in comparison to the linear regime for longitudinal modes with  $\mu \neq 0$ .

We note that no specific solitonic state was found at the EP. We suppose that the Kerr shift lifts the degeneracy between the two supermodes. However, an extensive investigation of the soliton generation in the close vicinity of the EP is beyond the scope of this study.

### 5.3.2 Deterministic soliton crystal and efficient comb generation

In this section, we study the generation of state C1, which corresponds to the deterministic generation of a soliton crystal [50]. Fig. 5.8 shows the numerical simulations of Eq. 3.2 setting the pump power to 0.2 W and  $J/2\pi = 75$  MHz. Fig. 5.8(a) shows the intracavity power in both resonators as a function of laser detuning. The incident light couples into both high- and low-loss, supermodes of the system simultaneously, such that the low-loss supermode features a chaotic regime while the high-loss supermode remains in the cnoidal wave regime [Fig. 5.8(c,e)]. After passing a critical detuning ( $\sim 7\kappa_0$ ), resonator 2 leaves the chaotic regime without any coherent structures generated while cnoidal waves of resonator 1 transition into a soliton crystal state. Fig. 5.8(b) shows that the crystal state at detuning I [Fig. 5.8(a)] is perfect [50] with more than 100 dB of extinction over almost the full existence range.

This state is known to exhibit a high conversion efficiency due to the high occupancy of the resonator 1 as shown in Fig. 5.8(b,d). Fig. 5.8(f) shows the output power in the pump mode

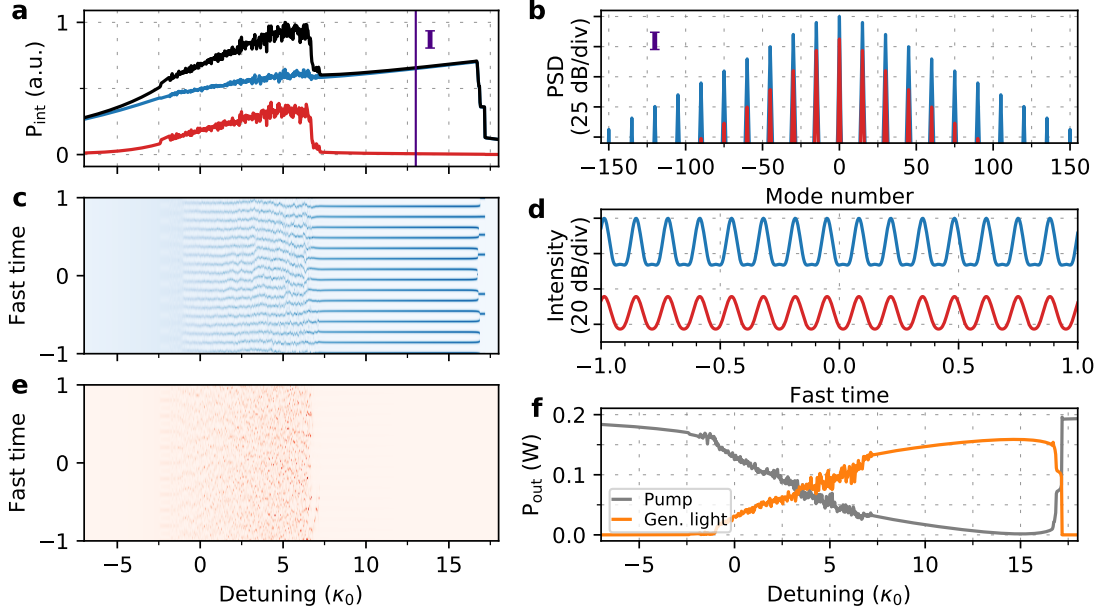


Figure 5.8: **Deterministic perfect soliton crystal generation in the  $\mathcal{PT}$ -symmetry broken phase.** (a) Intracavity power as a function of detuning. (b,d) Spectrum (b) and waveform (d) at detuning I. (c,e) Spatio-temporal diagrams for resonators 1 (c) and 2 (e). (f) Output of the through port, showing pump conversion above 75 % into coherent comb.  $P_{\text{in}} = 0.2$  W and  $J/2\pi = 75$  MHz. Other parameters are identical to Fig. 5.7.

( $\mu = 0$ ) and comb modes ( $\mu \neq 0$ ). We observe that the perfect soliton crystal formation leads to a conversion efficiency higher than 75%. Also, we note that the pump is almost completely absorbed by the system, such that an effective nonlinear critical coupling is achieved. According to [50], the soliton crystal is generated deterministically when the pump power is below the threshold to avoid spatiotemporal chaos under the condition that modal crossings with higher-order modes trigger background modulation. Here, we observe deterministic soliton generation in the absence of modal crossings.

### 5.3.3 Bright-dark solitons coexistence and their interaction with periodic coherent structures

We perform and analyze a simulation with  $J/2\pi = 75$  MHz,  $P_{\text{in}} = 0.1$  W, as shown in Fig. 5.9 in order to generate S2/C1 state depicted by green in the phase diagram [Fig. 5.7(a)]. The power trace [Fig. 5.9(a)] shows the presence of a step in each resonator. The spectrum and temporal intensity at detuning I are shown in Fig. 5.9(b). A soliton exists in resonator 2, while background modulation reminiscent of C1 state are present in both resonators. The comb modes in both resonators are excited in this state, hinting at nonlinearly-induced  $\mathcal{PT}$ -transition that restores the  $\mathcal{PT}$  symmetry in the comb modes [191, 192]. Spatiotemporal diagrams shown in Fig. 5.9(c,e) as a function of the laser detuning indicate that the S2/C1 state decays into a S2 state after the end of the soliton existence range in resonator 1. After

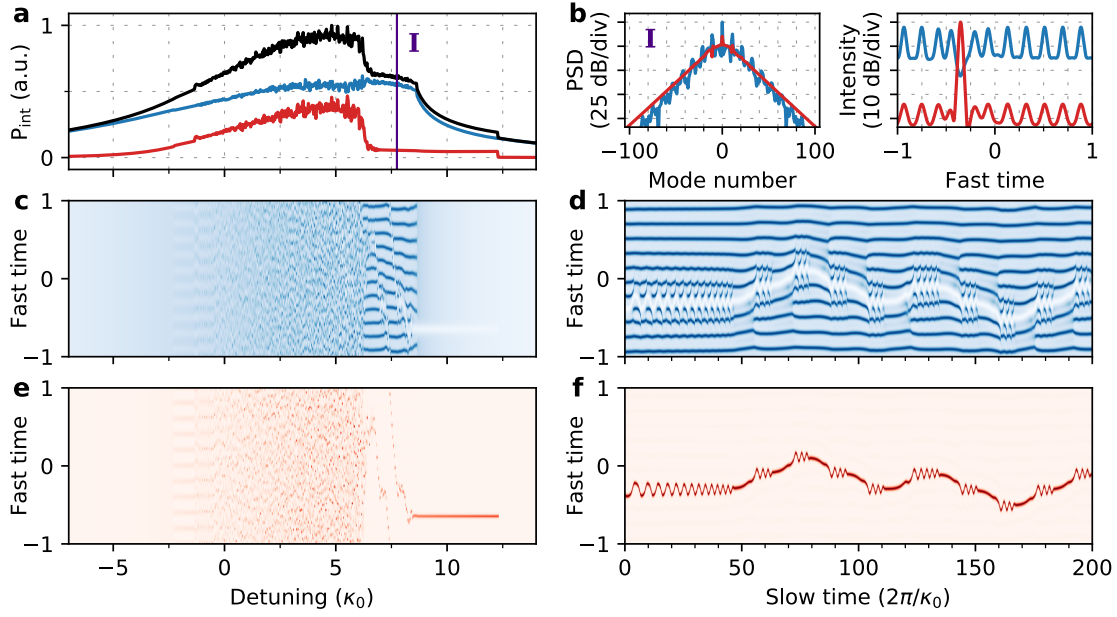


Figure 5.9: **Generation of bright-dark soliton pairs and interaction with periodic coherent structures in the  $\mathcal{PT}$ -symmetry broken phase.** (a) Intracavity power as a function of laser detuning. (b) Spectrum and waveform at detuning I. (c,e) Spatiotemporal diagram in resonator 1 and 2. (d,f) Simulation at fixed detuning seeded with the state from I, showing the evolution of the bright-dark soliton pair interacting with periodic coherent structures in resonator 1.  $P_{\text{in}}=0.1$  W. Other parameters are identical to Fig. 5.7.

transitioning to the S2 state, the field in resonator 1 acts as a source for resonator 2, resonantly supplying additional energy to the solitonic state. This results in a coexistence of a bright and dark solitons synchronously rotating in the resonators. This situation is similar to a dual fiber loop arrangement presented in [121] but in the limit of equal cavities.

While the existence of a periodic coherent structure in resonator 1, bright-dark soliton pair can be generated as well. A simulation at a fixed detuning starting from the initial conditions I [Fig. 5.9(b)] is shown in the spatiotemporal diagrams Fig. 5.9(d,f). We observe that the soliton pair is bounded by the effective nonlinear potential induced by the periodic structures in the neighbouring cavity. The spatiotemporal diagram depicts the possibility for the bright-dark soliton pair to tunnel from one potential unit cell to another interacting with their boundaries in an oscillatory manner. In addition to the fast oscillations, a random walk of the pair is observed at a slower timescale.

## 5.4 Conclusion

In this chapter we investigate nonlinear dynamics in a driven-dissipative photonic dimer exhibiting an exceptional point. We analyze the generation of dissipative Kerr solitons on both sides of the exceptional point which acts as a demarcation of the dimer critical coupling conditions. These two regimes are the split resonance regime (with the preserved symmetry) and split dissipation regime (with broken symmetry), as found in conventional  $\mathcal{PT}$ -symmetric systems with gain and loss. Each regime exhibits unique nonlinear dynamics not found in the single resonator.

In the split resonance regime, which has been substantially discussed in [122], we observe that dimer solitons can be generated in either supermodes, however, only the antisymmetric one exhibits non-conventional soliton dynamics related to the emerging efficient four-wave mixing pathways. The dynamics is conveniently expressed in the supermode basis, for which we developed the concepts of inter-band four wave mixing. Supermode representation reveal that, despite the complexity of the dimer system, we are able to separate conventional single-resonator soliton dynamics from the dispersive waves emerging in another supermode. Breathing state of the photonic dimer in the supermode basis appears remarkably similar to its single-resonator counterpart except for a small perturbation. In this case, the intra-resonator power of both cavities oscillates in phase. Rapid and counter-phase power oscillations (soliton hopping) are observed above a threshold pump power, originating from the generation of synchronized solitons in both supermodes. We highlight the fact that all the dynamics appearing in the split resonance regime can be well understood in the supermode representation.

The same does not apply to the regime of split dissipation. The absence of the resonance splitting implies the pumping of both supermodes simultaneously. Therefore, the most convenient representation in this case is the conventional resonator basis which exhibits the broken  $\mathcal{PT}$ -symmetry of the system. Satisfying the critical coupling condition, we impose different loss rates on the two resonators so resonator 1 becomes substantially overcoupled. We observe

## Chapter 5. Dissipative Kerr solitons in dimers

---

the generation of four different stable solitonic states localized in either or both resonators. In these states we observe: the synchronization of bright-dark soliton pairs (in resonators 2 and 1, respectively), the interaction of periodic coherent structures in resonator 1 with the bright-dark soliton pair, the deterministic generation of soliton crystal states with more than 75% pump conversion efficiency into the comb lines, and bright solitons in resonator 1. Thereby, the pump power enables the parametric switching of the soliton localization between resonator 1 and 2. The switching is induced by flipping the broken  $\mathcal{PT}$  symmetry so the lossy resonator 1 has more gain in the comb modes than resonator 2. We suspect nonlinearly induced  $\mathcal{PT}$  transition to take place in the intermediate regime [191, 192].

## 6 Avoided mode-crossings and dissipative solitons in coupled resonators

This chapter reports on the theoretical and experimental investigation of the avoided mode crossings in coupled resonator systems and their influence on the dissipative Kerr soliton generation. The results are partially adapted from A. Tikan *et al.*, “Protected generation of dissipative Kerr solitons in supermodes of coupled optical microresonators”, *Science Advances* **8** eabm6982(2022).

### 6.1 Introduction

The analogy between molecules and coupled resonator systems has been discussed in various studies [193, 194, 195]. Similar to the molecular energy surface non-crossings (first pointed out by von Neumann and Wigner [196] in the early years of molecular quantum mechanics), different eigenmode families of an optical resonator experience avoided mode crossings (AMXs) leading to distortions of initially smooth (i.e. unperturbed) dispersion profile [197, 198, 199, 200]. The dispersion profile is important in a plurality of resonant nonlinear wave-mixing schemes, including DKS [200] and platicon [74, 75, 135, 123] generation. Although in the domain of normal dispersion, AMXs play a role in initiating nonlinear dynamics, they are generally considered unfavorable for the formation of DKS [201], particularly when their position and intensity cannot be managed [200]. Even in scenarios where mode-crossings can be controlled, as demonstrated in Ref. [122] and in chapter 4, the presence of a shifted mode during soliton interaction results in a reduction of the DKS existence range. This challenge remains significant even in cases involving coupled resonators, where DKS consistently interacts with other supermodes. Even though, DKS were successfully generated in the antisymmetric (AS) mode (see chapter 5 and Ref. [122]), some of the predicted effects (such as soliton hopping) were not observed due to an unexpectedly enhanced interaction of the symmetric (S) supermode with higher-order modes (HOMs). Due to this interaction, AMX on the S supermodes strongly disrupts DKS generation and completely suppresses it above a certain power level. Contrary, the interaction of the AS modes with HOMs can be completely eliminated. As we show in this chapter, this effect is ubiquitous in strongly-coupled resonator arrangements. We propose a general model explaining the effect of protection and

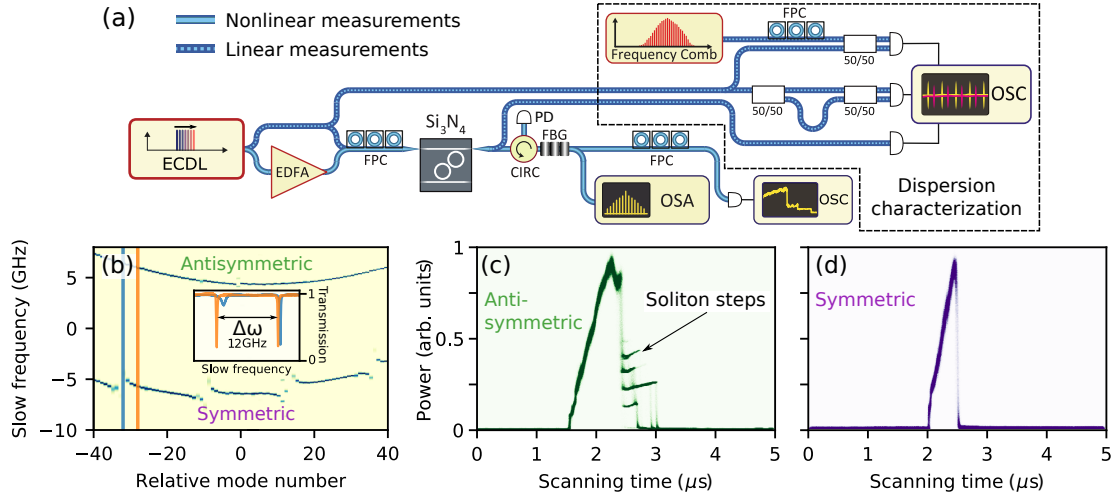


Figure 6.1: **Effect of protection against mode crossings in the photonic dimer and supermode DKS generation.** (a) Schematic representation of the experimental setup. Abbreviations: External cavity diode laser (ECDL); erbium doped fiber amplifier (EDFA); fiber polarization controller (FPC); optical circulator (CIRC); fiber Bragg grating (FBG); optical spectrum analyzer (OSA); sampling oscilloscope (OSC); photodiode (PD). ECDL is coupled into and out of the microresonator chip via lensed fibers. The dashed fiber path corresponds to the dispersion measurement scheme. (b) Dispersion profile measurements of the photonic dimer. Inset shows two cross-sections of plot (b) at mode numbers -32 and -28 corresponding to AMX and its close vicinity, respectively. (c,d) Experimental recording of generated light in AS and S modes of the photonic dimer, respectively. Each plot contains 600 superimposed oscilloscope traces. The color density indicates a number of superimposed traces at a given point.

apply it to the topological Su–Schrieffer–Heeger (SSH) arrangement, demonstrating the failure of the topological protection. Furthermore, we provide a recipe for harnessing the effect for on-demand protection of the dispersion profile, which is essential for the experimental generation of edge state soliton frequency combs.

### 6.1.1 Photonic dimer

We start with the description of AMXs in the supermodes of a photonic dimer. We studied strongly coupled microrings having  $\approx 200$  GHz free spectral range and loaded Q-factor of the order of 2 millions, realized on the Si<sub>3</sub>N<sub>4</sub> platform using the photonic Damascene reflow process [202]. The resonators are designed to feature an identical free spectral range. The intrinsic loss rate of the dimer is 50 MHz, and both resonators are interfaced with bus waveguides having external coupling rates of 100 MHz. Employing frequency comb calibrated diode laser spectroscopy (see Fig. 6.1a as well [203]), we retrieve first the dispersion profile of the photonic dimer. Figure 6.1b depicts the transmission spectrum of the photonic dimer in the form of an echellogram, where consecutive vertical lines are spaced by the free-spectral range  $D_1/2\pi$  of the microring resonator at the pump frequency  $\omega_0$ . The slow frequency denotes



the frequency offset of the resonance from the equidistant grid and, therefore, reveals the integrated dispersion ( $D_{\text{int}}(\mu) = \omega_{\mu} - (\omega_0 + D_1\mu)$ ) of the photonic dimer modes directly. The dispersion profile reveals two dimer supermode families. The fundamental S supermode family is strongly affected by AMXs while the AS supermode dispersion profile is almost unperturbed. The inset of Fig. 6.1b shows a cross-section of the plot at the mode crossed by a HOM (orange line) and before it (blue line). HOMs and, therefore, AMXs are likely to be present in soliton-generating microresonators because the waveguide constituting the microresonator is usually chosen to be multimode in order to guarantee low propagation losses (hence high Q factor) by reducing the influence of the fabrication-induced surface roughness [204].

We also study the influence of AMXs on the generation of supermode DKSs. Fig. 6.1c,d show a superposition of 600 transmission traces obtained by sweeping the pump laser frequency over the AS and S resonances at 1554 nm with an optical power in the waveguide of 43 mW. We use a conventional CW pumping scheme combined with fast single side-band tuning to eliminate thermal heating and resonance shifts [205]. The strong pump line is filtered using fiber Bragg gratings and the light generated by nonlinear processes in the resonator is sampled using a fast photodetector with 1 GHz bandwidth. Generated light profiles for the AS mode, detected with a photodiode after filtering out the pump comb line, systematically show the presence of characteristic steps signifying the stable access to the solitonic state [77, 64]. Contrary, S supermodes exhibit no solitonic feature at the equivalent pump power. At lower input powers, soliton generation can be observed in the S mode family, however, it depends on the particular distribution of AMXs on the dispersion profile. Indeed, as pointed out in [188] presence of the AMX leads to the intense generation of dispersive waves which perturb the solitonic state. Each soliton acts as a source of dispersive waves and, therefore, the number of solitons is naturally reduced until the perturbation becomes sufficiently weak to maintain the state. The strength of the perturbation depends on the position of AMX since the power spectral density of the soliton and, hence, the optical power transferred to the HOM decays exponentially from the pumped mode.

Even though, the soliton generation has several key aspects including the quality factor of the resonators and stability of the pump source, we refer to this effect as protected generation of DKSs in supermodes implying that the problems related to the soliton generation in a single resonator are addressed. Therefore, the key limitation in this case is the detuning rate between resonators which can only be controlled up to 70-80 GHz, resulting in the reduced (compared to the single resonator) fabrication yield.

### 6.1.2 Photonic trimer and plaquette

A similar effect is observed in the trimer configuration. Linear dispersion measurements (see Fig. 6.2a) reveal that the protection effect is the strongest for the trimer supermode with the highest relative frequency and gradually decreases for lower frequency states on the integrated dispersion profile. We also investigate a more complex resonator arrangement representing a

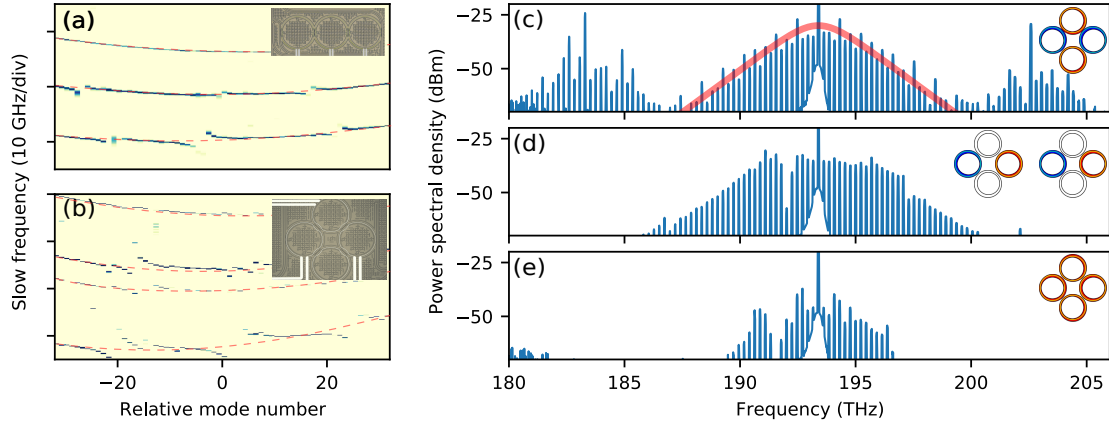


**Figure 6.2: Effect of protection in photonic trimer and plaquette.** (a) Linear dispersion measurement of a chain of three coupled resonators (photonic trimer). (b) The same for a square lattice (plaquette). Insets show microscope images of the Si<sub>3</sub>N<sub>4</sub> microresonators of  $\approx 200$  GHz free spectral range and imprinted system of heaters. (c-e) Optical spectra obtained by investigating the square lattice tuned into the degenerate state similar to the trimer configuration. Spectral corresponds to top, middle and bottom resonances of the effective trimer, respectively. The red line shows a fitting with the hyperbolic secant profile. Insets show a schematic representation of the supermode distribution.

fundamental element of the square lattice — a plaquette. Fig. 6.2b shows the corresponding dispersion profile. In the ideal case, two central mode families are degenerate. However, due to the presence of the finite inter-resonator detuning  $\delta$ , the degeneracy is lifted and we observe all four mode families. Imprinting metallic heaters on top of the device, we establish a control over the detuning of each individual resonator, thereby, bringing the plaquette system to the degenerate state. We choose to work with this system as it represents a more general case of coupled resonators, including the trimer to the degenerate case. Fig. 6.2c-e corresponding to the upper, middle (2x degenerate) and lower frequency resonance, show nonlinear probing of the plaquette structure. As follows from the figure, DKS in such configuration can be generated only in the upper resonance, which is expected to be protected from interaction with HOM.

The intersection of the soliton line with the dispersive parabolas in the nonlinear dispersion relation [122], as shown in Fig. D.1 of Appendix D.1, results in the generation of dispersive waves that can be identified by the presence of strong sidebands in the multisoliton spectrum show in Fig. 6.2c. Therefore, the low noise radio frequency generation in systems of coupled resonators is an open question which is a subject of future investigations.

### 6.1.3 Model of mode crossing suppression

In order to shed light on the protection phenomenon, we derive from Maxwell's equations a Hermitian model of four coupled modes interaction (see Appendix D.3). We consider two fundamental  $a_{1(2)}$  and two transverse HOMs  $b_{1(2)}$  of both resonators constituting the dimer.

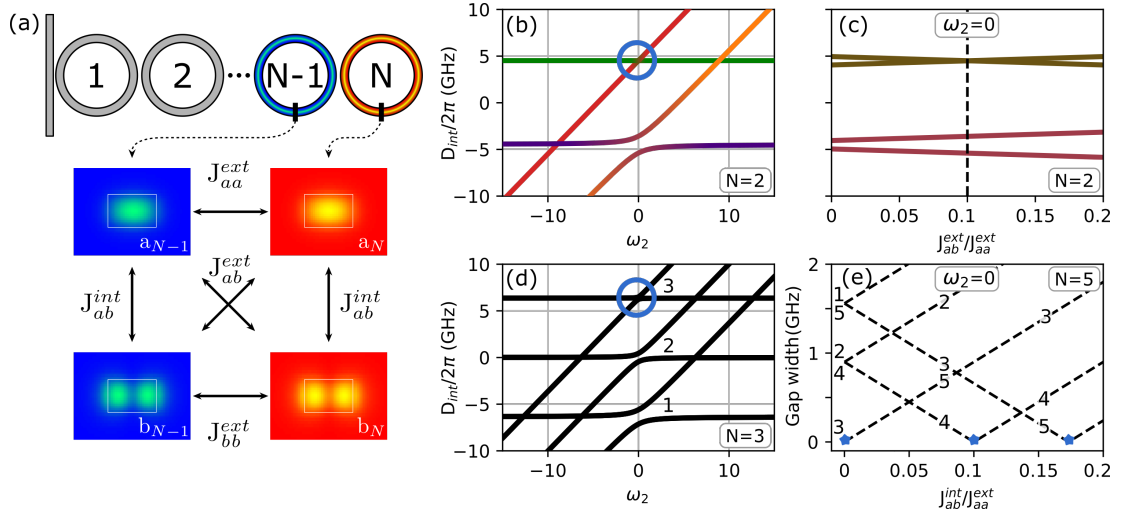


**Figure 6.3: Effect of protection in coupled resonators.** (a) Schematic representation of coupled resonators chain and description of the coefficients of the coupling matrix used in Eq. 6.1. (b) Protection in the photonic dimer. Protected state is highlighted by the blue circle. Green line corresponds to AS fundamental mode, violet to S fundamental mode, red — AS higher-order mode, and orange — S higher-order mode. Parameters are chosen to be close to the experimental ones:  $J_{aa}^{\text{ext}}/2\pi = 4.5$  GHz,  $J_{ab}^{\text{int}} = J_{ab}^{\text{ext}} = 0.1J_{aa}^{\text{ext}}$  (c) The splitting between hybridized supermodes with coinciding central frequencies. The dashed black line shows parameters corresponding to the cross-section of plot (b) at  $\omega_2 = 0$ . (d) Protection in the trimer configuration. (e) The gap distance between split resonances as a function of  $J_{ab}^{\text{int}}/J_{aa}^{\text{ext}}$  for a chain of 5 coupled resonators at  $\omega_2 = 0$ , keeping the value of  $J_{ab}^{\text{ext}}/2\pi = 0.1J_{aa}^{\text{ext}}/2\pi = 0.45$  GHz. Lines are numbered according to the relative frequency of the modes, as shown in plot (d). Blue stars depict the protected states.

The coupled mode equations can be written as follows [206]:

$$i \frac{dU}{dt} = - \begin{pmatrix} -\omega_1 & J_{aa}^{\text{ext}} & J_{ab}^{\text{int}} & J_{ab}^{\text{ext}} \\ J_{aa}^{\text{ext}} & -\omega_1 & J_{ab}^{\text{ext}} & J_{ab}^{\text{int}} \\ J_{ba}^{\text{int}} & J_{ba}^{\text{ext}} & -\omega_2 & J_{bb}^{\text{ext}} \\ J_{ba}^{\text{ext}} & J_{ba}^{\text{int}} & J_{bb}^{\text{ext}} & -\omega_2 \end{pmatrix} U, \quad (6.1)$$

where  $U = (a_1, a_2, b_1, b_2)^\top$ . Eigenvalues of the coupling matrix can be found analytically. Assuming that the coupling matrix is symmetric, we obtain:

$$\begin{aligned} \lambda_{1,2}(\text{as}) &= \frac{1}{2} \left( 2J_{aa}^{\text{ext}} \pm \sqrt{4(J_{ab}^{\text{int}} - J_{ab}^{\text{ext}})^2 + (\omega_1 - \omega_2)^2} + \omega_1 + \omega_2 \right) \\ \lambda_{3,4}(\text{s}) &= \frac{1}{2} \left( -2J_{aa}^{\text{ext}} \pm \sqrt{4(J_{ab}^{\text{int}} + J_{ab}^{\text{ext}})^2 + (\omega_1 - \omega_2)^2} + \omega_1 + \omega_2 \right). \end{aligned} \quad (6.2)$$

The notation for coupling coefficients is described in Fig. 6.3a.  $J_{aa}^{\text{ext}}$  corresponds to the coupling between fundamental modes of the nearest resonators,  $J_{ab}^{\text{ext}}$  — to the coupling between fundamental mode of one resonator and HOM of the neighbor, and  $J_{ab}^{\text{int}}$  is the coupling between fundamental and HOM within the same resonator. The coupling strength between two HOMs is set to  $J_{aa}^{\text{ext}}$  since it does not qualitatively change the result. The difference between  $J_{aa}^{\text{ext}}$  and  $J_{bb}^{\text{ext}}$  leads to a shift of the hybridization area along the direction of the HOM. As an example of the resonator HOM, we show TE<sub>10</sub>. The influence of the dissipative coupling in our system is negligible [207], and therefore is not included in the analysis. Thus, we find two pairs of eigenvalues that represent the mode interaction. The first couple  $\lambda_{1,2}$  corresponds to the AS supermodes while  $\lambda_{3,4}$  to S one. The expression under the square root in the first couple of eigenvalues contains the term  $(J_{ab}^{\text{int}} - J_{ab}^{\text{ext}})^2$ . Therefore, in the case when  $J_{ab}^{\text{int}}$  and  $J_{ab}^{\text{ext}}$  are of the same order, the influence of the AMX is reduced. However, in the second couple eigenvalues, the effect of AMX is increased in comparison to the conventional hybridization in the single resonator case.

Indeed, numerical simulations of the coupling region for parameters close to experimental ones (see Appendix D.5) demonstrated that the ratio between  $J_{ab}^{\text{ext}}$  and  $J_{ab}^{\text{int}}$  tends to one for silicon nitride based anomalous dispersion ring microresonators. The coupling sections to bus and drop waveguides will contribute to the coefficient  $J_{ab}^{\text{int}}$  as well, however, this contribution is found to be one order of magnitude smaller which is consistent with the experimentally observed strong protection of the AS supermode parabola (Fig. 6.1b).

The eigenvalue system Eq. 6.2 as a function of the central frequency of the HOM  $\omega_2$  with the ratio  $J_{ab}^{\text{int}}/J_{ab}^{\text{ext}} = 1$  is depicted in Fig. 6.3b. Fig. 6.3c shows the dependence of the hybridized modes position for  $\omega_1 = \omega_2$  (at the center of Fig. 6.3b) as a function of  $J_{ab}^{\text{ext}}/J_{aa}^{\text{ext}}$ . Black dashed line corresponds to the conditions considered in Fig. 6.3b. As predicted from Eq. 6.2, when  $J_{ab}^{\text{int}}$  and  $J_{ab}^{\text{ext}}$  coincide exactly, the gap distance tends to zero.

## 6.2 Protection of topological states in the Su–Schrieffer–Heeger model

The structure of the coupling matrix in Eq. 6.1 is notably similar to the Hamiltonian discussed in [208], which underpins the profound nature of the analogy with molecular systems. Similar effects, known as conical or diabolical crossings [209] in this community, have been actively investigated at the end of the last century.

This model can be easily extended to the case of arbitrary number of resonators (see Appendix D.4). An example of the mode hybridization for the trimer configurations is shown in Fig. 6.3d. Influence of the AMX increases with the decreasing relative frequency, as suggested by the experimental data. Numerical analysis of longer chains revealed that the index of the protected mode depends on the values  $J_{ab}^{\text{ext}}$  and  $J_{ab}^{\text{int}}$  and, therefore, *can be manipulated*. When  $J_{ab}^{\text{ext}}$  can be neglected then the effect of AMXs is the same for all the hybridized mode. In the opposite case, when  $J_{ab}^{\text{int}} \ll J_{ab}^{\text{ext}}$ , the protection falls into the middle mode family and symmetrically decreases towards modes with higher and lower relative frequencies. Therefore, the protection can be moved along the dispersion relation by changing the coupling coefficients ratio. Fig. 6.3e shows the dependence of the AMX-induced gap width as a function of normalized  $J_{ab}^{\text{int}}$  coefficient for a five resonator chain computed using the same parameters as previously. When  $J_{ab}^{\text{int}}$  can be neglected, the middle mode (3) becomes protected. With increasing  $J_{ab}^{\text{int}}$ , the protection moves towards the fourth mode family and subsequently to the fifth one.

Even though there is a number of techniques allowing one to suppress the excitation of higher-order modes in a microresonator [210, 150, 211], this can lead to the reduction of the coefficient  $J_{ab}^{\text{int}}$  while the control of both  $J_{ab}^{\text{int}}$  and  $J_{ab}^{\text{ext}}$  is required.

## 6.2 Protection of topological states in the Su–Schrieffer–Heeger model

In order to highlight the importance of protection for the future development of field of the soliton lattices, we study the effect of AMXs on topologically protected edge states in the SSH model [212] originally proposed for the explanation of mobile neutral defects in polyacetylene. This model is described by the following Hamiltonian:  $\hat{H}_{\text{SSH}} = \sum_n t_1 \hat{c}_n^\dagger \hat{c}_{n-1} + t_2 \hat{c}_{n+1}^\dagger \hat{c}_n$ , where  $\hat{c}_n^\dagger$  is the creation operator at the  $n_{th}$  site and  $t_{1,2}$  is the hopping amplitudes. Due to the simplicity of implementation [213], this model often serves as a primary verification platform for novel nonlinearity-related topological effects [118]. It can be realized in our system by varying the inter-resonator coupling coefficients  $J_{aa}^{\text{ext}}$  and  $J_{ab}^{\text{ext}}$  playing here the role of the hopping amplitudes. Schematic representation of the SSH chain is shown in Fig. 6.4a. The alternating coupling effectively divides the chain into a number of unit cells shown by dashed rectangles. The coupling strength ratio inside a unit cell and between unit cells ( $t_1/t_2 = J_{aa,ab,1}^{\text{ext}}/J_{aa,ab,2}^{\text{ext}}$ ) is chosen to be 0.1 which is sufficient for opening a wide photonic band gap and obtaining a nonzero integer winding number — a topological property, invariant under adiabatic perturbations [214].

Fig. 6.4b shows the mode hybridization for the SSH model realized with ten resonators. The topologically protected (against the disorder and variation of the coupling coefficients) edge

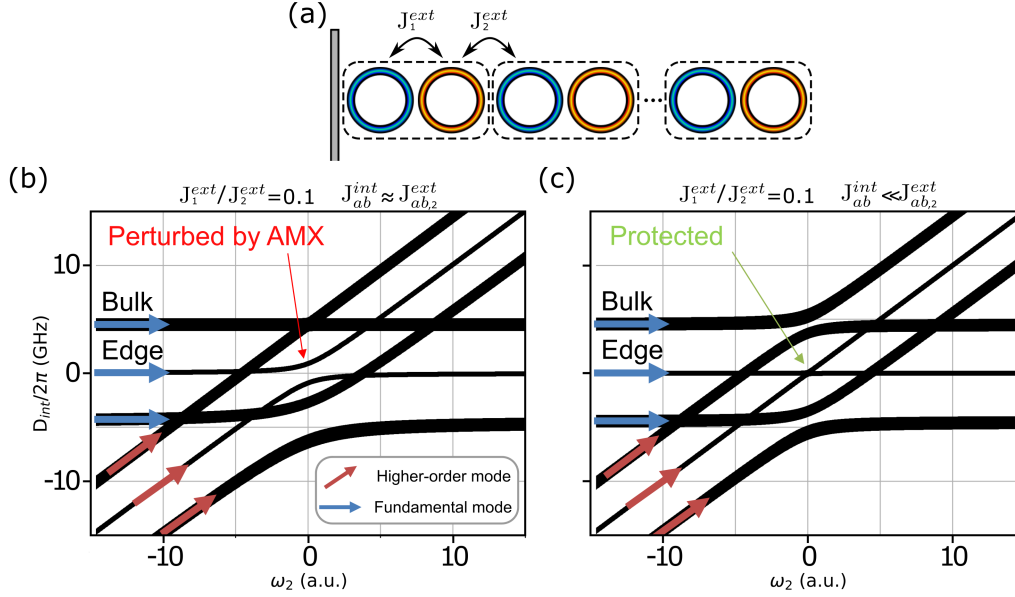


Figure 6.4: **Protection against mode crossing of the topological edge state in Su-Schrieffer-Heeger model.** (a) Schematic representation of 10 coupled resonators with alternating coupling, which constitutes the SSH chain. (b) Influence of AMX when  $J_{ab}^{int} \approx J_{ab,2}^{ext}$ . (c) The same configuration with  $J_{ab}^{int} \ll J_{ab,2}^{ext}$  ( $J_{ab}^{int} = 0.001 J_{ab,2}^{ext}$ ) exhibits the protection against AMX.

state is in the middle of the gap between two bulk states as shown in Fig. 6.4b. The same is observed for the HOM family. According to the model, a crucial influence of AMX on the topological state is expected, which potentially forbids or drastically obstructs the generation of topological DKSs if the protection is not controlled. Indeed, AMXs in this system, together with inter-resonator detuning in absolute frequency, act as on-side potential breaking the chiral symmetry of the SSH lattice [215] and omitting the inherent topological protection [216]. However, increasing the difference between  $J_{ab}^{int}$  and  $J_{ab,2}^{ext}$ , we observe enhancement of the protection effect on the edge state modes. This can be achieved by carefully designing the coupling section to suppress the internal transverse mode couplings. Choosing the ratio  $J_{ab}^{int} = 0.001 J_{ab,2}^{ext}$ , we observe a complete protection against AMX as shown in Fig. 6.4c.

### 6.3 Conclusion

Concluding, we introduced the notion of protection against AMX in chains of coupled multi-mode resonators, which exhibit a remarkable similarity with conical energy level crossings in molecular systems. The crucial influence of this effect on the dispersion profile and, therefore, the supermode DKS generation is demonstrated experimentally. We propose a simple model which fully explains the effect and proposes a way to harness it for stable DKS generation. Furthermore, we delve into the potential to manipulate the count of mode protections by adjusting the ratio between coupling to higher-order modes within a ring and that between

neighboring rings. Emphasizing its significance for the field's future advancement, we illustrate how this effect influences topologically protected edge states within the SSH model. This finding underscores the need to meticulously consider AMXs when designing experimental setups for observing topological gear solitons, ensuring accurate and reliable results.





# 7 Nonlinear dynamics in lattices of coupled resonators

This chapter reports on the theory of two-dimensional four-wave mixing processes in chains of coupled microresonators. The results are partially adapted from A. Tumnin *et al.*, “Nonlinear dynamics in lattices of coupled resonators,” *Communications Physics* **6**, (2023) and A. Tumnin *et al.*, “Dissipative Kerr solitons at the edge state of the Su-Schrieffer-Heeger model,” *Journal of Physics: Conference Series*, Volume 2015, 012159 (2021).

## 7.1 Introduction

While the previous chapters discussed optical frequency comb generation and nonlinear dynamics in systems of coupled resonators, these lattices were relatively small. The observed effects, which go beyond single-resonator physics, can still be understood using the one-dimensional Lugiato-Lefever equation. On the other hand, large-scale arrays of coupled resonators that combine spatial and frequency dimensions remain largely unexplored, both theoretically and experimentally. They can allow for significantly more complex dispersion landscapes, opening new ways to engineer dispersion. Moreover, such lattices can also enable the study of topological systems, such as the Su-Schrieffer-Heeger model or honeycomb lattices [214, 88], which have been extensively studied in the linear regime in photonics over the past decade.

In this chapter, we consider systems with many coupled resonators, naturally extending the problem dimensionality. For example, for a 1D chain of resonators, we obtain a 2D system with nonlinearly coupled frequency and spatial axes. We provide a leading-order model in the form of the 2D continuous-discrete LLE. This model demonstrates a striking difference in comparison with its lower-dimensional counterpart. The two-dimensional version of the LLE was first derived in the context of transverse pattern formation in nonlinear cavities [10] and was recently applied to a novel type of cylindrical high-Q cavities [217]. The extension of the LLE to the two-dimensional case makes inherent dissipative solitons stable (contrary to its conservative counterpart [218]) only in a narrow region of parameters in the monostable part of the tilted resonance [219]. In contrast, the bistable part features only hexagonal

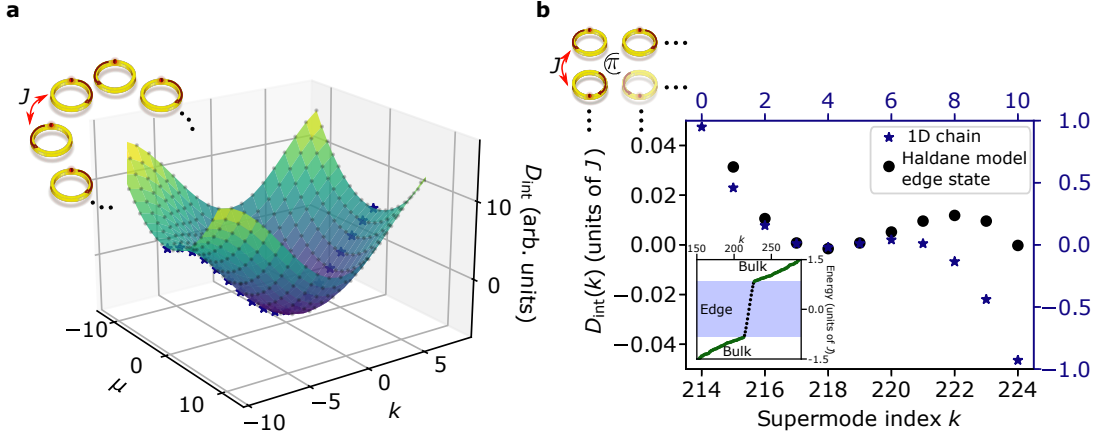


Figure 7.1: **Dispersion hybridization in lattices of resonators.** (a) Chain of equally coupled resonators. Dispersion of the spatial supermodes results in a two-dimensional hybridized surface. Blue asterisks represent the cosine band structure of a single mode for which integrated supermode dispersion at  $k = 4$  is presented in panel (b). (b) Integrated supermode dispersion of the edge state of the Haldane model compared to the dispersion of a chain of resonators. Inset: numerically computed band structure for  $21 \times 21$  resonators with phase flux in the unit cell  $\pi$ .

patterns [220]. We observe similar effects in a chain of 20 coupled optical resonators (Fig. 7.1a), demonstrating fundamentally distinct nonlinear regimes attributed to the local dispersion profile: elliptic and hyperbolic. We also demonstrate the emergence of two-dimensional spatiotemporal mode-locked solitons and discuss their correspondence to the observed solitons in the edge state of the Haldane model studied in Ref. [127], by comparing the local dispersion profiles (Fig. 7.1b). Similarly, we demonstrate that conventional 1D DKS are not expected to exist in arbitrary lattices of resonators. However, using the celebrated Su-Schrieffer-Heeger (SSH) model, we investigate the nonlinear dynamics of the edge state and demonstrate the generation of a 1D DKS, which is, however, strongly perturbed by dispersive waves in the bulk modes.

## 7.2 General theory

We start with a general description of nonlinear dynamics in an arbitrary N-dimensional lattice of resonators. Such system is shown to be governed by a set of linearly coupled Lugiato-Lefever equations (LLEs), which can be presented in matrix form as

$$\frac{\partial}{\partial t} \mathbf{A} = \hat{\mathbf{D}} \mathbf{A} + i \hat{\mathbf{M}} \mathbf{A} + i g_0 |\mathbf{A}|^2 \mathbf{A} + \mathbf{F}, \quad (7.1)$$

where vector  $\mathbb{A} = [A_0, \dots, A_{N-1}]^T$  contains optical field envelopes of each resonator in the lattice, matrix

$$\hat{\mathbb{D}} = \text{diag}\left[-\left(\frac{\kappa_0 + \kappa_{\text{ex},0}}{2} + i\delta\omega_0\right) + i\frac{D_2}{2}\frac{\partial^2}{\partial\varphi^2}, \dots, -\left(\frac{\kappa_0 + \kappa_{\text{ex},N-1}}{2} + i\delta\omega_0\right) + i\frac{D_2}{2}\frac{\partial^2}{\partial\varphi^2}\right]$$

contains detuning, losses, and dispersion for each resonator, the coupling between different rings is introduced in matrix  $\hat{\mathbb{M}}$ , the nonlinear term  $|\mathbb{A}|^2\mathbb{A} = [|A_0|^2 A_0, \dots, |A_{N-1}|^2 A_{N-1}]^T$  describes the conventional Kerr nonlinearity, and  $\mathbb{F} = [\sqrt{\kappa_{\text{ex},0}} s_{\text{in},0}, \dots, \sqrt{\kappa_{\text{ex},N-1}} s_{\text{ex},N-1}]^T$  represents the pump. In general, the coupling matrix  $\hat{\mathbb{M}}$  is diagonalizable and possesses a set of eigenvectors  $\{\mathbb{V}_i\}$  and associated eigenvalues  $\lambda_i$ , so any state  $\mathbb{A}$  can be represented in this basis

$$\mathbb{A} = \sum_j c_j \mathbb{V}_j, \quad (7.2)$$

where coefficients  $c_j = \langle \mathbb{A} | \mathbb{V}_j \rangle$  correspond to the amplitude of the collective mode  $\mathbb{V}_j$  and  $\langle \cdot | \cdot \rangle$  indicates scalar product. Therefore, Eq. (7.1) can be rewritten for the amplitudes  $c_j$  in the basis of eigenvectors  $\{\mathbb{V}_j\}$ , where the linear part of the equation will take a form of a matrix with eigenvalues  $\lambda_i$  on the diagonals corresponding to the resonance frequencies of the collective excitations. However, the nonlinear term will be no longer diagonal in this basis. In the resonator index basis, the nonlinear term takes form

$$|\mathbb{A}|^2\mathbb{A} = \sum_{j_1, j_2, j_3} c_{j_1} c_{j_2} c_{j_3}^* \mathbb{V}_{j_1} \mathbb{V}_{j_2} \mathbb{V}_{j_3}^*.$$

Projecting this expression onto the state  $\mathbb{V}_j$ , one obtains the coupled-mode equations for the amplitudes  $c_j$

$$\frac{\partial c_j}{\partial t} = -\left(\frac{\kappa_0 + \kappa_{\text{ex}}}{2} + i(\delta\omega_0 - \lambda_j)\right)c_j + i\frac{D_2}{2}\frac{\partial^2 c_j}{\partial\varphi^2} + i \sum_{j_1, j_2, j_3} c_{j_1} c_{j_2} c_{j_3}^* \langle \mathbb{V}_{j_1} \mathbb{V}_{j_2} \mathbb{V}_{j_3}^* | \mathbb{V}_j \rangle + \tilde{f}_j, \quad (7.3)$$

where  $\tilde{f}_j = \langle \mathbb{F} | \mathbb{V}_j \rangle$  is the projection of the pump on the eigenstate  $\mathbb{V}_j$ , the nonlinear term represents the conventional four-wave mixing process with the conservation law dictated by the product  $\langle \mathbb{V}_{j_1} \mathbb{V}_{j_2} \mathbb{V}_{j_3}^* | \mathbb{V}_j \rangle$ . The eigenvalues  $\lambda_j$ , showing the dependence of supermode frequency on supermode number, naturally start to play a role of dispersion, similar to the conventional LLE in a single resonator. In general, the eigenvalues  $\lambda_j$  are not equidistantly separated, and the supermode dispersion can be introduced similar to the integrated dispersion of a single resonator  $D_{\text{int}}(k) = \lambda_k - \lambda_{k_0} - J_1(k - k_0)$ , where  $J_1$  is the local free spectral range of the spatial supermodes in the vicinity of  $k_0$ . Depending on the system, the supermode dispersion has the same dimensionality  $\mathcal{D}$  as the system's band structure. Thus, the total hybridized dispersion (including the chromatic dispersion) profile for photons in the system has  $\mathcal{D} + 1$  dimensionality.

### 7.3 Chain of equally coupled resonators

We continue our analysis by considering a system of the equally coupled chain of resonators. First, we explicitly write Eq. (7.1) in the case of constant coupling in a chain

$$\begin{aligned} \frac{\partial A_\ell}{\partial t} = & -\left(\frac{\kappa_{\text{ex},\ell} + \kappa_0}{2} + i\delta\omega_0\right)A_\ell + iJ(A_{\ell-1} + A_{\ell+1}) \\ & + i\frac{D_2}{2}\frac{\partial^2 A_\ell}{\partial \varphi^2} + ig_0|A_\ell|^2 A_\ell + \sqrt{\kappa_{\text{ex},\ell}}s_{\text{in},\ell}e^{i\phi_\ell}. \end{aligned} \quad (7.4)$$

For simplicity, in the case of constant couplings to the bus waveguides  $\kappa_{\text{ex},\ell}$ , we introduce normalized variables  $d_2 = D_2/\kappa$ ,  $\kappa = \kappa_0 + \kappa_{\text{ex}}$ ,  $\zeta_0 = 2\delta\omega/\kappa$ ,  $j = 2J/\kappa$ ,  $f_\ell = \sqrt{8\kappa_{\text{ex}}g_0/\kappa^3}s_{\text{in},\ell}e^{i\phi_\ell}$ ,  $\Psi_\ell = \sqrt{2g_0/\kappa}A_\ell$ . In the normalized units, Eq. (7.4) reads

$$\frac{\partial \Psi_\ell}{\partial \tau} = -(1 + i\zeta_0)\Psi_\ell + id_2\frac{\partial^2 \Psi_\ell}{\partial \varphi^2} + ij(\Psi_{\ell-1} + \Psi_{\ell+1}) + i|\Psi_\ell|^2\Psi_\ell + f_\ell. \quad (7.5)$$

Further, we can readily diagonalize the linear part by taking the Fourier transform

$$\psi_{\mu k} = \frac{1}{2\pi\sqrt{N}} \int \sum_{\ell=1}^N \Psi_\ell e^{2\pi i(\ell k/N + \mu\varphi)} d\varphi, \quad (7.6)$$

where  $k$  is the supermode index and  $\mu$  is the comb line index. With the Kerr term, Eq. (7.5) transforms to

$$\begin{aligned} \frac{\partial \psi_{\mu k}}{\partial \tau} = & -(1 + i\zeta_0)\psi_{\mu k} - i[d_2\mu^2 - 2j\cos\frac{2\pi k}{N}]\psi_{\mu k} + \delta_{\mu 0}\tilde{f}_k + \\ & + \frac{i}{N} \sum_{\substack{k_1, k_2, k_3 \\ \mu_1, \mu_2, \mu_3}} \psi_{\mu_1 k_1} \psi_{\mu_2 k_2} \psi_{\mu_3 k_3}^* \delta_{\mu_1 + \mu_2 - \mu_3 - \mu} \delta_{k_1 + k_2 - k_3 - k}. \end{aligned} \quad (7.7)$$

In this form, we obtain the analytical expression for the hybridized 2D dispersion surface

$$d_{\text{int}}(\mu, k) = 2(\omega_{\mu k} - \omega_0 + D_1\mu)/\kappa = d_2\mu^2 - 2j\cos(2\pi k/N). \quad (7.8)$$

In the case of anomalous GVD ( $d_2 > 0$ , Fig. 7.1a) of the individual resonator, this surface with parabolic and cosine cross-sections is shown in Fig. 7.1a. Local dispersion topography changes along the  $k$  axis, revealing different regions with parabolic and saddle shapes. The pump term  $\tilde{f}_k$  stands for the projection of the pump on the  $k$ -th supermode

$$\tilde{f}_k = \frac{1}{\sqrt{N}} \sum_{\ell=1}^N f_\ell e^{2\pi i\ell k/N}. \quad (7.9)$$

#### 7.3.1 Spatial eigenstates and pump projection on the chain

The supermode dispersion (i.e., band structure) has regions of anomalous and normal supermode group velocity dispersion (sGVD). For a given supermode index  $k_0$ , the linear term in the

Taylor series of the cosine gives the supermode FSR equal to  $J_1/2\pi = 2J/N \sin(2\pi k_0/N)$  and the corresponding quadratic term yields sGVD  $J_2 = 2J(2\pi/N)^2 \cos(2\pi k_0/N)$  for eq. (7.4). The excitation of the individual supermode requires an accurate pump projection on its spatial profile. In case of imperfect projection of the pump, the number of the excited modes will depend on the local density of states within the width of the band. Moreover, the single-resonator pump scheme always leads to the excitation of supermodes in pairs due to their two-fold degeneracy, except for the modes from the very top and bottom of the band. According to Eq. (7.9), if the resonator  $\ell = 0$  is pumped, all the supermodes have a pump term with the projection amplitude  $1/\sqrt{N}$ . With the increasing number of resonators, a pumping scheme with a single resonator excitation becomes less efficient, and more sophisticated schemes are required. For simplicity of the further analysis, in the following we focus on the ideal case of a single supermode excitation. Accurate projection to the supermode with index  $k_0$  requires accurate adjustment the relative phases of the pump lasers according to

$$\mathbf{f} = f^{(0)} [1, e^{-2\pi i k_0/N}, e^{-4\pi i k_0/N}, \dots, e^{-2(N-1)\pi i k_0/N}], \quad (7.10)$$

where  $f^{(0)} = \sqrt{8g_0\kappa_{\text{ex}}P/\kappa^3\hbar\omega N}$  is normalized pump for a single resonator.

### 7.3.2 Modulation instability gain lobes.

Further, we investigate the stability of plane wave solutions  $\psi_{00}$ . Considering the pump at  $\mu_0 = 0$  and at the parabolic region  $k_0 = 0$  (saddle point  $k_0 = N/2$ ), we investigate FWM processes between the pump mode and the modes with indexes  $\mu, k$ . Linearizing the system, we identify the modes with positive parametric gain. We consider the system to be in a stable state  $\psi_{0k_0}$  with  $k_0 = 0$  or  $N/2$ . These two supermodes have opposite sGVD. Keeping only quadratic term in Taylor series of the cosine in Eq. (7.7) and performing inverse Fourier transform, we obtain the 2D LLE

$$\frac{\partial \Psi}{\partial \tau} = -(1 + i\zeta_0^{k_0})\Psi + id_2 \frac{\partial^2 \Psi}{\partial \varphi^2} + ij_2^{k_0} \frac{\partial^2 \Psi}{\partial \Theta^2} + i|\Psi|^2\Psi + f^{(0)}e^{-ik_0\Theta}, \quad (7.11)$$

with  $\Theta = 2\pi\ell/N$ ,  $j_2^{k_0} = \pm(2\pi/N)^2j$ ,  $\zeta_0^{k_0} = \zeta_0 \mp 2j$ , and  $+$  ( $-$ ) standing for excitation of  $k_0 = 0$  ( $N/2$ ). Further, we investigate unstable solutions  $c(t) \exp(i[\mu\varphi + k\Theta])$  [156]. The linearized system yields the following eigenvalues

$$\lambda_{1,2} = -1 \pm i \sqrt{(\zeta_0^{k_0} + j_2^{k_0} k^2 - 3|\psi_{0k_0}|^2)(\zeta_0^{k_0} + j_2^{k_0} k^2 - |\psi_{0k_0}|^2)}, \quad k \neq 0, \mu = 0 \quad (7.12)$$

$$\lambda_{3,4} = -1 \pm i \sqrt{(\zeta_0^{k_0} + d_2 \mu^2 - 3|\psi_{0k_0}|^2)(\zeta_0^{k_0} + d_2 \mu^2 - |\psi_{0k_0}|^2)}, \quad k = 0, \mu \neq 0 \quad (7.13)$$

$$\lambda_{5,6} = -1 \pm i \sqrt{(\zeta_0^{k_0} + d_2 \mu^2 + j_2^{k_0} k^2 - 5|\psi_{0k_0}|^2)(\zeta_0^{k_0} + d_2 \mu^2 + j_2^{k_0} k^2 - 3|\psi_{0k_0}|^2)}, \quad k \neq 0, \mu \neq 0. \quad (7.14)$$

With the stable state satisfying

$$(1 + i\zeta_0^{k_0})\psi_{0k_0} = i|\psi_{0k_0}|^2\psi_{0k_0} + f^{(0)}e^{-ik_0\Theta}, \quad (7.15)$$

similar to Ref. [55], we derive the position of the primary sidebands

$$d_2 \mu^2 \pm j_2 k^2 = 4|\psi_{00}|^4 + \sqrt{|\psi_{00}|^4 - 1} - \zeta_0^{k_0}, \quad \mu, k \neq 0, \quad (7.16)$$

$$d_2 \mu^2 = 2|\psi_{00}|^4 + \sqrt{|\psi_{00}|^4 - 1} - \zeta_0^{k_0}, \quad k = 0, \quad (7.17)$$

$$j_2 k^2 = 2|\psi_{00}|^4 + \sqrt{|\psi_{00}|^4 - 1} - [\zeta_0 - 2j], \quad \mu = 0, k_0 = 0 \quad (7.18)$$

with  $j_2 = (2\pi/N)^2 j$ . Eq. (7.16) indicates that the primary combs are formed on an ellipse (hyperbola) in the vicinity  $k_0 = 0$  ( $N/2$ ), equations (7.17, 7.18) reveal conventional position of the unstable solutions. Our analysis, similar to Ref. [156], shows that the modulationally unstable solutions form an ellipse (hyperbola) in the  $\mu - k$  space ( $k \neq 0, \mu \neq 0$ ).

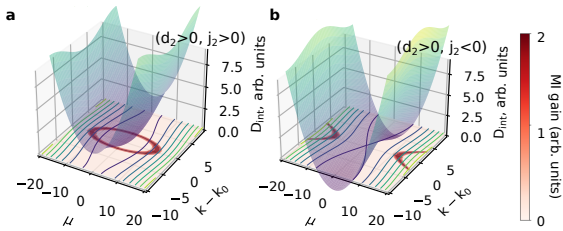


**Figure 7.2: Modulation instability gain lobes in chains of coupled resonators.** Hybridized dispersion profile shown as a surface in panel (a) for the elliptic and (b) for the hyperbolic regions. Contour plots in the  $k - \mu$  plane at  $D_{\text{int}} = 0$  highlight the different local topographies that result in the elliptic (a) or hyperbolic (b) modulation instability gain lobes depicted in red.

An example of the modulation instability gain lobes [Eq. (7.16)] is presented in Fig. 7.2(a,b) for both regions in case of  $d_2 = 0.04$  and  $j_2 = |J_2|/\kappa = 1$ . Fig. 7.2(a) reveals that the supermode corresponding to the excitation of all the resonators in-phase (anomalous sGVD) is unstable against small perturbations with  $\mu$  and  $k$  indexes that form an ellipse. The width and height of the ellipse are defined by pump power,  $d_2$ , and  $j_2$  coefficients that correspond to GVD and sGVD. In contrast, the state corresponding to the excitation of the neighboring resonators in the opposite phase (normal sGVD) is unstable against the perturbations with  $\mu$  and  $k$  forming a hyperbola (see Fig. 7.2(b)), showing that all the supermodes can experience

positive parametric gain.

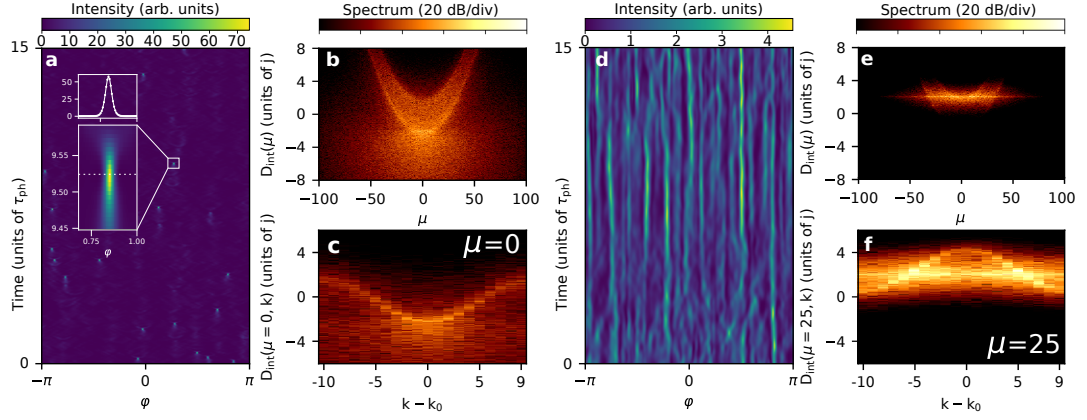


Figure 7.3: **Numerical reconstruction of the nonlinear dispersion relation in the elliptic and hyperbolic regions in the unstable regime.** Panels (a-c) correspond to the elliptic region ( $k_0 = 0$ ,  $d_2 > 0$ ,  $j_2 > 0$ ), panels (b-f) to the hyperbolic ( $k_0 = N/2$ ,  $d_2 > 0$ ,  $j_2 < 0$ ). Spatiotemporal diagrams of unstable states in 0th resonator are shown in (a) and (d); The corresponding nonlinear dispersion relation (NDR) in the elliptic region (b) demonstrates excitation of all the optical and spatial modes, whereas the NDR in the hyperbolic region (e) reveals that photon transfer between the spatial supermodes is suppressed in the vicinity of the pump mode  $\mu = 0$ ; The panes (c) and (f) represent the nonlinear supermode dispersion relation [Eq. (7.19)] of 0th comb line for the state in (a) and 25th comb line for the state in (d).

### 7.3.3 Wave collapse

We continue with the simulation of the coupled LLEs in Eq. (7.4) for 20 resonator chain and constant normalized coupling  $j = 10$  ( $j_2 = 1$ ). To simulate the temporal dynamics, we employ the step-adaptative Dormand-Prince Runge-Kutta method of Order 8(5,3) [179] and approximate the dispersion operator by the second-order finite difference scheme. We deliberately choose the pumping scheme allowing for exciting only a given mode. To trigger the FWM processes, we numerically scan the resonance with a fixed pump power and track field dynamics in all the resonators.

First, we focus on the investigation of the unstable behavior of the system pumping the elliptic ( $k_0 = 0$ ) and hyperbolic regions ( $k_0 = N/2$ ) with the pump  $f_\ell = 2.35$  and corresponding detunings  $\zeta_0 = 22.1$  and  $\zeta_0 = -17.0$ . In the former case, at a single resonator level we observe the random appearance of the pulses in different parts of the cavity and further their rapid compression, during which the peak amplitude significantly exceeds (60 times) the background level (cf. Fig. 7.3(a)). Computing the NDR, we observe the high photon occupancy of the pump region beneath the parabolas (cf. Fig. 7.3(b)), which indicates the presence of 2D dissipative nonlinear structures. Furthermore, all the hybridized parabolas are populated by the photons, meaning that supermodes from both dispersion regions are excited. To further confirm it, we reconstruct the supermode NDR for the 0th comb line ( $\mu_0 = 0$ ) for *all* resonators in the following way

$$NDR(\Omega, \mu_0, k) = \frac{1}{\sqrt{N_t N}} \sum_{\ell, n} \psi_{\mu_0 \ell}(t) e^{i(2\pi k \ell / N - \Omega t_n)}, \quad (7.19)$$

where  $\Omega$  is slow frequency,  $t_n = \Delta t n$  with  $\Delta t = T/N_t$  time-step,  $T$  is simulation time with  $N_t$  number of discretization points. The result is shown in Fig. 7.3(c). The whole cosine band structure is populated, including the region of the normal dispersion. In the opposite case, the spatiotemporal diagram [Fig. 7.3(d)] in hyperbolic region does not demonstrate any extreme events, showing slow (with respect to the elliptic case) incoherent dynamics. Comparing the NDR [Fig. 7.3(e)] with the elliptic case, we show less supermode occupancy. In the vicinity of  $\mu = 0$ , the normal sGVD suppresses the photon transfer along the  $k$  axis. Nevertheless, the photon transfer to other supermodes is stimulated with respect to eq. (7.16) that depicts MI gain lobes position, resulting in the generation of dispersive waves [122, 221]. Reconstructing the supermode NDR (Fig. 7.3(f)) for  $\mu = 25$  comb line [the average crossing position in Fig. 7.3(e)], we observe the predominant population of the center of the band.

We attribute this drastic difference in the chaotic dynamics to the effect called wave collapse [17, 222] that plays an important role in physics and leads to an effective mechanism of local energy dissipation. Our system, in the long-wavelength limit, can be modeled by 2D LLE with elliptic ( $\partial_{\varphi\varphi}^2 + \partial_{\theta\theta}^2$ ) or hyperbolic ( $\partial_{\varphi\varphi}^2 - \partial_{\theta\theta}^2$ ) dispersion (here  $\theta$  stands for the continuous coordinate along the circumference of the chain). Neglecting the pump and damping terms, we obtain the conservative 2D Nonlinear Schrödinger equation (NLSE), which in the elliptic case can result in full compression of a pulse to an infinitely small area concentrating there a finite amount of energy [218, 223]. Such pulse becomes ultra-broad in the spectral domain, and even the presence of dissipation in 2D LLE does not restrict this effect [224]. On the contrary, wave collapses do not occur in the 2D focusing NLSE with hyperbolic dispersion [223], signifying that it is the dispersion curvature that is responsible for the effect. Moreover, higher dispersion orders of the cosine limit the pulse compression in the elliptic region, regularizing the singularity [225, 226].

### 7.3.4 Coherent dissipative structures

#### Turing patterns.

As the different dispersion topographies result in completely different chaotic dynamics, the Turing patterns in the elliptic and hyperbolic regions differ in the same way. To observe the coherent structures, we first bring the system to into an unstable state. Stimulating the incoherent patterns, we further tune towards the monostable region ( $\zeta_0^{k_0} = \zeta_0 \mp 2j < \sqrt{3}$ ,  $+$  ( $-$ ) stands for  $k_0 = 0$  ( $N/2$ )) and obtain stable coherent structures in both regimes (Fig. 7.4). One can see that in the elliptic regime at  $|f_\ell| = 1.05$  and  $\zeta_0 = 20.5$ , we observe the formation of a Turing pattern [Fig. 7.4(a)] [227, 228, 220]. On a single resonator level, this corresponds to locked pulses [Fig. 7.4(b)] with a typical comb spectrum shown in Fig. 7.4(d). The corresponding 2D  $k$ - $\mu$  spectral profile in Fig. 7.4(c) shows that the sidebands form a disk, occupying the supermodes from both anomalous ( $|k - k_0| < 5$ ) and normal dispersion regimes. In the hyperbolic regime, at  $|f_\ell| = 2.35$  and  $\zeta_0 = -20.3$ , we observe a train of pulses in each resonator locked to each other [Fig. 7.4(e,f)]. The corresponding 2D spectral profile [Fig. 7.4(g)]



### 7.3 Chain of equally coupled resonators

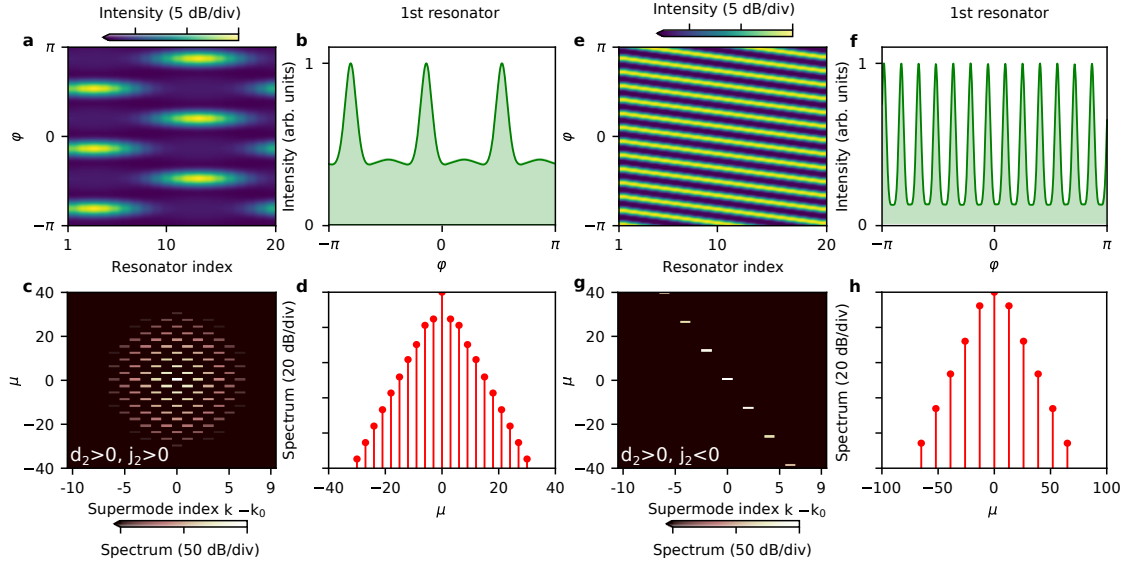
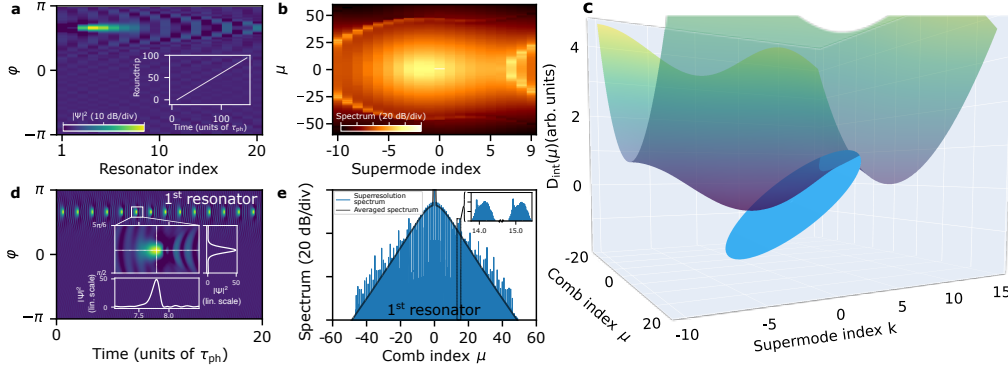


Figure 7.4: **Coherent dissipative structures in a driven nonlinear photonic ring lattice.** Panels (a-d) correspond to the elliptic region ( $k_0 = 0$ ,  $d_2 > 0$ ,  $j_2 > 0$ ), and panels (e-h) correspond to the hyperbolic ( $k_0 = N/2$ ,  $d_2 > 0$ ,  $j_2 < 0$ ). Spatiotemporal profiles of the mode-locked structures are shown in panels (a,e) with the corresponding field profile on a single resonator level in panels (b,f). The 2D spectral profiles of the states (a) and (e) obtained via Eq. (7.6) are presented in (c) and (g), respectively. The spectral profile in elliptic regime (c) forms a disk, whereas the spectrum of the pattern in hyperbolic regime (g) tends to align one of the asymptotes of the hyperbola depicting modulation instability gain in Eq. (7.16). The Fourier spectra of the states (b) and (f) are presented in (d) and (h).



**Figure 7.5: Localized 2D dissipative soliton in a chain of 20 resonators.** Instantaneous field profile in the chain of resonators and the corresponding 2D spectral profile in dB are shown in panels (a) and (b). Inset in (a) shows the roundtrip number of the soliton in time. c) Schematics of the soliton as a dispersionless structure (blue disk) beneath the hybridized dispersion surface (similar to Fig. 7.1a, spans over 1.25 of the Brillouin zone along  $k$  axis). Intersection between the soliton disk and the dispersion defines the position of the dispersive waves taking the form of a 'fish tail' in panel (b). d) Field dynamics on a single resonator level with an inset resolving one pulse. Color represents the amplitude in dB (see colorscale in panel (a)), the cross-sections of the inset are in linear scale normalized on the average amplitude in the cavity. The corresponding super-resolution and averaged spectrum are presented in panel (e).

forms a line in  $k$ - $\mu$  space, that qualitatively follows one of the asymptotes of the hyperbola that depicts modulation instability gain lobes in Fig. 7.2(b). Comparing the comb spectra at the 1st resonator Fig. 7.4(d)] with the elliptic case [Fig. 7.4(h)], one can notice that the state at the hyperbolic regime has a wider comb spectrum.

### Spatiotemporal two-dimensional dissipative soliton.

We also generate a localized 2D dissipative solitons [219] traveling along the circumference of the chain, which we describe in the following. To generate this spatiotemporal Kerr soliton (2D-DKS), we pump the 4th supermode in the elliptic regime (blue asterisk at  $k = 4$  in Fig. 7.1(b) with  $|f_\ell| = 2.35$  and  $\zeta_0 = 10.92$ , so the local dispersion has anomalous sGVD  $j_2 = j(\pi/10)^2 \cos 2\pi/5 = 0.30$  in addition to the non-zero supermode FSR  $j_1/2\pi = 0.1j \sin 2\pi/5 = 0.95$ . The obtained solution of the 2D-DKS corresponds to a continuously re-circulating spatial discrete soliton that forms an ellipse with a fish-like tail in the spectral domain cf. Fig. 7.5(a,b). Similar to Cherenkov radiation for conventional DKS, the disk-shaped soliton crosses the hybridized dispersion in the vicinity of the edge of the Brillouin zone (cf. Fig. 7.5(c)), resulting in the intensive generation of the dispersive waves, forming the fish-like spectrum, but presuming the soliton coherence. In the leading order, such 2D soliton is described by 2D LLE, therefore its approximate existence range can be inferred from Ref. [219].

On the single resonator level, the optical field envelope demonstrates breathing dynamics (Fig. 7.5(d)) due to the periodic appearance of the pulse in every individual resonator constituting the chain. Resolving the field envelope dynamics in time, one detects the periodic appearance of optical pulses and adjacent dispersive waves. Sampling this signal in time and computing the overall Fourier transform gives the so-called super-resolution spectrum shown in Fig. 7.5(e). The periodic nature of the signal reveals a typical comb spectrum, with the presence of a fine spectral structure around each comb line, shown in the inset of Fig. 7.5(e). These subcombs appear due to the breathing dynamics and emergence of the corresponding dispersive waves, and the number of spatial modes does not define the number of these subcombs. In fact, these subcombs correspond to just low-frequency breathing, which is also present in the single resonator case in the breathing regime [187]. The time-averaging of the signal yields a smooth spectral profile (solid line in Fig. 7.5(e)), indicating the periodic nature of the signal. Noteworthy, a similar (in terms of hybridized dispersion) 2D-DKS was observed in the edge state of the Haldane model [127]. Indeed, local dispersion profile of the edge-state is one-dimensional, and its dynamics should be close to the one we described in this chapter. However, the soliton coherence of the observed structure suffered from the presence of the bulk, which effect we investigate below with an example of the edge states of the SSH model.

## 7.4 Su-Schrieffer-Heeger model

Lattices of nonlinear resonators also provide a platform for studying topological systems, such as the Su-Schrieffer-Heeger (SSH) model or honeycomb lattices [214, 88], which have been extensively explored in the linear regime within photonics over the past decade. Nonlinear effects, including spatial solitons, have been studied and observed in arrays of coupled optical waveguides [115, 116, 117]. However, these nonlinear effects did not include parametric frequency conversion (i.e., parametric oscillations), which is the fundamental principle underlying soliton microcombs. A preliminary analysis of dissipative Kerr soliton (DKS) formation was conducted in Ref. [127], where the authors explored a Kerr nonlinear version of the photonic 2D Haldane model composed of coupled multi-mode optical microresonators with anomalous dispersion, coupled via link resonators. In this work, we shift our focus to the simpler SSH model, which, while simpler than the Haldane model, still provides insights into the nonlinear interactions of edge and bulk states. Notably, we demonstrate that this model possesses a band structure with different dimensionality: the edge state is 1D, while the bulk states are 2D (see Fig. 7.6a). This distinction allows for a direct comparison between the edge-state soliton and the conventional single-resonator DKS (see Fig. 7.6b).

First, we consider the staggered coupling system with periodic boundary conditions to simplify the analytical treatment. We introduce collective excitation amplitudes  $\psi_{\mu k}$  and  $\phi_{\mu k}$  for two

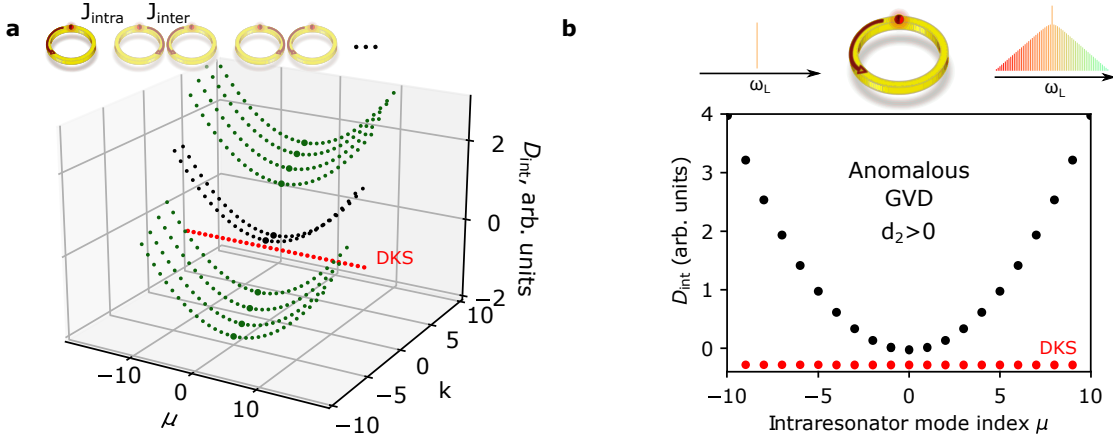


Figure 7.6: **Su-Schrieffer-Heeger model.** (a) Schematics of the Su-Schrieffer-Heeger model and its dispersion for a ten resonator chain. Each resonator mode from Fig. 7.1b hybridizes accordingly with the band structure, forming a total hybridized dispersion profile with the bulk (green dots) and the edge parabolas. Here the red line schematically represents the edge state DKS. (d) Schematics of a single Kerr microresonator and its chromatic dispersion. The red line represents the dissipative Kerr soliton (DKS).

sublattices constituting the chain.

$$\psi_{\mu k} = \frac{1}{2\pi\sqrt{N}} \int \sum_{\ell=1,3,5,\dots} A_{\ell} e^{2\pi i(\ell k/N + \mu\varphi)} d\varphi, \quad \phi_{\mu k} = \frac{1}{2\pi\sqrt{N}} \int \sum_{\ell=2,3,6,\dots} A_{\ell} e^{2\pi i(\ell k/N + \mu\varphi)} d\varphi, \quad (7.20)$$

where  $N$  is the number of unit cells. In contrast to the previous case, now the dynamics is described by a set of coupled equations on  $\psi_{\mu k}$ ,  $\phi_{\mu k}$

$$\begin{aligned} \frac{\partial \psi_{\mu k}}{\partial \tau} = & -(1 + i\zeta_0)\psi_{\mu k} - id_2\mu^2\psi_{\mu k} + i[J_{\text{inter}} + J_{\text{intra}}e^{-2\pi i k/N}]\phi_{\mu k} \\ & + \frac{i}{N} \sum_{\substack{k_1, k_2, k_3 \\ \mu_1, \mu_2, \mu_3}} \psi_{\mu_1 k_1} \psi_{\mu_2 k_2} \psi_{\mu_3 k_3}^* \delta_{\mu_1 + \mu_2 - \mu_3 - \mu} \delta_{k_1 + k_2 - k_3 - k} + \delta_{k, k_0} \delta_{\mu, 0} \tilde{f}_{k_0}^1, \end{aligned} \quad (7.21)$$

$$\begin{aligned} \frac{\partial \phi_{\mu k}}{\partial \tau} = & -(1 + i\zeta_0)\phi_{\mu k} - id_2\mu^2\phi_{\mu k} + i[J_{\text{inter}} + J_{\text{intra}}e^{2\pi i k/N}]\psi_{\mu k} \\ & + \frac{i}{N} \sum_{\substack{k_1, k_2, k_3 \\ \mu_1, \mu_2, \mu_3}} \phi_{\mu_1 k_1} \phi_{\mu_2 k_2} \phi_{\mu_3 k_3}^* \delta_{\mu_1 + \mu_2 - \mu_3 - \mu} \delta_{k_1 + k_2 - k_3 - k} + \delta_{k, k_0} \delta_{\mu, 0} \tilde{f}_{k_0}^2. \end{aligned} \quad (7.22)$$

According to Eq. (7.21), this system possesses two-dimensional dynamics as well, and the supermode dispersion can be obtained by diagonalizing the linear part of the system. The dynamics now incorporates interactions between two sublattices. Kerr nonlinearity acts within each of them, resulting into four-wave mixing processes on each of the dispersion surfaces. The coupling term can also lead to intraband mixing as shown in Ref. [122]. This property remains valid for open boundary conditions, where edge states can be found.

The edge eigenvalues  $\lambda_{\text{edge}}$  represent a 0D band. Thus, the hybridized dispersion profile corresponds to a conventional integrated dispersion of a single microresonator. The chain supports edge states in the case where inter-cell coupling  $J_{\text{inter}}$  is bigger than intra-cell coupling  $J_{\text{intra}}$  (shown in Fig. 7.6a). In the limit  $J_{\text{intra}} \rightarrow 0$  (trivial edge state [214]), the first resonator is completely decoupled from the chain, and its dynamics is described by conventional LLE. With the finite ratio  $J_{\text{intra}}/J_{\text{inter}} < 1$ , the formed band structure (see Fig. 7.6a) has upper and lower bulk regions with eigenmodes in the middle of the gap that correspond to the edge states [229]. With the chromatic dispersion taken into account, the nonlinear interactions happen on the hybridized dispersion surface. Due to the nontrivial topology, the hybridized dispersion of the bulk has a form of a two-dimensional surface, while the edge states have a 1D dispersion curve. To generate an edge soliton, one needs to pump the edge state ( $c_0$  is the corresponding amplitude in Eq. (7.3)). Neglecting the presence of the bulk states ( $c_j \ll c_0$ ), according to Eq. (7.3), the governing equation takes the form of a simple LLE. This analogy helps further to understand the soliton interaction with the bulk states. Generation of the edge soliton corresponds to the formation of the dispersionless line below the edge state parabola (schematically shown in Fig. 7.6a). If the width of the bandgap is large enough (effectively corresponds to the limit  $J_{\text{intra}}/J_{\text{inter}} \rightarrow 0$ ,  $J_{\text{inter}} \gg \kappa$ ), the dynamics of the soliton will be similar to the single-resonator dynamics, because the field will be still localized in the first ring. However, if the soliton line crosses the lower bulk band, additional photon transfer to the bulk modes will occur (a similar effect has already been observed in the system of just two coupled resonators considered in Ref. [122]). The photons scattered to the bulk will experience now 2D dynamics and can drastically affect the soliton stability and existence range.

To demonstrate this effect, we simulated an SSH chain of 10 resonators with typical parameters of  $\text{Si}_3\text{N}_4$ :  $\kappa_0/2\pi = 50$  MHz,  $D_2/2\pi = 4.1$  MHz, green  $J_{\text{inter}}/2\pi = 5$  GHz, FSR=182 GHz,  $J_{\text{intra}}/2\pi = 1$  GHz under 100 mW pump power (that corresponds to the normalized pump  $f^2 = 22$ , cf. Ref. [77] for the normalization) with critically coupled ( $\kappa_{\text{ex}} = \kappa_0$ ) first resonator. We excited the edge state resonance in the conventional way, scanning the pump laser from the blue- to red-detuned zone. We show the intracavity power in the first (blue line) and second (red line) resonators as a function of detuning in Fig. 7.7a along with the limit case of a decoupled single resonator (black line). As one can clearly see, the power dynamics in the first resonator generally has the same features as the decoupled resonator, but the soliton existence range ( $\delta\omega \approx 27.2\kappa/2$ ) is shortened in the case of the SSH chain ( $\delta\omega \approx 21.0\kappa/2$ ). In fact, the power in the second resonator reveals several resonance features with increased detuning. Investigating the field and spectral profiles of the DKS (detuning  $\delta\omega = 2\pi \cdot 1.48$  GHz =  $14.8\kappa/2$ ) itself in these resonators (cf. Fig. 7.7b,c), one can see that the soliton has a smooth sech profile in the first cavity, while there is a strong background modulation in the second with the soliton amplitude 200 times smaller. The reconstructed NDRs (Fig. 7.7d,e) reveal that the soliton, formed below the edge parabola crosses the lower bulk modes that lead to the generation of the dispersive waves in the second resonator, breaking the topological protection of the edge state. While here we presented a case of moderate edge-bulk interaction, stronger interactions can occur for spectrally broader solitons (smaller ratio  $D_2/\kappa$ ) or narrow bandgaps.

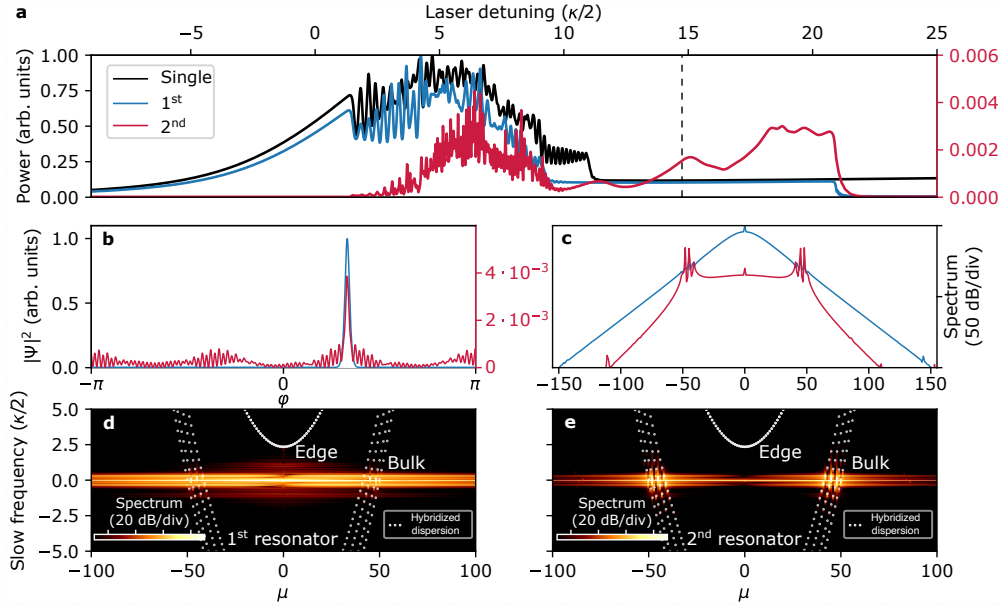


Figure 7.7: **Soliton dynamics at the edge state of the Su-Schrieffer-Heeger model (SSH).** (a) Intracavity power as a function of detuning in the first (solid blue line), second resonators (solid red line), and for the first resonator completely decoupled from the chain (solid black line). Vertical dashed line shows the detuning at which the soliton state is resolved below. (b,c) Temporal and spectral profiles of the soliton in the first (blue lines) and second (red lines) resonators normalized on the peak power in the first resonator. (d,e) The corresponding nonlinear dispersion relations. White dots represent the hybridized dispersion in the linear regime.

Nevertheless, our conclusions remain valid for a smaller gap size and can be generalized for higher dimension topological lattices: due to the presence of the other bands, the generated edge-state soliton (be it DKS or 2D-DKS) induces edge-to-bulk scattering that influences soliton stability and can result in its temporal decoherence.

## 7.5 Conclusion

We theoretically described nonlinear interactions via four-wave mixing (i.e. parametric oscillations) in lattices of driven photonic microresonators. We showed the hybridization of the chromatic dispersion with the  $N$ -spatial dimensional band structure gives rise to an effective  $(N+1)$ -dimensional dispersion surface that governs the FWM processes with the conservation law defined by the structure of the lattice's eigenfunctions. Further, we analytically and numerically explored the nonlinear dynamics of the 1D band in a chain of equally coupled resonators. We demonstrated that this system possesses a 2D dispersion surface and can be described in the long wavelength limit by the 2D LLE at its local extrema. Different parts of the dispersion surface correspond to two fundamentally different regimes of operation: elliptic and hyperbolic. This results in different local dispersion topography. Simulating the full set of coupled LLEs, we demonstrated nonlinear effects inherent to 2D systems which include Turing pattern formation, 2D spatial-temporal dissipative Kerr solitons, and wave collapses in the chaotic state. Considering the SSH model, we demonstrated that 0D bands that correspond to the edge state can be approximated by the conventional 1D-LLE. However, the coherence and existence range of the generated DKS is strongly perturbed by the DKS-induced edge-bulk mixing, breaking the protection that is present in the linear case. In summary, our theory sheds light on nonlinear interactions in integrated photonic lattices and will be helpful to guide future experimental investigations of multi-mode systems with complex band structures, and highlight the limitation of topological protection when it comes to the formation of Kerr frequency combs in lattices.





## 8 Conclusion and Outlook

The thesis reports on the experimental and theoretical investigation of nonlinear interactions in synthetic and real lattices of photonic microresonators. The first part, including chapter 1 and 2, covers effects of Kerr nonlinearity in electro-optic (EO) and dispersion modulated cavities respectively. The second part, chapters 3, 4, 5, 6, and 7 is devoted to the study of four-wave mixing processes in spatial lattices of resonators.

In synthetic frequency crystals created by EO phase modulation, we demonstrate the emergence of confined modulation instability and show that conventional dissipative Kerr solitons are formed in the stop-band of the synthetic band structure, i.e., in the region, where synthetic Bloch waves do not propagate along the lattice and nonlinear dynamics is determined purely by four-wave mixing processes. However, synthetic Bloch waves define the nonlinear dynamics of the cavity excited in the center of the synthetic band structure. We demonstrate that with increasing EO coupling between the adjacent modes, conventional EO frequency combs emerge as novel states termed *band solitons*. However, with increasing pump power, these coherent structures destabilize, resulting in coexistence of stable continuous wave (CW) solution in one part of the cavity and chaotic dynamics in another. Moreover, for 2D synthetic crystal, emergence of *chimera-like* states that exist due to the simultaneous presence of stop and propagation bands of the synthetic band structure. Investigating dispersion-modulated microresonators in chapter 2, we thoroughly analyzed its *Floquet dynamics* and demonstrated emergence of a slow synthetic frequency dimension. We show the 2D nature of four-wave mixing interactions in such lattices and analyze CW solution stability that results in primary sideband generation in normal and anomalous dispersion resonators. As a result, we observe *Faraday instability* in such systems as an efficient mechanism of optical microcombs broadening.

Second part of this thesis, covering chapters 3, 4, 5, 6, and 7 reports on the spatial lattices of microresonators. In chapter 3, we present an approach of using two coupled resonators with opposite dispersions for optical parametric oscillators. We investigate analytically the frequency conversion mechanism and verify it experimentally with  $\text{Si}_3\text{N}_4$  microresonators. Chapter 4 is devoted to the investigation of quiet points for low loss microwave generation

## Chapter 8. Conclusion and Outlook

---

using dissipative Kerr solitons in coupled resonator system. We present an approach how to reduce the noise transduction mechanism from the pump laser to the soliton repetition rate, and demonstrate how to expand the quiet point operation bandwidth. In chapter 5, we explore the variety of dissipative Kerr solitons states in a photonic dimer in two coupling regimes: split resonance and dissipation. We discuss in detail soliton breather and hopping states, discover the soliton crystal and dark soliton states. In chapter 6, we study avoided mode crossings in coupled resonators as a limiting factor for coherent structures generation. We discover that for conventional ring resonators, the coupling region results in the excitation of the higher order modes that lead to the enhanced strength of the mode crossings for lower energy states and suppressed for higher ones. We demonstrate this effect with generation of dissipative Kerr solitons in a chain of four microresonators and discuss the protection against mode crossing of the edge state in the Su-Schrieffer-Heeger model. Chapter 7 concludes the thesis with a theory of nonlinear interactions in coupled resonator lattices. We investigate in detail one-dimensional chains and discover a plethora of nonlinear phenomena such as *spatio-temporal 2D-DKS*, *elliptic* and *hyperbolic* Turing patterns, *the regularized wave collapse*, *edge-state DKS*, and *nonlinearly induced edge-bulk scattering*. Our findings encompass rich variety of nonlinear phenomena observed in many physical systems and will be helpful to guide future investigations of multi-mode systems with complex band structures, their phase transitions and frequency combs generation with a potential applications to quantum optics, metrology, sensing, etc.

Below, the author discusses possible future directions for development of the topics covered in this thesis.

**Synthetic Dimensions.** Photonics provides convenient means to emulate and test various systems with high accuracy. For instance, optical fibers have often been used to examine the nonlinear Schrödinger equation and compare its dynamics with deep water waves. Similarly, synthetic dimensions have the potential to investigate different Hamiltonians that are challenging to realize on alternative platforms. Systems with non-trivial topologies are of particular interest, as they often necessitate three or more dimensions [230]. In this thesis, we have focused on two approaches to extending dimensionality: through phase and dispersion modulations. However, there are numerous ways to explore even more complex systems, such as an EO-modulated cavity with clockwise and counter-clockwise coupling [104], or incorporating an additional amplitude modulation, resulting in a non-Hermitian topological system [111]. Four-wave mixing interactions in such systems can reveal different nonlinear phenomena, including various dissipative structures, which may also be of interest for applied photonics.

**Coupled Resonator Lattices.** Integrated coupled resonator networks, such as those fabricated with silicon nitride, offer a versatile platform for studying the rich physics and nonlinear dynamics at the intersection of topological and nonlinear photonics [118]. For instance, the supermodes of a lattice lead to dispersion hybridization and natural filtering due to their different spatial mode profiles. These effects hold potential for applications in broadband

---

frequency comb engineering and optical parametric oscillators for optical clocks [125], as well as for quantum photonics [231]. Recent demonstration of the self-injection locked dissipative Kerr solitons in coupled resonators using CMOS-compatible fabrication techniques also expands the engineering techniques for scalable production of optical microresonator frequency combs [125]. Additionally, as demonstrated in this thesis with the phenomenon of regularized wave collapse, extended dimensionality can result in the generation of chaotic states with extreme events. Such states could be applied to sensing, akin to the chaotic states used for distance ranging as presented in Ref. [65]. Overall, coupled resonator lattices possess significant potential in nonlinear optics for investigation various nonlinear phenomena with possible applications in future photonic technologies.



# A Appendix to chapter 3

## A.1 Pump suppression

Let's estimate the lower limit of pump suppression. For simplicity, we introduce a normalized version of the LLE, considering a CW-type solution and neglecting the nonlinear terms:

$$\begin{aligned}\frac{d}{dt}\psi_a &= -[1 + i(\xi_0 + \frac{1}{2}\delta_n)]\psi_a + iJ_n\psi_b + f \\ \frac{d}{dt}\psi_b &= -[\kappa_n + i(\xi_0 - \frac{1}{2}\delta_n)]\psi_b + iJ_n\psi_a,\end{aligned}\tag{A.1}$$

where the subscript index  $n$  stands for normalization by  $\kappa_A/2$ ,  $\kappa_n = \kappa_B/\kappa_A$ ,  $J_n = 2J/\kappa_A$ .

Alternatively, we can rewrite Eq. A.1 in matrix form, considering the stationary case in the symmetrically coupled dimer:

$$\begin{pmatrix} 0 \\ 0 \end{pmatrix} = \mathcal{M} \begin{pmatrix} \psi_a \\ \psi_b \end{pmatrix} + \begin{pmatrix} f \\ 0 \end{pmatrix},\tag{A.2}$$

where

$$\mathcal{M} = \begin{pmatrix} -1 - i\left(\xi_0 + \frac{\delta_n}{2}\right) & iJ_n \\ iJ_n & -1 - i\left(\xi_0 - \frac{\delta_n}{2}\right) \end{pmatrix}.\tag{A.3}$$

The solution of this system is given by:

$$\begin{pmatrix} \tilde{\psi}_a \\ \tilde{\psi}_b \end{pmatrix} = -\mathcal{M}^{-1} \begin{pmatrix} f \\ 0 \end{pmatrix} = \begin{pmatrix} -\frac{f(-1 - i(\xi_0 - \frac{\delta_n}{2}))}{\frac{\delta_n^2}{4} + J_n^2 - \xi_0^2 + 2i\xi_0 + 1} \\ \frac{ifJ_n}{\frac{\delta_n^2}{4} + J_n^2 - \xi_0^2 + 2i\xi_0 + 1} \end{pmatrix}.\tag{A.4}$$

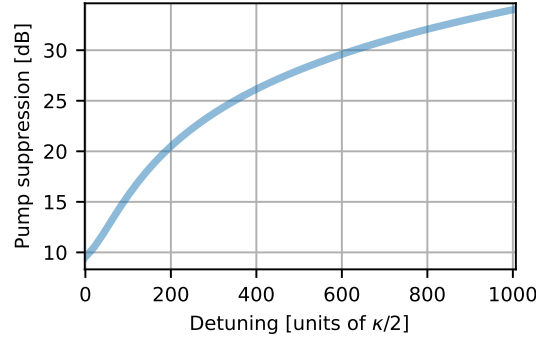


Figure A.1: **Pump suppression at the drop-port output.**

We define pump suppression as follows:

$$\eta = \left| \frac{S_{\text{out},1}}{S_{\text{out},2}} \right|^2 = \frac{|f - \psi_a|^2}{|\psi_b|^2}. \quad (\text{A.5})$$

Taking the normalized field amplitude at the center of the pumped resonance, we obtain:

$$\eta = \frac{3\delta_n \sqrt{\delta_n^2 + 4J_n^2} + 5\delta_n^2 + 18J_n^2 + 8}{2J_n^2}. \quad (\text{A.6})$$

The lower limit of the pump suppression given by Eq. A.6 is depicted in Fig. A.1. The pump detuning is chosen to be at the position of the resonance. It can be observed that when  $\delta_n \gg J_n$ , Eq. A.6 can be simplified as  $\eta \approx 4\delta_n^2/J_n^2$ . This value reaches 34 dB in the case of a large detuning, which corresponds to the largest signal-to-pump frequency offset presented in Fig. 3.3b in chapter 3.

## A.2 Resonators design

The search for the geometric parameters of resonators with different dispersion types was conducted using COMSOL Multiphysics. In the simulation, we varied the radius and width of the micro-ring, while keeping the height fixed. The simulated parameter is the effective refractive index for the fundamental TE mode, from which we calculated the free spectral range (FSR) and  $D_2/2\pi$ . The map displaying  $D_2/2\pi$  is presented in Fig. A.2a. The black lines in the figure denote equal FSR values in GHz. The final design choice was guided by two requirements. Firstly, the rings needed to possess different signs for  $D_2$ . Secondly, they were required to share an equal FSR. The significance of equal FSR is elucidated in Figs. A.2b and c. The hybridized dispersion with precisely matched FSR is portrayed in Fig. A.2b. The outcome depicted in Fig. A.2c corresponds to dispersions with a 1.1 GHz difference in FSR. Even such a minor difference (which constitutes less than 1 percent of FSR) leads to a deviation of the hybridization mode from the desired configuration.

### A.3 Experimental setup and uncoupled dispersion

Our experimental setup operates in two distinct regimes. The first regime, referred to as linear measurements, involves dispersion characterization [203], allowing for the measurement of free spectral range (FSR) and integrated dispersion. The second regime, designed for nonlinear optical pumping and measurement of optical spectra from generated light, is where the action takes place. In this second channel, a pump with a tunable wavelength sourced from an external-cavity diode laser is amplified by an erbium-doped fiber amplifier and subsequently coupled to the dimer. The generated signal is then subjected to analysis using an optical spectrum analyzer. The setup also incorporates a photodiode connected to an oscilloscope to facilitate the measurement of transmission traces. In both of these operational regimes, the heater elements of the microrings are powered by a DC power source, an essential aspect for tuning the interring detuning. With no power applied to the heaters, the detuning is significant enough to consider the rings optically uncoupled. The integrated dispersion measurements for normal and anomalous rings with zero power applied are depicted in Fig. A.3b and c. Notably, the fitting curves derived from these measurements are used for the analysis of hybridization regimes in Fig. 3.3c-e in chapter 3. According to the fitted curves, the  $D_2/2\pi$  values are 12.56 MHz and -1.15 MHz for the normal and anomalous rings, respectively. Additionally, the measured FSR deviation amounts to 0.1 GHz.

### A.4 Detuning calibration

Experimental data regarding the detuning-to-heaters voltage relationship is directly incorporated into the main experimental results depicted in Fig. 3.3b of the primary paper. In this experiment, each spectrum corresponds to a distinct heater voltage. Consequently, the original outcome showcases voltage on the y-axis (refer to Fig. A.4a). Since the pumping was executed on the same ring as the one undergoing heating, adjustments to the pump laser's frequency were essential for every voltage tuning iteration. As a result, by monitoring the shift of the pump laser (manifested as the center lines of the spectra in Fig. A.4a), we can deduce the conversion scale from voltage to an absolute frequency value. For translation of this data into a relative interring detuning, a preliminary condition is required. We chose a voltage value (2050 mV) that would yield zero relative detuning between the dispersions. The outcome of this process is presented in Fig. A.4b, wherein we applied a linear approximation. This approximation was subsequently employed to recompute each voltage from Fig. A.4, leading to the primary result showcased in Fig. 3.3b in chapter 3

## Appendix A. Appendix to chapter 3

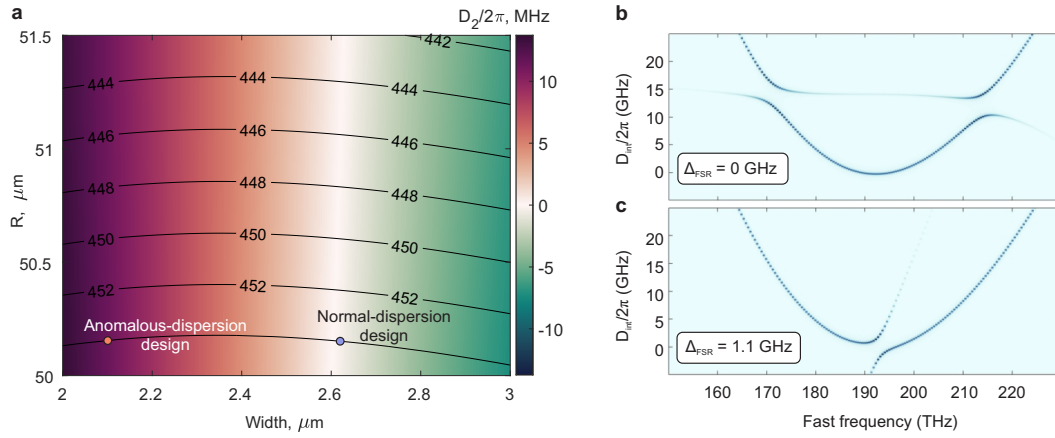


Figure A.2: **a** Normalized dispersion parameters map for different resonator widths and radii, and fixed height. Black lines are equal-FSR lines (labeled in GHz). Dots highlight the final design. **b** Hybridized dispersion for the chosen resonator parameters. The top figure shows the case with equal FSRs. In the lower one, an artificially introduced FSR difference of 1.1 GHz is depicted.

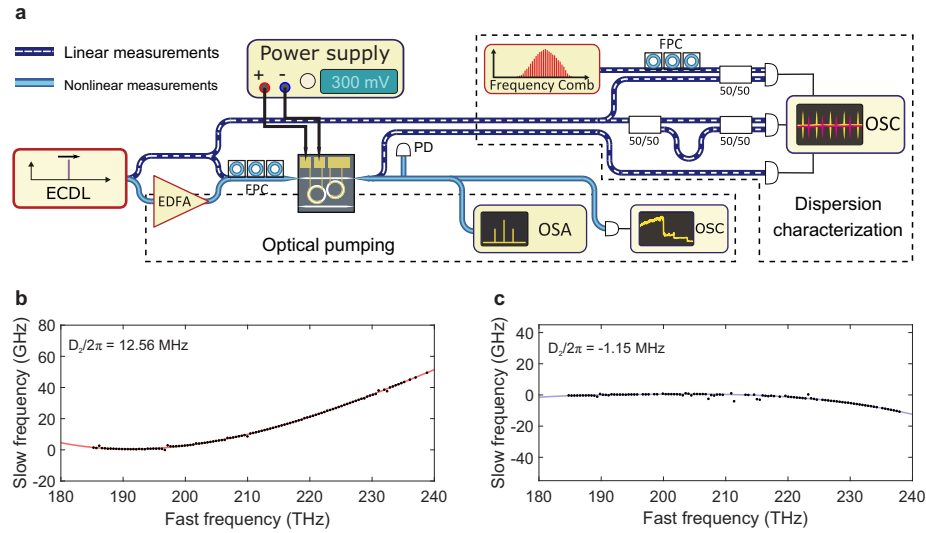


Figure A.3: **a** Experimental setup. **b,c** Fitted integrated dispersion (solid lines) for dispersion characterization data (dots) for anomalous- and normal-dispersion resonators, respectively.



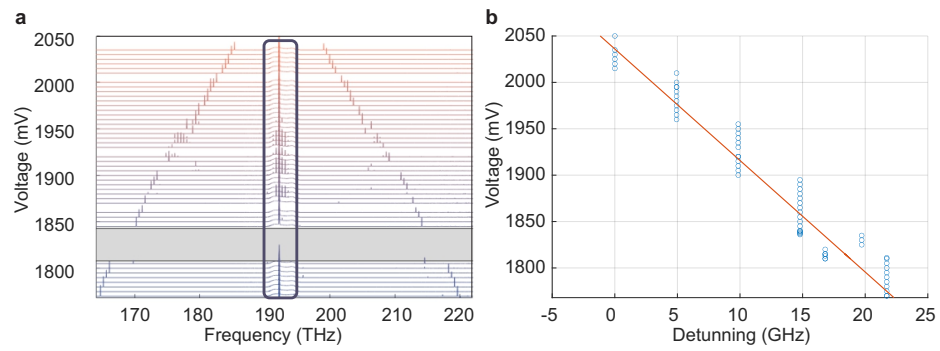


Figure A.4: **a** Measured spectra for different voltages. **b**



# B Appendix to chapter 4 — Quiet points in a coupled resonator system

## B.1 Newton-Raphson method

In this section, we illustrate the application of the Newton-Raphson (NR) method for finding stationary solutions of the Lugiato-Lefever equation (LLE). Initially, we consider the simplest form of the LLE as follows:

$$\frac{\partial \Psi}{\partial t} = i d_2 \frac{\partial^2 \Psi}{\partial \varphi^2} + i |\Psi|^2 \Psi - (1 + i \zeta_0) \Psi + f. \quad (\text{B.1})$$

In general, the NR method is utilized to determine approximate solutions for an arbitrary system of equations, denoted as  $F(x) = 0$ . Consequently, stationary solutions of the LLE (where  $\partial \Psi / \partial t = 0$ ) can also be found using this approach. The task involves solving the system  $F(\mathbf{X}) = 0$ , with the vector  $\mathbf{X}$  defined as  $\mathbf{X} = (\Psi, \Psi^*)^T$ , where the field envelope  $\Psi$  is considered as a variable. To locate a solution, an initial guess  $\Psi_0$  must be defined, followed by the computation of the corresponding Jacobian matrix:

$$J(\mathbf{X}_0) = \begin{pmatrix} -(1 + i \zeta_0) + i d_2 \frac{\partial^2}{\partial \varphi^2} + i 2 |\Psi_0|^2 & i \Psi_0^2 \\ -i (\Psi_0^2)^* & -(1 - i \zeta_0) - i d_2 \frac{\partial^2}{\partial \varphi^2} - i 2 |\Psi_0|^2 \end{pmatrix} \quad (\text{B.2})$$

Subsequently, the first approximation  $\mathbf{X}_1$  can be obtained using the equation:

$$\mathbf{X}_1 = \mathbf{X}_0 - J^{-1} \cdot F(\mathbf{X}_0). \quad (\text{B.3})$$

To refine the solution, the Jacobian is recalculated using the computed solution  $\mathbf{X}_1$ . This iterative process can be expressed as:

$$\mathbf{X}_{k+1} = \mathbf{X}_k - J^{-1} \cdot F(\mathbf{X}_k) \quad (\text{B.4})$$

## Appendix B. Appendix to chapter 4 — Quiet points in a coupled resonator system

---

This iteration continues until convergence to a solution  $\mathbf{X}_K$  at iteration  $K$ , with a specified tolerance  $\varepsilon$  such that:

$$\|\mathbf{X}_K - \mathbf{X}_{K-1}\|_2 < \varepsilon, \quad (\text{B.5})$$

where  $\|\cdot\|_2$  represents the  $L^2$  norm.

In this section, we demonstrate how the Newton-Raphson (NR) method is extended to find stationary solutions in cases where the soliton's group velocity ( $v_g$ ) depends on various parameters due to the presence of effects like Raman scattering or higher-order dispersion terms. In such scenarios,  $v_g$  becomes a variable in the iteration process and is included in the vector  $\mathbf{X} = (\Psi, \Psi^*, v_g)^T$ . To handle this variable, an additional equation is introduced to fix the soliton  $\Psi$  at a specific axial coordinate  $\varphi_{\max}$ , which defines the position of the maximum amplitude of the wave packet  $|\Psi|^2$ . The chosen equation for this purpose is:

$$\text{Re} \left( \frac{\partial \Psi}{\partial \varphi} \right) \bigg|_{\varphi=\varphi_{\max}} = 0. \quad (\text{B.6})$$

The LLE in this case needs to be modified accordingly, as shown in Eq. (4.1), to incorporate  $v_g$  into the equation. For the specific example of Eq. (4.1), the NR formulation takes the following form:

$$F(\mathbf{X}) = \begin{bmatrix} \tilde{F}_{1,1} & \tilde{F}_{1,2} & \tilde{F}_{1,3} \\ \tilde{F}_{2,1} & \tilde{F}_{2,2} & \tilde{F}_{2,3} \\ \tilde{F}_{3,1} & \tilde{F}_{3,2} & \tilde{F}_{3,3} \end{bmatrix} \begin{bmatrix} \Psi \\ \Psi^* \\ v_g \end{bmatrix} \quad (\text{B.7})$$

Here, the matrix elements are defined as shown below:

---

## B.2 Dynamical simulation of the noise transduction.

$$\begin{aligned}
\tilde{F}_{1,1} &= -1 - i(\zeta_0 - \frac{1}{2}\partial_\theta^2 + \Delta_{\tilde{\mu}} e^{i\tilde{\mu}\theta} \hat{\mathcal{F}}_{\tilde{\mu}}) \\
\tilde{F}_{1,2} &= i\psi^2(1 - \tau\partial_\theta) - i\tau\psi\partial_\theta\psi \\
\tilde{F}_{1,3} &= \tilde{F}_{2,3} = \partial_\theta \\
\tilde{F}_{2,2} &= (\tilde{F}_{1,1})^* \\
\tilde{F}_{2,1} &= (\tilde{F}_{1,2})^* \\
\tilde{F}_{3,1} = \tilde{F}_{3,2} &= \frac{1}{2} \int_{\mathcal{R}} d\theta \delta(\theta - \theta_{max}) \partial_\theta \\
\tilde{F}_{3,3} &= 0 \\
\hat{\mathcal{F}}\Psi &= \int d\theta \Psi e^{-i\mu\theta} = \Psi_\mu \\
\hat{\mathcal{F}}^{-1}\Psi_\mu &= \sum_{\mu} \Psi_\mu e^{i\mu\theta} = \Psi \\
\hat{\mathcal{F}}_{\tilde{\mu}}\Psi &= \sum_{\mu} \delta_{\mu,\tilde{\mu}} \hat{\mathcal{F}}\Psi = \Psi_{\tilde{\mu}}
\end{aligned}$$

Please note that the axial coordinate  $\varphi$  is transformed to fast time  $\theta$  through the transformation  $\theta = \sqrt{\frac{\kappa}{2D_2}}\varphi$ . The Jacobian matrix takes the form:

$$J(\mathbf{X}) = F(\mathbf{X}) + \begin{bmatrix} \hat{\Delta}(\Psi) & 0 & 0 \\ 0 & \hat{\Delta}^*(\Psi) & 0 \\ 0 & 0 & 0 \end{bmatrix} \quad (\text{B.8})$$

where  $\hat{\Delta}(\Psi) := 2i|\Psi|^2 + \nu_g\partial_\theta - i\tau(\partial_\theta|\Psi|^2 + |\Psi|^2\partial_\theta + \Psi\partial_\theta\Psi^*)$ . With these definitions, the iteration steps can be performed as defined in Eq. (B.4).

## B.2 Dynamical simulation of the noise transduction.

The dynamical simulations have been carried out with the step-adaptative Dormand-Prince Runge-Kutta method of Order 8(5,3) [179] with PyCORE described in detail in appendix E, hard seeded an approximate DKS solution. The input pump phase noise has been obtained from a linearization of the data of the power spectral density data of Toptica CTL 1550 Laser,  $S_\phi^{\text{in}}$ . In particular, it has been implemented through a detuning noise term  $\zeta_0(t)$  obtained as

$$\zeta_0(t) = \alpha \hat{\mathcal{F}}_t(\sqrt{\nu^2 S_\phi^{\text{in}}(\nu)} e^{ix(\nu)}), \quad (\text{B.9})$$

where a uniformly distributed random phase  $x(\nu)$  has been added to each frequency to obtain a random realization of the detuning noise and coefficient  $\alpha$  normalizes the standard deviation of the pump detuning. We used the following simulation parameters [77]:  $n_0 = 1.9$ ,  $n_2 = 2.4\text{e-}19$   $\text{m}^2/\text{W}$ ,  $\text{FSR} = 95.4$  GHz,  $\omega_0/2\pi = 192$  THz, waveguide dimensions:  $1.5 \times 0.85$   $\mu\text{m}$ ,  $\kappa_0/2\pi = 100$

## Appendix B. Appendix to chapter 4 — Quiet points in a coupled resonator system

---

MHz,  $\kappa_{\text{ex}}/2\pi = 100$  MHz,  $\tau_R = 1$  fs,  $D_2/2\pi = 1.3$  MHz. Output field in real units for the case of critical coupling ( $\kappa_{\text{ex}} = \kappa_0$ ):

$$P_{\text{out}}(\varphi, t) = \hbar\omega_0 \frac{\kappa_{\text{ex}}^2}{g_0} |f - \psi|^2 \quad (\text{B.10})$$

Spectrogram:

$$P_\mu(t) = \hat{\mathcal{F}}_\mu P_{\text{out}} \quad (\text{B.11})$$

where,  $\hat{\mathcal{F}}_\mu$  is the operator taking the  $\mu$ -th Fourier component of a function (the power in this case), as defined in the previous section. The phase of the first comb line (repetition rate phase):

$$\phi(t) = \arg[P_1(t)], \quad (\text{B.12})$$

where  $\arg[P_1(t)]$  denotes the phase of the first complex Fourier component of the detected optical power. The spectrum of phase noise:

$$S_\phi(\nu) = |\hat{\mathcal{F}}_\nu \phi(t)|^2 \quad (\text{B.13})$$

The transduction coefficient has been computed as:

$$\text{PM2PM} = 10 \log_{10} \frac{S_\phi}{S_\phi^{\text{in}}} \quad (\text{B.14})$$

We point out, in this analysis we assume an ideal photodetector, neglecting so its actual response function. As for the Newton-Raphson method, we discretized the fast time axis (i.e. azimuthal coordinate) in  $N_\psi = 2^{10}$  points while the slow time in  $N_t = 20000$  points. In addition, in order to obtain a sensitivity of the order of the kHz, we simulate the soliton dynamics for 1 ms. TRN phase noise limit is calculated using methods and parameters presented in Ref. [232]

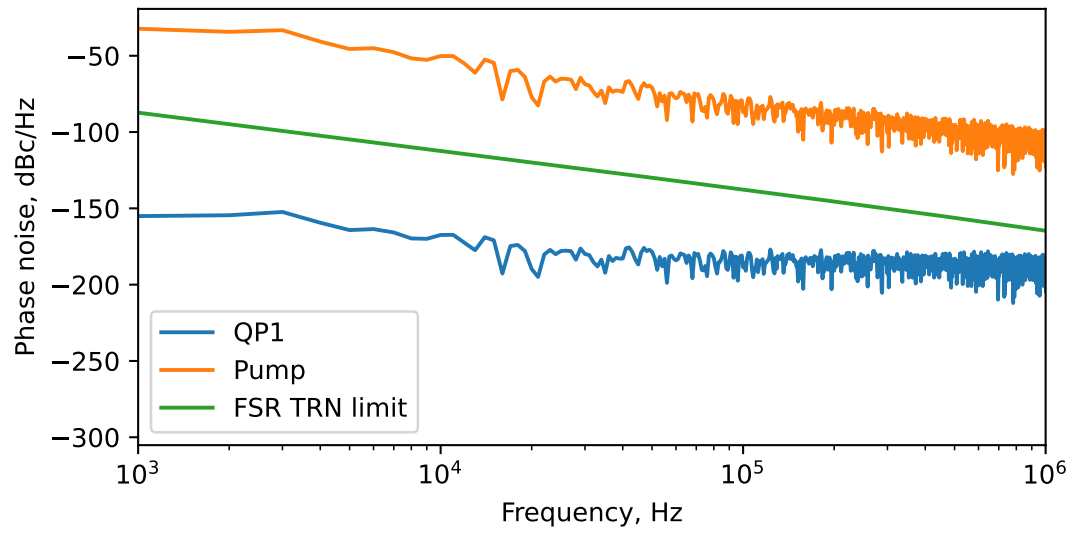


Figure B.1: SSB phase noise plot of a DKS at QP1 compared to pump laser phase noise and TRN phase noise limit.





# C Appendix to chapter 5 — Dissipative kerr solitons in dimers

## C.1 Projection into supermodes

### C.1.1 Single longitudinal mode closed system

In order to analyze Eq. 5.1, it is first simplified to a non-linear two level system isolated from the environment, that is

$$\begin{aligned}\frac{d}{dt}A &= -i\left(\omega_0 + \frac{\delta}{2}\right)A + iJB + ig_0A|A|^2 \\ \frac{d}{dt}B &= -i\left(\omega_0 - \frac{\delta}{2}\right)B + iJA + ig_0B|B|^2.\end{aligned}\tag{C.1}$$

For  $g_0 = 0$ , the system can be diagonalized by defining the variables:

$$A_s = \alpha A + \beta B \quad A_{as} = \beta A - \alpha B \tag{C.2}$$

$$\alpha = \frac{\sqrt{1-d}}{\sqrt{2}} \quad \beta = \frac{\sqrt{1+d}}{\sqrt{2}}, \tag{C.3}$$

where  $d = \delta/\Delta\omega$  and  $\Delta\omega = \sqrt{4J^2 + \delta^2}$ , such that the Eq. C.1 becomes

$$\begin{aligned}\frac{d}{dt}A_s &= -i\left(\omega_0 - \frac{\Delta\omega}{2}\right)A_s + ig_0(\alpha A|A|^2 + \beta B|B|^2) \\ \frac{d}{dt}A_{as} &= -i\left(\omega_0 + \frac{\Delta\omega}{2}\right)A_{as} + ig_0(\beta A|A|^2 - \alpha B|B|^2).\end{aligned}\tag{C.4}$$

We expand the non-linear part of Eq. C.4 using  $A = \alpha A_s + \beta A_{as}$  and  $B = \beta A_s - \alpha A_{as}$ . For the S

mode, for example,

$$\begin{aligned}
 \alpha A|A|^2 + \beta B|B|^2 = & \\
 (\alpha^2|\alpha|^2 + \beta^2|\beta|^2)A_s|A_s|^2 + 2\alpha\beta(|\alpha|^2 - |\beta|^2)A_{as}|A_s|^2 & \\
 + (\alpha^3\beta^* - \beta^3\alpha^*)A_s^2A_{as}^* + 2(\alpha^2|\beta|^2 + \beta^2|\alpha|^2)A_s|A_{as}|^2 & \\
 + (\beta^2|\alpha|^2 + \alpha^2|\beta|^2)A_{as}^2A_s^* + \alpha\beta(|\beta|^2 - |\alpha|^2)A_{as}|A_{as}|^2. & 
 \end{aligned} \tag{C.5}$$

Therefore, Eq. C.4 can be rewritten as

$$\begin{aligned}
 \frac{d}{dt}A_s = & -i(\omega_0 - \frac{\Delta\omega}{2})A_s + ig_0[\frac{1}{2}(1+d^2)A_s|A_s|^2 \\
 & - d\sqrt{1-d^2}A_{as}|A_s|^2 - \frac{1}{2}d\sqrt{1-d^2}A_s^2A_{as}^* \\
 & + (1-d^2)A_s|A_{as}|^2 + \frac{1}{2}(1-d^2)A_{as}^2A_s^* \\
 & + \frac{1}{2}d\sqrt{1-d^2}A_{as}|A_{as}|^2] \\
 \frac{d}{dt}A_{as} = & -i(\omega_0 + \frac{\Delta\omega}{2})A_{as} + ig_0[-\frac{1}{2}d\sqrt{1-d^2}A_s|A_s|^2 \\
 & + (1-d^2)A_{as}|A_s|^2 + \frac{1}{2}(1-d^2)A_s^2A_{as}^* \\
 & + d\sqrt{1-d^2}A_s|A_{as}|^2 + \frac{1}{2}d\sqrt{1-d^2}A_{as}^2A_s^* \\
 & + \frac{1}{2}(1+d^2)A_{as}|A_{as}|^2].
 \end{aligned} \tag{C.6}$$

### C.1.2 Derivation with complex inter-resonator detuning

The same analysis can be adapted when drive and dissipation are included. However, the inter-resonator detuning takes a complex component accounting for different loss rates between the resonators. We therefore start with

$$\begin{aligned}
 \frac{d}{dt}A = & \left[ -i(\omega_0 + \frac{\delta}{2}) - \frac{\kappa_0 + \kappa_{ex,1}}{2} \right] A + iJB + ig_0A|A|^2 + \sqrt{\kappa_{ex,1}}S_{in} \\
 \frac{d}{dt}B = & \left[ -i(\omega_0 - \frac{\delta}{2}) - \frac{\kappa_0 + \kappa_{ex,2}}{2} \right] B + iJA + ig_0B|B|^2,
 \end{aligned} \tag{C.7}$$

and define  $\Delta\kappa_{ex}$  to satisfy

$$\begin{aligned}
 \kappa_{ex,1} &= \kappa_{ex} + \frac{1}{2}\Delta\kappa_{ex} \\
 \kappa_{ex,2} &= \kappa_{ex} - \frac{1}{2}\Delta\kappa_{ex},
 \end{aligned} \tag{C.8}$$

such that we can define the complex inter-resonator detuning  $\delta_c = \delta - i\frac{1}{2}\Delta\kappa_{ex}$ . We apply the following non-unitary transformation to Eq. C.7

$$A_s = \alpha A + \beta B \quad A_{as} = \beta A - \alpha B \tag{C.9}$$

$$\alpha = \frac{\sqrt{1-d_c}}{\sqrt{2}} \quad \beta = \frac{\sqrt{1+d_c}}{\sqrt{2}} \tag{C.10}$$

with  $d_c = \delta_c / \Delta\omega_c$  and  $\Delta\omega_c = \sqrt{4J^2 + \delta_c^2}$  to obtain

$$\begin{aligned}\frac{d}{dt}A_s &= \left(-i\omega_0 - \frac{\kappa_0 + \kappa_{\text{ex}}}{2}\right)A_s + i\frac{1}{2}\Delta\omega_c A_s + ig_0(\alpha A|A|^2 + \beta B|B|^2) + \alpha\sqrt{\kappa_{\text{ex},1}}s_{\text{in}} \\ \frac{d}{dt}A_{\text{as}} &= \left(-i\omega_0 - \frac{\kappa_0 + \kappa_{\text{ex}}}{2}\right)A_{\text{as}} - i\frac{1}{2}\Delta\omega_c A_{\text{as}} + ig_0(\beta A|A|^2 - \alpha B|B|^2) + \beta\sqrt{\kappa_{\text{ex},1}}s_{\text{in}}.\end{aligned}\quad (\text{C.11})$$

Here, the square roots of the complex numbers are taken as the root with positive real part as is the case when  $\Delta\kappa_{\text{ex}} = 0$ . The complex inter-resonator detuning leads to a complex frequency splitting  $\Delta\omega_c$ , which can be approximated to second order in  $\frac{\Delta\kappa_{\text{ex}}}{\Delta\omega}$  in the split resonance regime as

$$\sqrt{4J^2 + (\delta - i\frac{1}{2}\Delta\kappa_{\text{ex}})^2} \approx \Delta\omega \left(1 + \frac{1}{8}(d^2 - 1)\left(\frac{\Delta\kappa_{\text{ex}}}{\Delta\omega}\right)^2\right) - i\frac{1}{2}\delta\frac{\Delta\kappa_{\text{ex}}}{\Delta\omega}.\quad (\text{C.12})$$

As in the closed case,  $A = \alpha A_s + \beta A_{\text{as}}$ ,  $B = \beta A_s - \alpha A_{\text{as}}$  and the non-linear expansions such as Eq. C.5 are retrieved, such that

$$\begin{aligned}\frac{d}{dt}A_s &= \left[-i\left(\omega_0 - \frac{1}{2}\text{Re}(\Delta\omega_c)\right) - \frac{1}{2}(\kappa_0 + \kappa_{\text{ex}} + \text{Im}(\Delta\omega_c))\right]A_s + \alpha\sqrt{\kappa_{\text{ex},1}}s_{\text{in}} \\ &\quad + ig_0\left[t_1(d_c)A_s|A_s|^2 + t_2(d_c)A_{\text{as}}|A_s|^2 + t_4(d_c)A_s^2A_{\text{as}}^* + t_3(d_c)A_s|A_{\text{as}}|^2 + \frac{1}{2}t_3(d_c)A_{\text{as}}^2A_s^* - \frac{1}{2}t_2(d_c)A_{\text{as}}|A_{\text{as}}|^2\right] \\ \frac{d}{dt}A_{\text{as}} &= \left[-i\left(\omega_0 + \frac{1}{2}\text{Re}(\Delta\omega_c)\right) - \frac{1}{2}(\kappa_0 + \kappa_{\text{ex}} - \text{Im}(\Delta\omega_c))\right]A_{\text{as}} + \beta\sqrt{\kappa_{\text{ex},1}}s_{\text{in}} \\ &\quad + ig_0\left[\frac{1}{2}t_2(d_c)A_s|A_s|^2 + t_3(d_c)A_{\text{as}}|A_s|^2 + \frac{1}{2}t_3(d_c)A_s^2A_{\text{as}}^* - t_2(d_c)A_s|A_{\text{as}}|^2 - t_4(d_c)A_{\text{as}}^2A_s^* + t_1(d_c)A_{\text{as}}|A_{\text{as}}|^2\right]\end{aligned}\quad (\text{C.13})$$

with

$$\begin{aligned}t_1(d_c) &= \frac{1}{4}((1 - d_c)|1 - d_c| + (1 + d_c)|1 + d_c|) \approx \frac{1}{2}(1 + d^2) \\ t_2(d_c) &= \frac{1}{2}\sqrt{1 - d_c^2}(|1 - d_c| - |1 + d_c|) \approx d\sqrt{1 - d^2} \\ t_3(d_c) &= \frac{1}{2}((1 - d_c)|1 + d_c| + (1 + d_c)|1 - d_c|) \approx 1 - d^2 \\ t_4(d_c) &= \frac{1}{4}\left((1 - d_c)\sqrt{1 - d_c + d_c^* - |d_c|^2} - (1 + d_c)\sqrt{1 + d_c - d_c^* - |d_c|^2}\right) \approx -\frac{d}{2}\sqrt{1 - d^2}.\end{aligned}\quad (\text{C.14})$$

This derivation is valid in both the split dissipation and split resonance regime. The approximations are considered for the latter regime, and are exact when  $\Delta\kappa_{\text{ex}} = 0$ , where the result coincides with those found in Subsect. C.1.1.

The same transformation can be applied for any pair of longitudinal mode, and the same

## **Appendix C. Appendix to chapter 5 — Dissipative kerr solitons in dimers**

---

coefficients are retrieved for the non-linear coupling terms. Due to the linearity of the Fourier transform, and in case of frequency independent inter-resonator detuning and coupling, it suffices to add the Fourier transform to the non-linear term to obtain Eq. 5.7.

# D Appendix to chapter 6 — Avoided mode-crossings and dissipative solitons in coupled resonators

## D.1 Numerical simulations of soliton generation in a degenerate photonic plaquette

In order to support the experimental data and justify the recorded shape of the solitonic spectrum of the photon, we perform numerical simulations of four coupled Lugiato-Lefever equations. We use step-adaptative Dormand-Prince Runge-Kutta method of Order 8(5,3) with numerical boxes each having 512 points. The simulation parameters are chosen be similar to the experimental ones: integrated group velocity dispersion  $D_2=10$  MHz, inter-resonator coupling  $J=4.5$  GHz, 1st (pumped) and 3rd rings are coupled to a waveguide with the rate  $\kappa_{ex}=70$  MHz,  $\text{Si}_3\text{N}_4$  waveguide has dimensions  $1.5 \times 0.8 \mu\text{m}$ , free spectral range is 181 GHz. The parameters are identical for every ring constituting the plaquette. Solitons were excited by tuning over the resonance to the soliton existence region and further hard-seeded with a fixed detuning. The pump (0.8 W) is injected to the first ring only. The integration time is 1 microsecond. The nonlinear dynamics over the slow time is sampled with 1000 points.

Fig. D.1 (a) shows an averaged optical spectrum, of the field generated in the pumped resonator. The spectrum demonstrates features similar to the experimentally recorded one. There is a symmetric enhancement of  $\approx 55$ th mode optical power which, taking in the account the free spectral ranges of the resonators, corresponds to  $\approx 10$  THz. This is in a good agreement with the reported experimental observations. The symmetric enhancement of comb lines signifies the presence of strong dispersive waves in the cavity. The corresponding intracavity temporal waveform is shown in Fig. D.1 (b). The main (sech-shaped) part of the spectrum has a periodic perturbation similar to the one recorded experimentally. This perturbation is caused by the presence of multiple (two in this case) solitons in the cavity. The dispersive waves appear as a periodic perturbation of the background as well as the solitons. This makes solitons oscillating with time as shown in the spatio-temporal diagram for the intracavity power profile. Using the spatio-temporal diagram, we can reconstruct the nonlinear dispersion relation by applying a double Fourier transform. The nonlinear dispersion relation reveals the origin of the of comb enhancement. The soliton line (since the dispersion is compensated by the nonlinearity)

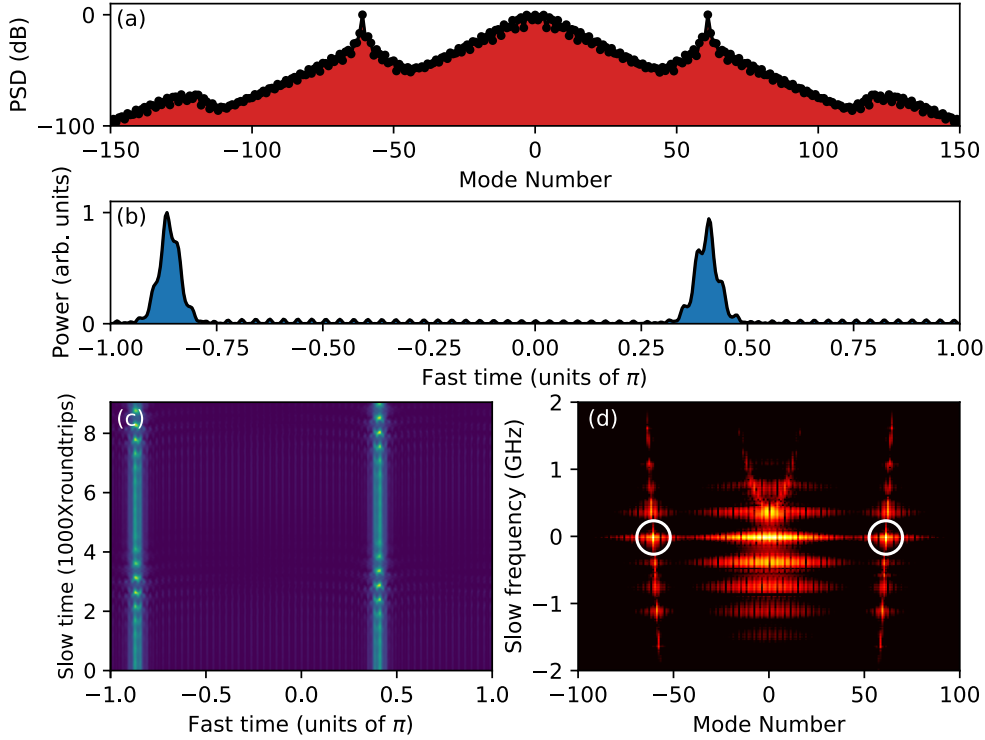


Figure D.1: **Solitons in a phonic plaquette.** All data is shown for the pumped resonator. (a) Power spectra density (PSD) of two solitons averaged over  $0.5 \mu\text{sec}$ . (b) Temporal profile of dissipative Kerr solitons (DKSs). The horizontal axis depicts the inter-resonator azimuth angle  $\epsilon \in (-\pi, \pi)$ . (c) Spatio-temporal diagram. (d) Corresponding nonlinear dispersion relation. White circles show crossing points of the soliton line with the lower parabola.

crosses the dispersion parabola which corresponds to another supermode of the system. The crossing point is shown with white circles.

## D.2 Additional experimental data

In order to demonstrate that the effect of protection is not linked to a particular device, we present here a set of linear measurements. Fig.D.2 suggests that we observe a similar behavior in a number of devices.

Further, we present additional data for the soliton generation in the photonic plaquette. Namely, simultaneously with the optical spectra, we recorded the transmission trace. The presence of distinct steps in the transmission trace is one of the key signatures of the dissipative Kerr soliton generation in microresonators. The traces were generated by using a fast single-sideband tuning technique. As follows from Fig. D.3, only the resonance having higher absolute frequency (tuning is done from the blue-detuned to the red-detuned side of the resonance) demonstrates the presence of steps.

## D.2 Additional experimental data

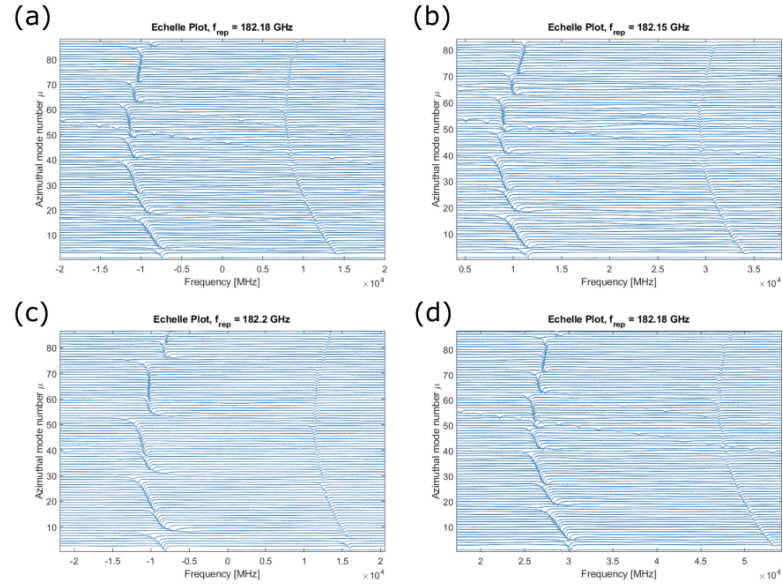


Figure D.2: **Linear spectroscopy of different photonic dimers.** All the devices have similar parameters and fabricated on the same wafer.

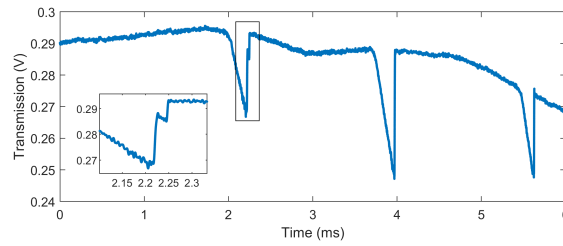


Figure D.3: **Filtered transmission trace. The case of a phonic plaquette.** The resonance on the left demonstrates the presence of soliton steps. The pump laser detuning is swept from higher to lower frequencies.

### D.3 Mode interactions in two evanescently coupled resonators

We examine here the mode interaction of two ring resonators using a perturbation approach. Taking the solution of the Maxwell's equations for single resonator as a basis for the field profile in the coupled system, we derive coupling coefficients between different modes as a function of mode overlaps. The obtained expressions can be used for the exact evaluation of the coupling coefficients for whispering gallery mode resonators, since analytical expressions are known in this case [233, 234], while for integrated microresonator dimers they, however, help to qualitatively understand the mode-crossing mechanism.

We start from the scalar wave equation on electric field in the system comprising two identical evanescently coupled optical resonators. The wave equation

$$(\Delta + \frac{n_g^2}{c^2} \frac{\partial^2}{\partial t^2})E = 0 \quad (\text{D.1})$$

governs the electric field in the media with the group index  $n_g$ . In a single resonator case, rotational symmetry allows one to obtain a set of eigenfrequencies and eigenfunctions supported by the system. Typically there are two polarization mode families (TE and TM), and within each polarization mode family there is a set of eigenfunctions (i.e. states) which have different spatial distributions. In the ideal case, all the eigenfunctions are orthogonal, even if they correspond to degenerate eigenfrequencies. The presence of perturbations which cause the axial symmetry breaking leads to the interaction between the modes breaking, thereby their orthogonality. This interaction manifest itself as avoided mode crossings (AMXs) in the dispersion profile. The AMXs appear at degenerate frequencies, where two different modes have close eigenvalues [235, 236].

The scenario of mode interaction in the photonic dimer is similar to the conventional conventional single resonator case, but the difference arises from the fact that we investigate two sets of eigenmodes which belong to different rings. In order to obtain the coupling coefficients, we employ the perturbation approach. Starting from independent eigenfunctions for both rings, implying at first the infinite distance between the resonators, we decompose the electric field on a series of eigenfunctions and obtain a system of coupled ordinary differential equations on amplitudes of the modes.

We start with a single resonator case which has the group index  $n_{g_I}$ . Using the ansatz of harmonic time dependence  $E \rightarrow Ee^{-i\omega t}$ , one obtains the Helmholtz equation

$$(\Delta + n_{g_I}^2 k_0^2)E = 0, \quad (\text{D.2})$$

where  $k_0 = \omega/c$  is the wavenumber. Eq. (D.2) defines eigenfrequencies  $\omega_\mu^I$  and eigenfunctions  $\Psi_\mu^I$  with orthogonality relation:

$$\int \Psi_\mu^I (\Psi_\nu^I)^* n_{g_I}^2 dV = \delta_{\mu,\nu}. \quad (\text{D.3})$$



### D.3 Mode interactions in two evanescently coupled resonators

Here asterisk stands for complex conjugation. The electric field is  $E = A_\mu^I \Psi_\mu^I$ , where  $A_\mu^I$  is the normalization constant. Note, that same is valid for the second resonator for which it is sufficient simply to replace  $I$  by  $II$ . Moreover, we consider the resonators to be identical, meaning that  $\omega_V^I = \omega_V^{II}$ .

Now, we suppose that the two resonators are placed closed so their eigenfunctions overlap. In order to exploit the eigenfunctions of each ring, we rewrite the group index  $n_g$  in following form:

$$n_g^2 = \begin{cases} n_{gI}^2 + n_{II} \\ n_{gII}^2 + n_I, \end{cases} \quad (\text{D.4})$$

depending on the basis we want to use. We decompose further the electric field in the following way:

$$E = \sum_i A_i^I(t) \Psi_i^I e^{-i\omega_i t} + \sum_i A_i^{II}(t) \Psi_i^{II} e^{-i\omega_i t}. \quad (\text{D.5})$$

Substituting this to the Eq. D.1 and using the slowly varying envelope approximation ( $d^2 A_i^I / dt^2 \ll \omega_i dA_i^I / dt$ ) we obtain the following equation:

$$\begin{aligned} \Delta E - \frac{n_g^2}{c^2} \frac{\partial^2 E}{\partial t^2} = \\ \sum_i \left( n_{II} \Psi_i^I A_i^I \lambda_i^2 + 2i\lambda_i \dot{A}_i^I \Psi_i^I \frac{(n_{gI}^2 + n_{II})}{c} \right) e^{-i\omega_i t} + \\ \sum_i \left( n_I \Psi_i^{II} A_i^{II} \lambda_i^2 + 2i\lambda_i \dot{A}_i^{II} \Psi_i^{II} \frac{(n_{gII}^2 + n_I)}{c} \right) e^{-i\omega_i t} = 0, \end{aligned} \quad (\text{D.6})$$

where  $\lambda_i = \omega_i / c$  and  $\dot{A}$  stands for the time derivative of  $A$ . Now, we multiply this equation by  $(\Psi_k^{I(II)})^*$  and integrate it over the whole volume. Using the orthogonality relation (D.3), one obtains a system of ordinary differential equations on the mode amplitudes with coupling coefficients proportional to the mode overlap.

Considering the case of two mode families in both resonators, one can derive the matrix model introduced in the main text. In order to keep the same notations, we denote  $A_1^I \equiv a_1$ ,  $A_2^I \equiv b_1$ ,  $A_1^{II} \equiv a_2$ ,  $A_2^{II} \equiv b_2$ . Taking only leading order coefficients, system (D.6) takes form

$$\begin{cases} \dot{a}_1 = i(J_{a_1 a_1} a_1 + J_{a_1 a_2} a_2 + J_{a_1 b_1} b_1 + J_{a_1 b_2} b_2) \\ \dot{a}_2 = i(J_{a_2 a_1} a_1 + J_{a_2 a_2} a_2 + J_{a_2 b_1} b_1 + J_{a_2 b_2} b_2) \\ \dot{b}_1 = i(J_{b_1 a_1} a_1 + J_{b_1 a_2} a_2 + J_{b_1 b_1} b_1 + J_{b_1 b_2} b_2) \\ \dot{b}_2 = i(J_{b_2 a_1} a_1 + J_{b_2 a_2} a_2 + J_{b_2 b_1} b_1 + J_{b_2 b_2} b_2), \end{cases} \quad (\text{D.7})$$

where diagonal terms indicate self-frequency shift due to presence of the coupling sections.

## Appendix D. Appendix to chapter 6 — Avoided mode-crossings and dissipative solitons in coupled resonators

---

They can be expressed through the mode overlap integrals as follows:

$$J_{a_1 a_1} = \frac{\lambda_0 c}{2} \int \Psi_0^I \Psi_0^{I*} n_{II} dV; J_{a_2 a_2} = \frac{\lambda_0 c}{2} \int \Psi_0^{II} \Psi_0^{II*} n_I dV \quad (D.8)$$

$$J_{b_1 b_1} = \frac{\lambda_1 c}{2} \int \Psi_1^I \Psi_1^{I*} n_{II} dV; J_{b_2 b_2} = \frac{\lambda_1 c}{2} \int \Psi_1^{II} \Psi_1^{II*} n_I dV. \quad (D.9)$$

Due to the symmetry, the expressions in each line of Eq. (D.8) are equal. Applying the notations from the main text, we obtain  $\omega_1 = J_{a_1 a_1}$  and  $\omega_2 = J_{b_1 b_1}$ .

The off-diagonal coefficients in system (D.7) depict the mode interaction. Let us consider the interaction between the fundamental and higher order modes of one resonator. The corresponding coefficients are expressed as

$$J_{a_1 b_1} = \frac{\lambda_1^2 c}{2 \lambda_0} \int \Psi_1^I \Psi_0^{I*} n_{II} dV e^{-i(\omega_1 - \omega_0)t}, \quad (D.10)$$

$$J_{a_2 b_2} = \frac{\lambda_1^2 c}{2 \lambda_0} \int \Psi_1^{II} \Psi_0^{II*} n_I dV e^{-i(\omega_1 - \omega_0)t}, \quad (D.11)$$

$$J_{b_1 a_1} = \frac{\lambda_0^2 c}{2 \lambda_1} \int \Psi_0^I \Psi_1^{I*} n_{II} dV e^{-i(\omega_0 - \omega_1)t}, \quad (D.12)$$

$$J_{b_2 a_2} = \frac{\lambda_0^2 c}{2 \lambda_1} \int \Psi_0^{II} \Psi_1^{II*} n_I dV e^{-i(\omega_0 - \omega_1)t}. \quad (D.13)$$

As one can see, the interaction efficiency is enhanced at the points of degeneracy, where the eigenfrequencies coincide. These points correspond to the exact positions of the mode crossings. In the main text we consider this particular example, thus  $J_{ab}^{\text{int}} = J_{a_1 b_1} |_{\omega_0 = \omega_1} = J_{a_2 b_2} |_{\omega_0 = \omega_1}$  and  $J_{ba}^{\text{int}} = J_{b_1 a_1} |_{\omega_0 = \omega_1} = J_{b_2 a_2} |_{\omega_0 = \omega_1}$ , where we assumed the coupling purely real for simplicity.

The coupling coefficients between the fundamental modes of both resonators take form:

$$J_{a_1 a_2} = \frac{\lambda_0 c}{2} \int \Psi_0^{II} \Psi_0^{I*} n_I dV, \quad (D.14)$$

$$J_{a_2 a_1} = \frac{\lambda_0 c}{2} \int \Psi_0^I \Psi_0^{II*} n_{II} dV, \quad (D.15)$$

and they are equal due to the symmetry. The corresponding coefficient in the main text  $J_{aa}^{\text{ext}} = J_{a_1 a_2} J_{a_2 a_1}$ . In similar way we express coupling between higher order modes

$$J_{b_1 b_2} = \frac{\lambda_1 c}{2} \int \Psi_1^{II} \Psi_1^{I*} n_I dV, \quad (D.16)$$

$$J_{b_2 b_1} = \frac{\lambda_1 c}{2} \int \Psi_1^I \Psi_1^{II*} n_{II} dV, \quad (D.17)$$

with  $J_{bb}^{\text{ext}} = J_{b_1 b_2} = J_{b_2 b_1}$ .

The coefficients governing interactions between fundamental and higher order modes of

distinct resonators are placed on the side diagonal of the system (D.7), and their expressions are by

$$J_{a_1 b_2} = \frac{\lambda_1^2 c}{2\lambda_0} \int \Psi_1^{II} \Psi_0^{I*} n_I dV e^{-i(\omega_1 - \omega_0)t}, \quad (D.18)$$

$$J_{a_2 b_1} = \frac{\lambda_1^2 c}{2\lambda_0} \int \Psi_1^I \Psi_0^{II*} n_{II} dV e^{-i(\omega_1 - \omega_0)t}, \quad (D.19)$$

$$J_{b_2 a_1} = \frac{\lambda_0^2 c}{2\lambda_1} \int \Psi_0^I \Psi_1^{II*} n_{II} dV e^{-i(\omega_0 - \omega_1)t}, \quad (D.20)$$

$$J_{b_1 a_2} = \frac{\lambda_0^2 c}{2\lambda_1} \int \Psi_0^{II} \Psi_1^{I*} n_I dV e^{-i(\omega_0 - \omega_1)t}. \quad (D.21)$$

As one can see, the interaction increases at degenerate frequencies, and then  $J_{ab}^{ext} = J_{a_1 b_2}|_{\omega_1=\omega_2} = J_{a_2 b_1}|_{\omega_1=\omega_2}$ ,  $J_{ba}^{ext} = J_{b_2 a_1}|_{\omega_1=\omega_2} = J_{b_1 a_2}|_{\omega_1=\omega_2}$ . It is important to note, that the intraresonator interaction originates from the mode overlap in the area where both modes decay exponentially (for example see Eq. (D.10)), when the interresonator coupling originates from the area where one is localized and second one is evanescent (e.g. Eq. (D.18)). However, it is hard to estimate the ratio between these coefficients because it also depends on the integral along azimuth coordinate. In order to obtain this ration we provide FDTD simulations in Lumerical, which are presented in the next sections.

## D.4 Matrix model

Generalized to the case of N coupled resonators, the coupling matrix of the size  $2N \times 2N$  can be represented as follows:

$$i \frac{dU}{dt} = - \begin{pmatrix} -\omega_1 & J_{aa}^{ext} & & J_{ab}^{int} & J_{ab}^{ext} & & \\ J_{aa}^{ext} & -\omega_1 & \ddots & J_{ab}^{ext} & J_{ab}^{int} & \ddots & \\ & \ddots & \ddots & J_{aa}^{ext} & \ddots & \ddots & J_{ab}^{ext} \\ & & J_{aa}^{ext} & -\omega_1 & & J_{ab}^{ext} & J_{ab}^{int} \\ J_{ba}^{int} & J_{ba}^{ext} & & -\omega_2 & J_{bb}^{ext} & & \\ J_{ba}^{ext} & J_{ba}^{int} & \ddots & J_{bb}^{ext} & -\omega_2 & \ddots & \\ & \ddots & \ddots & J_{ba}^{ext} & \ddots & \ddots & J_{bb}^{ext} \\ & & J_{ba}^{ext} & J_{ba}^{int} & & J_{bb}^{ext} & -\omega_2 \end{pmatrix} U, \quad (D.22)$$

where  $U = (a_1, \dots, a_N, b_1, \dots, b_N)^T$ . The coupling matrix is comprised of four blocks of symmetric tridiagonal matrices, implying that empty spaces are zeros. For the calculations presented in the article we suppose that  $J_{ab}^{ext, int}$  and  $J_{ba}^{ext, int}$  are equal due to the apparent summery, therefore second and third blocks of the coupling matrix are identical. Blocks one and four are also set to be identical since the difference between  $J_{aa}^{ext}$  and  $J_{bb}^{ext}$  will lead to a simple shift along the direction of the higher-order mode and the mode interaction therefore has to be

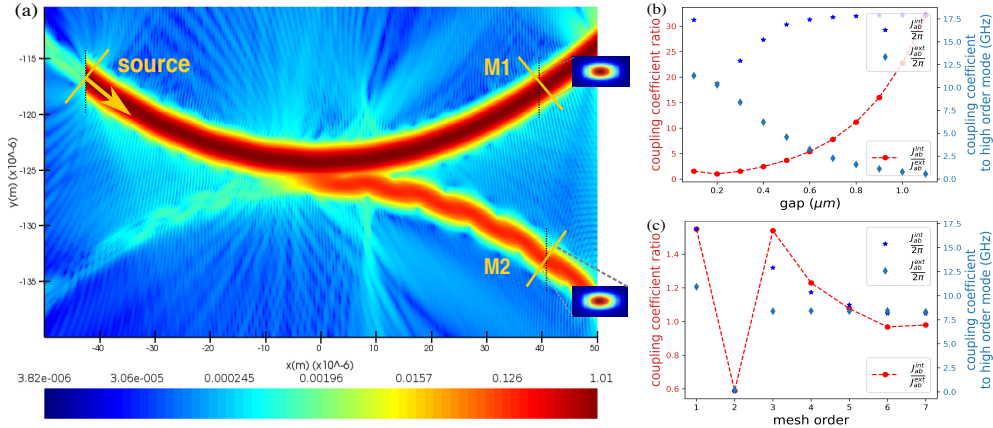


Figure D.4: FDTD simulations of the coupling section. (a) Normalized electric field distribution shown in log scale, the colour bar measures the field power. The mode source is launched normal to the waveguide propagation direction with unity power. Insets present spatial field distributions recorded by monitor M1 and M2. The gap distance is set as  $0.3 \mu\text{m}$ . (b) Dependence of the coupling coefficients to higher-order modes on gap distance, at mesh 3. (c) Convergence of the coupling coefficients to higher-order modes with mesh order, as illustrated by the red dashed line, the coupling coefficient ratio converges closely to unity.

examined at  $\omega_1 = \omega_2 = 0$ .

## D.5 FDTD simulations of the coupling section

In order to confirm the coupling coefficient ratio expected from the analytical model of four-mode interaction, we provide FDTD simulations of the coupling section of the photonic dimer. We constructed a model of a dimer device comprised of two 200 GHz ring resonators. The silicon nitride ( $\text{Si}_3\text{N}_4$ ) resonator core is fully cladded with Silicon dioxide ( $\text{SiO}_2$ ). Both resonators are  $1.5 \mu\text{m}$  wide and  $0.82 \mu\text{m}$  high, with sidewall angle  $\alpha = 90^\circ$ , as used in the experiments. The mode source was configured to inject at an angle of  $20^\circ$  with unity power, as shown in Fig. D.4a, and to excite only the fundamental mode of the ring. In this way, we shrank the simulation region to  $100 \times 30 \times 8 \mu\text{m}^3$  and the simulation time to 900 fs, which is sufficient to capture correctly the coupling to higher-order modes with much less processing time. The boundary of the simulation region is fixed with a perfectly matched layer (PML) condition to absorb the incident light and therefore to prevent backreflection. The light field then propagated in the full simulation region until a stationary state is reached. Monitors M0, M1 and M2 recorded the spatial distributions of the mode source, the transmitted field and the coupled field respectively. In addition, two mode expansion monitors were placed in the same plane as M1 and M2 to calculate the power of selected resonator eigenmode ( $\text{TE}_{10}$ ). All powers are normalized as they derived from the resonator fundamental mode that is launched with unity power. The coupling coefficients,  $J_{ab}^{int}$  and  $J_{ab}^{ext}$ , are estimated using a simplified coupled mode equation, by  $J_{ab}^i = D_1 \times \arccos(\sqrt{1 - P_{ab}^i})$ , where  $D_1/2\pi = \text{FSR}$ .

## D.5 FDTD simulations of the coupling section

---

Numerical simulations reveal that increasing the gap distance between two resonators,  $J_{ab}^{ext}$  rapidly (eventually exponentially) decays, while  $J_{ab}^{int}$  remains constant at 18 GHz except the region 0.2-0.4  $\mu\text{m}$  where it demonstrates lower values at mesh order 3 as shown in Fig. D.4. Careful analysis of the ratio  $J_{ab}^{int}/J_{ab}^{ext}$  convergence with increasing mesh order (decreasing the simulation net size) suggests that the ratio converges to unity. The simulations with mesh order 3 gives a considerable error of  $\approx 35\%$ .

The coupling of the ring resonator to the bus and drop waveguides was also simulated at 0.3  $\mu\text{m}$ , rendering a converged result of 0.75 GHz, which contributes to the coefficient  $J_{ab}^{int}$ .



# **E Appendix: numerical simulations with PyCOrE**

Numerical simulations often remain the primary tool for the investigation of complex systems where the analytical treatment fails to predict the dynamics. An important example is nonlinear systems that exhibit complex behavior including turbulence, chaos, formation of patterns, solitons, etc. Nonlinear optics is one of the primary platforms for the investigation of complex nonlinear dynamics.

We developed a numerical tool to efficiently simulate nonlinear dynamics and optical frequency combs in a single resonator, synthetic frequency dimension discussed in chapters 1, 3, 5, 6, and 7.

## **E.1 Functionality and utilities**

The solver is implemented in Python, wrapping a fast C++ core. It operates with an arbitrary number of coupled resonators and modes, including the following functionalities and features:

- Arbitrary dispersion profile
- Raman scattering
- Periodic perturbation leading to the Faraday dynamics
- Thermal effects
- Hard seeding of solitons and CW solutions
- Interactive plotter of the spatiotemporal diagram
- Eigenmode plotter for single resonator and chains of coupled resonators

This solver includes the following simulation methods for finding dynamical and stationary solutions:

## Appendix E. Appendix: numerical simulations with PyCOrE

---

- Split operators method also known as split-step method for single resonator class
- Step adaptive Dormand-Prince Runge-Kutta method of Order 8(5,3) [179]
- Newton-Raphson method for the search of stationary solutions
- Linear stability analysis of the stationary solutions obtained using the Newton-Raphson method

### E.2 Installation

- Clone the repository from <https://github.com/ElKosto/PyCOrE>;
- Install Anaconda. Make sure that Numpy and Scipy are installed.

If the user intends to use only the single resonator solver or the Newton-Raphson stationary solver, the preceding steps should be sufficient. The solver functions on both Unix and Windows systems. However, to utilize the solver for chains of resonators, users will need to install additional packages. This functionality is compatible only with Unix-based systems, such as Ubuntu or MacOS.

1. Download boost (<https://www.boost.org/>, free) or Numerical recipes (<https://www.boost.org/>, 50\$) headers;
2. Locate your local C header folder in terminal via the command

```
1 cpp -v
```

Usually, it is */usr/local/include/*

3. Copy there the boost or numerical recipes headers. Make sure that numerical recipes headers are in the folder named as *NR/code/*, and boost headers are in the folder *boost/*.

```
1 sudo scp -r boost/ /usr/local.include/
```

or

```
1 sudo scp -r NR/ /usr/local.include/
```

4. Install fftw (<https://www.fftw.org/download.html>). The best way is to download the full source code, go to the downloaded folder and execute

```
1 ./configure  
2 make  
3 sudo make install
```

5. Compile the needed solvers. All the commands are available in the README file located in *PyCOrE/lib/*.



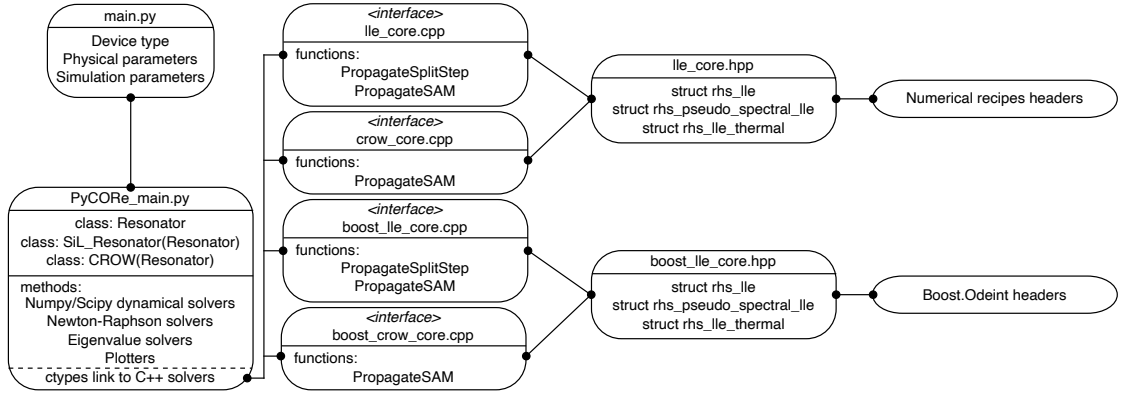


Figure E.1: Solver architecture.

In the following, we present the compilation commands for different solvers:

- For single resonator solver:

```
1 g++ -fPIC -shared -lfftw3 -lm -O3 -o lib_ile_core.so ile_core.cpp
```

- For chains of resonators with open boundary conditions:

```
1 g++ -fPIC -shared -lfftw3 -lm -O3 -o lib_crow_core.so crow_core.cpp
```

- For chains of resonators with closed in a chain:

```
1 g++ -fPIC -shared -lfftw3 -lm -O3 -o lib_periodic_crow_core.so  
periodic_crow_core.cpp
```

### E.3 Solver architecture

The overall architecture of the solver is depicted in Fig. E.1. Python serves as the primary interface for utilizing the library. Users define both the physical parameters of the resonators and the simulation parameters for the solvers within this environment. This schematic representation is available in Fig. E.1 and can be found in the file *main.py*. Following this, users are required to create specific classes corresponding to the devices they intend to simulate. These classes, exemplified in Fig. E.1 and implemented in the file *PyCORE\_main.py*, encompass fields defined by the physical parameters. Once this preparatory step is complete, users can select a suitable solver method within the chosen class. The chosen method then performs the necessary computations. Certain methods exclusively require the Numpy and Scipy libraries for simulation execution. These libraries can be conveniently installed using package managers such as *pip* or *conda*. In such cases, the method produces simulation data without involving any of the C++ modules. However, to accelerate dynamical simulations within coupled systems, we've developed methods that utilize Runge-Kutta integrator functions. These functions are implemented in C++ and can be accessed through resources like Numerical Recipes [179]

## Appendix E. Appendix: numerical simulations with PyCOrE

or Boost.Odeint [237]. This integration is facilitated by *ctypes*, a Python library that allows for function calls and collaboration with C libraries from Python code. This capability can also be viewed as a specialized Application Programming Interface (API)."

### E.3.1 Code structure

In the following we provide a description of the different components, classes, and methods of the solver.

#### main.py

In the main file, users define the physical parameters of the resonator using a Python dictionary. For instance, a typical  $\text{Si}_3\text{N}_4$  resonator can be defined as follows:

```
1 PhysicalParameters = {'n0' : 1.9,
2                       'n2' : 2.4e-19, # m^2/W
3                       'FSR' : 181.7e9, #Hz
4                       'w0' : 2*np.pi*192e12, #rad Hz
5                       'width' : 1.5e-6, #m
6                       'height' : 0.85e-6, #m
7                       'kappa_0' : 50e6*2*np.pi, #rad Hz
8                       'kappa_ex' : 50e6*2*np.pi, #rad Hz
9                       'Dint' : Dint, #rad Hz
10                      }
```

Here,  $n_0$  represents the group index,  $n_2$  stands for the nonlinear refractive index (measured in  $\text{m}^2/\text{W}$ ), FSR indicates the free spectral range (measured in [Hz]),  $w_0$  corresponds to the carrier angular frequency  $\omega_0 = 2\pi f_0$ , while *width* and *height* denote the dimensions of the resonator waveguide (measured in [m]). These dimensions are used to estimate the effective mode area as  $A_{\text{eff}} = \text{width} \times \text{height}$ , which is subsequently employed to compute the single-photon Kerr frequency shift:  $g_0 = \frac{\hbar \omega_0^2 c n_2}{n_0^2 V_{\text{eff}}}$ . The effective volume is determined as  $V_{\text{eff}} = \frac{A_{\text{eff}} c}{n_0 \text{FSR}}$ . Internal linewidth is represented by  $\text{kappa}_0$ , while coupling to the bus waveguide is denoted by  $\text{kappa}_{\text{ex}}$ . Additionally, *Dint* refers to the array of integrated dispersion values  $D_{\text{int}}$  as a function of the integer mode index  $\mu$ .

To create the resonator object, the user needs to call the empty constructor of the class *Resonator* and then call the method *Init\_From\_Dict* to initialize its parameters from the dictionary, as follows

```
1 import PyCOrE_main as pcm
2 single_ring = pcm.Resonator()
3 single_ring.Init_From_Dict(PhysicalParameters)
```

There are three main classes:

- **Resonator:** Used for single resonator simulations, including synthetic frequency dimen-

sions and electro-optical combs.

- **SiL\_Resonator**: Used for self-injection locked resonator simulations. Users also need to provide parameters of the laser that is locked to the resonator.
- **CROW** (Coupled Resonator Optical Waveguide): Used for strongly coupled chains of microresonators. Users need to specify the coupling strength  $J$ .

Pump laser parameters are initiated as

```

1 dNu_ini = -1e9 #Hz
2 dNu_end = 3e9 #Hz
3 sampling_points = 2000
4 dOm = 2*np.pi*np.linspace(dNu_ini,dNu_end,sampling_points)
5 scan_time = 1e-6 #s
6 P0 = 0.15# W
7 Pump = np.zeros(len(mu),dtype='complex')
8 Pump[0] = np.sqrt(P0)

```

In this particular scenario, we consider the pump laser operating in continuous-wave (CW) mode at a power of 150 mW, designated as the variable  $P0$ . The laser's frequency undergoes a linear sweep from  $\omega_0 + 2\pi \cdot dNu\_ini$  to  $\omega_0 + 2\pi \cdot dNu\_end$  over the course of one microsecond, as defined by the variable  $scan\_time$ . The level of discretization for the laser scan array  $dOm$  is determined by the  $sampling\_points$  variable. Additionally, the variable  $Pump$  shares the same length as the mode index array  $\mu$  and is structured as an array to represent both continuous-wave (CW) and pulsed-pumping schemes. This array is defined in the spectral domain, incorporating frequency shifts. Specifically, within the *Pump* array, frequency bin 0 contains the CW signal at the carrier frequency  $\omega_0$ . Frequency bins 1 to  $Pump.size/2$  encompass positive frequencies in ascending order, aligned with increasing positive values of  $\mu$ . The frequency bin at  $Pump.size/2+1$  holds the most negative frequencies, mirroring the absolute values of the positive frequencies in bin  $(Pump.size/2)-1$ . These negative frequencies gradually decrease in absolute value as the bin numbers increase. It's noteworthy that the frequency bin at  $Pump.size-1$  accommodates the least negative frequencies, which correspond in absolute value to the positive frequencies present in bin 1.

The variables, defined above, are used to initialize the `simulation_parameters` dictionary

```

1 simulation_parameters = {'slow_time' : scan_time,
2                          'detuning_array' : dOm,
3                          'noise_level' : 1e-9,
4                          'output' : 'map',
5                          'absolute_tolerance' : 1e-10,
6                          'relative_tolerance' : 1e-6,
7                          'max_internal_steps' : 2000}

```

Here, `noise_level` defines the amplitude of the white noise in the frequency domain. This variable is necessary to initiate four-wave mixing processes under continuous-wave (CW)

## Appendix E. Appendix: numerical simulations with PyCOrE

---

pumping. 'output' : 'map' defines the dense output from the solver, while `absolute_tolerance`, `relative_tolerance`, and `max_internal_steps` establish the conditions for the step-adaptive solvers.

To execute the simulations, it is necessary to invoke an integrator method from the instantiated class object using the following approach:

```
1 map2d = single_ring.Propagate_PseudoSpectralSAMCLIB(simulation_parameters
    , Pump)
```

In this example, the output array `map2d` possesses two dimensions, `[sample_points, mu.size]`, and encapsulates the simulation results in the spectral domain for each time step throughout the entire `scan_time`.

The generated data can be stored using the class method `Save_Data` with the following syntax:

```
1 single_ring.Save_Data(map2d,Pump,simulation_parameters,dOm,'./data/')
```

In the selected directory, `'./data/'` in this instance, this method saves the detuning array `dOm`, simulation data `map2d`, and pump array `Pump` as Numpy binary files: `'dOm.npy'`, `'map2d.npy'`, and `'Pump.npy'`, respectively. Moreover, it generates two subdirectories: `'./data/class_parameters/'` and `'./data/sim_parameters/'`, which encompass all the variables in a Numpy binary format. These files can be utilized to initialize the class, thus enabling further work with the current model. To achieve this, one must invoke the constructor `Init_From_File` using the subsequent syntax:

```
1 simulation_parameters,map2d_scan,dOm_scan,Pump=single_ring.Init_From_File
    ('./data/')
```

### PyCOrE\_main.py

Here, we outline the contents of the `'PyCOrE_main.py'` file.

**Single resonator class** In this section, we present an in-depth explanation of the *Resonator* class. The subsequent code block depicts the constructor, initialization, and saving methods.

```
1 class Resonator:
2     def __init__(self): #Empty constructor
3     def Init_From_Dict(self, resonator_parameters): #Class initialization
    from dictionary
4     def Init_From_File(self,data_dir): #Class initialization from folder
5     def Save_Data(self,map2d,Pump,Simulation_Params,dOm=[0],directory='./
    '):#method to save the data
```

The physical parameters of the device are established as class fields. The technique to generate white noise with an amplitude `a` and randomized phases in the spectral domain for each comb line is as follows:

```

1     def noise(self, a):
2         return a*(np.random.uniform(-1,1,self.N_points) + 1j*np.random.
           uniform(-1,1,self.N_points))

```

The solvers, which exclusively rely on the Numpy and Scipy libraries for dynamic simulations, are defined as follows:

```

1     def Propagate_SplitStep(self, simulation_parameters, Pump, Seed=[0],
           dt=5e-4, Normalized_Units=False):
2     def Propagate_SAM(self, simulation_parameters, Pump, Seed=[0],
           Normalized_Units=False):

```

The first solver is the conventional split-step method of second order in time. Here,  $dt$  is the fixed time step, which has to be carefully chosen to avoid numerical instabilities [29, 238]. The boolean variable `Normalized_units` is *True* in case the user performs the simulations in normalized units. The second method uses the step-adaptative Dormand-Prince Runge-Kutta method of Order 8(5,3) from the Scipy library. These solvers are used within the standard Python installation and do not require any additional steps. However, to accelerate simulations, users can use solvers from the C++ libraries defined below.

```

1     def Propagate_SplitStepCLIB(self, simulation_parameters, Pump, Seed
           =[0], dt=5e-4, HardSeed=False):
2     def Propagate_SAMCLIB(self, simulation_parameters, Pump, Seed=[0],
           dt=5e-4, HardSeed=False):
3     def Propagate_PseudoSpectralSAMCLIB(self, simulation_parameters,
           Pump, Seed=[0], dt=5e-4, HardSeed=False, lib='NR'):

```

These solvers offer equivalent functionality but operate more swiftly than their Python counterparts. The variable `lib=NR` or `lib=boost` empowers the user to select the integrator from either Numerical Recipes or Boost headers. Moreover, we distinguish between the methods `Propagate_SAMCLIB` and `Propagate_PseudoSpectralSAMCLIB`. In the former, we solely consider second-order dispersion and approximate the second derivative  $\partial_\varphi^2$  through finite differences. Specifically,

$$\left. \frac{\partial^2}{\partial \varphi^2} A \right|_{\varphi=\varphi_i} \approx \frac{A_{i+1} - 2A_i + A_{i-1}}{\Delta \varphi^2}, \quad (\text{E.1})$$

where  $\Delta \varphi = \varphi_{i+1} - \varphi_i$ . This approach results in a numerical complexity per iteration of  $O(n)$ . In the latter method, denoted as `Propagate_PseudoSpectralSAMCLIB`, we calculate the dispersion operator in the frequency domain. As a consequence, the numerical complexity is reduced to  $O(n \log n)$ , enabling more accurate simulations.

The stationary Newton-Raphson solver is built upon the Numpy library and employs the standard gradient descent technique to locate the solution. The functions used to compute it are established as methods of the class, as illustrated below:

```

1     def Jacobian(self, zeta_0, A, D1):
2     def JacobianForLinAnalysis(self, zeta_0, A):
3     def D1A(self, A):

```

## Appendix E. Appendix: numerical simulations with PyCORE

```
4 def DispersionMatrix(self, D1=0, order=0):
5 def LinMatrix(self, zeta_0, dense=True):
6 def NewtonRaphson(self, A_input, d0m, Pump, vg=0, HardSeed = True, tol=1e
-5, max_iter=50):
7 def NewtonRaphsonFixedD1(self, A_input, d0m, Pump, HardSeed = True, tol
=1e-5, max_iter=50):
8 def LinearStability(self, solution, d0m, v=0, plot_eigvals=True):
```

Here, the function `NewtonRaphson` calculates the stationary solution and determines its group velocity  $vg$ . On the other hand, `NewtonRaphsonFixedD1` is utilized in the context of a pure LLE, where the soliton revolves with the group velocity  $D_1$ . The remaining functions serve as subroutines to compute the Jacobian matrix and its eigenvalues for the obtained stationary solution.

### Chains of coupled resonators class.

This class is named `CROW`, and it is a subclass of the `Resonator` class. The initialization method is the similar to the `Resonator` class, but the user needs to provide the following parameters in the `resonator_parameters` dictionary:

- `resonator_parameters['Inter-resonator_coupling']`: An array of the size of the number of modes  $\times$  the number of coupling sections that contains coupling parameters  $J$  between the resonators. The user can define an open chain or a closed ring configuration. In the first case, the number of coupling sections is the number of resonators minus 1; in the second case, they are equal.
- `resonator_parameters['Resonator detunings']`: An array of the relative absolute detunings between the resonators.

The following methods allow calling dynamical simulation solvers. Their syntax is similar to the methods in the `Resonator` class.

```
1 def Propagate_SAMCLIB(self, simulation_parameters, Pump, Seed=[0], dt=5e
-4, HardSeed=False):
2 def Propagate_PSEUDO_SPECTRAL_SAMCLIB(self, simulation_parameters, Pump,
Seed=[0], dt=5e-4, HardSeed=False, lib='NR'):
```

The stationary Newton-Raphson method relies on the following methods:

```
1 def DispersionMatrix(self, order=0):
2 def LinMatrix(self, j, d2, dphi, delta, kappa, zeta_0):
3 def Jacobian(self, j, d2, dphi, delta, kappa, zeta_0, A):
```

These methods construct matrices corresponding to the dispersion term and then the linear term. The linear matrix is subsequently used to construct the complete Jacobian. These functions are called in the `NewtonRaphson` method, which employs them during the gradient descent.

```
1 def NewtonRaphson(self, Seed_sol, dOm, Pump, HardSeed=True, tol=1e-5,
    max_iter=50, learning_rate=1e-1):
```

This method is designed for stationary solutions only and cannot determine the velocity of moving solutions.

### C++ Routines for Single Resonator Solvers

In this section, we will describe the functions utilized to solve various versions of the Lugiato-Lefever Equation.

`lle_core.cpp`

Below, we provide descriptions of the functions utilized to solve the LLE and its various versions in C++. These functions serve as interfaces for invoking Numerical Recipes headers.

- `std::complex<double>* WhiteNoise(const double amp, const int Nphi)`

This function is used to generate random white noise for each frequency component at every simulation time step.

- `void* PropagateSS(double* In_val_RE, double* In_val_IM, double* Re_F, double* Im_F, const double *detuning, const double J, const double *phi, const double* Dint, const int Ndet, const int Nt, const double dt, const int Nphi, double noise_amp, double* res_RE, double* res_IM)`

This is the Split-step integrator.

- `void* PropagateSAM(double* In_val_RE, double* In_val_IM, double* Re_F, double* Im_F, const double *detuning, const double J, const double *phi, const double* Dint, const int Ndet, const int Nt, const double dt, const double atol, const double rtol, const int Nphi, double noise_amp, double* res_RE, double* res_IM)`

This is the step-adaptive Dormand-Prince (SAMDP) integrator with the dispersion term approximated by second-order finite differences.

- `void* Propagate_PseudoSpectralSAM(double* In_val_RE, double* In_val_IM, double* Re_F, double* Im_F, const double *detuning, const double J, const double *phi, const double* Dint, const int Ndet, const int Nt, const double dt, const double atol, const double rtol, const int Nphi, double noise_amp, double* res_RE, double* res_IM)`

This solver is the same as the previous one, but we compute the dispersion term in the frequency domain, enabling a complex dispersion profile and higher precision.

## Appendix E. Appendix: numerical simulations with PyCOrE

---

```
• void* PropagateThermalSAM(double* In_val_RE, double* In_val_IM,
    double* Re_F, double* Im_F, const double *detuning, const double J
    , const double t_th, const double kappa, const double n2, const
    double n2t, const double *phi, const double* Dint, const int Ndet,
    const int Nt, const double dt, const double atol, const double
    rtol, const int Nphi, double noise_amp, double* res_RE, double*
    res_IM)
```

This solver solves LLE using SAMDP in the presence of thermal effects in the cavity. The dispersion term is approximated by second-order finite differences.

```
• void* Propagate_SiL_PseudoSpectralSAM(double* In_val_RE, double*
    In_val_IM, const double *detuning, const double kappa, const double
    kappa_laser ,const double kappa_sc, const double kappa_inj, const
    double coupling_phase, const double g0, const double alpha, const
    double gamma, const double V, const double a, const double e, const
    double NO, const double eta, const double I_laser, const double
    zeta, const double* Dint, const int Ndet, const double Tmax, const
    double T_step, const int Nt, const double dt, const double atol,
    const double rtol, const int Nphi, double noise_amp, double* res_RE
    , double* res_IM)
```

This solver solves LLE coupled to a laser using SAMDP. The dispersion term is computed in the frequency domain.

```
• void* Propagate_PseudoSpectralSAM_Raman(double* In_val_RE, double*
    In_val_IM, double* Re_F, double* Im_F, const double *detuning,
    const double *tau_r_mu, const double* Dint, const int Ndet, const
    int Nt, const double dt, const double atol, const double rtol,
    const int Nphi, double noise_amp, double* res_RE, double* res_IM)
```

This solver solves LLE with Raman effect. The dispersion term is computed in the frequency domain.

The functions defined above receive all the necessary parameters from Python. Their descriptions are presented below:

- `*In_val_RE`: Pointer to the array of the real part of the initial distribution of the field.
- `*In_val_IM`: Pointer to the array of the imaginary part of the initial distribution of the field.
- `*res_RE`: Pointer to the output array of the real part of the solution.
- `*res_IM`: Pointer to the output array of the imaginary part of the solution.
- `*Re_F`: Pointer to the array of the real part of the pump.
- `*Im_F`: Pointer to the array of the imaginary part of the pump.



- `*detuning`: Pointer to the array of detunings.
- `*phi`: Pointer to the array of the azimuth coordinate  $\varphi$  inside the resonator.
- `*Dint`: Pointer to the array of the integrated dispersion  $D_{\text{int}}$ .
- `Nphi`: Length of the azimuth coordinate array.
- `Ndet`: Length of the detuning array.
- `Nt`: Total number of integration steps in time for one value of detuning.
- `dt`: Time step measured in units of  $\kappa/2$ .
- `noise_amp`: White noise amplitude.
- `J`: Amplitude of the electro-optical coupling to simulate electro-optical combs and synthetic frequency dimension with one FSR modulation.
- `atol`: Absolute tolerance for the step-adaptive methods.
- `rtol`: Relative tolerance for the step-adaptive methods.
- `n2`: Kerr nonlinearity coefficient.
- `n2t`: Thermal nonlinearity coefficient.
- `t_th`: Thermal relaxation time.
- `kappa`: Total linewidth of the resonator.
- `kappa_laser`: Laser cavity loss rate.
- `kappa_sc`: Coupling rate between clockwise and counter-clockwise modes in the resonator.
- `kappa_inj`: Laser-microresonator coupling rate.
- `theta`: Optical feedback phase.
- `g0`: Single-photon Kerr frequency shift  $g_0$ .
- `alpha`: Linewidth enhancement Henry factor.
- `gamma`: Carrier recombination rate.
- `V`: Volume of the active section.
- `a`: Differential gain.
- `e`: Elementary electronic charge.
- `N0`: Carrier density at transparency.

## Appendix E. Appendix: numerical simulations with PyCOrE

---

- eta: Conversion factor.
- I: Laser biased current.
- zeta: Current-frequency tuning coefficient.
- tau\_r\_mu: Normalized Raman shock time.

### lle\_core.hpp

In this header, we created structures for different modifications of LLE.

- `struct rhs_lle{}`

This structure is used to solve pure LLE with dispersion approximated by second-order finite differences.

- `struct rhs_pseudo_spectral_lle{}`

This structure is used to solve pure LLE with dispersion computed in the frequency domain.

- `struct rhs_lle_thermal{}`

This structure is used to solve LLE with thermal effects with dispersion approximated by second-order finite differences.

- `struct rhs_pseudo_spectral_sil_lle{}`

This structure is used to solve LLE coupled to an external laser to simulate self-injection locking with dispersion computed in the frequency domain.

- `struct rhs_pseudo_spectral_lle_w_raman{}`

This structure is used to solve LLE with Raman effect with dispersion computed in the frequency domain.

### lle\_core\_boost.cpp

For the Boost library, we have implemented only a solver from Boost/Odeint that employs the `runge_kutta_fehlberg78` solver. However, we adhere to the same naming convention.

- `void* Propagate_PseudoSpectralSAM(double* In_val_RE, double* In_val_IM, double* Re_F, double* Im_F, const double *detuning, const double J, const double *phi, const double* Dint, const int Ndet, const int Nt, const double dt, const double atol, const double rtol, const int Nphi, double noise_amp, double* res_RE, double* res_IM)`

The corresponding structure is defined in the header `lle_core_boost.hpp`.

- `struct rhs_pseudo_spectral_lle{}`

The functions and structures described above possess the same functionality as the functions with the same names that employ Numerical Recipes headers. The integration of Boost solvers for different models is currently in progress.

### C++ Routines for Chains of Coupled Resonators

In this section, we describe the functions used to solve the coupled Lugiato-Lefever Equation, which models nonlinear dynamics in chains of coupled resonators.

`crow_core.cpp`

Below, we present a set of functions that we have implemented. They follow the same naming convention and functionality as the solvers for single LLE, unless otherwise specified.

- `std::complex<double>* WhiteNoise(const double amp, const int Nphi)`
- `void* PropagateSAM(double* In_val_RE, double* In_val_IM, double* Re_F, double* Im_F, const double *detuning, const double* kappa, const double kappa0, const double *delta, const double* J, const double *phi, const double* d2, const int Ndet, const int Nt, const double dt, const double atol, const double rtol, const int Nphi, const int Ncrow, double noise_amp, double* res_RE, double* res_IM)`

This is the SAMDP integrator for coupled LLEs with the dispersion term approximated by second-order finite differences.

- `void* PropagatePseudoSpectralSAM(double* In_val_RE, double* In_val_IM, double* Re_F, double* Im_F, const double *detuning, const double* kappa, const double kappa0, const double *delta, const double* J, const double *phi, const double* Dint, const int Ndet, const int Nt, const double dt, const double atol, const double rtol, const int Nphi, const int Ncrow, double noise_amp, double* res_RE, double* res_IM)`

This solver is the same as the previous one, but we compute the dispersion term in the frequency domain, enabling a complex dispersion profile and higher precision.

- `void* PropagateThermalSAM(double* In_val_RE, double* In_val_IM, double* Re_F, double* Im_F, const double *detuning, const double* kappa, const double kappa0, const double t_th, const double n2, const double n2t, const double *delta, const double* J, const double *phi, const double* d2, const int Ndet, const int Nt, const double dt, const double atol, const double rtol, const int Nphi, const int Ncrow, double noise_amp, double* res_RE, double* res_IM)`

## Appendix E. Appendix: numerical simulations with PyCORE

---

This solver solves coupled LLEs using SAMDP in the presence of thermal effects in the cavity. The dispersion term is approximated by second-order finite differences.

```
• void* Propagate_PseudoSpectralThermalSAM(double* In_val_RE, double* In_val_IM, double* Re_F, double* Im_F, const double* detuning, const double* kappa, const double kappa0, const double t_th, const double n2, const double n2t, const double* delta, const double* J, const double* phi, const double* Dint, const int Ndet, const int Nt, const double dt, const double atol, const double rtol, const int Nphi, const int Ncrow, double noise_amp, double* res_RE, double* res_IM)
```

This solver solves coupled LLEs using SAMDP in the presence of thermal effects in the cavity. The dispersion term is computed in the frequency domain.

The input variables presented here have the same meanings as in the single-resonator routines. The coupled-resonator related variables are:

- *\*kappa*: Pointer to the array of coupling strengths of the bus waveguide to different resonators.
- *\*J*: Pointer to the array of couplings between the resonators.
- *\*delta*: Pointer to the array of relative detunings between the resonators.
- *\*d2*: Pointer to the array of group velocity dispersions.
- *kappa0*: Internal linewidth of the resonators.
- *Ncrow*: Total number of resonators.

`crow_core.hpp`

In this header, we have created structures for different modifications of coupled LLEs:

```
• struct rhs_crow{}
```

This structure is used to solve coupled LLEs with dispersion approximated by second-order finite differences.

```
• struct rhs_pseudo_spectral_crow{}
```

This structure is used to solve coupled LLEs with dispersion computed in the frequency domain.

```
• struct rhs_crow_thermal{}
```

This structure is used to solve coupled LLEs with thermal effects with dispersion approximated by second-order finite differences.

- `struct rhs_pseudo_spectral_crow_thermal{}`

This structure is used to solve coupled LLEs with thermal effects with dispersion computed in the frequency domain.

`boost_crow_core.cpp`

Just as with the single resonator solvers, we have implemented the `runge_kutta_fehlberg78` solver from Boost/Odeint.

- `void* Propagate_PseudoSpectralSAM(double* In_val_RE, double* In_val_IM, double* Re_F, double* Im_F, const double *detuning, const double* kappa, const double kappa0, const double *delta, const double* J, const double *phi, const double* Dint, const int Ndet, const int Nt, const double dt, const double atol, const double rtol, const int Nphi, const int Ncrow, double noise_amp, double* res_RE, double* res_IM)`

The corresponding structure in the header file `boost_crow_core.hpp`:

- `struct rhs_pseudo_spectral_crow{}`

## E.4 Examples

In this section, we provide a code and simple examples of the functionality explained above. In the first part of the section, we provide a simulation code that works both in Python and C++. This implies that the scripts from the sections allows for out-of-box Python simulations that do not require any additional steps. The usage of the Python-based CROW solver is not recommended because of the large integration time.

### E.4.1 Single LLE soft excitaton

To simulate the single LLE dynamics with real resonator parameters, the following code can be used:

```
1
2 import matplotlib.pyplot as plt
3 import numpy as np
4 import sys,os
5 import PyCRe_main as pcm
```

## Appendix E. Appendix: numerical simulations with PyCORE

---

```
6
7 curr_dir = os.getcwd()
8 PyCore_dir = os.path.dirname(curr_dir)
9 sys.path.append(PyCore_dir)
10
11 Num_of_modes = 2**9 # Number of modes (Box size)
12 nn = 2000 # number of output steps
13
14 # Integrated dispersion constructor
15 D2 = 4.1e6#-1*beta2*L/Tr*D1**2 ## From beta2 to D2
16 D3 = -25e3
17 mu = np.arange(-Num_of_modes/2,Num_of_modes/2)
18 Dint = 2*np.pi*(mu**2*D2/2 + mu**3*D3/6)
19
20 # Pump laser-resonator detuning range in Hz
21 dNu_ini = -1e9
22 dNu_end = 3e9
23
24 ramp_stop = 0.99 # Detuning sweep stop
25 d0m = 2*np.pi*np.concatenate(
26     [np.linspace(dNu_ini,dNu_end, int(nn*ramp_stop)),dNu_end*np.ones(
27         int(np.round((1-ramp_stop)*nn)))]
28
29 PhysicalParameters = {'n0' : 1.9, # refractive index
30                       'n2' : 2.4e-19,# nonlinear RI [m^2/W]
31                       'FSR' : 181.7e9, # free spectral range
32                       'w0' : 2*np.pi*192e12, # pump frequency
33                       'width' : 1.5e-6, # waveguide width
34                       'height' : 0.85e-6, # waveguide height
35                       'kappa_0' : 50e6*2*np.pi, # internal loss rate
36                       'kappa_ex' : 50e6*2*np.pi, # external loss rate
37                       'Dint' : Dint}
38
39 simulation_parameters = {'slow_time' : 1e-6,# seconds
40                         'detuning_array' : d0m,
41                         'electro-optical coupling' : 0,
42                         'noise_level' : 1e-12,# shot noise
43                         'output' : 'map', # choose the output type
44                         'absolute_tolerance' : 1e-8,
45                         'relative_tolerance' : 1e-8,
46                         'max_internal_steps' : 2000}
47
48 # Pump vector construction
49 P0 = 0.15# Pump power in [W]
50 Pump = np.zeros(len(mu),dtype='complex')
51 Pump[0] = np.sqrt(P0)
52
53 # Class initialization
54 single_ring = pcm.Resonator()
55 single_ring.Init_From_Dict(PhysicalParameters)
56
57 # Uncomment to choose the integrator of interest
```

```

58 map2d = single_ring.Propagate_SplitStep(simulation_parameters, Pump, dt
    =0.5e-3)
59 #map2d = single_ring.Propagate_SAM(simulation_parameters, Pump)
60
61 #Save all the simulation parameter in the local folder 'data'
62 single_ring.Save_Data(map2d,Pump,simulation_parameters,d0m,'./data/')
63 %\end{minted}

```

Line-by-line description:

- Lines (1-4) packages import. Note: some packages can be duplicated inside the PyCORE main file.
- Lines (6-8) getting the current working directory of the process, and appending it to PyCore directory
- Lines (11-12) dimensions of the numerical box
- Lines (14-18) We construct the integrated dispersion using  $D_2$  and  $D_3$  coefficient of the expansion.
- Lines (21-27) We defined the laser detuning range in Hz and convert it the angular frequency adding an option to stop the sweep earlier depending on the value of ramp\_stop.
- Lines (29-37) Physical Parameters dictionary in the microresonator units.
- Lines (39-46) Simulation parameters dictionary (see ref for details)
- Lines (49-51) Pump vector construction in the Fourier domain. The vector is reversed in the way that the central frequency is placed at 0th index.
- Lines (53-55) pcm class construction with the Physical Parameters dictionary.
- Lines (57-59) Calling a solver method providing the simulation parameters and pump vector.
- Line (62) Save data

As a result, we obtain the spatio-temporal diagram plotted with the interactive viewer "Plot\_Map". It is displayed in Fig. 1. Parameters of the simulation and corresponding output data are saved in the /data/ folder using binaries of NumPy.

#### E.4.2 Hard seeding of solitons

To resolve the spatio-temporal dynamics of the intracavity field at fixed detuning, the hard seeding techniques must be used. It includes the following steps:

## Appendix E. Appendix: numerical simulations with PyCOrE

---

- Perform the dynamical simulations as described in Ch..
- Choose the detuning of interest using the interactive viewer.
- Load the parameter files
- Perform simulations with a fixed laser detuning

The code for the last two files is the following:

```
1
2 import matplotlib.pyplot as plt
3 import numpy as np
4 import sys,os
5 import PyCOrE_main as pcm
6 import time
7
8 curr_dir = os.getcwd()
9 PyCore_dir = os.path.dirname(curr_dir)
10 sys.path.append(PyCore_dir)
11
12 start_time = time.time()
13 map2d_scan = np.zeros([], dtype=complex)#np.load('map2d_scan.npy')
14 d0m_scan = np.zeros([])
15 Pump=np.zeros([], dtype=complex)
16 simulation_parameters={}
17 single_ring = pcm.Resonator()
18 #single_ring=pcm.CROW()
19 simulation_parameters, map2d_scan, d0m_scan,
20     Pump=single_ring.Init_From_File('./data/')
21
22 idet = 1000
23 nn = 10000
24 d0m = np.ones(nn)*d0m_scan[idet]
25 simulation_parameters['slow_time']=1e-6
26 simulation_parameters['detuning_array']=d0m
27
28 Seed = map2d_scan[idet,:]/single_ring.N_points
29
30 map2d = single_ring.Propagate_SplitStep(simulation_parameters, Pump, Seed
    =Seed,
31     dt=0.5e-3, HardSeed=True)
32
33 #plt.figure()
34 #plt.plot(d0m/2/np.pi,np.mean(np.abs(map2d)**2,axis=1))
35
36 #pcm.Plot_Map(np.fft.ifft(map2d,axis=1),d0m*2/single_ring.kappa)
37 pcm.Plot_Map(np.fft.ifft(map2d,axis=1),np.arange(nn))
38
39 #np.save('map2d_'+str(idet),map2d[:, :], allow_pickle=True)
```

Line-by-line description:



- Lines (11-16) Creating the arrays
- Lines (18-19) Loading the simulation parameters from data file
- Line 21 Choosing the slice index at which the solution of LLE is taken for the hard seed.
- Line 22 Number of output steps
- Line (23-25) Defining the constant detuning and slow time arrays.
- Line 27 Defining seed
- Line (29-30) Performing simulation. The result is given in the Fourier domain
- Line 35 Plotting the solution
- Line 36 Plotting the solution for selected number of steps
- Line 38 Save data

### E.4.3 Nonlinear dispersion relation

Nonlinear systems often exhibit complex dynamics that can be extremely challenging to analyze. Moreover, despite the existence of many analytical methods, they cannot always be applied to every specific system. Therefore, there is a continual need for new approaches to describe these systems. One such method is the nonlinear dispersion relation (NDR), which was recently introduced for the nonlinear Schrödinger equation (NLSE) in Refs. [190, 175], and we actively utilize it in this thesis. This method helps to readily identify the presence of nonlinear structures and understand how they give rise to dispersive waves in different regimes.

Here, we start with the simplest treatment that however helps to qualitatively understand it. Let us first consider the simplest version of LLE with only dispersion term

$$\frac{\partial A}{\partial t} = i \frac{\partial^2 A}{\partial \varphi^2}. \quad (\text{E.2})$$

Its beauty lies in the algebraic solvability in the Fourier basis

$$A(t, \varphi) = \sum_{\mu} a_{\mu} \exp(i\mu\varphi - i\omega_{\mu}t) \quad (\text{E.3})$$

that yields the famous parabolic dispersion relation

$$\omega_{\mu} = \mu^2 \quad (\text{E.4})$$

that can be readily generalized to take into account higher-order dispersion terms.

## Appendix E. Appendix: numerical simulations with PyCOrE

---

In other words, if the Fourier amplitudes  $a_\mu$  are well defined in the initial moment of time  $t = 0$ , the equation is algebraically solved in the Fourier domain where the dispersion relation is also defined. Now, let's generalize the dispersion relation in the nonlinear regime for the NLSE

$$\frac{\partial A}{\partial t} = i \frac{\partial^2 A}{\partial \varphi^2} + i |A|^2 A. \quad (\text{E.5})$$

In the Fourier space, considering  $\partial_t a_\mu = 0$ , we get

$$a_\mu \omega_\mu = a_\mu \mu^2 - \sum_{\mu_1, \mu_2, \mu_3} a_{\mu_1} a_{\mu_2} a_{\mu_3}^* \delta(\mu_1 + \mu_2 - \mu_3 - \mu). \quad (\text{E.6})$$

This expression already identifies dispersive (first term) and nonlinear (second term) of the cavity. For example, taking into account only the self-phase modulation term, we obtain the modified dispersion relation

$$\omega_\mu = \mu^2 - |a_\mu|^2, \quad (\text{E.7})$$

which yields a well known result: Kerr nonlinearity leads to the frequency shifting to the towards longer wavelength.

In practice, computing this expression analytically is challenging, especially for systems described by the Lugiato-Lefever equation (LLE) or others. However, it can still be obtained via a two-dimensional fast Fourier transform (FFT) of the resolved field dynamics. Essentially, applying the FFT transform to the field  $A$  governed by NLSE or LLE is equivalent to Eq. (E.3), resulting in an expression similar to (E.6). In other words, the Nonlinear Dispersion Relation (NDR) is essentially the Fourier transform of the spatio-temporal diagram along two axes: time ( $t$ ) and space ( $\varphi$ ). This two-dimensional Fourier transform provides information about the effective NDR and reveals insights about linear dispersive and nonlinear waves in the system [190]. To demonstrate this, we consider three examples of field distribution for LLE with third-order dispersion: chaotic state (Fig. E.2a), soliton breather (Fig. E.2b), and stable solitons (Fig. E.2c). By taking the 2D FFT, we obtain the two-dimensional spectra presented in Fig. E.2d-f. For the chaotic state, one can see the dispersion parabola with the highlighted region on top. This region represents solitons with different velocities that interact with each other. In the breather state, NDR shows a set of equally spaced lines, indicating the presence of a coherent structure oscillating in time. The tilt angle indicates the group velocity. A coherent structure, e.g., dissipative Kerr soliton, is represented by a single line under the dispersion curve. The intersection of these lines indicates the additional phase-matching condition and, consequently, the position of the dispersive wave.

First, one needs to simulate field dynamics with fixed detuning. An example of such code is presented below

```
1 # add data folder
2
3 #!/usr/bin/env python3
4 # -*- coding: utf-8 -*-
```

```

5  """
6  Created on Tue May 23 15:25:20 2023
7
8  @author: aleksandrtusnin
9  """
10 import matplotlib.pyplot as plt
11 import numpy as np
12 import sys, os
13 sys.path.append('/Users/aleksandrtusnin/Documents/Projects/PyC0Re/')
14 import PyC0Re_main as pcm
15
16 import time
17 from scipy.constants import c, hbar
18 import scipy.signal as signal
19
20 import scipy as scp
21
22 start_time = time.time()
23
24 map2d_scan = np.zeros([], dtype=complex)#np.load('map2d_scan.npy')
25 d0m_scan = np.zeros([])
26 Pump=np.zeros([], dtype=complex)
27 simulation_parameters={}
28 device = pcm.Resonator()
29
30 simulation_parameters, map2d_scan, d0m_scan, Pump=device.Init_From_File('./
    data/')
31
32 idet = 1163
33 nn = 100000
34 d0m = np.ones(nn)*d0m_scan[idet]
35 simulation_parameters['slow_time']=1e-6
36 simulation_parameters['detuning_array']=d0m
37
38
39 Seed = map2d_scan[idet,:]
40
41 map2d = device.Propagate_PseudoSpectralSAMCLIB(simulation_parameters,
    Pump, Seed=Seed, HardSeed=True)
42
43 np.save('./data/map2d_'+str(idet), map2d[:, :], allow_pickle=True)
44 #%%
45 pcm.Plot_Map(np.fft.ifft(map2d[:, :], axis=1), np.arange(d0m.size))
46 #%%
47 print("--- %s seconds ---" % (time.time() - start_time))

```

Further, we can readily reconstruct the NDR

```

1 import matplotlib.pyplot as plt
2 import numpy as np
3 import sys, os
4 sys.path.append('/Users/aleksandrtusnin/Documents/Projects/PyC0Re/')

```

## Appendix E. Appendix: numerical simulations with PyCOrE

---

```
5
6 import PyCOrE_main as pcm
7 import time
8 plt.rcParams.update({'font.size': 8})
9
10 #map2d_scan=np.load('./data/map2d.npy')
11 #map2d=np.load('./data/map2d_672.npy')
12 map2d=np.load('./data/map2d_758.npy')
13 #d0m=np.load('./data/d0m.npy')
14 map2d_scan = np.zeros([],dtype=complex)
15 d0m_scan = np.zeros([])
16 Pump=np.zeros([],dtype=complex)
17 simulation_parameters={}
18 device = pcm.Resonator()
19
20 simulation_parameters,map2d_scan,d0m_scan,Pump=device.Init_From_File('./
    data/')
21 #det = d0m_scan[672]/2/np.pi
22 det = d0m_scan[758]/2/np.pi
23 nn = map2d[:,0].size
24
25 Time=1e-6
26 hann_window = np.hanning(nn)
27
28 N_modes = map2d[0,:].size
29 phi = np.linspace(0,2*np.pi,N_modes)
30 mu = np.arange(0,N_modes) - N_modes/2
31 slow_freq = (np.arange(0,nn) - nn/2)/Time
32 map2d_direct = np.zeros([nn,N_modes],dtype=complex)
33 ###
34 text_width = 146.8*0.0393701 #in inches
35 fig_width = text_width
36 fig_height = fig_width*6/4
37
38 fig,axs = plt.subplots(ncols=3, nrows=2,figsize=[fig_width,fig_height],
    frameon=False,dpi=300,layout="constrained")
39
40
41 name_list = ['./data/map2d_672.npy','./data/map2d_758.npy','./data/
    map2d_1163.npy']
42 file_iter = 0
43 for name in name_list:
44     map2d=np.load(name)
45     for jj in range(nn):
46         map2d_direct[jj,:] = np.fft.ifft(map2d[jj,:],axis=0)
47     for jj in range(0,N_modes):
48         map2d_direct[:,jj]*= hann_window
49
50
51
52 NDR =(np.fft.fftshift(np.fft.fft2(map2d_direct[:,:])))
53 max_val =np.max(abs(NDR)**2)
```

```

54
55
56
57     ax = axs[0][file_iter]
58     ax.pcolormesh(np.linspace(0,Time,nn)/1e-6,device.phi,abs(np.fft.ifft(
map2d,axis=1).T)**2,cmap='viridis',rasterized=True)
59     ax.set_xticklabels([])
60     ax.set_yticklabels([])
61
62
63
64
65     ax = axs[1][file_iter]
66     colbar=ax.pcolormesh(-mu,-slow_freq/1e9,10*np.log10(np.abs(NDR)**2/
max_val),cmap='afmhot',rasterized=True)
67     colbar.set_clim(-300,0)
68
69     ax.set_xlim(-250,250)
70     ax.set_ylim(-25,10)
71
72
73
74
75     ax.set_xticklabels([])
76     ax.set_yticklabels([])
77
78     file_iter+=1
79
80     axs[0,0].set_ylabel(r'\varphi$')
81     axs[0,0].set_yticks([0,np.pi,2*np.pi])
82     axs[0,1].set_yticks([0,np.pi,2*np.pi])
83     axs[0,2].set_yticks([0,np.pi,2*np.pi])
84     axs[0,0].set_yticklabels([r'$-\pi$',r'$0$',r'$\pi$'])
85
86     axs[0,0].set_xticks([0,Time/1e-6])
87     axs[0,0].set_xticklabels([r'$0$',r'$1$'])
88     axs[0,0].set_xlabel(r'Time ($\mu s$)')
89     axs[0,1].set_xticks([0,Time/1e-6])
90     axs[0,1].set_xticklabels([r'$0$',r'$1$'])
91     axs[0,1].set_xlabel(r'Time ($\mu s$)')
92     axs[0,2].set_xticks([0,Time/1e-6])
93     axs[0,2].set_xticklabels([r'$0$',r'$1$'])
94     axs[0,2].set_xlabel(r'Time ($\mu s$)')
95
96
97
98     axs[1,0].set_ylabel(r'Slow frequency (GHz)')
99     axs[1,0].set_yticks([-20,-10,0,10])
100    axs[1,0].set_yticklabels([r'$-20$',r'$-10$',r'$0$',r'$10$'])
101    axs[1,1].set_yticks([-20,-10,0,10])
102    axs[1,2].set_yticks([-20,-10,0,10])
103

```

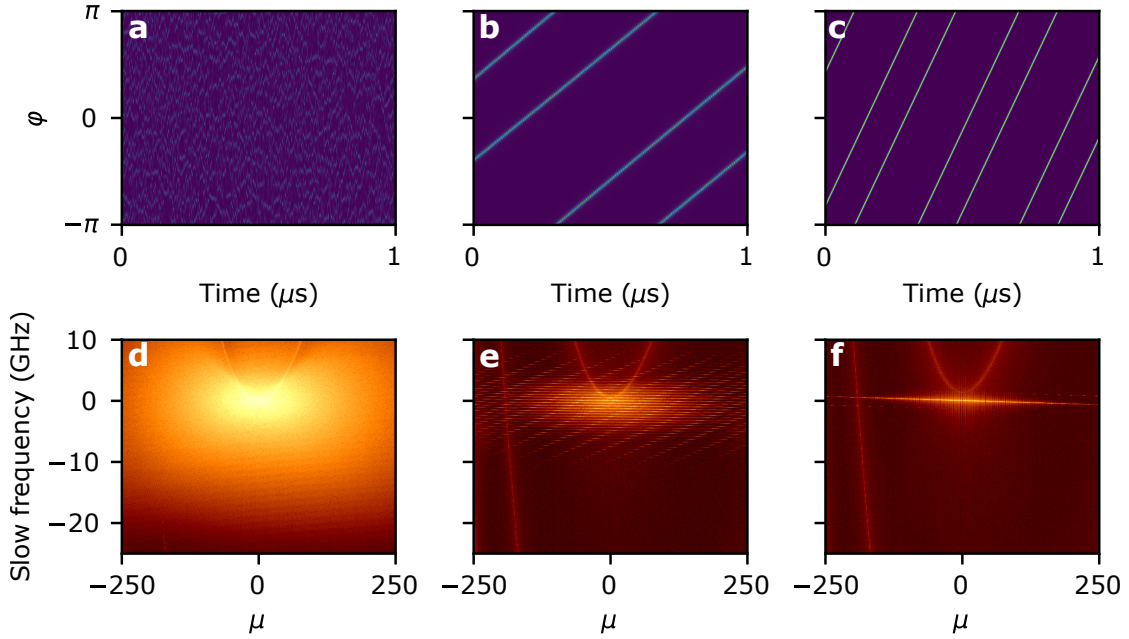


Figure E.2: **Nonlinear states and the corresponding nonlinear dispersion relation.** Spatiotemporal dynamics of the cavity field in the a) chaotic, b) breather, and c) soliton states. Corresponding nonlinear dispersion relation in panels d-f.

```

104 axs[1,0].set_xticks([-250,0,250])
105 axs[1,0].set_xticklabels([r'$-250$',r'$0$',r'$250$'])
106 axs[1,0].set_xlabel(r'$\mu$')
107 axs[1,1].set_xticks([-250,0,250])
108 axs[1,1].set_xticklabels([r'$-250$',r'$0$',r'$250$'])
109 axs[1,1].set_xlabel(r'$\mu$')
110 axs[1,2].set_xticks([-250,0,250])
111 axs[1,2].set_xticklabels([r'$-250$',r'$0$',r'$250$'])
112 axs[1,2].set_xlabel(r'$\mu$')
113 plt.show()

```

As a result, we obtain the results presented in Fig. E.2.

We successfully applied this method in Chapters 1 to investigate localized modulation instability states and Band solitons. In chapter 2, NDR identified the Floquet zones in the numerical experiment and provided further evidence for the analytical results. To investigate quiet points in coupled resonators in chapter 4, NDR qualitatively demonstrated the reduction in noise transfer. In lattices of resonators (chapters 5-7), this method proved invaluable in analyzing the complex dynamics within different resonators.

### E.4.4 Two coupled resonators

In this section, we present an example of nonlinear dynamics simulation in photonic dimer. We provide the simulation code below

```

1 import matplotlib.pyplot as plt
2 plt.rcParams['figure.dpi'] = 150
3 plt.rcParams['savefig.dpi'] = 150
4 import numpy as np
5 import sys, os
6 my_PyCore_dir = os.path.dirname('/Users/aleksandrtusnin/Documents/
   Projects/PyCORE/')
7 sys.path.append(my_PyCore_dir)
8 import PyCORE_main as pcm
9 from scipy.constants import c, hbar
10
11 ###
12 Num_of_modes = 2**9
13 mu = np.arange(-Num_of_modes/2, Num_of_modes/2)
14 N_res = 2
15 Dint = np.zeros([Num_of_modes, N_res])
16 D2 = 4.1e6*2*np.pi
17 Dint[:,0] = (mu**2*D2/2)
18 Dint[:,1] = (mu**2*D2/2)
19 Delta = np.zeros([Num_of_modes, (N_res)])
20 J = 2*1e9*2*np.pi*np.ones([mu.size, (N_res-1)])
21 kappa_ex_ampl = 20e6*2*np.pi
22 kappa_ex = np.zeros([Num_of_modes, N_res])
23 kappa_ex[:,0] = kappa_ex_ampl*np.ones([Num_of_modes])
24 kappa_ex[:,1] = 2*kappa_ex_ampl*np.ones([Num_of_modes])
25 omega = 2*np.pi*193.414489e12
26
27 PhysicalParameters = {'Inter-resonator_coupling': J,
28                       'Resonator detunings' : Delta,
29                       'n0' : 1.9,
30                       'n2' : 2.4e-19, ### m^2/W
31                       'FSR' : 457.9e9 ,
32                       'w0' : omega,
33                       'width' : 2.35e-6,
34                       'height' : 0.8e-6,
35                       'kappa_0' : 20e6*2*np.pi,
36                       'kappa_ex' : kappa_ex,
37                       'Dint' : Dint}
38 crow = pcm.CROW()
39 crow.Init_From_Dict(PhysicalParameters)
40 dNu_ini = -3*1e9
41 dNu_end = 4e9
42
43 nn = 1000
44 dOm = 2*np.pi*np.linspace(dNu_ini, dNu_end, nn)
45 simulation_parameters = {'slow_time' : 1e-6,
46                           'detuning_array' : dOm,

```

## Appendix E. Appendix: numerical simulations with PyCORE

```

47         'noise_level' : 1e-9,
48         'output' : 'map',
49         'absolute_tolerance' : 1e-10,
50         'relative_tolerance' : 1e-12,
51         'max_internal_steps' : 2000}
52
53 P0 = 0.3### W
54
55 Pump = np.zeros([len(mu),N_res],dtype='complex')
56
57 Pump[0,0] = np.sqrt(P0)
58 ###
59 map2d = crow.Propagate_PSEUDO_SPECTRAL_SAMCLIB(simulation_parameters,
60         Pump, BC='OPEN')
61 ###
62 Sin = Pump/np.sqrt(hbar*PhysicalParameters['w0'])
63 Sout = np.zeros_like(map2d)
64
65 Sout = Sin - np.sqrt(crow.kappa_ex)*map2d/Num_of_modes
66
67 fig = plt.figure(figsize=[11.7,4],frameon=False,dpi=150)
68 ax = fig.add_subplot(1,2,1)
69 ax.plot(dOm[10:]/2/np.pi/1e9,np.sum(abs(Sout[10:,:,0])**2,axis=1)/np.max(
70     abs(Sin)**2),label='1$\mathrm{th}$ resonator')
71 ax.set_ylabel(r'Transmission $S_{\mathrm{out}}/S_{\mathrm{in}}$')
72 ax.set_xlabel('Pump detuning (GHz)')
73 plt.legend()
74 ax = fig.add_subplot(1,2,2)
75 ax.plot(dOm[10:]/2/np.pi/1e9,np.sum(abs(Sout[10:,:,1])**2,axis=1)/np.max(
76     abs(Sin)**2),c='r',label='2$\mathrm{nd}$ resonator')
77 ax.set_xlabel('Pump detuning (GHz)')
78 plt.legend()
79 plt.tight_layout()
80 fig.savefig('./trans_trace.pdf')

```

The computed transmission traces through the pump and drop waveguides defined as

$$S_{\text{out}} = S_{\text{in}} - \sqrt{\kappa_{\text{ex}}} A \quad (\text{E.8})$$

shown in Fig. E.3



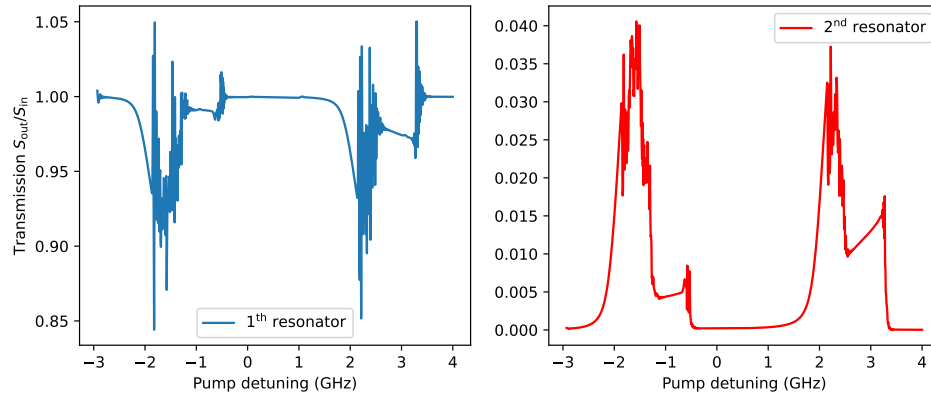


Figure E.3: **Transmission trances in a dimer.** a) Pump waveguide output. b) Drop waveguide output.



# Bibliography

- [1] L. Lam, *Introduction to nonlinear physics*. Springer Science & Business Media, 2003.
- [2] G. Datseris and U. Parlitz, *Nonlinear dynamics: a concise introduction interlaced with code*. Springer Nature, 2022.
- [3] E. N. Lorenz, “Deterministic nonperiodic flow,” *Journal of atmospheric sciences*, vol. 20, no. 2, pp. 130–141, 1963.
- [4] P.A. Davidson, *Turbulence: an introduction for scientists and engineers*. Oxford university press, 2015.
- [5] S. Nazarenko, *Wave turbulence*, vol. 825. Springer Science & Business Media, 2011.
- [6] I. Prigogine, “Time, structure, and fluctuations,” *Science*, vol. 201, no. 4358, pp. 777–785, 1978.
- [7] P. Engels, C. Atherton, and M. A. Hoefer, “Observation of faraday waves in a bose-einstein condensate,” *Phys. Rev. Lett.*, vol. 98, p. 095301, Feb 2007.
- [8] L. A. Lugiato and R. Lefever, “Spatial dissipative structures in passive optical systems,” *Phys. Rev. Lett.*, vol. 58, pp. 2209–2211, May 1987.
- [9] K. Panajotov, M. G. Clerc, and M. Tlidi, “Spatiotemporal chaos and two-dimensional dissipative rogue waves in lugiato-lefever model,” *The European Physical Journal D*, vol. 71, pp. 1–8, 2017.
- [10] A. Scroggie, W. Firth, G. McDonald, M. Tlidi, R. Lefever, and L. Lugiato, “Pattern formation in a passive kerr cavity,” *Chaos, Solitons & Fractals*, vol. 4, no. 8, pp. 1323–1354, 1994. Special Issue: Nonlinear Optical Structures, Patterns, Chaos.
- [11] E. A. Kuznetsov, “Solitons in a parametrically unstable plasma,” *DoSSR*, vol. 236, pp. 575–577, 1977.
- [12] K. Andriopoulos, T. Bountis, K. Van Der Weele, and L. Tsigaridi, “The shape of soliton-like solutions of a higher-order kdv equation describing water waves,” *Journal of Nonlinear Mathematical Physics*, vol. 16, no. supp01, pp. 1–12, 2009.

## Bibliography

---

- [13] R. Richter and I. V. Barashenkov, "Two-dimensional solitons on the surface of magnetic fluids," *Phys. Rev. Lett.*, vol. 94, p. 184503, May 2005.
- [14] Y. K. Chembo and C. R. Menyuk, "Spatiotemporal lugiato-lefever formalism for kerr-comb generation in whispering-gallery-mode resonators," *Phys. Rev. A*, vol. 87, p. 053852, May 2013.
- [15] T. J. Kippenberg, A. L. Gaeta, M. Lipson, and M. L. Gorodetsky, "Dissipative kerr solitons in optical microresonators," *Science*, vol. 361, no. 6402, p. eaan8083, 2018.
- [16] Z. Qi, S. Wang, J. Jaramillo-Villegas, M. Qi, A. M. Weiner, G. D'Aguanno, T. F. Carruthers, and C. R. Menyuk, "Dissipative cnoidal waves (turing rolls) and the soliton limit in microring resonators," *Optica*, vol. 6, no. 9, pp. 1220–1232, 2019.
- [17] V. E. Zakharov, "Wave collapse," *Soviet Physics Uspekhi*, vol. 31, pp. 672–674, jul 1988.
- [18] J. S. Russell, *Report on Waves: Made to the Meetings of the British Association in 1842-43*. 1845.
- [19] N. J. Zabusky and M. D. Kruskal, "Interaction of "solitons" in a collisionless plasma and the recurrence of initial states," *Phys. Rev. Lett.*, vol. 15, pp. 240–243, Aug 1965.
- [20] C. S. Gardner, J. M. Greene, M. D. Kruskal, and R. M. Miura, "Method for solving the korteweg-devries equation," *Phys. Rev. Lett.*, vol. 19, pp. 1095–1097, Nov 1967.
- [21] M. J. Ablowitz and H. Segur, *Solitons and the inverse scattering transform*. SIAM, 1981.
- [22] V. E. Zakharov and A. B. Shabat, "A scheme for integrating the nonlinear equations of mathematical physics by the method of the inverse scattering problem. i," *Funktsional'nyi Analiz i ego Prilozheniya*, vol. 8, no. 3, pp. 43–53, 1974.
- [23] M. J. Ablowitz, D. J. Kaup, A. C. Newell, and H. Segur, "Method for solving the sine-gordon equation," *Phys. Rev. Lett.*, vol. 30, pp. 1262–1264, Jun 1973.
- [24] B. B. Kadomtsev and V. I. Petviashvili, "On the stability of solitary waves in weakly dispersing media," in *Dokl. Akad. Nauk SSSR*, vol. 192, pp. 753–756, 1970.
- [25] Y. S. Kivshar and G. P. Agrawal, *Optical solitons: from fibers to photonic crystals*. Academic press, 2003.
- [26] R. Y. Chiao, E. Garmire, and C. H. Townes, "Self-trapping of optical beams," *Phys. Rev. Lett.*, vol. 13, pp. 479–482, Oct 1964.
- [27] A. Barthelemy, S. Maneuf, and C. Froehly, "Propagation soliton et auto-confinement de faisceaux laser par non linearité optique de kerr," *Optics communications*, vol. 55, no. 3, pp. 201–206, 1985.
- [28] R. Stolen and A. Ashkin, "Optical kerr effect in glass waveguide," *Applied Physics Letters*, vol. 22, no. 6, pp. 294–296, 1973.

- 
- [29] G. P. Agrawal, *Nonlinear Fiber Optics*. Springer, 2000.
- [30] R. Ramaswami, K. Sivarajan, and G. Sasaki, *Optical networks: a practical perspective*. Morgan Kaufmann, 2009.
- [31] D. R. Solli, C. Ropers, P. Koonath, and B. Jalali, “Optical rogue waves,” *nature*, vol. 450, no. 7172, pp. 1054–1057, 2007.
- [32] J. M. Soto-Crespo, N. Devine, and N. Akhmediev, “Integrable turbulence and rogue waves: Breathers or solitons?,” *Phys. Rev. Lett.*, vol. 116, p. 103901, Mar 2016.
- [33] P. Suret, A. Picozzi, and S. Randoux, “Wave turbulence in integrable systems: nonlinear propagation of incoherent optical waves in single-mode fibers,” *Optics express*, vol. 19, no. 18, pp. 17852–17863, 2011.
- [34] A. Picozzi, J. Garnier, T. Hansson, P. Suret, S. Randoux, G. Millot, and D. N. Christodoulides, “Optical wave turbulence: Towards a unified nonequilibrium thermodynamic formulation of statistical nonlinear optics,” *Physics Reports*, vol. 542, no. 1, pp. 1–132, 2014.
- [35] A. Tikan, S. Bielawski, C. Szewaj, S. Randoux, and P. Suret, “Single-shot measurement of phase and amplitude by using a heterodyne time-lens system and ultrafast digital time-holography,” *Nature Photonics*, vol. 12, no. 4, pp. 228–234, 2018.
- [36] P. Grelu and N. Akhmediev, “Dissipative solitons for mode-locked lasers,” *Nature Photonics*, vol. 6, no. 2, pp. 84–92, 2012.
- [37] N. Akhmediev and A. Ankiewicz, “Dissipative solitons in the complex ginzburg-landau and swift-hohenberg equations,” *Dissipative solitons*, pp. 1–17, 2005.
- [38] M. F. Ferreira, *Dissipative Optical Solitons*, vol. 238. Springer Nature, 2022.
- [39] S. Novikov, S. Manakov, L. Pitaevskii, and V. E. Zakharov, *Theory of solitons: the inverse scattering method*. Springer Science & Business Media, 1984.
- [40] G. A. El and A. M. Kamchatnov, “Kinetic equation for a dense soliton gas,” *Phys. Rev. Lett.*, vol. 95, p. 204101, Nov 2005.
- [41] W. Chang, A. Ankiewicz, J. Soto-Crespo, and N. Akhmediev, “Dissipative soliton resonances,” *Physical Review A*, vol. 78, no. 2, p. 023830, 2008.
- [42] A. Ankiewicz and N. Akhmediev, “Comparison of lagrangian approach and method of moments for reducing dimensionality of soliton dynamical systems,” *Chaos: An Interdisciplinary Journal of Nonlinear Science*, vol. 18, no. 3, 2008.
- [43] K. Nozaki and N. Bekki, “Low-dimensional chaos in a driven damped nonlinear schrödinger equation,” *Physica D: Nonlinear Phenomena*, vol. 21, no. 2, pp. 381–393, 1986.

## Bibliography

---

- [44] S. Wabnitz, “Control of soliton train transmission, storage, and clock recovery by cw light injection,” *J. Opt. Soc. Am. B*, vol. 13, pp. 2739–2749, Dec 1996.
- [45] K. J. Blow and N. J. Doran, “Global and local chaos in the pumped nonlinear schrödinger equation,” *Physical review letters*, vol. 52, no. 7, p. 526, 1984.
- [46] M. Haelterman, S. Trillo, and S. Wabnitz, “Dissipative modulation instability in a nonlinear dispersive ring cavity,” *Optics Communications*, vol. 91, no. 5, pp. 401–407, 1992.
- [47] I. Yarutkina, O. Shtyrina, M. Fedoruk, and S. Turitsyn, “Numerical modeling of fiber lasers with long and ultra-long ring cavity,” *Optics Express*, vol. 21, no. 10, pp. 12942–12950, 2013.
- [48] P. Grelu, *Nonlinear optical cavity dynamics: from microresonators to fiber lasers*. John Wiley & Sons, 2015.
- [49] A. Cherenkov, V. Lobanov, and M. Gorodetsky, “Dissipative kerr solitons and cherenkov radiation in optical microresonators with third-order dispersion,” *Physical Review A*, vol. 95, no. 3, p. 033810, 2017.
- [50] M. Karpov, M. H. Pfeiffer, H. Guo, W. Weng, J. Liu, and T. J. Kippenberg, “Dynamics of soliton crystals in optical microresonators,” *Nat. Phys.*, vol. 15, no. 10, pp. 1071–1077, 2019.
- [51] D. V. Skryabin, Z. Fan, A. Villois, and D. N. Puzyrev, “Threshold of complexity and arnold tongues in kerr-ring microresonators,” *Phys. Rev. A*, vol. 103, p. L011502, Jan 2021.
- [52] T. Hansson and S. Wabnitz, “Frequency comb generation beyond the lugiato–lefever equation: multi-stability and super cavity solitons,” *JOSA B*, vol. 32, no. 7, pp. 1259–1266, 2015.
- [53] C. Godey, I. V. Balakireva, A. Coillet, and Y. K. Chembo, “Stability analysis of the spatiotemporal lugiato-lefever model for kerr optical frequency combs in the anomalous and normal dispersion regimes,” *Phys. Rev. A*, vol. 89, p. 063814, Jun 2014.
- [54] S. Wabnitz, “Suppression of interactions in a phase-locked soliton optical memory,” *Opt. Lett.*, vol. 18, no. 8, p. 601, 1993.
- [55] T. Herr, K. Hartinger, J. Riemensberger, C. Wang, E. Gavartin, R. Holzwarth, M. Gorodetsky, and T. Kippenberg, “Universal formation dynamics and noise of kerr-frequency combs in microresonators,” *Nature photonics*, vol. 6, no. 7, pp. 480–487, 2012.
- [56] D. C. Cole, E. S. Lamb, P. Del’Haye, S. A. Diddams, and S. B. Papp, “Soliton crystals in kerr resonators,” *Nat. Photonics*, vol. 11, no. 10, pp. 671–676, 2017.
- [57] E. F. Perez, G. Moille, X. Lu, J. Stone, F. Zhou, and K. Srinivasan, “High-performance kerr microresonator optical parametric oscillator on a silicon chip,” *Nature Communications*, vol. 14, no. 1, p. 242, 2023.

- 
- [58] X. Ji, F. A. S. Barbosa, S. P. Roberts, A. Dutt, J. Cardenas, Y. Okawachi, A. Bryant, A. L. Gaeta, and M. Lipson, "Ultra-low-loss on-chip resonators with sub-milliwatt parametric oscillation threshold," *Optica*, vol. 4, p. 619, June 2017.
- [59] X. Lu, G. Moille, A. Singh, Q. Li, D. A. Westly, A. Rao, S.-P. Yu, T. C. Briles, S. B. Papp, and K. Srinivasan, "Milliwatt-threshold visible-telecom optical parametric oscillation using silicon nanophotonics," *Optica*, vol. 6, p. 1535, Dec. 2019.
- [60] I. V. Barashenkov and Y. S. Smirnov, "Existence and stability chart for the ac-driven, damped nonlinear schrödinger solitons," *Phys. Rev. E*, vol. 54, pp. 5707–5725, Nov 1996.
- [61] M. Anderson, F. Leo, S. Coen, M. Erkintalo, and S. G. Murdoch, "Observations of spatiotemporal instabilities of temporal cavity solitons," *Optica*, vol. 3, pp. 1071–1074, Oct 2016.
- [62] F. Leo, L. Gelens, P. Emplit, M. Haelterman, and S. Coen, "Dynamics of one-dimensional Kerr cavity solitons," *Opt. Express*, vol. 21, no. 7, p. 9180, 2013.
- [63] S. Coulibaly, M. Taki, A. Bendahmane, G. Millot, B. Kibler, and M. G. Clerc, "Turbulence-induced rogue waves in kerr resonators," *Phys. Rev. X*, vol. 9, p. 011054, Mar 2019.
- [64] H. Guo, M. Karpov, E. Lucas, A. Kordts, M. H. Pfeiffer, V. Brasch, G. Lihachev, V. E. Lobanov, M. L. Gorodetsky, and T. J. Kippenberg, "Universal dynamics and deterministic switching of dissipative kerr solitons in optical microresonators," *Nat. Phys.*, vol. 13, no. 1, pp. 94–102, 2017.
- [65] A. Lukashchuk, J. Riemensberger, A. Tusnin, J. Liu, and T. J. Kippenberg, "Chaotic microcomb-based parallel ranging," *Nature Photonics*, vol. 17, no. 9, pp. 814–821, 2023.
- [66] Y.-C. Ma, "The perturbed plane-wave solutions of the cubic schrödinger equation," *Studies in Applied Mathematics*, vol. 60, no. 1, pp. 43–58, 1979.
- [67] B. Kibler, J. Fatome, C. Finot, G. Millot, G. Genty, B. Wetzol, N. Akhmediev, F. Dias, and J. M. Dudley, "Observation of kuznetsov-ma soliton dynamics in optical fibre," *Sci. Rep.*, vol. 2, p. 463, 2012.
- [68] I. S. Chekhovskoy, O. V. Shtyrina, M. P. Fedoruk, S. B. Medvedev, and S. K. Turitsyn, "Nonlinear Fourier Transform for Analysis of Coherent Structures in Dissipative Systems," *Phys. Rev. Lett.*, vol. 122, no. 15, p. 153901, 2019.
- [69] S. K. Turitsyn, I. S. Chekhovskoy, and M. P. Fedoruk, "Nonlinear fourier transform for characterization of the coherent structures in optical microresonators," *Optics Letters*, vol. 45, no. 11, pp. 3059–3062, 2020.
- [70] S. K. Turitsyn, I. S. Chekhovskoy, and M. P. Fedoruk, "Nonlinear fourier transform for analysis of optical spectral combs," *Phys. Rev. E*, vol. 103, p. L020202, Feb 2021.

## Bibliography

---

- [71] T. Hansson, D. Modotto, and S. Wabnitz, “Dynamics of the modulational instability in microresonator frequency combs,” *Phys. Rev. A*, vol. 88, p. 023819, Aug 2013.
- [72] V. Lobanov, G. Lihachev, T. J. Kippenberg, and M. Gorodetsky, “Frequency combs and platicons in optical microresonators with normal gvd,” *Opt. Express*, vol. 23, no. 6, p. 7713, 2015.
- [73] P. Parra-Rivas, D. Gomila, E. Knobloch, S. Coen, and L. Gelens, “Origin and stability of dark pulse kerr combs in normal dispersion resonators,” *Opt. Lett.*, vol. 41, pp. 2402–2405, Jun 2016.
- [74] X. Xue, Y. Xuan, Y. Liu, P. H. Wang, S. Chen, J. Wang, D. E. Leaird, M. Qi, and A. M. Weiner, “Mode-locked dark pulse kerr combs in normal-dispersion microresonators,” *Nat. Photonics*, vol. 9, no. 9, pp. 594–600, 2015.
- [75] X. Xue, Y. Xuan, P.-H. Wang, Y. Liu, D. E. Leaird, M. Qi, and A. M. Weiner, “Normal-dispersion microcombs enabled by controllable mode interactions,” *Laser Photonics Rev.*, vol. 9, no. 4, pp. L23–L28, 2015.
- [76] M. H. Anderson, W. Weng, G. Lihachev, A. Tikan, J. Liu, and T. J. Kippenberg, “Zero dispersion kerr solitons in optical microresonators,” *Nature Communications*, vol. 13, no. 1, p. 4764, 2022.
- [77] T. Herr, V. Brasch, J. D. Jost, C. Y. Wang, N. M. Kondratiev, M. L. Gorodetsky, and T. J. Kippenberg, “Temporal solitons in optical microresonators,” *Nature Photonics*, vol. 8, no. 2, pp. 145–152, 2014.
- [78] P. Trocha, M. Karpov, D. Ganin, M. H. P. Pfeiffer, A. Kordts, S. Wolf, J. Krockenberger, P. Marin-Palomo, C. Weimann, S. Randel, W. Freude, T. J. Kippenberg, and C. Koos, “Ultrafast optical ranging using microresonator soliton frequency combs,” *Science*, vol. 359, no. 6378, pp. 887–891, 2018.
- [79] J. Riemensberger, A. Lukashchuk, M. Karpov, W. Weng, E. Lucas, J. Liu, and T. J. Kippenberg, “Massively parallel coherent laser ranging using a soliton microcomb,” *Nature*, vol. 581, no. 7807, pp. 164–170, 2020.
- [80] P. Marin-Palomo, J. N. Kemal, M. Karpov, A. Kordts, J. Pfeifle, M. H. P. Pfeiffer, P. Trocha, S. Wolf, V. Brasch, M. H. Anderson, R. Rosenberger, K. Vijayan, W. Freude, T. J. Kippenberg, and C. Koos, “Microresonator-based solitons for massively parallel coherent optical communications,” *Nature*, vol. 546, p. 274, 06 2017.
- [81] D. T. Spencer, T. Drake, T. C. Briles, J. Stone, L. C. Sinclair, C. Fredrick, Q. Li, D. Westly, B. R. Ilic, A. Bluestone, N. Volet, T. Komljenovic, L. Chang, S. H. Lee, D. Y. Oh, M.-G. Suh, K. Y. Yang, M. H. P. Pfeiffer, T. J. Kippenberg, E. Norberg, L. Theogarajan, K. Vahala, N. R. Newbury, K. Srinivasan, J. E. Bowers, S. A. Diddams, and S. B. Papp, “An optical-frequency synthesizer using integrated photonics,” *Nature*, vol. 557, pp. 81–85, May 2018.



- [82] J. Feldmann, N. Youngblood, M. Karpov, H. Gehring, X. Li, M. Stappers, M. Le Gallo, X. Fu, A. Lukashchuk, A. S. Raja, *et al.*, “Parallel convolutional processing using an integrated photonic tensor core,” *Nature*, vol. 589, no. 7840, pp. 52–58, 2021.
- [83] J. Liu, E. Lucas, A. S. Raja, J. He, J. Riemensberger, R. N. Wang, M. Karpov, H. Guo, R. Bouchand, and T. J. Kippenberg, “Photonic microwave generation in the x- and k-band using integrated soliton microcombs,” *Nature Photonics*, vol. 14, no. 8, pp. 486–491, 2020.
- [84] O. Boada, A. Celi, J. I. Latorre, and M. Lewenstein, “Quantum simulation of an extra dimension,” *Phys. Rev. Lett.*, vol. 108, p. 133001, Mar 2012.
- [85] F. Morichetti, C. Ferrari, A. Canciamilla, and A. Melloni, “The first decade of coupled resonator optical waveguides: bringing slow light to applications,” *Laser & Photonics Reviews*, vol. 6, no. 1, pp. 74–96, 2012.
- [86] O. Klein, “Quantum theory and five-dimensional relativity theory,” in *The Oskar Klein Memorial Lectures: Vol 1: Lectures by CN Yang and S Weinberg*, pp. 67–80, World Scientific, 1991.
- [87] P. S. Wesson, *Five-dimensional physics: classical and quantum consequences of Kaluza-Klein cosmology*. World Scientific, 2006.
- [88] T. Ozawa, H. M. Price, A. Amo, N. Goldman, M. Hafezi, L. Lu, M. C. Rechtsman, D. Schuster, J. Simon, O. Zilberberg, and I. Carusotto, “Topological photonics,” *Rev. Mod. Phys.*, vol. 91, p. 015006, Mar 2019.
- [89] A. Aspuru-Guzik and P. Walther, “Photonic quantum simulators,” *Nat. Phys.*, vol. 8, no. 4, pp. 285–291, 2012.
- [90] A. Regensburger, C. Bersch, B. Hinrichs, G. Onishchukov, A. Schreiber, C. Silberhorn, and U. Peschel, “Photon propagation in a discrete fiber network: An interplay of coherence and losses,” *Phys. Rev. Lett.*, vol. 107, p. 233902, Dec 2011.
- [91] M. Wimmer, M.-A. Miri, D. Christodoulides, and U. Peschel, “Observation of bloch oscillations in complex pt-symmetric photonic lattices,” *Sci. Rep.*, vol. 5, p. 17760, 2015.
- [92] A. Regensburger, C. Bersch, M.-A. Miri, G. Onishchukov, D. N. Christodoulides, and U. Peschel, “Parity–time synthetic photonic lattices,” *Nature*, vol. 488, no. 7410, pp. 167–171, 2012.
- [93] I. D. Vatnik, A. Tikan, G. Onishchukov, D. V. Churkin, and A. A. Sukhorukov, “Anderson localization in synthetic photonic lattices,” *Sci. Rep.*, vol. 7, no. 4301, 2017.
- [94] A. V. Pankov, I. D. Vatnik, D. V. Churkin, and S. A. Derevyanko, “Anderson localization in synthetic photonic lattice with random coupling,” *Opt. Express*, vol. 27, no. 4, pp. 4424–4434, 2019.

## Bibliography

---

- [95] L. Lu, J. D. Joannopoulos, and M. Soljačić, “Topological photonics,” *Nature Photon.*, vol. 8, no. 11, p. 821, 2014.
- [96] A. B. Khanikaev and G. Shvets, “Two-dimensional topological photonics,” *Nature Photon.*, vol. 11, no. 12, pp. 763–773, 2017.
- [97] T. Ozawa, H. M. Price, A. Amo, N. Goldman, M. Hafezi, L. Lu, M. C. Rechtsman, D. Schuster, J. Simon, O. Zilberberg, and I. Carusotto, “Topological photonics,” *Rev. Mod. Phys.*, vol. 91, p. 015006, Mar 2019.
- [98] Q. Lin, M. Xiao, L. Yuan, and S. Fan, “Photonic Weyl point in a two-dimensional resonator lattice with a synthetic frequency dimension,” *Nat. Comm.*, vol. 7, pp. 1–7, 2016.
- [99] A. Dutt, M. Minkov, Q. Lin, L. Yuan, D. A. B. Miller, and S. Fan, “Experimental band structure spectroscopy along a synthetic dimension,” *Nat. Commun.*, vol. 10, no. 3122, 2019.
- [100] Z. Dong, X. Chen, A. Dutt, and L. Yuan, “Topological dissipative photonics and topological insulator lasers in synthetic time-frequency dimensions,” *arXiv preprint arXiv:2304.11660*, 2023.
- [101] E. Lustig, S. Weimann, Y. Plotnik, Y. Lumer, M. A. Bandres, A. Szameit, and M. Segev, “Photonic topological insulator in synthetic dimensions,” *Nature*, vol. 567, no. 7748, pp. 356–360, 2019.
- [102] Z. Yang, E. Lustig, G. Harari, Y. Plotnik, Y. Lumer, M. A. Bandres, and M. Segev, “Mode-locked topological insulator laser utilizing synthetic dimensions,” *Phys. Rev. X*, vol. 10, p. 011059, Mar 2020.
- [103] W. Zhang and X. Zhang, “Quadrupole topological phases in the zero-dimensional optical cavity,” *Europhysics Letters*, vol. 131, no. 2, p. 24004, 2020.
- [104] A. Dutt, Q. Lin, L. Yuan, M. Minkov, M. Xiao, and S. Fan, “A single photonic cavity with two independent physical synthetic dimensions,” *Science*, vol. 367, no. 6473, pp. 59–64, 2020.
- [105] L. Fan, K. Wang, H. Wang, A. Dutt, and S. Fan, “Experimental realization of convolution processing in photonic synthetic frequency dimensions,” *arXiv preprint arXiv:2305.03250*, 2023.
- [106] L. Yuan, Q. Lin, M. Xiao, and S. Fan, “Synthetic dimension in photonics,” *Optica*, vol. 5, no. 11, pp. 1396–1405, 2018.
- [107] A. Schreiber, K. N. Cassemiro, V. Potoček, A. Gábris, P. J. Mosley, E. Andersson, I. Jex, and C. Silberhorn, “Photons walking the line: a quantum walk with adjustable coin operations,” *Phys. Rev. Lett.*, vol. 104, no. 5, p. 050502, 2010.

- 
- [108] T. Ozawa, H. M. Price, N. Goldman, O. Zilberberg, and I. Carusotto, “Synthetic dimensions in integrated photonics: From optical isolation to four-dimensional quantum hall physics,” *Phys. Rev. A*, vol. 93, no. 4, p. 043827, 2016.
- [109] L. Yuan, Y. Shi, and S. Fan, “Photonic gauge potential in a system with a synthetic frequency dimension,” *Opt. Lett.*, vol. 41, no. 4, pp. 741–744, 2016.
- [110] L. Yuan and S. Fan, “Bloch oscillation and unidirectional translation of frequency in a dynamically modulated ring resonator,” *Optica*, vol. 3, no. 9, pp. 1014–1018, 2016.
- [111] K. Wang, A. Dutt, K. Y. Yang, C. C. Wojcik, J. Vučković, and S. Fan, “Generating arbitrary topological windings of a non-hermitian band,” *Science*, vol. 371, no. 6535, pp. 1240–1245, 2021.
- [112] J. Fan, A. Migdall, and J. Taylor, “Imaging topological edge states in silicon photonics,” *Nature Photonics*, vol. 7, no. 12, pp. 1001–1005, 2013.
- [113] G. Harari, M. A. Bandres, Y. Lumer, M. C. Rechtsman, Y. D. Chong, M. Khajavikhan, D. N. Christodoulides, and M. Segev, “Topological insulator laser: theory,” *Science*, vol. 359, no. 6381, p. eaar4003, 2018.
- [114] M. A. Bandres, S. Wittek, G. Harari, M. Parto, J. Ren, M. Segev, D. N. Christodoulides, and M. Khajavikhan, “Topological insulator laser: Experiments,” *Science*, vol. 359, no. 6381, p. eaar4005, 2018.
- [115] S. Xia, D. Jukić, N. Wang, D. Smirnova, L. Smirnov, L. Tang, D. Song, A. Szameit, D. Leykam, J. Xu, *et al.*, “Nontrivial coupling of light into a defect: the interplay of nonlinearity and topology,” *Light: Science & Applications*, vol. 9, no. 1, pp. 1–10, 2020.
- [116] L. J. Maczewsky, M. Heinrich, M. Kremer, S. K. Ivanov, M. Ehrhardt, F. Martinez, Y. V. Kartashov, V. V. Konotop, L. Torner, D. Bauer, *et al.*, “Nonlinearity-induced photonic topological insulator,” *Science*, vol. 370, no. 6517, pp. 701–704, 2020.
- [117] S. Mukherjee and M. C. Rechtsman, “Observation of unidirectional solitonlike edge states in nonlinear floquet topological insulators,” *Physical Review X*, vol. 11, no. 4, p. 041057, 2021.
- [118] D. Smirnova, D. Leykam, Y. Chong, and Y. Kivshar, “Nonlinear topological photonics,” *Appl. Phys. Rev.*, vol. 7, no. 2, p. 021306, 2020.
- [119] X. Ji, S. Roberts, M. Corato-Zanarella, and M. Lipson, “Methods to achieve ultra-high quality factor silicon nitride resonators,” *APL Photonics*, vol. 6, no. 7, p. 071101, 2021.
- [120] J. Liu, G. Huang, R. N. Wang, J. He, A. S. Raja, T. Liu, N. J. Engelsen, and T. J. Kippenberg, “High-yield, wafer-scale fabrication of ultralow-loss, dispersion-engineered silicon nitride photonic circuits,” *Nature communications*, vol. 12, no. 1, pp. 1–9, 2021.

## Bibliography

---

- [121] X. Xue, X. Zheng, and B. Zhou, “Super-efficient temporal solitons in mutually coupled optical cavities,” *Nat. Photonics*, vol. 13, no. 9, pp. 616–622, 2019.
- [122] A. Tikan, J. Riemensberger, K. Komagata, S. Hönl, M. Churaev, C. Skehan, H. Guo, R. N. Wang, J. Liu, P. Seidler, *et al.*, “Emergent nonlinear phenomena in a driven dissipative photonic dimer,” *Nat. Phys.*, pp. 604–610, 2021.
- [123] Ó. B. Helgason, F. R. Arteaga-Sierra, Z. Ye, K. Twayana, P. A. Andrekson, M. Karlsson, J. Schröder, and V. Torres-Company, “Dissipative solitons in photonic molecules,” *Nature Photonics*, vol. 15, no. 4, pp. 305–310, 2021.
- [124] Ó. B. Helgason, M. Girardi, Z. Ye, F. Lei, J. Schröder, and V. Torres-Company, “Surpassing the nonlinear conversion efficiency of soliton microcombs,” *Nature Photonics*, 2023.
- [125] Q.-X. Ji, W. Jin, L. Wu, Y. Yu, Z. Yuan, W. Zhang, M. Gao, B. Li, H. Wang, C. Xiang, J. Guo, A. Feshali, M. Paniccia, V. S. Ilchenko, A. B. Matsko, J. E. Bowers, and K. J. Vahala, “Engineered zero-dispersion microcombs using cmos-ready photonics,” *Optica*, vol. 10, pp. 279–285, Feb 2023.
- [126] A. Yariv, Y. Xu, R. K. Lee, and A. Scherer, “Coupled-resonator optical waveguide: a proposal and analysis,” *Opt. Lett.*, vol. 24, pp. 711–713, Jun 1999.
- [127] S. Mittal, G. Moille, K. Srinivasan, Y. K. Chembo, and M. Hafezi, “Topological frequency combs and nested temporal solitons,” *Nat. Phys.*, pp. 1169–1176, 2021.
- [128] T. Ozawa and I. Carusotto, “Synthetic dimensions with magnetic fields and local interactions in photonic lattices,” *Phys. Rev. Lett.*, vol. 118, no. 1, p. 013601, 2017.
- [129] L. Yuan, A. Dutt, M. Qin, S. Fan, and X. Chen, “Creating locally interacting hamiltonians in the synthetic frequency dimension for photons,” *Photon. Res.*, vol. 8, pp. B8–B14, Sep 2020.
- [130] L. Barbiero, L. Chomaz, S. Nascimbene, and N. Goldman, “Bose-hubbard physics in synthetic dimensions from interaction trotterization,” *Phys. Rev. Res.*, vol. 2, p. 043340, Dec 2020.
- [131] W. Stephan, “Suppression of soliton interactions by phase modulation,” *Electron. Lett.*, vol. 29, no. 19, pp. 31–33, 1993.
- [132] Y. HE, J. Ling, M. Li, and Q. Lin, “Perfect soliton crystals on demand,” in *Conference on Lasers and Electro-Optics*, p. SF2B.1, Optica Publishing Group, 2020.
- [133] A. U. Nielsen, Y. Xu, C. Todd, M. Ferré, M. G. Clerc, S. Coen, S. G. Murdoch, and M. Erkintalo, “Nonlinear localization of dissipative modulation instability,” *Phys. Rev. Lett.*, vol. 127, p. 123901, Sep 2021.

- 
- [134] J. K. Jang, M. Erkintalo, S. Coen, and S. G. Murdoch, “Temporal tweezing of light through the trapping and manipulation of temporal cavity solitons,” *Nat. Commun.*, vol. 6, pp. 1–7, 2015.
- [135] B. Y. Kim, Y. Okawachi, J. K. Jang, M. Yu, X. Ji, Y. Zhao, C. Joshi, M. Lipson, and A. L. Gaeta, “Turn-key, high-efficiency kerr comb source,” *Opt. Lett.*, vol. 44, no. 18, p. 4475, 2019.
- [136] S. Coulibaly, M. Taki, A. Bendahmane, G. Millot, B. Kibler, and M. G. Clerc, “Turbulence-induced rogue waves in kerr resonators,” *Phys. Rev. X*, vol. 9, no. 2, p. 11054, 2019.
- [137] Y. Lumer, M. C. Rechtsman, Y. Plotnik, and M. Segev, “Instability of bosonic topological edge states in the presence of interactions,” *Phys. Rev. A*, vol. 94, p. 021801(R), Aug 2016.
- [138] D. D. Solnyshkov, O. Bleu, B. Teklu, and G. Malpuech, “Chirality of topological gap solitons in bosonic dimer chains,” *Phys. Rev. Lett.*, vol. 118, p. 023901, Jan 2017.
- [139] M. Zhang, B. Buscaino, C. Wang, A. Shams-Ansari, C. Reimer, R. Zhu, J. M. Kahn, and M. Lončar, “Broadband electro-optic frequency comb generation in a lithium niobate microring resonator,” *Nature*, vol. 568, no. 7752, pp. 373–377, 2019.
- [140] K. P. Ho and J. M. Kahn, “Optical Frequency Comb Generator Using Phase Modulation in Amplified Circulating Loop,” *IEEE Photonics Technol. Lett.*, vol. 5, no. 6, pp. 721–725, 1993.
- [141] M. Kourogi, N. Ken’ichi, and M. Ohtsu, “Wide-Span Optical Frequency Comb Generator for Accurate Optical Frequency Difference Measurement,” *IEEE J. Quantum Electron.*, vol. 29, no. 10, pp. 2693–2701, 1993.
- [142] L. D. Tzuan, K. Fang, P. Nussenzveig, S. Fan, and M. Lipson, “Non-reciprocal phase shift induced by an effective magnetic flux for light,” *Nat. Photonics*, vol. 8, no. 9, pp. 701–705, 2014.
- [143] D. Agafontsev and V. E. Zakharov, “Integrable turbulence and formation of rogue waves,” *Nonlinearity*, vol. 28, no. 8, p. 2791, 2015.
- [144] A. E. Kraych, D. Agafontsev, S. Randoux, and P. Suret, “Statistical properties of the nonlinear stage of modulation instability in fiber optics,” *Phys. Rev. Lett.*, vol. 123, no. 9, p. 093902, 2019.
- [145] Y. He, Q.-F. Yang, J. Ling, R. Luo, H. Llang, M. Li, B. Shen, H. Wang, K. Vahala, and Q. Lin, “Self-starting bi-chromatic linbo3 microcomb,” *Optica*, vol. 6, no. 9, 2019.
- [146] A. W. Bruch, X. Liu, Z. Gong, J. B. Surya, M. Li, C.-L. Zou, and H. X. Tang, “Pockels soliton microcomb,” *Nature Photonics*, vol. 15, no. 1, pp. 21–27, 2021.
- [147] D. J. Wilson, K. Schneider, S. Hönl, M. Anderson, Y. Baumgartner, L. Czornomaz, T. J. Kippenberg, and P. Seidler, “Integrated gallium phosphide nonlinear photonics,” *Nat. Photonics*, vol. 14, no. 1, pp. 57–62, 2020.

## Bibliography

---

- [148] Z. Gong, X. Liu, Y. Xu, M. Xu, J. B. Surya, J. Lu, A. Bruch, C. Zou, and H. X. Tang, “Soliton microcomb generation at 2  $\mu\text{m}$  in z-cut lithium niobate microring resonators,” *Opt. Lett.*, vol. 44, no. 12, p. 3182, 2019.
- [149] N. Englebert, N. Goldman, M. Erkintalo, N. Mostaan, S.-P. Gorza, F. Leo, and J. Fatome, “Bloch oscillations of coherently driven dissipative solitons in a synthetic dimension,” *Nature Physics*, pp. 1–8, 2023.
- [150] S.-W. Huang, H. Liu, J. Yang, M. Yu, D.-L. Kwong, and C. Wong, “Smooth and flat phase-locked kerr frequency comb generation by higher order mode suppression,” *Scientific reports*, vol. 6, no. 1, pp. 1–7, 2016.
- [151] F. m. c. Copie, M. Conforti, A. Kudlinski, A. Mussot, and S. Trillo, “Competing turing and faraday instabilities in longitudinally modulated passive resonators,” *Phys. Rev. Lett.*, vol. 116, p. 143901, Apr 2016.
- [152] S. Coen and M. Haelterman, “Modulational instability induced by cavity boundary conditions in a normally dispersive optical fiber,” *Phys. Rev. Lett.*, vol. 79, pp. 4139–4142, Nov 1997.
- [153] K. Staliunas, C. Hang, and V. V. Konotop, “Parametric patterns in optical fiber ring nonlinear resonators,” *Phys. Rev. A*, vol. 88, p. 023846, Aug 2013.
- [154] A. U. Nielsen, B. Garbin, S. Coen, S. G. Murdoch, and M. Erkintalo, “Invited article: Emission of intense resonant radiation by dispersion-managed kerr cavity solitons,” *APL photonics*, vol. 3, no. 12, 2018.
- [155] M. Conforti, A. Mussot, A. Kudlinski, and S. Trillo, “Modulational instability in dispersion oscillating fiber ring cavities,” *Optics Letters*, vol. 39, no. 14, p. 4200, 2014.
- [156] M. J. Ablowitz and J. T. Cole, “Transverse instability of rogue waves,” *Phys. Rev. Lett.*, vol. 127, p. 104101, Sep 2021.
- [157] V. Zakharov and A. Rubenchik, “Instability of waveguides and solitons in nonlinear media,” *Zh. Eksp. Teor. Fiz*, vol. 65, no. 3, pp. 997–1011, 1973.
- [158] M. H. Anderson, A. Tikan, A. Tusnin, J. Riemensberger, A. Davydova, R. N. Wang, and T. J. Kippenberg, “Dissipative solitons and switching waves in dispersion-modulated kerr cavities,” *Phys. Rev. X*, vol. 13, p. 011040, Mar 2023.
- [159] S. Kelly, “Characteristic sideband instability of periodically amplified average soliton,” *Electron. Lett*, vol. 28, no. 8, pp. 806–807, 1992.
- [160] W. Zhao, C. Yang, and M. Shen, “Enhanced kelly sidebands of mode-locking fiber lasers for efficient terahertz signal generation,” *Optics & Laser Technology*, vol. 137, p. 106802, 2021.

- 
- [161] C. Wang, B. Chang, T. Tan, C. Qin, Z. Wu, G. Yan, B. Fu, Y. Wu, Y. Rao, H. Xia, *et al.*, “High energy and low noise soliton fiber laser comb based on nonlinear merging of kelly sidebands,” *Optics Express*, vol. 30, no. 13, pp. 23556–23567, 2022.
- [162] L. Chang, S. Liu, and J. E. Bowers, “Integrated optical frequency comb technologies,” *Nat. Photon.*, vol. 16, pp. 95–108, Feb. 2022.
- [163] A. Hermans, K. Van Gasse, and B. Kuyken, “On-chip optical comb sources,” *APL Photonics*, vol. 7, p. 100901, Oct. 2022.
- [164] T. J. Kippenberg, S. M. Spillane, and K. J. Vahala, “Kerr-Nonlinearity Optical Parametric Oscillation in an Ultrahigh- Q Toroid Microcavity,” *Phys. Rev. Lett.*, vol. 93, p. 083904, Aug. 2004.
- [165] X. Lu, G. Moille, A. Rao, D. A. Westly, and K. Srinivasan, “On-chip optical parametric oscillation into the visible: Generating red, orange, yellow, and green from a near-infrared pump,” *Optica*, vol. 7, p. 1417, Oct. 2020.
- [166] Y. Okawachi, M. Yu, J. K. Jang, X. Ji, Y. Zhao, B. Y. Kim, M. Lipson, and A. L. Gaeta, “Demonstration of chip-based coupled degenerate optical parametric oscillators for realizing a nanophotonic spin-glass,” *Nat Commun*, vol. 11, p. 4119, Aug. 2020.
- [167] J. R. Stone, X. Lu, G. Moille, and K. Srinivasan, “Efficient chip-based optical parametric oscillators from 590 to 1150 nm,” *APL Photonics*, vol. 7, p. 121301, Dec. 2022.
- [168] Y. Sun, J. Wu, M. Tan, X. Xu, Y. Li, R. Morandotti, A. Mitchell, and D. J. Moss, “Applications of optical microcombs,” *Adv. Opt. Photon.*, vol. 15, p. 86, Mar. 2023.
- [169] P. Marin-Palomo, J. N. Kemal, M. Karpov, A. Kordts, J. Pfeifle, M. H. Pfeiffer, P. Trocha, S. Wolf, V. Brasch, M. H. Anderson, *et al.*, “Microresonator-based solitons for massively parallel coherent optical communications,” *Nature*, vol. 546, no. 7657, pp. 274–279, 2017.
- [170] T. Brydges, A. S. Raja, A. Gelmini, G. Lihachev, A. Petitjean, A. Siddharth, H. Tian, R. N. Wang, S. A. Bhave, H. Zbinden, T. J. Kippenberg, and R. Thew, “Integrated photon-pair source with monolithic piezoelectric frequency tunability,” *Phys. Rev. A*, vol. 107, p. 052602, May 2023.
- [171] Q. Lin, T. J. Johnson, R. Perahia, C. P. Michael, and O. J. Painter, “A proposal for highly tunable optical parametric oscillation in silicon micro-resonators,” *Opt. Express*, vol. 16, p. 10596, July 2008.
- [172] N. L. B. Sayson, K. E. Webb, S. Coen, M. Erkintalo, and S. G. Murdoch, “Widely tunable optical parametric oscillation in a Kerr microresonator,” *Opt. Lett.*, vol. 42, p. 5190, Dec. 2017.

## Bibliography

---

- [173] N. L. B. Sayson, T. Bi, V. Ng, H. Pham, L. S. Trainor, H. G. L. Schwefel, S. Coen, M. Erkintalo, and S. G. Murdoch, “Octave-spanning tunable parametric oscillation in crystalline Kerr microresonators,” *Nat. Photonics*, vol. 13, pp. 701–706, Oct. 2019.
- [174] X. Yi, Q. F. Yang, X. Zhang, K. Y. Yang, X. Li, and K. Vahala, “Single-mode dispersive waves and soliton microcomb dynamics,” *Nature Communications*, vol. 8, Mar. 2017.
- [175] A. Tikan, F. Bonnefoy, G. Ducrozet, G. Prabhudesai, G. Michel, A. Cazaubiel, E. Falcon, F. Copie, S. Randoux, and P. Suret, “Nonlinear dispersion relation in integrable turbulence,” *Scientific Reports*, vol. 12, no. 1, p. 10386, 2022.
- [176] A. B. Matsko and L. Maleki, “On timing jitter of mode locked Kerr frequency combs,” *Opt. Express*, vol. 21, p. 28862, Nov. 2013.
- [177] M. H. Anderson, R. Bouchand, J. Liu, W. Weng, E. Obrzud, T. Herr, and T. J. Kippenberg, “Photonic chip-based resonant supercontinuum via pulse-driven kerr microresonator solitons,” *Optica*, vol. 8, no. 6, pp. 771–779, 2021.
- [178] F. Lei, Z. Ye, Ó. B. Helgason, A. Fülöp, M. Girardi, and V. Torres-Company, “Optical linewidth of soliton microcombs,” *Nat Commun*, vol. 13, p. 3161, June 2022.
- [179] W. H. Press, S. A. Teukolsky, W. T. Vetterling, and B. P. Flannery, *Numerical recipes 3rd edition: The art of scientific computing*. Cambridge university press, 2007.
- [180] E. Lucas, S.-P. Yu, T. C. Briles, D. R. Carlson, and S. B. Papp, “Tailoring microcombs with inverse-designed, meta-dispersion microresonators,” *Nature Photonics*, 2023.
- [181] T. Hansson, D. Modotto, and S. Wabnitz, “On the numerical simulation of Kerr frequency combs using coupled mode equations,” *Opt. Commun.*, vol. 312, pp. 134–136, 2014.
- [182] A. Yariv, “Critical coupling and its control in optical waveguide-ring resonator systems,” *IEEE Photonics Technol. Lett.*, vol. 14, no. 4, pp. 483–485, 2002.
- [183] A. B. Matsko and V. S. Ilchenko, “Optical resonators with whispering-gallery modes-part i: basics,” *IEEE J. Sel. Top. Quantum Electron.*, vol. 12, no. 1, pp. 3–14, 2006.
- [184] S. A. Miller, Y. Okawachi, S. Ramelow, K. Luke, A. Dutt, A. Farsi, A. L. Gaeta, and M. Lipson, “Tunable frequency combs based on dual microring resonators,” *Opt. Express*, vol. 23, no. 16, pp. 21527–21540, 2015.
- [185] M. A. Miri and A. Alù, “Exceptional points in optics and photonics,” *Science*, vol. 363, p. eaar7709, 2019.
- [186] A. K. Tusnin, A. M. Tikan, and T. J. Kippenberg, “Nonlinear states and dynamics in a synthetic frequency dimension,” *Phys. Rev. A*, vol. 102, p. 023518, Aug 2020.
- [187] E. Lucas, M. Karpov, H. Guo, M. L. Gorodetsky, and T. J. Kippenberg, “Breathing dissipative solitons in optical microresonators,” *Nat. Commun.*, vol. 8, no. 736, pp. 1–11, 2017.



- 
- [188] C. Bao, Y. Xuan, D. E. Leaird, S. Wabnitz, M. Qi, and A. M. Weiner, “Spatial mode-interaction induced single soliton generation in microresonators,” *Optica*, vol. 4, no. 9, pp. 1011–1015, 2017.
- [189] V. Brasch, M. Geiselmann, T. Herr, G. Lihachev, M. H. P. Pfeiffer, M. L. Gorodetsky, and T. J. Kippenberg, “Photonic chip-based optical frequency comb using soliton cherenkov radiation,” *Science*, vol. 351, no. 6271, pp. 357–360, 2016.
- [190] K. P. Leisman, D. Zhou, J. W. Banks, G. Kovačič, and D. Cai, “Effective dispersion in the focusing nonlinear schrödinger equation,” *Phys. Rev. E*, vol. 100, p. 022215, Aug 2019.
- [191] Y. Lumer, Y. Plotnik, M. C. Rechtsman, and M. Segev, “Nonlinearly induced  $pt$  transition in photonic systems,” *Phys. Rev. Lett.*, vol. 111, p. 263901, Dec 2013.
- [192] A. U. Hassan, H. Hodaei, M.-A. Miri, M. Khajavikhan, and D. N. Christodoulides, “Non-linear reversal of the  $\mathcal{PT}$ -symmetric phase transition in a system of coupled semiconductor microring resonators,” *Phys. Rev. A*, vol. 92, p. 063807, Dec 2015.
- [193] M. Bayer, T. Gutbrod, J. Reithmaier, A. Forchel, T. Reinecke, P. Knipp, A. Dremin, and V. Kulakovskii, “Optical modes in photonic molecules,” *Phys. Rev. Lett.*, vol. 81, no. 12, pp. 2582–2585, 1998.
- [194] S. V. Boriskina, *Photonic Molecules and Spectral Engineering*, pp. 393–421. Boston, MA: Springer US, 2010.
- [195] M. Zhang, C. Wang, Y. Hu, A. Shams-Ansari, T. Ren, S. Fan, and M. Lončar, “Electronically programmable photonic molecule,” *Nat. Photonics*, vol. 13, no. 1, pp. 36–40, 2019.
- [196] J. von Neumann and E. P. Wigner, “Über das verhalten von eigenwerten bei adiabatischen prozessen,” in *The Collected Works of Eugene Paul Wigner*, pp. 294–297, Springer, 1993.
- [197] T. Carmon, H. G. L. Schwefel, L. Yang, M. Oxborrow, A. D. Stone, and K. J. Vahala, “Static envelope patterns in composite resonances generated by level crossing in optical toroidal microcavities,” *Phys. Rev. Lett.*, vol. 100, p. 103905, Mar 2008.
- [198] A. Savchenkov, A. Matsko, W. Liang, V. Ilchenko, D. Seidel, and L. Maleki, “Kerr frequency comb generation in overmoded resonators,” *Opt. Express*, vol. 20, no. 24, pp. 27290–27298, 2012.
- [199] Y. Liu, Y. Xuan, X. Xue, P.-H. Wang, S. Chen, A. J. Metcalf, J. Wang, D. E. Leaird, M. Qi, and A. M. Weiner, “Investigation of mode coupling in normal-dispersion silicon nitride microresonators for kerr frequency comb generation,” *Optica*, vol. 1, no. 3, pp. 137–144, 2014.
- [200] T. Herr, V. Brasch, J. D. Jost, I. Mirgorodskiy, G. Lihachev, M. L. Gorodetsky, and T. J. Kippenberg, “Mode spectrum and temporal soliton formation in optical microresonators,” *Phys. Rev. Lett.*, vol. 113, p. 123901, Sep 2014.

## Bibliography

---

- [201] H. Guo, E. Lucas, M. H. Pfeiffer, M. Karpov, M. Anderson, J. Liu, M. Geiselmann, J. D. Jost, and T. J. Kippenberg, “Intermode breather solitons in optical microresonators,” *Phys. Rev. X*, vol. 7, no. 4, p. 041055, 2017.
- [202] M. H. P. Pfeiffer, J. Liu, A. S. Raja, T. Morais, B. Ghadiani, and T. J. Kippenberg, “Ultra-smooth silicon nitride waveguides based on the damascene reflow process: fabrication and loss origins,” *Optica*, vol. 5, no. 7, p. 884, 2018.
- [203] P. Del’Haye, O. Arcizet, M. L. Gorodetsky, R. Holzwarth, and T. J. Kippenberg, “Frequency comb assisted diode laser spectroscopy for measurement of microcavity dispersion,” *Nat. Photonics*, vol. 3, no. 9, p. 529, 2009.
- [204] X. Ji, J. K. Jang, U. D. Dave, M. Corato-Zanarella, C. Joshi, A. L. Gaeta, and M. Lipson, “Exploiting Ultralow Loss Multimode Waveguides for Broadband Frequency Combs,” *Laser and Photonics Reviews*, vol. 15, pp. 6–11, 2021.
- [205] J. R. Stone, T. C. Briles, T. E. Drake, D. T. Spencer, D. R. Carlson, S. A. Diddams, and S. B. Papp, “Thermal and nonlinear dissipative-soliton dynamics in kerr-microresonator frequency combs,” *Phys. Rev. Lett.*, vol. 121, no. 6, p. 063902, 2018.
- [206] H. A. Haus and W. Huang, “Coupled-mode theory,” *Proceedings of the IEEE*, vol. 79, no. 10, pp. 1505–1518, 1991.
- [207] Z.-H. Peng, C.-X. Jia, Y.-Q. Zhang, J.-B. Yuan, and L.-M. Kuang, “Level attraction and  $\mathcal{PT}$  symmetry in indirectly coupled microresonators,” *Phys. Rev. A*, vol. 102, p. 043527, Oct 2020.
- [208] G. Hatton, W. Lichten, and N. Ostrove, “Non-non-crossings in molecular potential energy curves,” *Chemical Physics Letters*, vol. 40, no. 3, pp. 437–440, 1976.
- [209] D. R. Yarkony, “Diabolical conical intersections,” *Rev. Mod. Phys.*, vol. 68, no. 4, p. 985, 1996.
- [210] A. Kordts, M. H. P. Pfeiffer, H. Guo, V. Brasch, and T. J. Kippenberg, “Higher order mode suppression in high-q anomalous dispersion sin microresonators for temporal dissipative kerr soliton formation,” *Opt. Lett.*, vol. 41, pp. 452–455, Feb 2016.
- [211] C. Kim, K. Yvind, and M. Pu, “Suppression of avoided resonance crossing in microresonators,” *Optics Letters*, vol. 46, no. 15, pp. 3508–3511, 2021.
- [212] W. Su, J. Schrieffer, and A. J. Heeger, “Solitons in polyacetylene,” *Phys. Rev. Lett.*, vol. 42, no. 25, p. 1698, 1979.
- [213] D. Dobrykh, A. Yulin, A. Slobozhanyuk, A. Poddubny, and Y. S. Kivshar, “Nonlinear control of electromagnetic topological edge states,” *Phys. Rev. Lett.*, vol. 121, no. 16, p. 163901, 2018.

- 
- [214] J. K. Asbóth, L. Oroszlány, and A. Pályi, *A short course on topological insulators*, vol. 919. Springer, 2016.
- [215] C.-K. Chiu, J. C. Y. Teo, A. P. Schnyder, and S. Ryu, “Classification of topological quantum matter with symmetries,” *Rev. Mod. Phys.*, vol. 88, p. 035005, Aug 2016.
- [216] P. St-Jean, V. Goblot, E. Galopin, A. Lemaître, T. Ozawa, L. Le Gratiet, I. Sagnes, J. Bloch, and A. Amo, “Lasing in topological edge states of a one-dimensional lattice,” *Nat. Photonics*, vol. 11, no. 10, pp. 651–656, 2017.
- [217] S. B. Ivars, Y. V. Kartashov, L. Torner, J. A. Conejero, and C. Milián, “Reversible self-replication of spatiotemporal kerr cavity patterns,” *Phys. Rev. Lett.*, vol. 126, p. 063903, Feb 2021.
- [218] E. A. Kuznetsov, *Wave Collapse in Nonlinear Optics*, pp. 175–190. New York, NY: Springer New York, 2009.
- [219] W. J. Firth, G. K. Harkness, A. Lord, J. M. McSloy, D. Gomila, and P. Colet, “Dynamical properties of two-dimensional kerr cavity solitons,” *J. Opt. Soc. Am. B*, vol. 19, pp. 747–752, Apr 2002.
- [220] W. J. Firth, A. J. Scroggie, G. S. McDonald, and L. A. Lugiato, “Hexagonal patterns in optical bistability,” *Phys. Rev. A*, vol. 46, pp. R3609–R3612, Oct 1992.
- [221] K. Komagata, A. Tikan, A. Tusnin, J. Riemensberger, M. Churayev, H. Guo, and T. J. Kippenberg, “Dissipative kerr solitons in a photonic dimer on both sides of exceptional point,” *Communications Physics*, 2021.
- [222] Y. V. Kartashov, M. L. Gorodetsky, A. Kudlinski, and D. V. Skryabin, “Two-dimensional nonlinear modes and frequency combs in bottle microresonators,” *Opt. Lett.*, vol. 43, pp. 2680–2683, Jun 2018.
- [223] J. J. Rasmussen and K. Rypdal, “Blow-up in nonlinear schroedinger equations – a general review,” *Physica Scripta*, vol. 33, pp. 481–497, jun 1986.
- [224] M. Tsutsumi, “Nonexistence of global solutions to the cauchy problem for the damped nonlinear schrödinger equations,” *SIAM journal on mathematical analysis*, vol. 15, no. 2, pp. 357–366, 1984.
- [225] B. Ilan, G. Fibich, and G. Papanicolaou, “Self-focusing with fourth-order dispersion,” *SIAM Journal on Applied Mathematics*, vol. 62, no. 4, pp. 1437–1462, 2002.
- [226] Y. S. Kivshar and D. E. Pelinovsky, “Self-focusing and transverse instabilities of solitary waves,” *Physics Reports*, vol. 331, no. 4, pp. 117–195, 2000.
- [227] A. Scroggie, W. Firth, G. McDonald, M. Tlidi, R. Lefever, and L. Lugiato, “Pattern formation in a passive kerr cavity,” *Chaos, Solitons & Fractals*, vol. 4, no. 8, pp. 1323–1354, 1994. Special Issue: Nonlinear Optical Structures, Patterns, Chaos.

## Bibliography

---

- [228] G. D'Alessandro and W. J. Firth, "Spontaneous hexagon formation in a nonlinear optical medium with feedback mirror," *Phys. Rev. Lett.*, vol. 66, pp. 2597–2600, May 1991.
- [229] A. K. Tusnin, A. M. Tikan, and T. J. Kippenberg, "Dissipative kerr solitons at the edge state of the su-schrieffer—heeger model," *Journal of Physics: Conference Series*, vol. 2015, p. 012159, 11 2021.
- [230] E. Lustig and M. Segev, "Topological photonics in synthetic dimensions," *Adv. Opt. Photon.*, vol. 13, pp. 426–461, Jun 2021.
- [231] M. A. Guidry, D. M. Lukin, K. Y. Yang, R. Trivedi, and J. Vučković, "Quantum optics of soliton microcombs," *Nature Photonics*, vol. 16, no. 1, pp. 52–58, 2022.
- [232] G. Huang, E. Lucas, J. Liu, A. S. Raja, G. Lihachev, M. L. Gorodetsky, N. J. Engelsen, and T. J. Kippenberg, "Thermorefractive noise in silicon-nitride microresonators," *Physical Review A*, vol. 061801, pp. 1–5, 2019.
- [233] M. L. Gorodetsky and A. E. Fomin, "Geometrical theory of whispering-gallery modes," *IEEE Journal of Selected Topics in Quantum Electronics*, vol. 12, no. 1, pp. 33–39, 2006.
- [234] B. Sturman, E. Podivilov, C. S. Werner, and I. Breunig, "Vectorial perturbation theory for axisymmetric whispering gallery resonators," *Phys. Rev. A*, vol. 99, p. 013810, Jan 2019.
- [235] J. Zhu, S. K. Ozdemir, Y.-F. Xiao, L. Li, L. He, D.-R. Chen, and L. Yang, "On-chip single nanoparticle detection and sizing by mode splitting in an ultrahigh-q microresonator," *Nat. Photon.*, vol. 4, no. 1, pp. 46–49, 2010.
- [236] D. V. Strekalov, C. Marquardt, A. B. Matsko, H. G. L. Schwefel, and G. Leuchs, "Nonlinear and quantum optics with whispering gallery resonators," *Journal of Optics*, vol. 18, p. 123002, nov 2016.
- [237] K. Ahnert and M. Mulansky, "Odeint—solving ordinary differential equations in c++," in *AIP Conference Proceedings*, vol. 1389, pp. 1586–1589, American Institute of Physics, 2011.
- [238] T. I. Lakoba, "Study of instability of the fourier split-step method for the massive gross-neveu model," *Journal of Computational Physics*, vol. 402, p. 109100, 2020.



# Alexander Tusnin

[alextusnin.github.io](https://alextusnin.github.io) | [LinkedIn](#) | [GitHub](#)

Email: [alextusnin@gmail.com](mailto:alextusnin@gmail.com) | Mobile: +41 788292022

11, Ch. du Fontenay, Yverdon-les-Bains, Vaud, Switzerland

## KEY STRENGTHS

---

- Modeling and Simulations
- Software design and development in Python and C++
- High-performance computing
- Data analysis and visualization

## EDUCATION

---

### Swiss Federal Institute of Technology Lausanne (EPFL)

PhD in Physics

Lausanne, Switzerland

2019-Present

### Superior National School of Advanced Techniques (ENSTA Paris, IP Paris)

Diplôme d'ingénieur: Analysis, Modeling, Simulation, with honors

Palaiseau, France

2017-2019

### Paris-Saclay University

MSc in Applied Mathematics, with honors

Versailles, France

2018-2019

### Novosibirsk State University

MSc in Physics, with honors

Novosibirsk, Russia

2012-2019

## PROFESSIONAL EXPERIENCE

---

### Laboratory of Photonics and Quantum Measurements, EPFL, PhD

"Emergent nonlinear dynamics in photonic lattices"

2019 – Present

Lausanne, Switzerland

- Designed and developed an open-source software [PyCORE](#) for optical frequency combs simulations using **Python** and **C++**, resulting in a 5x speed improvement over previous tools
- Conducted extensive numerical investigations using [PyCORE](#) and **Lumerical** to design novel photonic devices
- Contributed to experimental result verification by developing **analytical models**
- Managed a project focused on the study and initial experimental demonstration of optical frequency combs in topological lattices
- Produced comprehensive documentation for [PyCORE](#)
- Supervised master students in conducting numerical simulations
- Contributed to the preparation of several successful project proposal submissions

### Photonics Laboratory, Institute of Automation and Electrometry, Research Assistant (Part-time)

"Light-induced plasmon forces"

2016-2019

Novosibirsk, Russia

- Advanced the theory of surface plasmon interactions
- Performed extensive calculations using **Wolfram Mathematica**

- Verified theoretical predictions through **Comsol** simulations

**PHELIQS Laboratory**, Institute for Nanoscience and Cryogenics (CEA), Summer Intern

2018

*"Theoretical investigation of dipolar magnetic materials"*

Grenoble, France

- Investigated magnetic ordering in  $\text{GdLiF}_4$  using **C++**
- Contributed to the development of models for studying dipole-dipole interactions

**CMD-3 Endcap Calorimeter Lab**, Budker Institute of Nuclear Physics, Research Assistant (Part-time)

2013-2016

*Electron-positron collisions and detector maintenance*

Novosibirsk, Russia

- Analyzed electron-positron collisions data from the VEPP-2000 collider using **C++** and **ROOT**
- Developed the calibration for trigger electronics in the CMD-3 detector using **Python**
- Investigated the impact of irradiation on the luminescence of  $\text{Bi}_3\text{Ge}_4\text{O}_{12}$  crystals

## EXPERTISE

---

**Software:** Proficient in Python, Numpy/Scipy, Matplotlib, Plotly, C/C++, Numerical recipes, Odeint, Eigen, MPI, Comsol, Lumerical, Wolfram Mathematica, Jupyter book, Git, Matlab, Linux/Unix,  $\text{\LaTeX}$

**Physics & Math:** Specialized in nonlinear dynamics, nonlinear optics, data analysis, statistics, optimization, partial differential equations, finite element method, and parallel computing

**Communication:** Skilled in intercultural communication, presenting technical concepts, science communication, reviewing scientific work, teaching, project management, and student supervision

**Experiment:** Experience in designing and testing integrated photonic circuits, generating optical frequency combs, analyzing electron-positron collision data, and maintaining calorimeter detectors

## LANGUAGES

---

**English** Fluent spoken and written (C1)

**French** Fluent spoken (B2) and intermediate written (B1). Diplôme d'ingénieur in France, TCF certificate

**Russian** Native

## EXTRACURRICULAR ACTIVITIES

---

Former member of the "Teaching Quality at the Department of Physics" committee at Novosibirsk State University from 2015 to 2017.

Currently holding the position of Editor for the internal scientific journal at LPQM since 2020.

Actively contributed to the organization of the CMEP 2020 workshop at EPFL and Microcomb 2022 in Saanen.

Engaged in science popularization efforts, including participation in the organization of the "Scientastic 2022" science festival at EPFL.

A former member of BEST (Board of European Students of Technology) at ENSTA Paris from 2017 to 2018.

Played bass in *Diable Rabattable* and guitar in a jazz band at NSU and a rock group called *Krai* (in Perm).

Participated in the Techniques Avancées rugby club during 2017-2018.

Explored snowboarding in various locations including the French and Swiss Alps, Sheregesh, and the Ural mountains.

## SCHOLARSHIPS

---

Awarded the French Government scholarship (BGF) for degree training in 2017-2018.

Received the ENSTA Paris scholarship for international students in 2018-2019.

## PERSONAL INFORMATION

---

28 years old, married, Russian citizenship, Swiss B permit